University of Thessaly
Department of Mechanical Engineering

UNIVERSITY OF
THESSALY

Diploma Thesis

Academic Year: 2020 - 2021

NUMERICAL INVESTIGATION OF THE FLOW FIELD OF A FULLY DETAILED GENERIC SUV BODY

by

Konstantinos D. Polyzos

Submission Date: September 26, 2021
Supervisors: Dr Georgios Charalampous, University of Thessaly
Vangelis Skaperdas, BETA CAE Systems SA

This thesis is submitted in partial fulfilment of the requirements
for the award of the Diploma in Mechanical Engineering

"If you can't fly, then **run**.
If you can't run, then **walk**.
If you can't walk, then **crawl**,
but by all means, **keep moving**."
- Martin Luther King Jr.

Abstract

In the last thirty years, the shape of automobiles has changed significantly with the main criterion being the reduction of the aerodynamic resistance, which is explicitly linked to the energy/fuel consumption of the vehicle. A recent research revealed that 43.4% of the total greenhouse gas emissions are attributed to cars and as a consequence, both the European and the United States Commission proposed restrictions on the emission levels to prevent air pollution and protect the environment.

To meet these targets, automotive manufacturers, apart from wind tunnel testing, spent a sizeable amount of their resources for virtual simulation of their cars with the use of Computational Fluid Dynamics (CFD). Reliable simulation of the complex separated turbulent flow around vehicles is becoming an even more crucial goal towards increasing fuel efficiency. In the context of this work, a thorough investigation of various CFD parameters was conducted firstly at the simplified SAE Notchback 20° Backlight reference model and the most accurate CFD setup was used to simulate the realistic AeroSUV reference model, as an attempt to bridge the gap between simplified and realistic models.

The investigation started with the surface and volume mesh type and resolution, continued with the layers approach and the turbulence modelling, and the last step was to conduct transient simulations in order to capture in greater detail the unsteady flow phenomena. Simulation accuracy was assessed against aerodynamic forces and surface pressures, as measured during wind tunnel testing. The most accurate CFD setup predicted the drag coefficient for the SAE Notchback 20° Backlight with -0.26% error and the pressure distribution across the centerline with Mean Absolute Percentage Error equal to 8.9% and Standard Deviation (SD) equal to 5.3 percentage units.

This CFD setup was then used to simulate all the variants of the realistic AeroSUV reference model, namely the fastback, the notchback and the squareback configuration. The CFD setup provided an accurate solution for the fastback and the notchback configurations, predicting the drag coefficient (C_D) with -0.28% and -0.97% error from the experimental value. However, the setup failed to provide a high fidelity prediction for the squareback configuration and a new investigation started resulting in -1.76% error in the predicted C_D.This study resulted in a robust CFD methodology for highly detailed SUV models, which was implemented using a simplified model for time and resources saving purposes.

Keywords:
Aerodynamics, CFD, Wind Tunnel, Correlation, AeroSUV, SAE Notchback, ANSA, OpenFOAM

Funding

This thesis has been funded completely by BETA CAE Systems SA and was conducted at the company's headquarters located in Thessaloniki, Greece.

Acknowledgments

This work would not have been possible without the endless support and guidance of my colleagues at BETA CAE Systems SA. Thank you all for your help and especially I am more than grateful to my manager Vangelis Skaperdas and my colleagues Nikolaos Christodoulou, Grigoris Fotiadis and Aristotelis Ioannidis for their practical and moral support from back to 2017 until now.

I would like to express my sincere gratitude to my family for trusting and supporting me in every step of my life from day one. A very special thank you goes to my brother Nikos for always being there when I needed him and for pushing me to become better and better every single day. Your relentless support is the main reason why I am feeling confident to delve deeper into demanding tasks, to take challenges that seem impossible and to never give up on chasing my dreams!

Special acknowledgement goes to my friends Michalis, Spiros, Panagiotis, Vasilis, Gerasimos, Giannis, Jason, Spiros and Vangelis for all the moments that we shared and are going to share in the future. I would like to thank them for all the encouragement and for reminding me that there is life outside of the formula student in cases when I got lost. Last but for sure not least, I would like to thank my colleague and friend Stratos for being there in every difficult moment throughout the last months of conducting this research. Time flies but memories last forever!

To all former, present and future members of Centaurus Racing Formula Student Team, thank you for all the fun and the moments that we shared. Even though I am not an active member any more, my door will always be open for advice.

The best is yet to come!

Contents

List of Tables

List of Figures

List of Equations

Nomenclature

α	Road Inclination	$^\circ$
ϵ	Semi Empirical Log-Law Coefficient	9.793
κ	Semi Empirical Log-Law Coefficient	0.4187
λ	Eigenvalue	
μ	Viscosity	kg/m/s
μ_{road}	Rolling Friction Coefficient	
ν	Kinematic Viscosity	m^2/s
Ω	Anti-symmetric Tensor	
ω	Specific Turbulent Dissipation Rate	m^2/s^3
$\overline{\phi}$	Time Averaged Component	
ϕ'	Fluctuating Component	
ψ	Distance from the Wall	m
ρ	Density	kg/m^3
τ_w	Wall Shear Stress	Pa
θ	Face-Non-Orthogonality	
A	Projected Frontal Area	m^2
a	Acceleration	m/s^2
C_D	Drag Coefficient	
C_f	Skin Friction Coefficient	
C_L	Lift Coefficient	
C_M	Momentum Coefficient	
C_{Lf}	Front Lift Coefficient	
C_{Lr}	Rear Lift Coefficient	
d	Cell Center Distance	m
f	Vortex Shedding Frequency	s^{-1}
F_X	Drag Force	N

F_Y	Side Force	N
F_Z	Lift Force	N
F_{accel}	Acceleration Resistance Force	N
F_{climb}	Inclination Resistance Force	N
F_{drag}	Air Resistance Force	N
$F_{rolling}$	Rolling Resistance Force	N
F_{tr}	Tractive Force	N
F_{Zf}	Front Lift Force	N
F_{Zr}	Rear Lift Force	N
g	Acceleration of Mass	9.81 m/s^2
k	Turbulent Kinetic Energy	J/kg = m$^2/s^2$
L_{ref}	Reference Length	m
m	Mass	kg
M_X	Rolling Moment	N$\cdot m$
M_Y	Pitching Moment	N$\cdot m$
M_Z	Yawing Moment	N$\cdot m$
Re	Reynolds Number	
S	Symmetric Tensor	
Sr	Strouhal Number	
U	Velocity	m/s
U^+	Non Dimensional Flow Velocity	
WB	Wheelbase Distance	m
y^+	Non Dimensional Distance from the Wall	

Acronyms

CFD Computational Computational Fluid Dynamics. 4

CFL Courant-Friedrichs-Lewy. 55

CFR Code of Federal Regulations. 9

DDES Delayed Detached Eddy Simulation. 88

DES Detached Eddy Simulation. 53

DNS Direct Numerical Solution. v, 21

ECARA European Car Aerodynamic Research Association. 12

FKFS Forschungsinstitut fur Kraftfahrwesen und Fahrzeugmotoren Stuttgart. 14

GIS Grid Induced Separation. 54

ICE Internal Combustion Engine. 4

L2 Lambda 2 Criterion. 67

LDV Laser Doppler Velocimetry. v, 11

LES Large Eddy Simulation. v, 20

M1G Off-road Vehicle Category defined by UNECE. 9

MAPE Mean Absolute Percentage Error. 63

MaxPE Maximum Percentage Error. 63

NEDC New European Driving Cycle. 2

PID Property Identification. 33

RANS Reynolds-Averaged Navier-Stokes. 50

RMS Root Mean Square. 102

SAE Society of Automotive Engineers. 10

SD Standard Deviation. 63

SGS Sub-Grid Scale. 50

SST Shear Stress Transport. 51

SUV Sport Utility Vehicle. 4

TKE Turbulent Kinetic Energy. 17

UNECE United Nations Economic Commission for Europe. 2

URANS Unsteady-Reynolds Averaged Navier-Stokes. 52

USA United States of America. 9

VPP Vector Penalty Projection. 14

WLTP World harmonised Light Vehicle Test Procedure. 2

WMLES Wall-Modelled Large Eddy Simulation. 53

WTT Wind Tunnel Test. 10

1 Introduction

"Quality means doing it right when no one is looking"

-Henry Ford

1.1 Historical Context

The history of automobile started in 1769 when the first steam powered car, built by Nicolas-Joseph Cugnot [19], was introduced to serve human transportation purposes. Through the next years, the steam engines were replaced by the well-known internal combustion petrol engines and significant changes were made to the overall shape of the vehicle. In 1908, the mass production of Ford's Model T [20], the first middle-class-affordable automobile, set the milestone for the modern day car to become the most widespread means of transport.

In the very first years, the main objectives during the external design of a car were passenger comfort and manufacturability of the various car parts; that is also reflected in their "boxy" shape, comprised of numerous sharp edges and bluff surfaces. Considering the low transportational speeds of early vehicles, the impact of air resistance in their performance was minor and was completely neglected during the design process. In contrast to naval and airplane designers, who were inspired by fish and birds respectively, there is nothing relative to a car in nature. After numerous trials and experimental tests, aerodynamics were gradually incorporated in vehicle technology and design.

The oil crisis of 1973 [21], revealed the crucial role of automotive aerodynamics with regards to fuel consumption. Numerous companies focused on increasing the fuel efficiency of cars in an attempt to balance out the soaring oil costs. Of utmost importance was the reduction of the aerodynamic drag force by improving the shape of the car. The evolution of vehicle's shape though the years is clearly depicted in Figure 1.1.

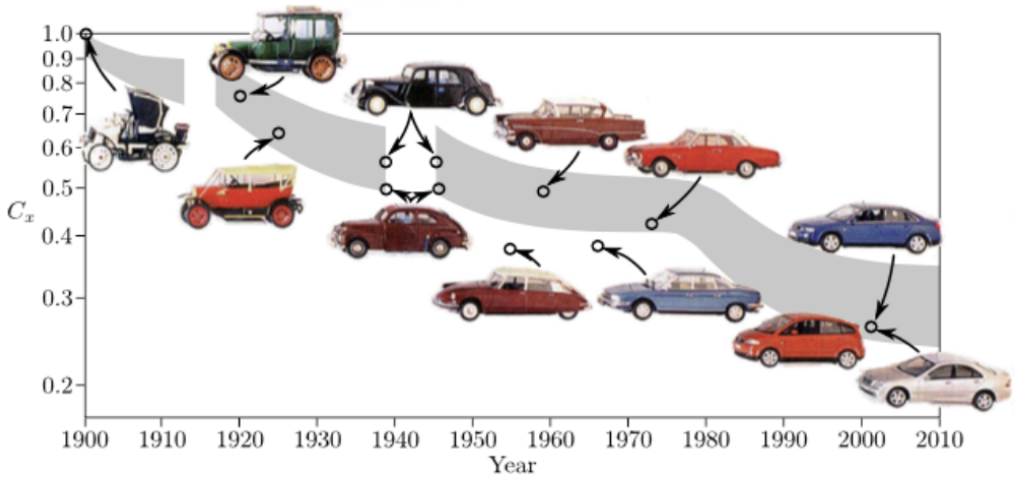

Figure 1.1: Vehicle shape evolution through the years [3].

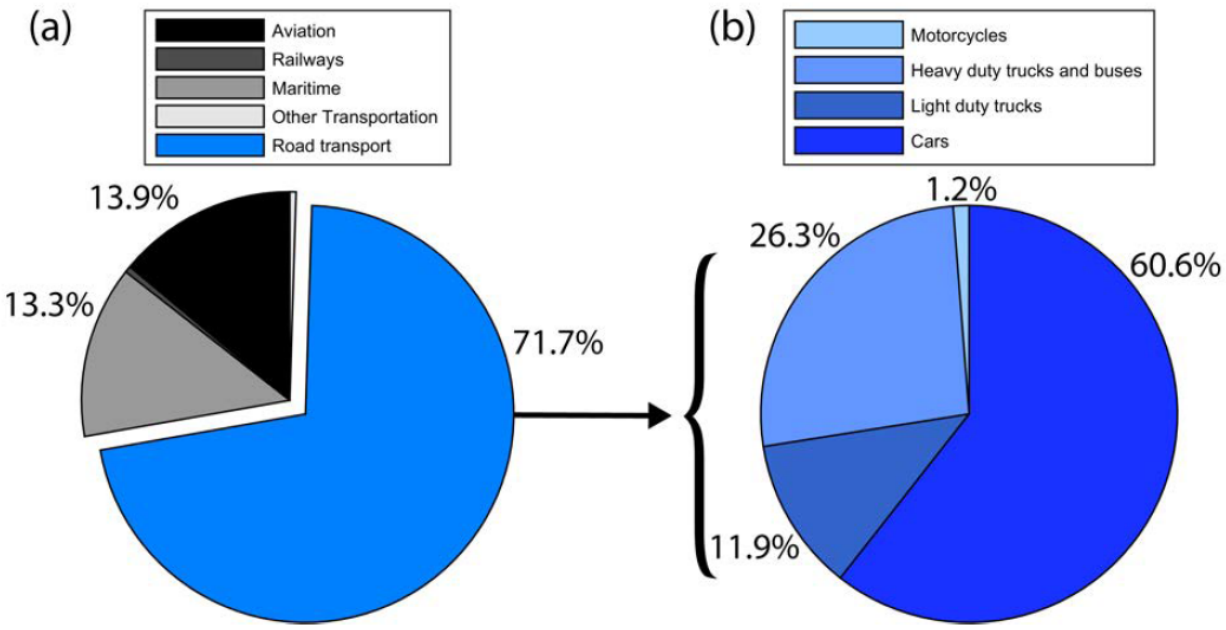

Figure 1.2: (a) Greenhouse gas emissions from transports in Europe 2019. (b) Divisions of road transport gas emissions [4].

The oil crisis, however, was not the only stimulus that led to this change. A driving force of the latter days is global warming and climate change that is explicitly linked to vehicle emissions. During the last thirty years, greenhouse gas emissions from means of transport have gradually increased in Europe, covering 25% of the global footprint in 2017 [4]. Analysing further the emissions coming from transports, 71.7% are from road transport (Figure 1.2) and more precisely, 60.6% of this division is due to cars; the main source of air pollution in cities [22]. After cars, heavy duty trucks and buses are responsible for more than a quarter percent of transport-related greenhouse gas emissions.

As a consequence, restrictions had to be applied to prevent air pollution and protect the environment. The European Commission introduced legislation and directives with main objective the reduction of carbon dioxide (CO_2) emissions in 2009. The next goal has been set for 2021, with the emissions to be lowered to 95 grams CO_2/km. To meet these emission levels, fuel consumption of petrol and diesel internal combustion engines of modern passenger cars must be lower than 4.1 Liters/100km and 3.6 Liters/100km, respectively. Similar emission restrictions were also applied to trucks and buses. The CO_2 emitted by these vehicles must be decreased from 2019 levels by 15% until 2025 and 30% until 2030 [23].

To achieve an enhanced control of vehicle emissions, the Inland Transport Committee of the United Nations Economic Commission for Europe (UNECE) adopted the World harmonised Light Vehicle Test Procedure (WLTP) [24] in 2017, replacing the obsolete New European Driving Cycle (NEDC) [25] homologation procedure, used from the early 1990s. One of the main goals of the WLTP was to better match the laboratory estimates of fuel consumption and emissions with the measures of an on-road driving condition.

The key differences between these two procedures are that WLTP:

- Incorporates higher average and maximum road speeds
- Includes a wider range of driving conditions
- Simulates a longer driving distance
- Has higher average and maximum drivepower
- Examines more abrupt accelerations and decelerations
- Tests optional equipment separately

The strict modern testing procedure in combination with the emission regulations, led automotive manufacturers to focus on enhancing the energy efficiency of vehicles by cutting down all forms of resistances and losses. Sorting all sources of energy loss, the tractive force plays a primary role for a vehicle moving under its own power and can be decomposed into four discerned parts, shown in Equation 1.1.

$$F_{tr} = F_{climb} + F_{accel} + F_{rolling} + F_{drag} \quad \text{(Eq. 1.1)}$$

where F_{tr} is the tractive force, F_{climb} is the resistance due to driving on an inclined road, F_{accel} is the resistance due to acceleration, $F_{rolling}$ is the resistance due the rolling motion of the tyres relative to the road surface, also known as rolling friction, and F_{drag} is the air resistance also known as aerodynamic drag. These terms can be also written as:

$$F_{tr} = mgsin(\alpha) + ma + mg\mu_{road} + 0.5\rho_{\infty}{U_{\infty}}^2 A_{ref} C_D \quad \text{(Eq. 1.2)}$$

Here m is the total mass of the vehicle, g is the gravitational constant, α is the inclination of the road, a is the acceleration of the vehicle, μ_{road} is the rolling friction coefficient between the tyres and the road surface, ρ_{∞} is the air density, U_{∞} is the relative speed between the vehicle and the air around it, A_{ref} is the reference area and for automotive applications the projected frontal area of the vehicle is used and C_D is the aerodynamic drag coefficient of the vehicle.

For a vehicle moving on a flat road the F_{climb} term of Equation 1.2 is zero. The term F_{accel} has a linear dependency with speed and $F_{rolling}$ is almost constant. However, the aerodynamic drag force F_{drag} increases with the square of velocity. This means that at high speeds, this term dominates in Equation 1.2 and aerodynamic drag force has a vital role on vehicle's fuel consumption and thus on the emitted greenhouse gases. For cars, aerodynamic resistance dominates for driving speeds over 60 km/h and for trucks this speed is approximately 80 km/h.

Finally through the last years, hybrid or fully-electric vehicles have become increasingly popular and they constitute a crucial factor in the aerodynamic optimisation of modern day

vehicles, since air resistance explicitly affects the achievable driving range. A recent research conducted by AUDI AG, revealed that a change of 0.005 in the aerodynamic drag coefficient (C_D) of a vehicle, corresponds to 2.5km in driving range for their all-electric Sport Utility Vehicle (SUV) Audi e-tron [26].

Electric vehicles are capable of recovering part of the energy consumed to accelerate during deceleration and in particular through the kinetic energy recovery system. However, there is no such system to recover the energy consumed to overcome aerodynamic resistance. Any amount of energy spent in this direction is characterized as a complete loss. Kawamata *et al.* [27], reported that the relative proportion of the consumed total energy due to aerodynamic resistance for an all-electric vehicle is 4.4 times larger than that of an Internal Combustion Engine (ICE) vehicle. All the above, indicate that aerodynamic development is a key factor in the production of a high range electric vehicle.

1.2 Computational Fluid Dynamics for Aerodynamic Applications

Historically, wind tunnel testing has been the main tool for aerodynamic assessment and development. Over the last twelve years, eight wind tunnels have been, or are planned to be, built in Europe [2] revealing the great need for extensive aerodynamic investigation. The urgent demand for constructing these multi-million facilities indicates the increasing difficulty in further reducing the drag of the already well-optimised geometries.

However, the construction, operational and maintenance costs of a wind tunnel are tremendous and many companies cannot even afford using them. As a result, they turn to digital solutions and more precisely to virtual simulations with the use of Computational Computational Fluid Dynamics (CFD). Open source codes can now handle complex flows and geometries efficiently and produce accurate results, leading to ever-decreasing computational costs for aerodynamic simulations. Moreover, a single run of a CFD simulation can provide data for the whole flow field an not only the aerodynamic forces. Thus, through a single run, a lot more information can be derived compared to the data that can be gathered from the same experimental measurements.

The use of virtual simulations, gives the chance to simulate various flow scenaria which cannot be easily or accurately represented in experimental testing, such as cornering conditions or upstream turbulence. The simulation of different flow conditions increases the possibility of enhancing the aerodynamic efficiency of the vehicle and the accuracy of the predicted fuel or energy consumption and vehicle emissions.

Nonetheless, setting up a CFD simulation in order to give accurate predictions by means of minimizing the error between CFD and the experimentally derived data, is quite challenging since numerous parameters can affect the final outcome. As a side note, the continuous investment in physical facilities also illustrates the lack of maturity of computational techniques revealing a great need for further research on that field. Reliable CFD simulations of the complex separated turbulent flow around vehicles is becoming an even more crucial goal towards increasing fuel efficiency; this subject is further analysed in the following chapters.

1.3 Automotive Specific Nomenclature

Before delving deeper into automotive aerodynamics, it would be wise to have a quick introduction to the specific terminology used in automotive.

1.3.1 Vehicle Coordinate System

Throughout this research, the Z-Up coordinate system is used. More precisely, as shown in Figure 1.3 below, the x-axis is aligned with the longitudinal axis of the vehicle and the positive direction is the same as the direction of the fluid flow at the inlet. The y-axis is aligned with the lateral axis of the vehicle and the positive direction is derived by assuming a Right-Handed Coordinate System. The origin is located at the center of gravity of the car. For a model with no wheels, the mid-track and wheelbase position is defined as the lateral and longitudinal center of the 4 pins used to mount the model.

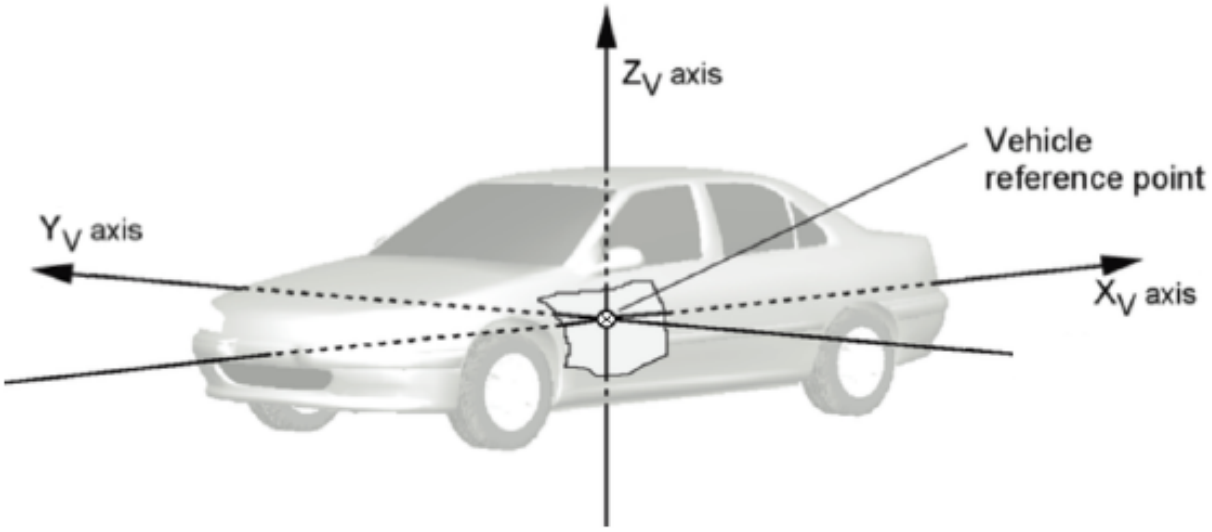

Figure 1.3: The Z-Up coordinate system used throughout this work [2] *(edited by the author)*.

1.3.2 Aerodynamic Forces and Moment Convention

The convention used for forces and moments throughout this research is clearly depicted in Figure 1.4.

– **Drag (F_X):** Force acting along the vehicle's longitudinal axis (x-axis) and it is positive when it opposes the vehicle's direction of travel.

– **Lift (F_Z):** Force acting along the z-axis and it is positive when acting to lift the vehicle from the ground. The opposite of Lift is called Downforce and it is commonly used for automotive applications.

– **Side Force (F_Y):** Force acting along the lateral axis (y-axis) and it is positive when acting to pull the vehicle to the right.

– **Rolling Moment (M_X):** Moment is the product of a force and a distance. A rolling moment tends to cause a vehicle rotation about the longitudinal axis and it is positive when acting to lift the right portion of the vehicle from the road surface.

– **Pitching Moment (M_Y):** The moment that tends to rotate the vehicle around the lateral axis and it is positive when acting to lift the front portion of the vehicle from the road surface.

– **Yawing Moment (M_Z):** The moment that tends to rotate the vehicle around the vertical axis (parallel to z-axis) and it is positive when acting to tilt the rear portion of the vehicle to the right direction.

The lift force produced by the vehicle is often decomposed into front (F_{Zf}) and rear (F_{Zr}) lift force. These forces are applied on the axles and are positive when acting to lift the front and rear axle respectively from the road surface. These components are calculated based on the pitching moment (M_Y) and the model's wheelbase *(WB)* from Equations 1.3 and 1.4.

$$F_{Zf} = \frac{M_Y}{WB} + \frac{F_Z}{2} \qquad \text{(Eq. 1.3)}$$

$$F_{Zr} = \frac{M_Y}{WB} - \frac{F_Z}{2} \qquad \text{(Eq. 1.4)}$$

where WB is defined as the distance between the axis of rotation of the front and rear axles.

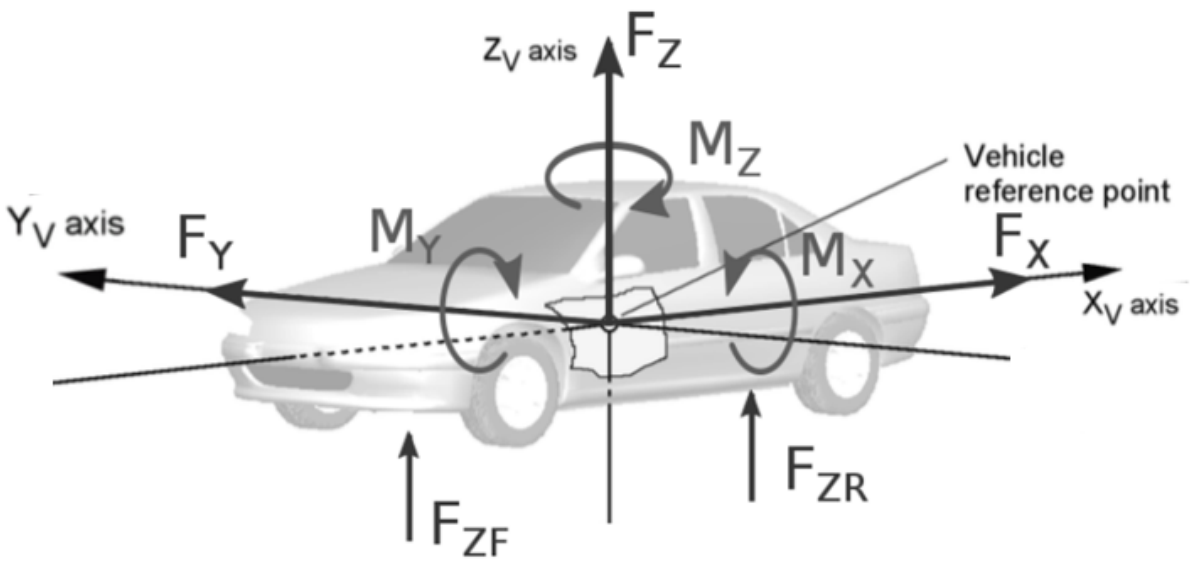

Figure 1.4: Forces and moments convention used throughout this work [2] *(edited by the author).*

1.3.3 Automotive Geometrical Terms

Throughout this work a number of automotive specific geometrical terms are used; these are discrebed below and shown visually in Figure 1.5.

- **A-Pillar:** The first pillar in the glasshouse.
- **B-Pillar:** The second pillar in the glasshouse.
- **C-Pillar:** The third pillar in the glasshouse.
- **Trailing-Pillar:** The most rearward pillar in a vehicle's glasshouse.
- **Roof Header:** The transition between the roof and the rear windshield.
- **Backlight:** The rear windshield of a vehicle.
- **Bootdeck:** The horizontal surface between the backlight and the rear end.
- **Base:** The surfaces of the rear end of the vehicle.

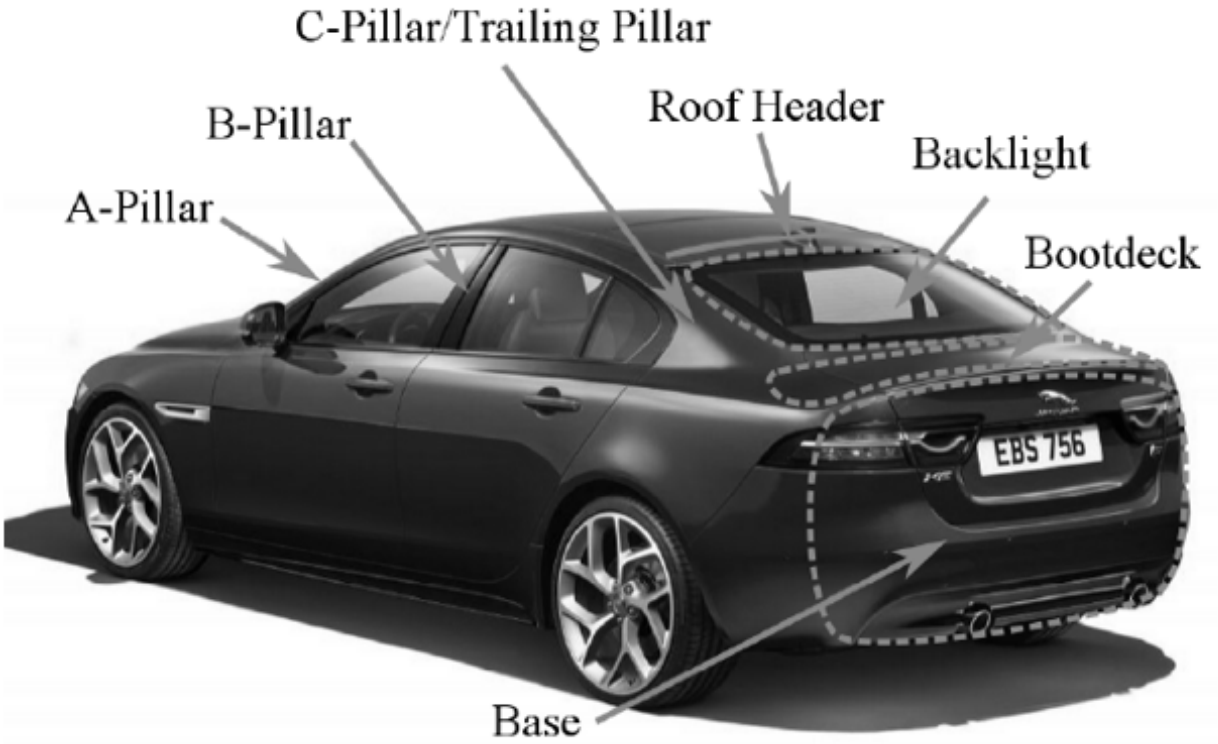

Figure 1.5: Geometrical term for automotive applications [2] *(edited by the author).*

1.4 Sport Utility Vehicles

Within the last few years, Sport Utility Vehicles (SUVs) have gained a big share of the automotive global market. SUV is a car classification that combines basic elements of a classic road-going sedan and an off-road vehicle. In order for an automobile to be classified as SUV, it must comply with basic geometric requirements. But before proceeding with the European Union legal requirements for SUVs, it would be advisable to take a look at the basic geometrical characteristics of an automobile:

– **Front Overhang:** The distance between the frontmost point of the front wheels and the frontmost point of the car. A vehicle with a short overhang at the front will have a greater approach angle than one with a longer overhang.

– **Approach Angle:** The angle formed between the ground and the line drawn between the front tire and the lowest-hanging part of the vehicle at the front overhang. It is the maximum angle of a ramp onto which a vehicle can climb from a horizontal plane without interference.

– **Break-Over Angle:** The angle formed between the two straight lines that join the middle point of the underbody with the contact patch of the front and the rear wheels with the road surface respectively. It is also known as ramp-over angle.

– **Rear Overhang:** The distance between the rearmost point of the rear wheels and the rearmost point of the car.

– **Departure Angle:** The angle formed between the ground and the line drawn between the rear tire and the lowest-hanging part of the vehicle at the rear overhang. It is the maximum ramp angle from which a vehicle can descend to a horizontal plane without interference.

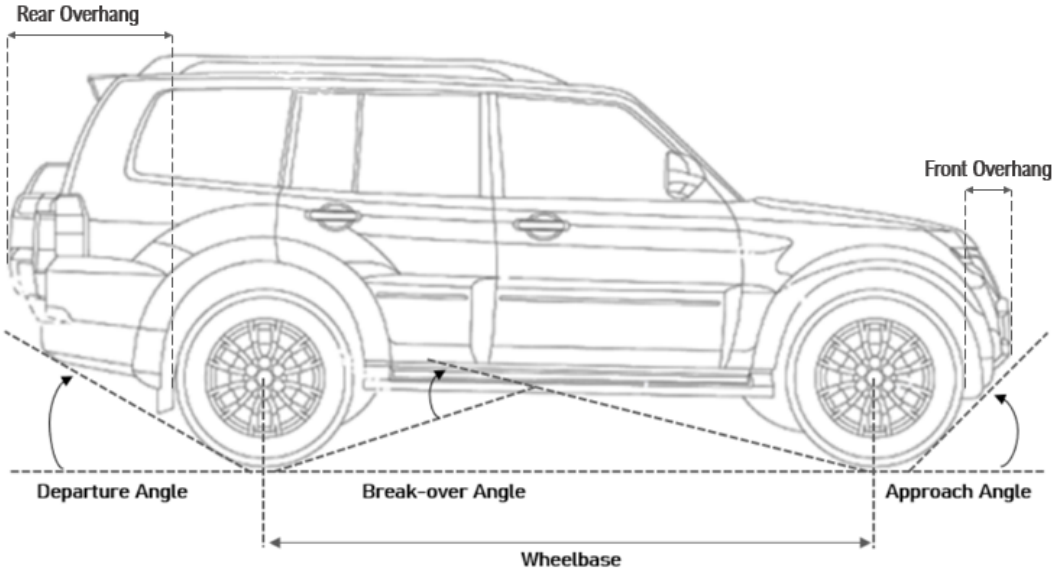

Figure 1.6: Basic geometric characteristics of a road-vehicle [5] *(edited by the author).*

Modern-day SUVs have greater ride height and wheel size compared to the rest road-going vehicles. The approach, break-over and departure angles, seen in Figure 1.6, are greater as well compared to estates and sedans. However, these angles are not unique or constant. Some SUVs have lower ride heights, in order to emphasize on their on-road ability, known as city-crossover SUVs. On the other hand, some have a higher chassis, enhancing their off-road look and ability. It is clear that numerous combinations of these characteristics can be made resulting in an extended variety of SUV geometries.

1.4.1 Requirements

In the European Union, the classification of vehicles is based on UNECE standards. The SUV category is mentioned with the abbreviation M1 [28] and the requirements regarding their geometrical characteristics are:

- Minimum ground clearance:
  - 180mm underneath the axles
  - 200mm in the middle of the vehicle
- Approach angle to be at least 25°
- Departure angle to be at least 20°
- Break-over angle to be at least 20°

In the United States of America (USA), SUVs are referred as light-duty tracks and, according to the Code of Federal Regulations (CFR), the legal requirements are similar to the M1G category in Europe. The only differences are noticed in the approach and break-over angles, which in the USA are set to be at least 28° and 14°, respectively. In both sets of regulations, a vehicle is allowed to not comply with one geometric regulation and still be considered as a legal SUV. Finally, both the European and USA legislation do not set any limitation on the overall dimensions of the vehicle.

As it was mentioned before, SUVs can be typified into various categories; the most important of them being:

- **Crossover SUV:** Also known as CSUV, shares platform with a passenger car
- **Mini SUV:** The smallest segment of the SUV class
- **Compact SUV:** The next bigger size after the mini SUV
- **Full-Size SUV:** The most commonly produced type of SUV
- **Extended-Length SUV:** It is similar to a full-size SUV but has greater wheelbase

The model analysed in this research is a generic full-size sport utility vehicle.

1.5 Reference Models

A reference model is a geometry that often leads to the formation of complex flow phenomena (such as unsteady wake topologies or strong vortical structures) or consists of surfaces in critical angles near the flow detachment point. These models are extensively analysed through wind tunnel testing and by utilizing numerous data acquisition methods, a set of experimental data is derived. This set is then deployed to improve CFD setups, and more precisely to decrease the deviation between CFD and Wind Tunnel Test (WTT) data. Numerous reference models have been created through the years and can be divided into two main categories: simple bodies and basic car shapes.

The first category includes geometries such as the Ahmed [15] or the SAE Notchback [29] reference body depicted in Figure 1.7(a). These models have a very simple geometry but form three dimensional flow fields similar to those of realistic road-vehicles. In an attempt to expand the experimental data envelop, the shape of their rear end can be altered resulting in different variants. The SAE Notchback model will be further analyzed in Chapter 4: "Results I – SAE Notchback" and results about the fidelity of the CFD model will be presented.

The models of the second category have more complex shapes that can represent different vehicle classes. The first generic model that best depicts the SUV geometry is shown in Figure 1.7(b) and it was introduced by Al-Garni *et al.* [30]. The cross section of this model is similar to an SUV projected frontal area but the approach and departure angles do not comply with the SUV restrictions defined by UNECE and CFR. In addition, the wheels are simplified and fully integrated into the main geometry. In 2015, Wood *et al.* [2] improved this geometry by generating the generic SUV, shown in Figure 1.7(c).

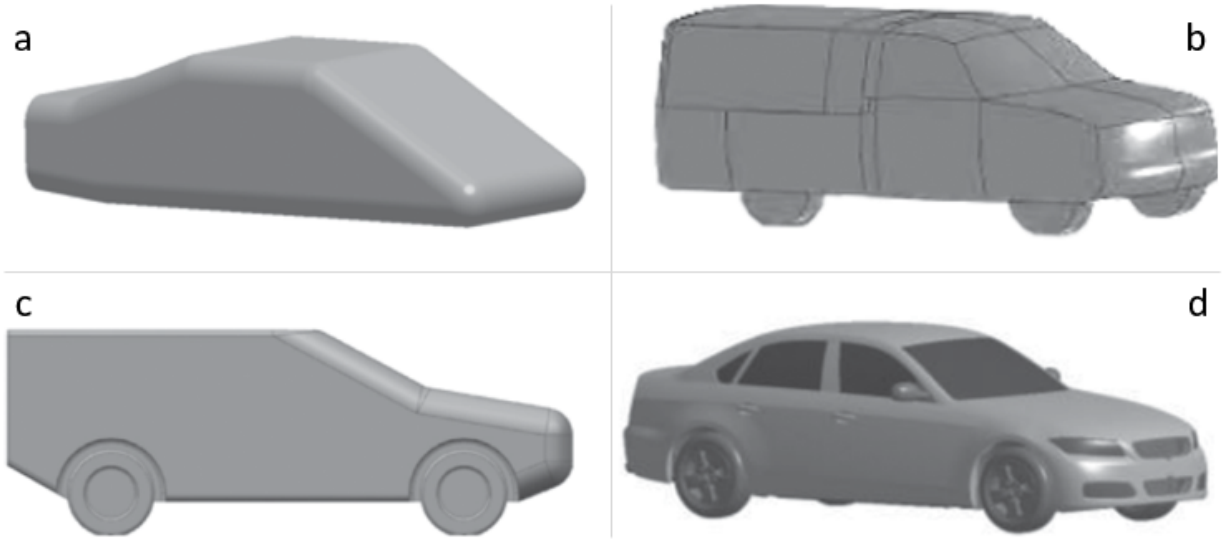

Figure 1.7: (a) The SAE Notchback reference geometry. (b) The Generic SUV corresponding to Al-Garni *et al.* (c) The Generic SUV corresponding to Wood et al. (d) The DrivAer model [1] *(edited by the author).*

The aforementioned reference models were released in a period when the automotive wind tunnels were unable to simulate the translational motion of the road and that is the main reason why most of them have no or simplified non-rotating wheels. In addition, the cooling air flow in the engine bay was also neglected. In 2007, Wäschle [6] studied the influence of the rotating wheels on vehicle aerodynamics on both a simplified and a realistic production car. The outcome of this research was that the rotation of the wheels is of utmost importance for the aerodynamic shape optimisation of a road-vehicle. The flow structures formed around the wheels and inside the wheelhouse arches, shown in Figure 1.8, have significant impact on the aerodynamic performance of the vehicle, with the total drag to increase when the wheels are stationary.

The problem with the level of detail of reference models was tackled by Heft *et al.* [31] with the introduction of a realistic model of a generic road-vehicle, shown in Figure 1.7(d). This model is called DriveAer and comes in three different variants regarding its rear end shape, namely the estate, the notchback and the fastback, and two variants for the undertray, a simplified and a detailed one. The model was later enhanced by Wittmeier and Kuthada [32] by adding a drivetrain and a detailed cooling system with a simplified engine block, resulting in the so-called Open-Cooling DriveAer model (OCDA). In this model, all the characteristics of a production car are present and the flow field formed around it is similar to numerous production cars, making it the most reliable reference model for this category of vehicles.

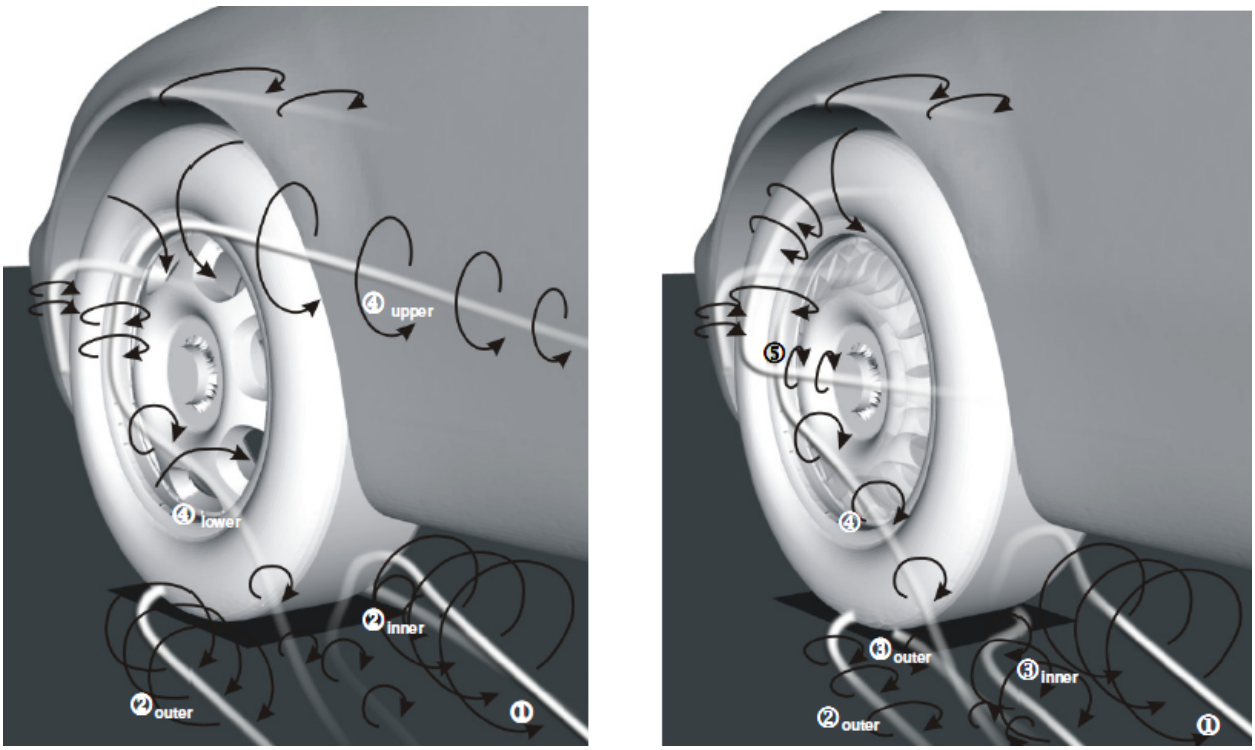

Figure 1.8: Laser Doppler Velocimetry (LDV) on a model with stationary *(left)* and with rotating *(right)* wheels [6].

1.5.1 Introduction to the AeroSUV Reference Model

Even though the DriveAer model features the level of detail that makes it a very accurate and robust reference model, it cannot provide accurate enough details for the flow characteristics of an SUV. The larger wheels, the difference in the width and the increased ground clearance result in a completely new flow field.

In 2019, Zhang *et al.* [1] attempted to bridge the gap between on-road and off-road vehicles by introducing the AeroSUV reference model; its geometry can be downloaded from the European Car Aerodynamic Research Association (ECARA) site. This is a highly optimised model in terms of aerodynamics, that comes in three rear end variants as well: the squareback, the fastback and the notchback, shown in Figure 1.9*(left)*.

The model had to be compatible with DriveAer's rear ends, fact that sets a limit on the parameters that can be altered during the shape optimisation process. The optimisation started by selecting the appropriate sweep, hood and slope angles, illustrated in Figure 1.10, to minimise the air resistance and lift force. Then, by increasing the pitch angle of the model, the underbody formed a diffuser that led to further reduction of the drag force. Finally, the rear end of the underbody was optimised as well. A curved section was added at the rearmost portion of the underbody and two exhaust pipes were also incorporated, in contrary to the DriveAer model that had only one.

Regarding the geometry characteristics, the AeroSUV has a wheelbase of 2786mm, which is the same as the DriveAer. The front and rear tracks are equal to 1552mm, the tires correspond to 235/55 $R19$ and their shape is a result of 3D scanning the contour of a real tire. The mirrors have been redesigned, the new width of the car is 1828mm and the cross-sectional area is $2.47m^2$, similar to a mid-class SUV. Moreover, in order to meet the SUV requirements, the minimum ground clearance was increased to 196mm and the approach,

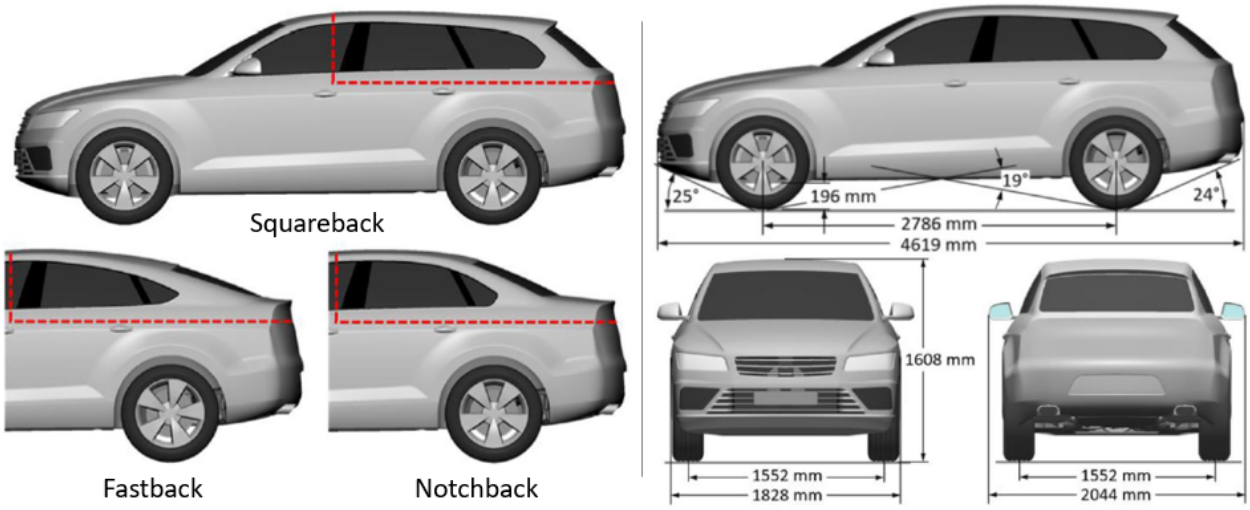

Figure 1.9: The AeroSUV model with the three rear end parts, squareback, fastback and notchback *(left)*. Overall dimensions of the full scale AeroSUV model *(right)* [1] *(edited by the author)*.

break-over and departure angles are 24°, 19° and 24° respectively. All the dimensions are clearly illustrated in Figure 1.9*(right)*.

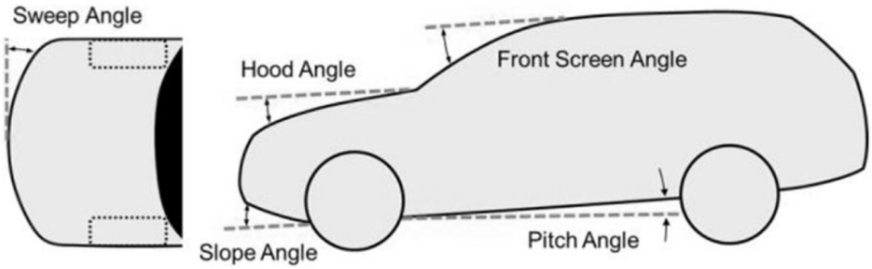

Figure 1.10: Optimisation parameters for the AeroSUV model [1] *(edited by the author)*.

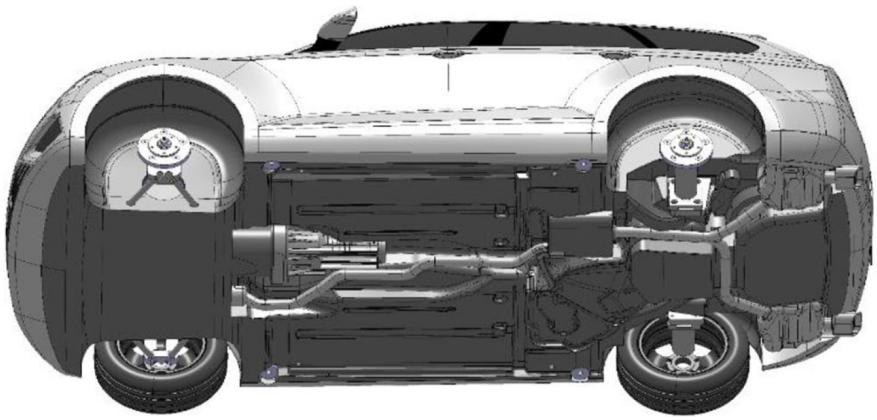

Figure 1.11: Fully detailed underbody of the AeroSUV reference model [1].

1.5.2 Wind tunnel testing of the AeroSUV

The AeroSUV was extensively tested at the wind tunnel of University of Stuttgart, which is operated by the *Forschungsinstitut fur Kraftfahrwesen und Fahrzeugmotoren Stuttgart (FKFS)* and can achieve maximum air speed of 80m/s. For the experiment, an 1:4 scale model was used which was mounted on four struts with adjustable length. The translational motion of the road and the rotation of the wheels was attained with state-of-the-art ground simulation technics including a 5-belt rolling-road system, boundary layer suction, tangential blowing and four wheels rotating units [33], [34].

Through wind tunnel testing, data regarding the produced aerodynamic loads were derived and with the use of a 31-probe rake, the total pressure was also measured in numerous regions [1]. However, the rake system cannot measure the total pressure accurately enough since there is an angular dependency of the incident flow angle. This issue was addressed by incorporating the Vector Penalty Projection (VPP) method [35] which bettered the comparison of the WTT and CFD results. The model was tested in a flow speed of 50m/s, the total drag and the front and rear lift coefficients were measured for the baseline model in all three variants. The drag coefficient was 0.314 for the squareback and for the fastback and notchback variants was measured to be 0.286, highlighting the significant influence the geometry of the rear end has on the total aerodynamic performance of the vehicle. The results are clearly illustrated in Table 1.1.

Table 1.1: Drag and lift coefficients derived by WTT [1].

Type	C_D	C_{Lf}	C_{Lr}
Squareback	0.314	0.024	-0.016
Fastback	0.286	0.053	0.080
Notchback	0.286	0.057	0.061

Finally, Zhang *et al.* [1] conducted CFD simulations as well and compared the derived results with the experimental ones. Through virtual simulations, apart from the rear end wake, three more basic wake topologies were identified and are highlighted in Figure 1.12. These results will be presented and extensively analysed in Chapter 5: "Results II – AeroSUV".

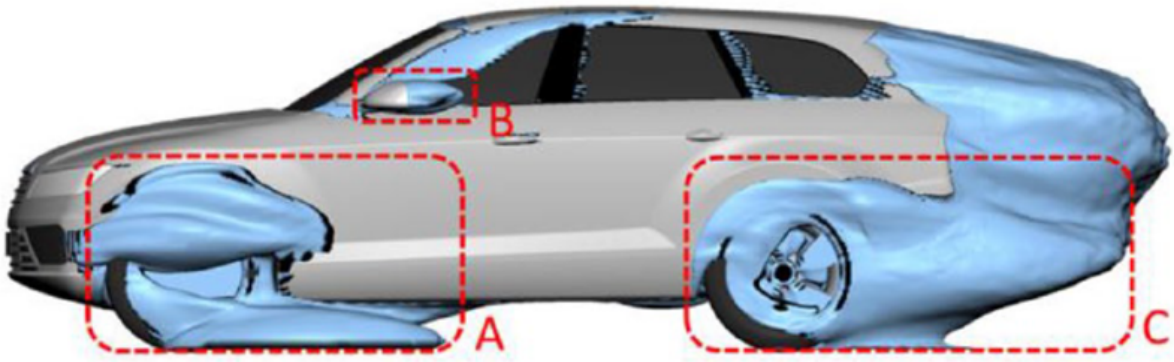

Figure 1.12: Basic wake isosurfaces derived by CFD simulation [1] *(edited by the author).*

1.6 Scope of Work

This study aims to check the validity of a CFD setup exported using a simplified model when applied on the realistic fully detailed AeroSUV reference model [2]. The project is a qualitative research with main objective being the accuracy of the simulations. The simplified SAE Notchback 20° Backlight model was selected in order to reduce the computational demands during the investigation. The research was conducted at the headquarters of BETA CAE Systems SA in Thessaloniki, Greece and lasted about 9 months.

1.7 Objectives

Towards the completion of the aforementioned scope, a set of objectives has been defined, that can be summarised as follows:

- Use the SAE Notchback 20° Backlight [29] reference model for the preliminary CFD study.
- Test surface and volume mesh parameters and assess the results of the simulations with the experimental forces and pressures.
- Examine the influence of the boundary layer simulation approach on the simulation.
- Test different OpenFOAM solver settings and compare the results with the experimental values.
- Export the parameters of the CFD setup that provided the best prediction for the SAE Notchback 20° Backlight.
- Check the validity of this CFD setup on all the three variants of the more realistic, fully detailed AeroSUV model.
- Conduct transient simulations on both cases to assess the deviation of the simulations from the wind tunnel data.

1.8 Limitations

This research is mainly focused on automotive industrial applications. The geometries used are models which have been extensively studied through wind tunnel experiments. The geometries cannot be altered or modified and the internal flow was not modeled to minimize potential sources of error. The main variable used to assess the accuracy of the simulations is the generated drag force, since it is explicitly linked with the energy/fuel consumption.

The simulation were conducted on the company's computers, equipped with Intel Xeon CPU E5 - 2600 v3 @ 2.60GHz with 24 cores and 256GB RAM. For the transient simulations Archimedes, one of the company's clusters, was used consisting of 4 nodes with specifications similar to the aforementioned, resulting in 88 cores and 1024GB RAM. These computers were also used by other employees and thus excessive use of computational sources should be avoided.

2 Theoretical Background

"Nature always tends to act in the simplest way"

-Daniel Bernoulli

2.1 Automotive Aerodynamics

In terms of fluid dynamics, automobiles can be characterised as bluff or quasi-streamlined bodies operating in close proximity to the ground. The flow around them is dominated by three dimensional structures that sometimes are detached from the body and others are reattaching. The interaction of these structures with the body, in combination with the wake of the car are responsible for the majority of the so-called induced and pressure drag. The wake of a car is explicitly linked to its shape; cars with bluff rear end, also known as squarebacks, produce simple wakes since clearly defined flow separations occur. On the other hand, more streamlined vehicles with close-to-critical backlight angle produce more chaotic wakes and very complex unstable flow fields in general. The flow behind each vehicle category will be further analyzed below.

An important indicator used in fluid dynamics is the Reynolds Number (Re), which can provide information about the flow patterns that will be formed in different fluid flow situations. It is a non-dimensional number and expresses the ratio of inertial to viscous forces of the flow, as given from the Equation (3.7). At low Reynolds number, the flow is dominated by viscous forces and for a specific range of Reynolds number, the flow can be laminar. At higher Reynolds number, the effect of the inertial forces becomes more important and the flow is dominated by turbulence.

$$Re = \frac{inertial\ forces}{viscous\ forces} = \frac{U_\infty \rho L_{ref}}{\mu} \qquad \text{(Eq. 2.1)}$$

where U_∞ is the reference or free-stream velocity, ρ is the density of the fluid, L_{ref} is the characteristic length and μ is the viscosity of the fluid.

In automotive applications, a typical Reynolds number for a vehicle with 5 meters length (L_{ref}), moving at 100 km/h (U_∞), at sea level and in nominal atmospheric conditions ($\rho = 1.205 kg/m^3$, $\mu = 1.81 \times 10^{-5} kg/m/s$), is approximately $Re = 9.5 \times 10^6$. In Reynolds number of that order, the flow around the vehicle is dominated by inertial forces and it can be characterized as completely turbulent.

Except for predicting flow patterns, Reynolds number can be also used to scale similar in pattern but different-sized flow situations. By utilizing the Reynolds number analogy, models such as aircrafts or wind turbines can be simulated in wind tunnels and generate the same flow structures as the full-size model. In a scaled case, the flow velocity and/or the density of the fluid can be adjusted to obtain the same Reynolds number.

2.2 Boundary Layer

The boundary layer is a thin layer of fluid near the surface of an object which is dominated by viscosity and has great influence on the whole flow field. Devoid of upstream turbulence, the boundary layer will start as laminar until a critical distance is reached where the transition from laminar to turbulent boundary layer occurs, as illustrated in Figure 2.1. The point of transition can be approximately predicted based on the Reynolds number, Equation (3.7). Moreover, the boundary layer transition can be affected by the surface roughness, the pressure gradient along the surface, the free-stream turbulence and other flow parameters such as the crosswinds and fluid temperature. For the simple case of air flowing over a flat plate, the transition from laminar to turbulent boundary layer occurs at $Re = 1.56 \times 10^6$ [3][8]. Figure 2.2 depicts how the boundary layer features change with increasing Reynolds number. Comparing the two sketches, it is evident that the transition region moves upstream as the Reynolds number increase and the thickness of the turbulent region increases faster for higher Reynolds number.

The boundary layer is often referred to as a shear flow; it begins to form at the stagnation point on a surface and its thickness is increased proportionally to the distance. In cases where complex geometries are involved, the boundary layer behaviour depends on the surface curvature; the front end of an automobile , for example, consists of surfaces that cause the flow to accelerate locally. This acceleration can diminish some instabilities of the flow near the wall caused due to turbulence, and thus can delay the transition by reducing the boundary layer thickness. On the other hand, if the geometry has a diffuser-like shape, the energy of the flow will decrease resulting in an unstable boundary layer and even in flow separation. This is clearly illustrated in Figure 2.3 where the normalized Turbulent Kinetic Energy (TKE) (k) is inversely proportional to the time-averaged normalized velocity.

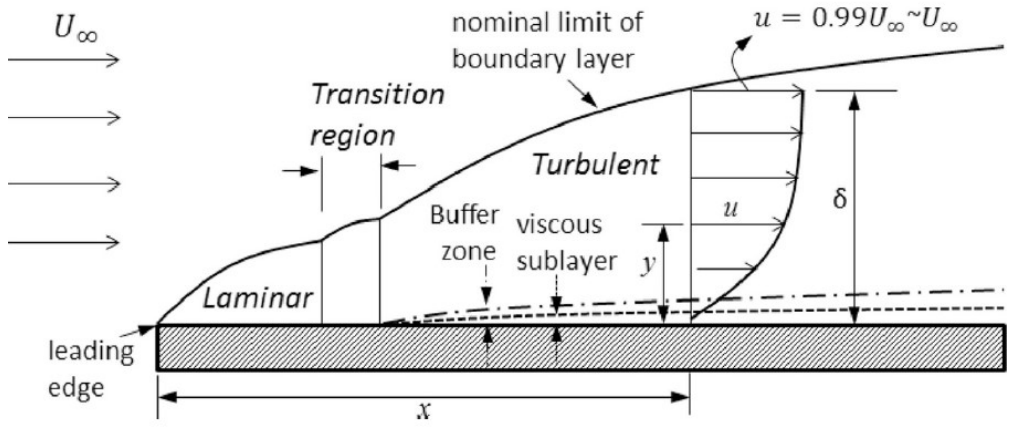

Figure 2.1: Boundary layer regions for flow over a flat plate with neutral downstream pressure gradient [7].

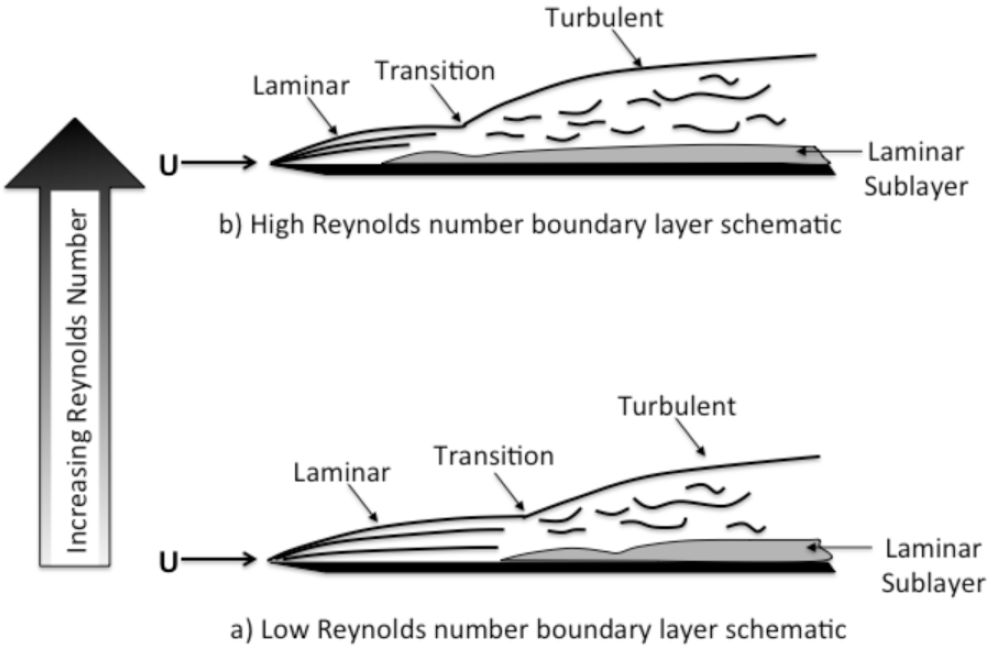

Figure 2.2: Effect of Reynolds number on boundary layer flow [8].

2.2.1 Laminar Boundary Layer

As it was mentioned above, all boundary layers begin as laminar, with constant velocity gradient normal to the wall surface. Due to its steady behaviour, the friction between the fluid and the surface, also known as skin friction, inside a laminar boundary layer is low, the flow exchanges mass and momentum only between adjacent layers and the mixing rate is negligible. In every case with low free-stream turbulence, laminar boundary layer will always formed in certain regions of the body surface, but it can be strongly affected by external disturbances that can excite resonances, resulting in early transition from laminar to turbulent.

2.2.2 Turbulent Boundary Layer

The turbulent portion exists downstream of the transition region (see Figure 2.1 and 2.2) and in contrast to the laminar boundary layer, it is dominated by rapid velocity and pressure fluctuations due to the enhanced mixing rate between several layers and the near-wall eddies motion. The turbulent boundary layer is thicker than the laminar one and the mass and momentum transfer is greater resulting in higher skin friction.

2.2.3 Boundary Layer Transition

The boundary layer transition can be achieved via both natural and forced way. In this thesis, no mechanism for forced boundary layer transition is used and only the natural way will be examined. The start of transition is characterized by strong velocity and pressure fluctuations resulting from turbulent bursts that appear in the flow field (see image Figure 2.4).

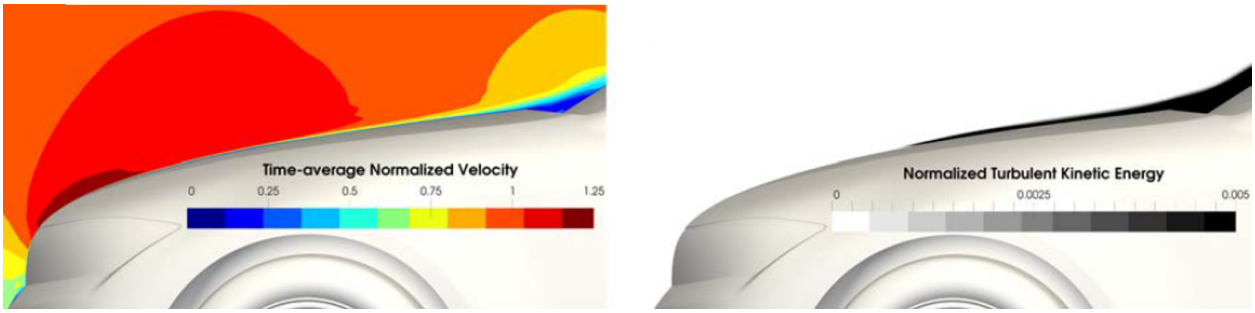

Figure 2.3: Flow field over the bonnet of a generic vehicle [4] *(edited by the author)*.

The first stage of the natural transition process includes the transformation of the environmental disturbances into small perturbations that are convected inside the boundary layer. The next stage is the growth and the decay of these disturbances resulting in an unsteady behaviour of the laminar boundary layer. The unsteady behaviour is firstly seen with the generation of the so-called Tollmien waves [36] which are transferred on the flow direction and then are transformed into three-dimensional hairpin vortices [37]. A layer of high shear stress is generated above these vortical structures which break down into smaller structures with random frequency spectrum [38] resulting in a chaotic fully-turbulent boundary layer.

In Figure 2.5, the skin friction was measured across the red line on the bonnet. The chart illustrates the time-averaged and the instantaneous skin friction coefficient across this line. The high skin friction at the beginning of the bonnet is caused due to the local acceleration of the flow at that region. The small instabilities between $x = 0.04m$ and $x = 0.13m$ are due to the two-dimensional instabilities ought to the Tollmien waves. For $x > 0.14m$ these instabilities increase as well as the skin friction and the boundary layer becomes turbulent.

2.2.4 Wall y^+ and U^+

To describe the exact location in a fully developed turbulent boundary layer, the non-dimensional wall unit Y–Plus (y^+) is used. y^+ is an indicator of the distance from the nearest wall and along with it, another non-dimensional wall unit is used, called U–Plus

Figure 2.4: Photograph of turbulent spot in a transitional boundary layer, flow from left to right [9].

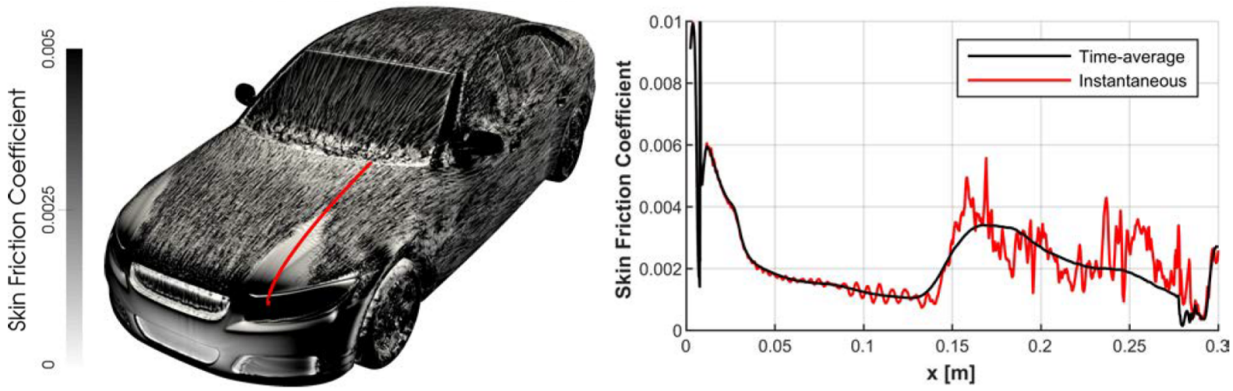

Figure 2.5: Skin friction calculated through a Large Eddy Simulation (LES) of the DriveAer reference model [4] *(edited by the author)*.

(U^+) and indicates the flow velocity on the boundary layer. Both of them are expressed based on υ_τ, a reference velocity based on wall shear stress (τ_w), as shown in Equations (2.2) and (2.3).

$$y^+ = \frac{y\upsilon_\tau}{\nu} \qquad \text{(Eq. 2.2)}$$

$$U^+ = \frac{U}{\upsilon_\tau} \qquad \text{(Eq. 2.3)}$$

Here y is the distance from the wall, ν is the kinematic viscosity and υ_τ is the reference velocity based on the wall shear stress (τ_w) and is given by:

$$\upsilon_\tau = \sqrt{\frac{\tau_w}{\rho}} \qquad \text{(Eq. 2.4)}$$

and

$$\tau_w = \mu\frac{\partial u}{\partial y} \qquad \text{(Eq. 2.5)}$$

In Equations (2.5) and (2.4), μ is the dynamic viscosity and ρ is the density of the fluid.

2.2.5 Turbulent Boundary Layer Regions

The turbulent boundary layer on a fully-developed flow consists of the viscous, the buffer and the fully turbulent sub-layer, as shown in Figure 2.1.

Viscous Sub-layer ($0 \leq y^+ \leq 5$) Starting with the viscous or linear sub-layer, the fluid very close to the surface is not moving relative to the wall and is devoid of swirling motion due to turbulence, known as turbulent eddying motion, similar to a laminar flow regime. The

fluid is dominated by viscous shear in the absence of turbulent shear stress effects, and it can be assumed that the total shear stress in that region is equal to the wall shear stress given by Equation (2.5). The gradient of the velocity in this region is steep and approximately constant.

Buffer Sub-layer ($5 \leq y^+ \leq 30$) Adjacent to the viscous sub-layer is the buffer sub-layer. The velocity gradient is still high, the flow is partially turbulent and the main characteristic is that both the viscous shear stress and the turbulent shear stress have notable influence on the flow, as shown in Figure 2.6, thus none of them can be neglected. Small-scale energetic eddies are formed there in combination with a big rate of conversion of kinetic energy to turbulent kinetic energy and thus increase in the turbulence dissipation is observed. This layer is also called turbulence generation layer and some of the turbulence is moved upper to the fully-turbulent boundary layer region and a small amount of turbulence is carried inward into the viscous sub-layer but dissipates immediately. The buffer layer is thin but not thinner than the viscous sub-layer [39].

Turbulent Sub-layer ($y^+ \leq 30$) The outer region of the boundary layer is called turbulent sub-layer and it occupies the most of the total boundary layer depth. This region is fully dominated by turbulent shear stress (Reynolds stresses) and viscous shear stress can be neglected. The eddies formed in this sub-layer are of larger scale, compared to the buffer sub-layer eddies, but contain much less kinetic energy per unit volume of fluid. Due to their size, the eddies transport momentum normal to the flow easier and this is why the profile of flow velocity on this region has more gentle gradient.
From another perspective, the total boundary layer can be simply classified into two main categories. The first is the viscosity-dominated region where the viscous shear stress dominates and include the viscous sub-layer and the lower part of the buffer layer. The second category is the turbulence-dominated region that contains the top buffer layer and the fully

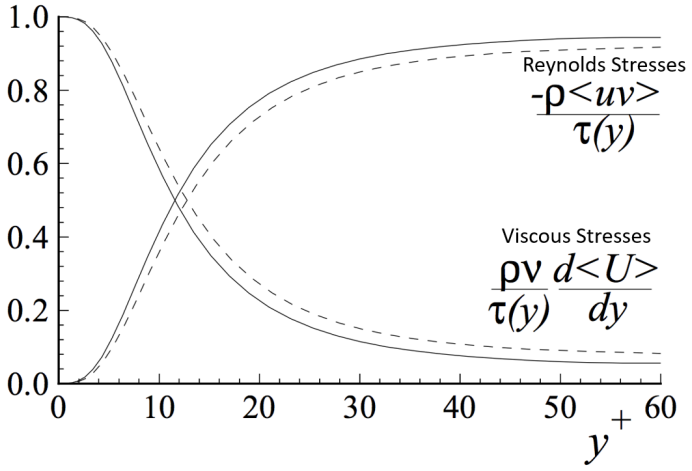

Figure 2.6: Contribution of viscosity and turbulence (Reynolds stresses) on the shear stress with regards to y^+. Data exported by Direct Numerical Solution (DNS). Solid line: Re=13.750. Dashed line: Re=5.600 [10] *(edited by the author).*

turbulent region. A very thin layer inside the buffer layer exists, in which the two kinds of shear stresses are equal. The transition from one region to the other is smooth and no sharp divisions exist [39].

2.2.6 Boundary Layer Separation

Due to Coanda effect [40], a fluid has the tendency to follow an adjacent flat or curved surface so that a region of lower pressure is developed. When the energy of the flow dissipates, the boundary layer has the tendency to separate due to excessive momentum loss near the wall. This tendency depends not only on the Reynolds number and the current state of the boundary layer, but also on the pressure distribution along the surface which is explicitly linked with the shape of the vehicle. The downstream pressure gradient can strongly affect the evolution of the boundary layer as shown in Figure 2.7. A downstream negative pressure gradient is a favorable condition and increases the velocity inside the lower sub-layers of the boundary layer, In contrast, a positive pressure gradient is an unfavorable condition, it reduces the energy of the flow and it can lead to reversed flow and boundary layer separation. Possible locations on a vehicle where flow separation can occur is the transition from a convex to concave surface or a flat surface, within an abrupt convex surface or at a sharp convex edge where clearly defined separations take place.
The evolution of the boundary layer within a region of adverse pressure gradient is depicted in Figure 2.8. Boundary layer separation and thus flow separation occurs when the fluid near the wall appears to flow backwards. The thickness of the boundary layer is increasing continuously but when the boundary layer separates, the reversed flow forces the boundary

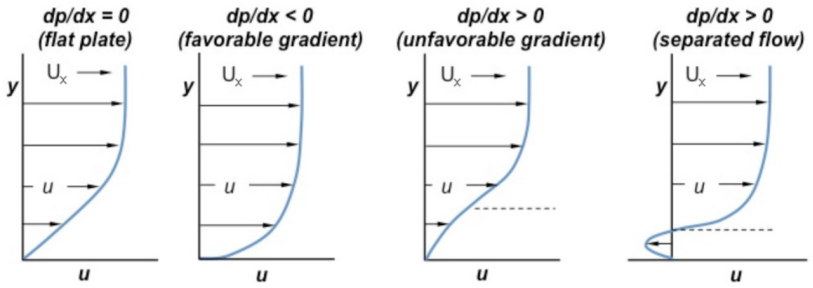

Figure 2.7: Boundary layer velocity profiles for different pressure gradients [8] *(edited by the author)*.

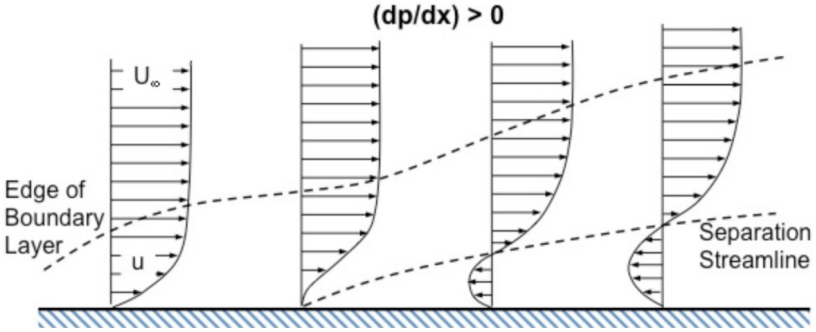

Figure 2.8: Boundary layer evolution within an adverse pressure gradient [8].

layer away from the surface leading to an abrupt increase in boundary layer thickness which often results in an increase in pressure drag. A laminar boundary layer contains less momentum, compared to a turbulent boundary layer and thus cannot withstand steep pressure gradients since it is more prone to separation than a turbulent one. Attention should be given to devices that operate in free-stream flow with low turbulence, such as the mirrors, since separation can occur easier. Turbulent boundary layers are characterized by greater transfer of momentum and mixing between the sub-layers resulting in higher energy near the wall which is the main reason why they are less sensitive to steep curvature changes and thus steep pressure gradients.

2.3 Time Dependence

As it was mentioned before, road vehicles operate at high Reynolds number and the flow field is dominated by turbulence. In contrast to laminar flow, a turbulent flow is three-dimensional, chaotic, irregular and time-dependent. Moving vehicles generate very complex and time-dependent unsteady flow fields (see Figure 2.10) and their examination needs special treatment. More precisely, aerodynamic loads consist of a mean and a time-varying component. The fluctuating loads are strongly affected by the wake generated by the quasi-streamlined body of the vehicle and their contribution to the aerodynamic loads is significant.

The bluff body of road vehicles causes a premature flow separation which is closely associated with the formation of vortical structures and the expansion of the wake region which further increases the pressure drag. Downstream of vehicle devices that operate in moderate Reynolds number, periodic flow structures are formed consisted of free travelling alternating vortices, known as von Kármán vortex street [41]. The mechanism behind the formation of the von Kármán vortex street is the boundary layer interaction between adjacent sides of the body. Strong oscillatory vortical structures can affect the aerodynamic forces generated by the translational motion of the vehicle.

For a specific range of Reynolds Number a coherent set of vortices is generated and the shedding frequency can be calculated through the Strouhal number (Sr), Equation (2.6).

$$Sr = \frac{fL}{U} \qquad \text{(Eq. 2.6)}$$

where f is the frequency of vortex shedding, L is the characteristic length and U is the flow velocity.

For Reynolds number out of this range, the vortex shedding process is random, resulting in non-periodic and chaotic oscillations of the aerodynamic loads, as seen in Figure 2.9.

2.4 Governing Equations

The governing equations of a fluid flow are mathematical statements of the conservation laws of physics, namely the conservation of mass, the conservation of momentum and the

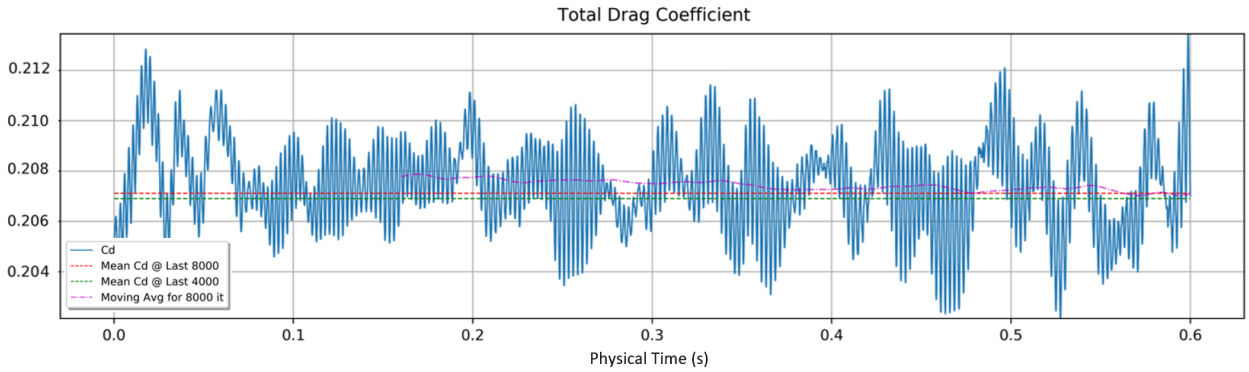

Figure 2.9: Drag force oscillations in a Delayed Detached Eddy Simulation (DDES) of the SAE Notchback reference model.

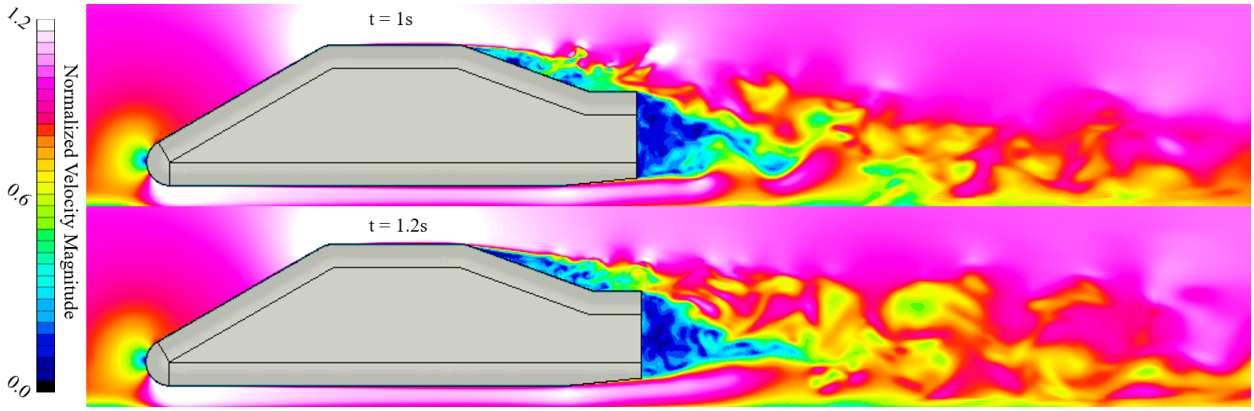

Figure 2.10: Instantaneous velocity distribution on a y-normal plane located at the centerline calculated via Delayed Detached Eddy Simulation (DDES) of the SAE Notchback reference model.

conservation of energy, also known as the first law of thermodynamics stating that the rate of increase of energy is equal to the net rate of heat added and the net rate of work done on a fluid particle.

For the simulations conducted in this thesis, the fluid is assumed to be isothermal and incompressible, since the investigated flows are below Mach 0.3, hence the conservation of energy equation is neglected [38]. The fluid is regarded as a continuum, only macroscopic length scales are studied and molecular structure of matter and molecular motions will be ignored in this thesis. The flows will be described by macroscopic properties such as pressure, velocity, density (constant due to incompressible fluid assumption) and temperature (constant due to isothermal fluid assumption) and their space and time derivatives. The value of these properties can be thought as the average value of a suitably large number of molecules. To apply these equations to the fluid, an infinitesimal fluid block is assumed as the smallest possible element of fluid in this macroscopic approach.

Starting with the law of mass conservation, it states that the mass contained in a fluid element is constant, or the rate of mass flow entering a fluid element is equal to the rate of

mass flow that exits from it and mathematically is expressed by Equation 2.7.

$$\nabla \cdot \overrightarrow{u} = \frac{\partial u_i}{\partial x_i} = 0 \qquad \text{(Eq. 2.7)}$$

where $i = 1, 2, 3$ represents the three directions in the Cartesian coordinate system, u_i is the velocity component for every direction and x_i i the coordinate direction.

The second law of physics is the conservation of momentum stating that the rate of increase of a momentum of a fluid particle is equal to the sum of forces on a fluid particle, and for incompressible flow is discrebed mathematically by Equation 2.8.

$$\rho \frac{\partial u_i}{\partial t} + \rho u_j \frac{\partial u_i}{\partial x_j} = -\frac{\partial p}{\partial x_i} + \frac{\partial \tau_{ij}}{\partial x_j} \qquad \text{(Eq. 2.8)}$$

where

$$\tau_{ij} = 2\mu S_{ij} \qquad \text{(Eq. 2.9)}$$

and

$$S_{ij} = \frac{1}{2}\left(\frac{\partial u_i}{\partial x_j} + \frac{\partial u_j}{\partial x_i)}\right) \qquad \text{(Eq. 2.10)}$$

Here, ρ is the fluid density, u is the velocity, p is the pressure, t is the time, μ is the fluid viscosity, τ_{ij} is the viscous shear stress component on every face of the block and for every direction and S_{ij} is the symmetric deformation tensor also called as rate of strain tensor. The indicators i, j are used as a result of the Einstein summation convention. These equations are represented with three equations, one for each direction of the current coordinate system. The equations (2.7) and (2.8) are also known as the Navier-Stokes equations.

2.5 Aerodynamic Forces

A travelling road vehicle is subjected to resistant forces due to the movement inside a fluid, known as aerodynamic force consisted of two components, the friction and the pressure force component. The friction component is due to the viscosity of the fluid and acts parallel to the the surface of the body, while the pressure component acts normal to the surface of the body. The resultant aerodynamic force can be also divided into three main components based on the acting direction, namely drag, lift and side force as it was extensively analyzed in Chapter 1.3.2: “Aerodynamic Forces and Moment Convention”.

The main parameter that will be evaluated in this thesis is the drag force since it strongly affects the fuel or energy consumption and thus the effective driving range of a road vehicle. Lift and side forces are of significant importance for the stability and handling of race cars

when moving in high speeds but for passenger cars travelling at moderate speeds are less important and will not be considered. Throughout this research, non-dimensional aerodynamic force coefficients (C_F) will be used and are defined such as:

$$C_F = \frac{F}{0.5\rho_\infty U_\infty^2 A} \qquad \text{(Eq. 2.11)}$$

where F is the aerodynamic force (drag, lift, side force), ρ_∞ is the air density, U^2 is the free-steam velocity and A is the projected frontal area of the vehicle.

In a modern vehicle, the aerodynamic drag consists of about 80% of pressure drag, 10% of internal flow and another 10% of friction drag due to surface roughness. For a generic fastback sedan vehicle, the drag coefficient (C_D) is approximately 0.25 and for a squareback SUV is approximately 0.31. The lowest drag coefficient achieved by a production car is $C_D = 0.2$ by Mercedes-Benz EQS, second comes the Tesla Model S with $C_D = 0.208$ and third is the Lucid Air with $C_D = 0.21$ [42] [43] [44], fact that reveals the endless effort of automotive industries to reduce the drag coefficient at the lowest possible level.

2.6 Flow Field of a Generic Road Vehicle

After the mid-1970s' oil crisis, the main kinds of vehicles, based on their rear-end geometry, that was sold in Europe were the squareback, or sometimes can be mentioned as estate, the fastback and the notchback which are depicted in Figure 2.11. The flow field that each one generates will be further analyzed below.

2.6.1 Squareback

The squareback geometry is found on hatchback models with steep backlight angle and on Sport Utility Vehicles (SUVs). It is the least aerodynamically efficient geometry compared to the other two geometries and produces the simplest wake structure compared to the other models. The flow is separated completely at the highly curved rear face, forming a separation bubble, characterised by high recirculation and low pressure. The wake of it is represented in Figure 2.12, and it consists of two major imbalanced recirculation areas due to the restricted air flow beneath the vehicle, and numerous small vortices in the shear layer.

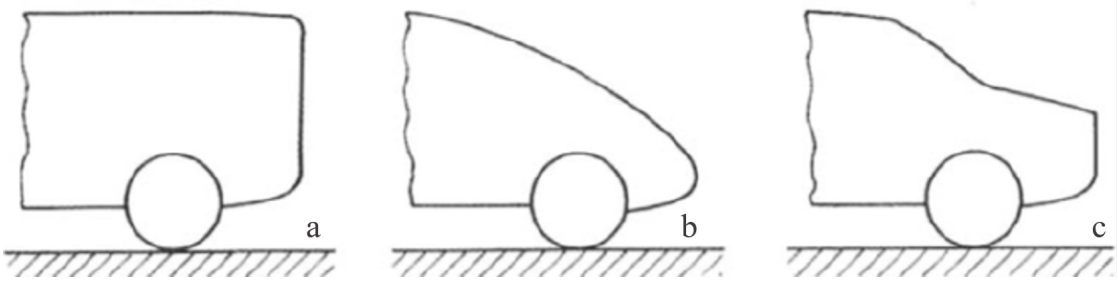

Figure 2.11: (a) Squareback or Estate, (b) Fastback, (c) Notchback [11] *(edited by the author).*

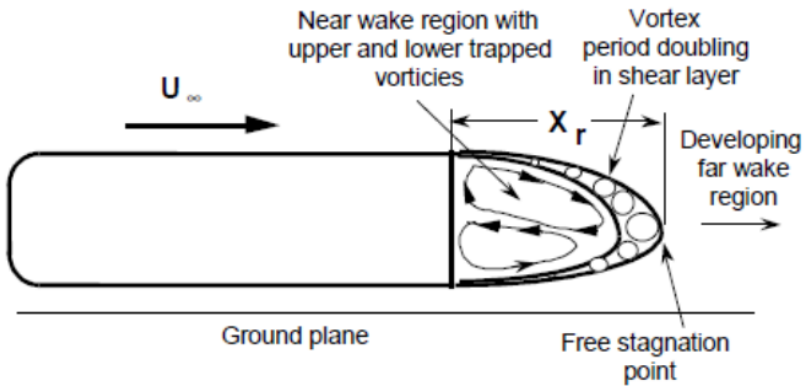

Figure 2.12: Flow regime downstream of a Squareback vehicle [12].

Interesting phenomenon in such geometries is the so-called wake pumping [30]. As the air is entrained, the volume of the near wake region increases resulting in an elongation of the wake region as the free stagnation point moves rearward. Subsequently, the pressure behind the model decreases further and the fluid volume that is encapsulated in the wake region is reduced causing it to shorten again. This periodic phenomenon is the main source of instabilities in the generated aerodynamic forces and can be also found in a smaller scale in the other two vehicle categories.

A most recent research by Littlewood, Passmore *et al.* [13], analysing the wake of a simplified squareback geometry with the use of Particle Image Velocimetry (PIV) provides a clear image of near wake recirculations and shear layer shedding processes. Many works consider the wake structure as two counter rotating vortices, giving the sense of a two dimensional flow field, however this is actually a three dimensional phenomenon. From this research they observed that the large recirculations that appear are artefacts due to time-averaging and no longer appear when the flow is instantaneously examined, as shown in Figure 2.13. This research highlights the importance of conducting not only time-averaged but also temporal analysis

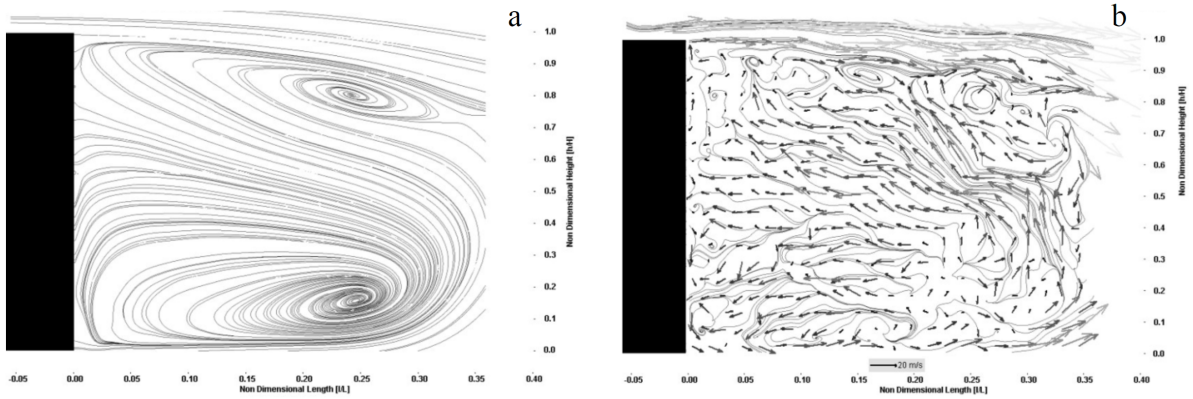

Figure 2.13: Time-averaged flow field *(left)*, Instantaneous flow field *(right)* behind a squareback model [13].

on wake topologies, something that will be extensively presented later on the thesis.

2.6.2 Fastback

Hatchback vehicles with smooth transition from the roof to the backlight and various sedans with small trunk can be included in the fastback category. It is the most streamlined geometry compared to the other two, and the flow field at the rear of the car is dominated by a pair of counter rotating vortices on the trailing pillars and a wake region at the rear sharp face of the model as shown in Figure 2.14. The pair of trailing vortices, are causing a strong downwash at the backlight allowing the designer to increase the relative angle between the roof and the backlight without risking a flow detachment. However, the higher the angle the stronger the vortices resulting in enhanced induced drag.

The force produce due to the low-pressure region at the backlight can be decomposed into two perpendicular forces, one acting at the z-axis as a lift component, and one at the longitudinal x-axis that is pulling the car back, contributing further to the total drag force. For high backlight angles, above the critical value, the downwash generated by the trailing vortices is not sufficient to keep the flow attached on the centerline and the wake topology is similar to the squareback.
An assiduous research on the flow field formed downstream of a fastback was conducted by Ahmed *et al.* [15] using a simplified model with a rounded bluff front face and an elongated main section which results in an angled backlight as shown in Figure 2.15(left). The study focuses on the influence of the backlight angle in the wake topology. After testing various geometries, it was revealed that the flow was fully attached at the centerline of the backlight until the critical angle of 12°. The drag generated from the base of the rear end decreases as the angle of the backlight increases. For backlight angle greater than 12°, post-critical phenomena appear, the flow detaches and two separations regions are formed, one at the base and one at the backlight. The different flow topologies are depicted in Figure 2.15(right).

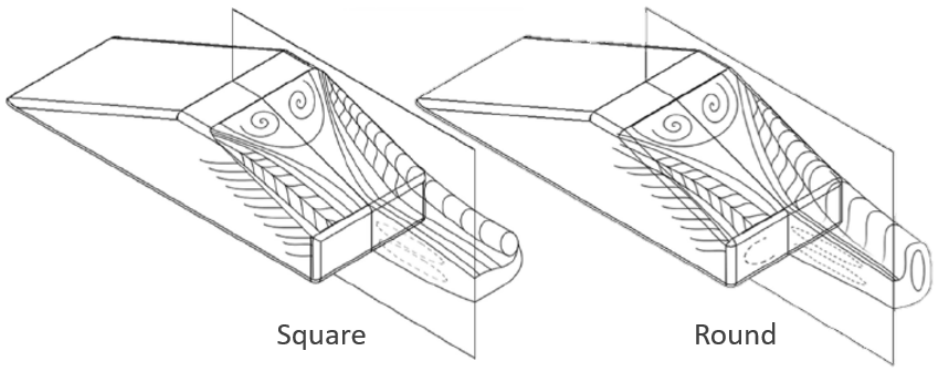

Figure 2.14: Flow regime downstream of a Fastback vehicle with square *(left)* and round *(right)* trailing pillars [14] *(edited by the author).*

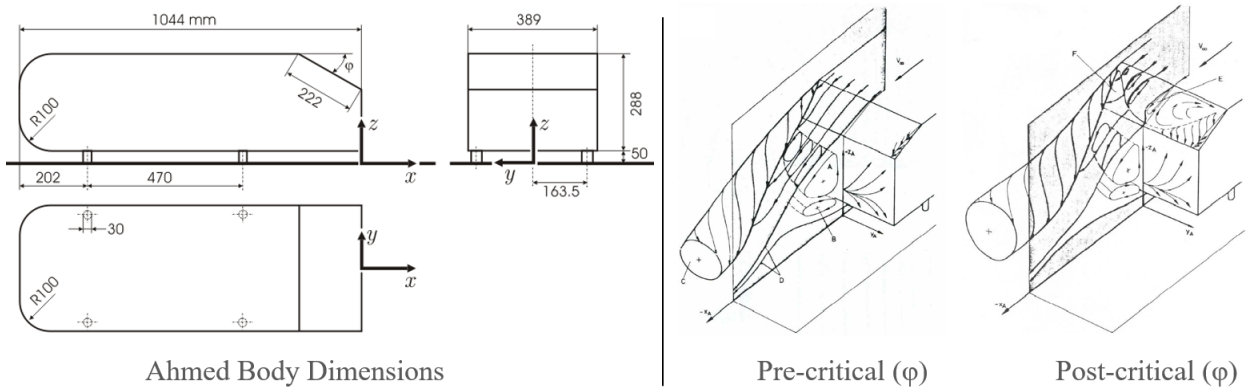

Figure 2.15: Ahmed Body model with dimensions *(left)*. Flow field for pre-critical and post-critical backlight angle (ϕ) *(right)* [15] *(edited by the author)*.

2.6.3 Notchback

Normal sedan and saloon type vehicles can be characterised as notchbacks. This type of vehicles generate the most complex wake topology compared to the three geometry types. Carr *et al.* [45] conducted an investigation on a range of different notchback geometries by utilizing both balance measurements and flow visualization technics on the surface of the model. The lines generated by the flowing paint, revealed the general wake topology, with the flow to separate at the rear end of the roof and if the trunk is of adequate size, then it reattaches, forming a separation region at the backlight. At the lowest point of the backlight, where it meets the trunk, a transverse vortex is formed and Carr likened this flow topology to the one observed on the flow over a backward facing step.

Nouzawa *et al.* [16] studied further the flow pattern on the rear portion of a notchback model in order to give a better explanation of the effective parameters of a vehicle and how they affect of the wake structure and thus the produced drag. The model he used is shown in Figure 2.16(left). Nouzawa's research revealed a more detailed wake structure behind a

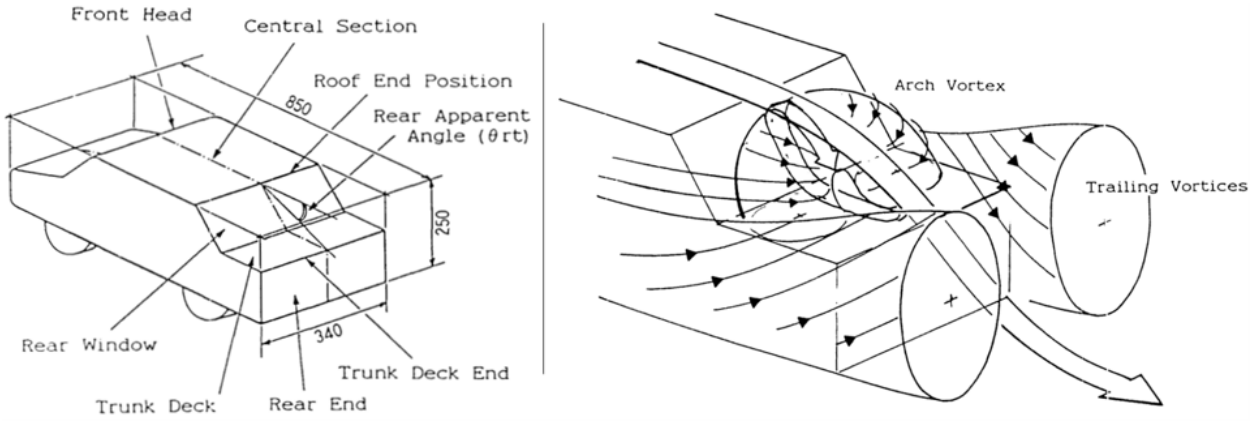

Figure 2.16: Dimensions of Scale Model used by Nouzawa *(left)* Notchback flow structure proposed by Nouzawa *(right)* [16] *(edited by the author)*.

notchback model, with an arch-type vortex behind the backlight that tend to reinforce the trailing pillar vortices. Also this arch-type vortex push the separated shear layer downwards at the centerline of the car, Figure 2.16(right), resulting in a more complex transverse vortex than the one proposed by Carr.

3 CFD Methodology

"Imagination is everything. It is the preview of life's coming attractions"

-Albert Einstein

The AeroSUV, presented in Chapter 1: "Introduction", is a highly detailed model that demands adequate computational sources and as a result the time required for a complete simulation can be markedly sizeable. It is wise to use a simplified model at first, to test various setups and parameters and then to continue with the research with the AeroSUV. The model that was chosen for the preliminary research is the SAE Notchback 20° Backlight [2]. It is a simplified car-like model used as a CFD reference case and is extensively analysed in Chapter 4: "Results I – SAE Notchback".

The research of the most suitable CFD setup for a specific model is a multi-parameter problem. Hence it is essential to decompose it into smaller ones and set a number of objectives for each. Prior to that it is important to clarify what a CFD setup exactly is.

An aerodynamic simulation consists of the following discerned steps:

- Pre-Processing
- Numerical Solution
- Post-Processing

A CFD setup, is a combination of the parameters and settings used for the pre-processing and the numerical solution. The results of each setup are assessed by the cross-examination of numerically and experimentally derived data through the post-processing. These steps are analysed further below to provide a clearer picture of their meaning.

3.1 Pre-processing

The pre-processing phase includes the geometry clean-up, the computational domain and refinement regions integration, the definition of the boundary conditions and finally the spatial discretization of both the surfaces and the main volume of the flow domain. For this process, the ANSA v21.1.0 software was used developed by BETA CAE Systems SA, Thessaloniki, Greece.

3.1.1 Domain and Boundary Conditions

During the geometry clean-up, the CAD file is imported in ANSA and the geometry is transformed to watertight in order to start the meshing process. In this thesis, the open-road wind tunnel type was used. For the SAE Notchback model, the dimensions of the domain used for the CFD simulation are the same as the domain used for the experiment

conducted by Wood *et al.* [2]. The domain used for the AeroSUV was based on the guidelines for CFD simulations of ground vehicle aerodynamics published by SAE International [46] and the specific dimensions will be presented below.

SAE Notchback Reference Model

The SAE Notchback experiment was conducted in a fixed floor wind tunnel with length 11.7m, width 1.94m and height 1.32m [2]. The blockage ratio, the projected frontal area of the model divided by the cross section of the wind tunnel at the location where the model is placed, is 2.97% which is an acceptable value in order to minimize the effects from the boundary conditions on the flow field formed around the car.

The distance between the frontmost face of the model and the domain's inlet is five times the car length in order to avoid interference between the flow field around the model and the boundary condition set for the velocity inlet. Figure 3.1 illustrates that the influence of the inlet is already negligible at two car lengths upstream of the vehicle. The tunnel extends eight car lengths downstream of the rearmost face of the model so as adequate space exists for the wake to be fully developed and to ensure low turbulence regime near the outlet.

The flow at the inlet is modeled with the velocity inlet boundary condition that imposes a uniform velocity profile across that face; when values regarding the turbulence are available,

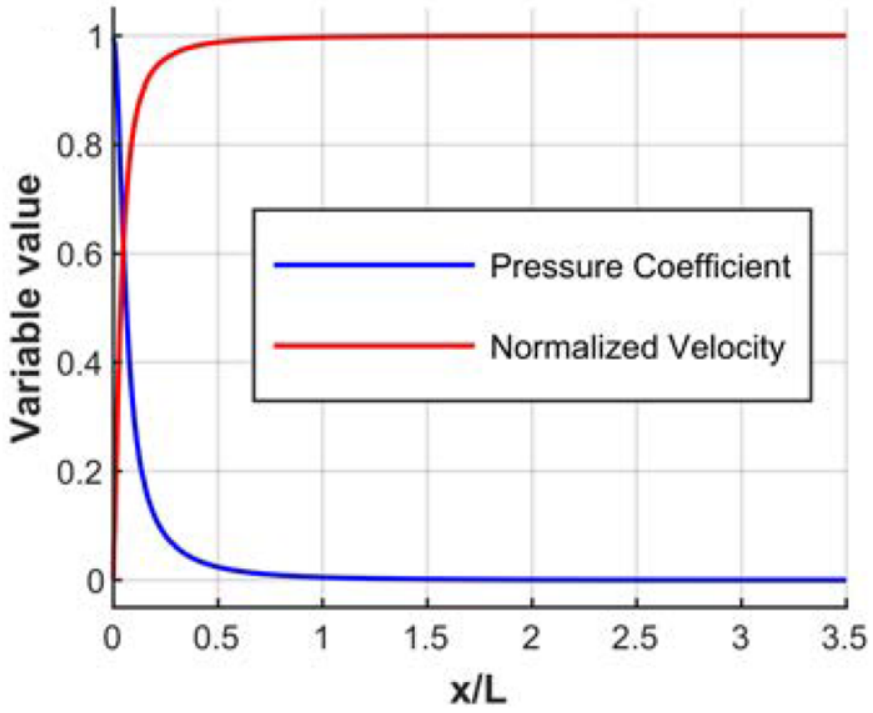

Figure 3.1: Pressure and velocity distribution across an empty computational open-road domain with velocity inlet and pressure outlet boundary conditions for the inlet and the outlet respectively [4].

the simulation setup is tuned so as experimental and computational values near the inlet are matching. The flow outlet of the tunnel is modelled with zero gauge pressure outlet boundary condition. Since the SAE Notchback was tested in a wind tunnel with fixed floor, the road, the side and the top walls are modeled as no-slip stationary walls (see Figure 3.2). Prior to the simulation of the model, an empty domain simulation was conducted to check if the boundary layer height calculated through CFD at the location where the model will be placed is the same with the one measured through the experiment.

The faces of the model were classified into groups called PIDs (ANSA terminology), as seen in Figure 3.3, for better control during the surface meshing and layers generation process. In addition, after the numerical solution process, data regarding every individual Property Identification (PID) were derived making the examination of each group easier and providing a clearer image of the pressure and wall shear stress oscillations for every device.

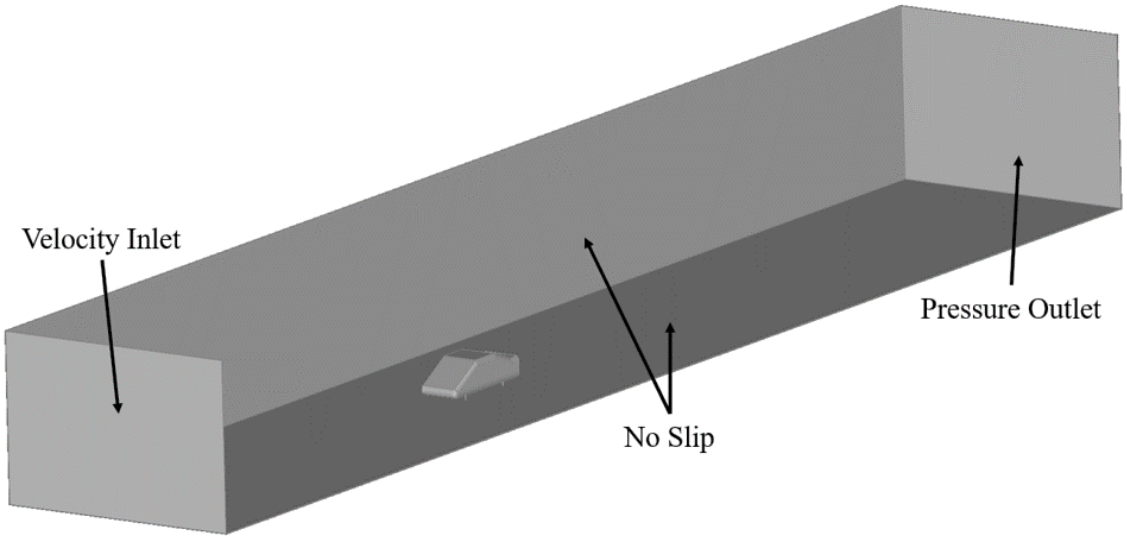

Figure 3.2: Boundary conditions used for the SAE Notchback simulation.

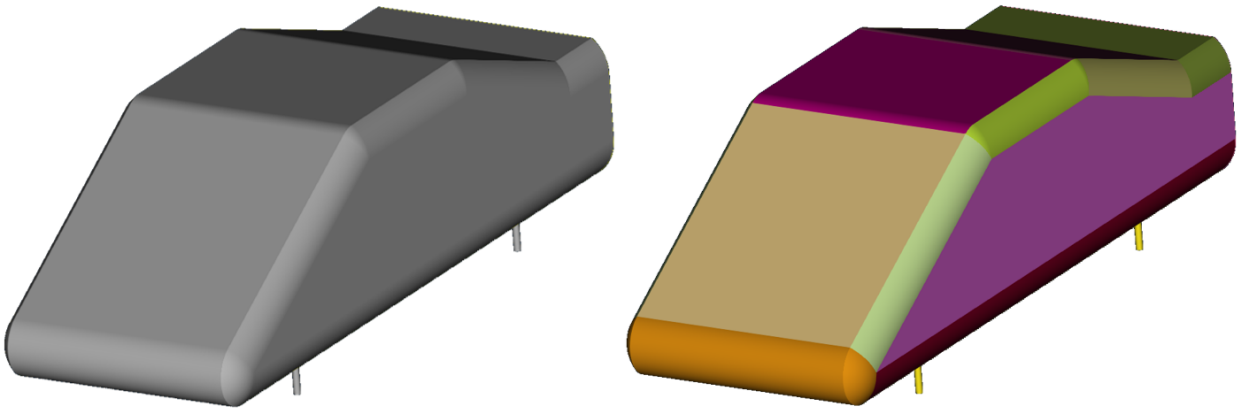

Figure 3.3: SAE Notchback model *(left)*, model divided into properties for better control *(right)*.

AeroSUV Reference Model

The AeroSUV model was tested at Forschungsinstitut für Kraftfahrwesen und Fahrzeugmotoren Stuttgart (FKFS) wind tunnel using state-of-the-art techniques to simulate the translational motion of the road and the rotation of the wheels. A boundary layer suction system was used so as uniform velocity profile near the wall is achieved at the location where the model was placed [33][34]. To maintain the Reynolds number analogy, since an 1:4 scaled down model is used, the inlet velocity was set at 50m/s (180km/h).

For the CFD simulation, a computational domain with length 16.3m, width 7.3m and height 3m was used resulting in a blockage ratio equal to 0.7% to ensure zero influence of the boundaries on the flow field around the car. The domain extends 3.3 model lengths upstream and 9.8 car lengths downstream. Similarly to the SAE Notchback setup, the inflow to the domain is modelled with a uniform velocity inlet boundary condition and the outflow is modelled with a zero gauge pressure outlet. The road is modelled with a no-slip moving wall boundary condition with translational velocity equal to the flow velocity at the inlet. The wheels are modelled as well as no-slip moving walls with rotational velocity such as no slip occurs between the road and the wheels at the contact patch. Since the side and top walls are adequately far from the model, they are modelled as fixed free-slip walls or with symmetric conditions.

The grilles of the model are solid and the internal flow is not simulated to reduce potential sources of uncertainty and errors. This model contains fully detailed wheels with realistic rims which need special treatment during the pre-processing , the meshing and the set-up of the simulation. The wheels are constructed by hard rubber-like material with zero deflection due to the weight of the model, thus the wheels are in contact with the road like billiard balls. In the model used for the CFD, the smallest possible contact patch was used with height 1mm, as seen in Figure 3.5, to ensure that even the flow inside the tyre grooves is simulated. Without the use of contact patch, a very sharp concave angle is formed between the road and the wheels' surface which lead to bad mesh quality, thus the use of contact patches is inevitable.

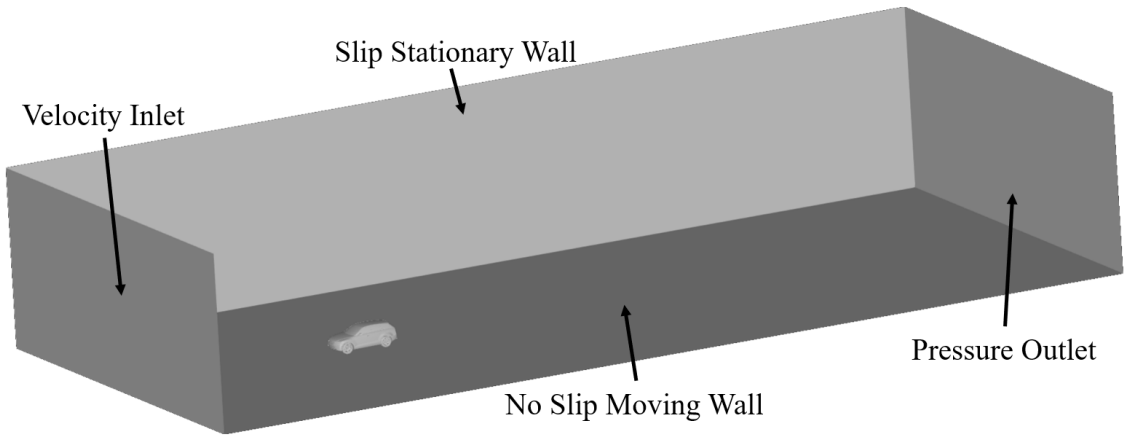

Figure 3.4: Boundary Conditions used for the AeroSUV simulation.

Finally, for the steady state simulations, the rotating motion of the wheels and rims is modelled with the Multiple Reference Frame (MRF) technique, where an angular velocity component is imposed in the fluid particles between the rim spokes. For transient simulations, the Dynamic Mesh technique was used, the mesh was rotating with a constant angular velocity at the end of every time-step and the communication between the rotating and the outer volume was achieved via interpolation between non-conformal meshes.

Similarly to the SAE Notchback, the AeroSUV was divided into several PIDs, as seen in Figure 3.6 to achieve a better control of the meshing process and to export more analytical data regarding the aerodynamic load in different regions of the vehicle.

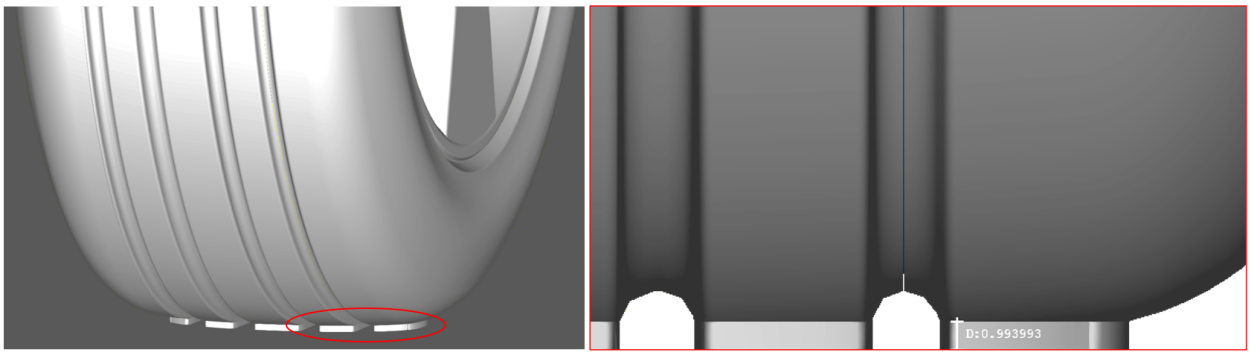

Figure 3.5: Contact patches of 1mm height used to connect road and wheels without blocking the airflow passing through the grooves.

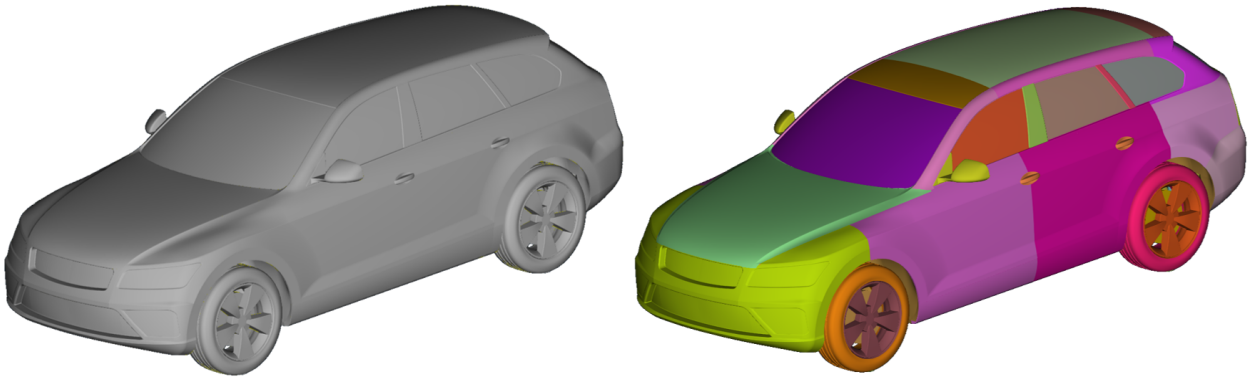

Figure 3.6: AeroSUV Squareback reference model *(left)*, surfaces classification into various PIDs *(right)*

3.1.2 Surface Meshing

The surface mesh is generated with the use of the batch-mesh utility, provided by ANSA software, that automatically meshes the desired geometry based on pre-defined scenarios. The PIDs that were set at the previous stage are now categorised into the aforementioned scenarios with the use of user-defined filters. By classifying the parts of the model, a high quality mesh is generated and every group of PIDs is meshed with different settings based on their geometrical characteristics.

ANSA software provides four first-order surface meshing algorithms, as seen in Figure 3.7. The first called Trias and produces shell mesh dominated by triangular shaped elements. The next one is called Ortho Trias and produces a shell mesh dominated by rectangular triangular shaped elements. The third one is the Quads algorithm which generates quadrilateral shell elements and the last one is called Mixed and generates a shell mesh consisting of elements of all the above categories [18].

The shell mesh type is one of the most important parameters of a CFD setup. For the simulations conducted in this study, the geometry is mainly discretized with triangular cells and in specific cases the mixed algorithm is also utilized. Other important parameters regarding the surface mesh are the minimum and maximum mesh size, the growth ratio and the distortion angle, defined as the maximum allowed angle between adjacent shell elements. Moreover, ANSA can isolate surfaces with special geometrical characteristics, such as high surface curvature or trailing edges, and mesh them with different parameters.

To reduce the complexity of the surface mesh parameters, three mesh categories are defined for every model, namely a fine, a medium and a coarse mesh, and their parameters are presented for every case at the corresponding section.

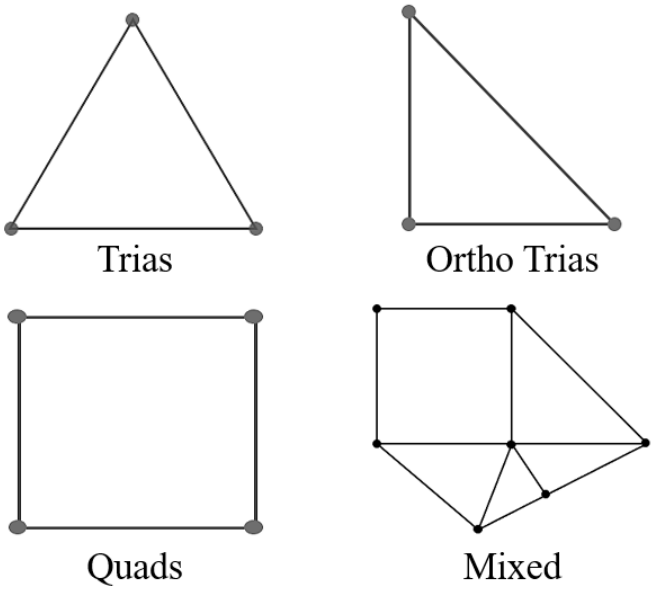

Figure 3.7: Two-dimensional cell types used for the shell mesh.

3.1.3 Layers Generation

The layers generation process, also known as mesh inflation, is the extrusion of the surface mesh normal to every individual cell face. Through this process , a semi–structured three–dimensional mesh, essential for the accurate resolution of the boundary layer, is generated. The most important parameters regarding the mesh creation are the total number of layers, the first layer height and the growth ratio of each layer separately. These parameters are inextricably linked with the non-dimensional wall units, Y-Plus (y^+) and U-Plus (U^+), Equations (2.2) and (2.3).

CFD simulations can be classified into two main categories based on the layers approach. The first one is called Low-Reynolds approach, where the boundary layer is directly resolved down to the wall and the second is the High-Reynolds approach where the boundary layer is modelled by empirically derived pre-defined wall functions. Low-Reynolds simulations demand an adequately fine mesh compared to the High-Reynolds approach, but they provide a better prediction of the flow field near the wall and thus a high fidelity computation of the wall shear stress. For geometries where the flow is fully attached, both models provide realistic predictions and the High-Reynolds approach is preferred since it demands coarser mesh resulting in less computational sources and time.

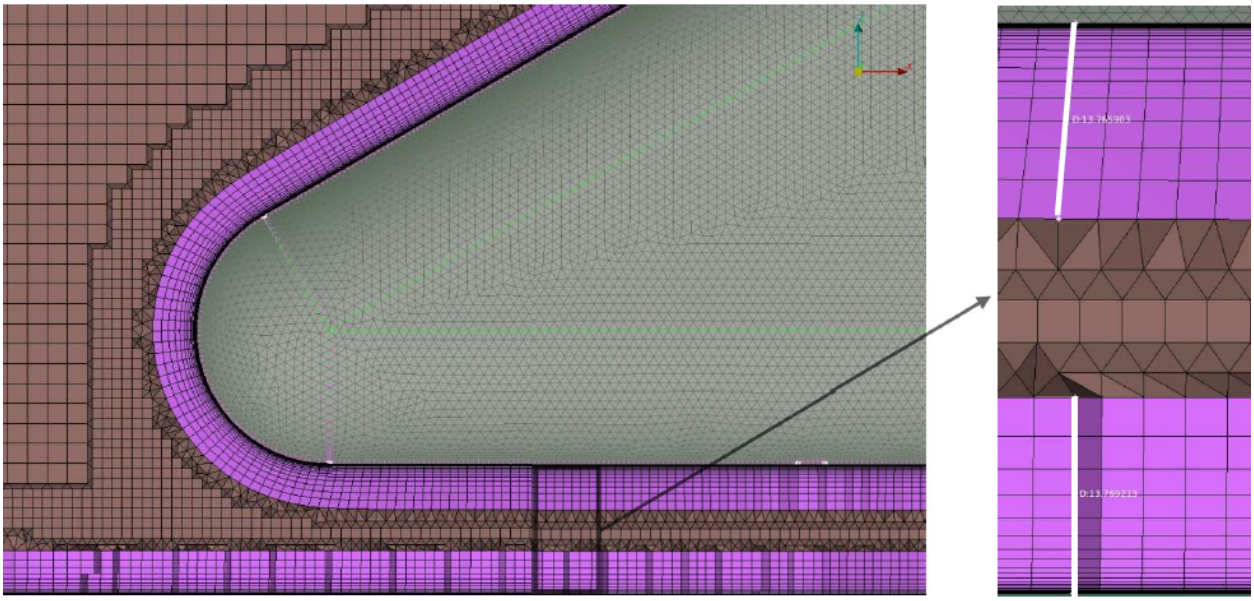

Figure 3.8: The volume mesh is comprised of the main volume elements, displayed with brown colour and the layers with purple colour *(left)*. A closer image of the near wall region reveals that the layers consist of structured mesh that forms an offset of the base geometry *(right)*.

Low-Reynolds Approach

The approach of modelling the boundary layer explicitly down to wall affects one of the main layers' parameters, the first layer height. Through this approach, the turbulence is integrated to the wall and the boundary layer is fully resolved down to the wall including the viscous layer as well. This means that the mesh resolution should be fine enough close to the wall, and the first cell center must be inside the viscous sub-layer.

The main objective of a CFD code towards the near wall region, is the accurate calculation of the shear stress which is proportional to the local velocity gradient, as seen in Equation (2.5). Figure 3.9 is a hybrid logarithmic-scale chart depicting with black colour the velocity inside the boundary layer that was calculated from Direct Numerical Solution (DNS). For $0 \leq y^+ \leq 5$ the linear blue curve can accurately predict the real velocity profile. This is actually a linear equation and since the second order CFD codes give linear variation between the cells, as shown in Figure 3.10 *(middle)*, then the gradient can be easily calculated. The velocity on the cell centroid (U_P) is calculated from the governing equations presented at Chapter 2: "Theoretical Background", namely the continuity (2.7) and the momentum equations (2.8); the velocity on the wall is defined from the boundary conditions.

By replacing the linear variation of the velocity across the cell in Equation (2.5), the wall shear stress for the Low-Reynolds approach can be calculated by:

$$\tau_w = \mu \frac{\partial U}{\partial y} = \mu \left(\frac{U_P - 0}{y_P} \right) = \mu \left(\frac{U_P}{y_P} \right) \qquad for \quad y^+ \leq 5 \qquad \text{(Eq. 3.1)}$$

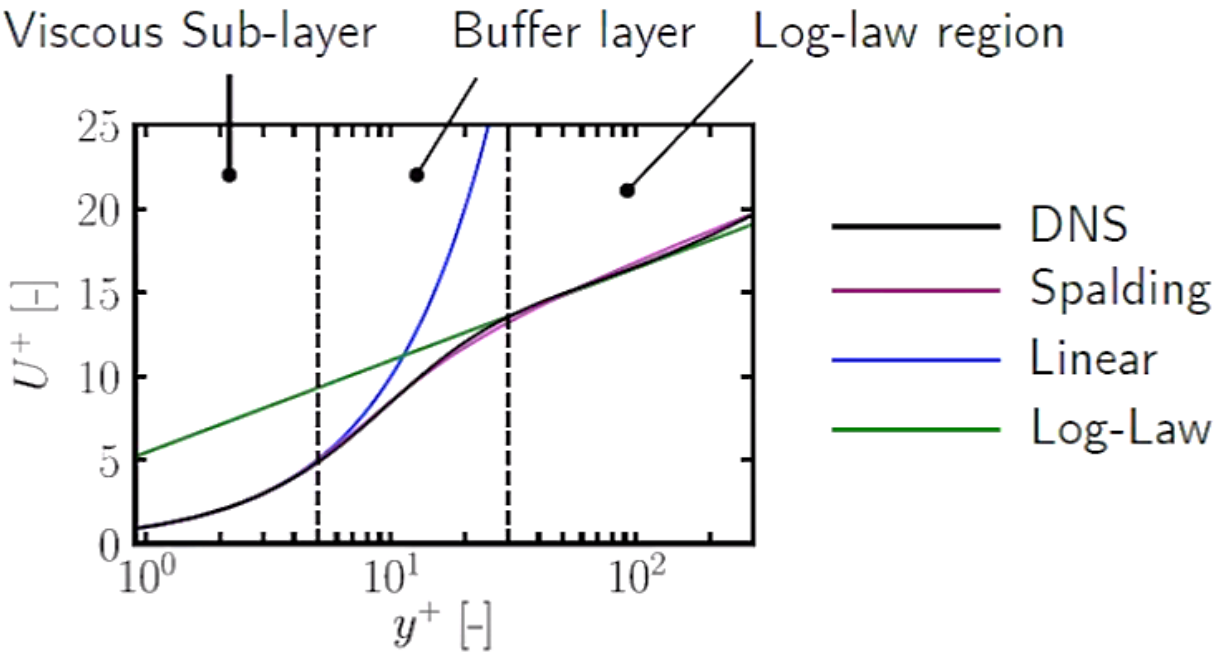

Figure 3.9: The law of wall [17].

High-Reynolds Approach

For $y^+ \geq 30$ the near wall region is modelled with the use of empirically derived equations, the so-called wall functions, depicted in the Figure 3.9 with blue line, representing a logarithmic variation of U^+ with y^+, with the "Log-Law" label given by:

$$U^+ = \frac{1}{k} log(\epsilon y^+) \qquad \text{(Eq. 3.2)}$$

and

$$\tau_w = \mu \left(\frac{\partial U}{\partial y} \right)_{y=0} = \frac{u_t U_p}{\frac{1}{k} log(E y^+)} \qquad \text{(Eq. 3.3)}$$

Where k and ϵ are semi-empirical coefficients, with values 0.4187 and 9.793 respectively, in order to fit the two curves. This approach reduces significantly the elements' count since it does not demand fine grid resolution near the wall. The height of the first cell center should now be between $30 \leq y^+ \leq 200$.

Attention must be given since the empirical parabolic profile of the boundary layer applied across the cell at the High-Reynolds approach, was extracted from wind tunnel testing of a flat plate placed parallel to the flow. Throughout this experiment, there was no separation, no surface curvature and the flow field was devoid of strong pressure gradients. If this empirical velocity profile is used in a flow scenario when critical curvature and strong pressure gradients exist, for example flow behind a cylinder, then that universal profile is no longer likely to be accurate and valid. Hence, using this wall treatment approach on such cases, then the predicted flow solution is highly likely to be incorrect and wrong.

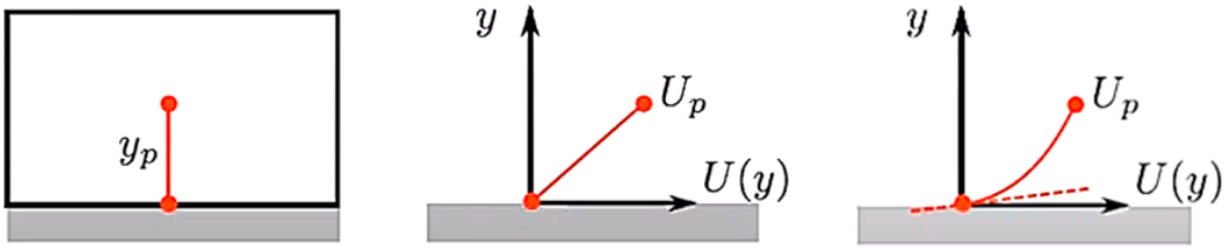

Figure 3.10: A cell adjacent to the wall with y_p being the distance between the wall and the cell centroid *(left)*, linear velocity variation across the cell for Low-Reynolds approach *(middle)*, parabolic velocity variation across the cell for High-Reynolds approach with the use of wall functions *(right)* [17].

First Layer Height Calculation For Given y^+ Value

The calculation of the first layer height based on a given y^+ value is presented below. The first step is to rearrange the y^+ equation, and solve for y:

$$y^+ = \frac{yu_\tau}{\nu} \quad \rightarrow \quad y = \frac{y^+\nu}{u_\tau} \tag{Eq. 3.4}$$

As it was mentioned before, u_τ is the wall shear stress based velocity and is given by equation (2.4). The wall shear stress τ_w can be calculated as:

$$\tau_w = \frac{1}{2} C_f \rho U_\infty^2 \tag{Eq. 3.5}$$

Where C_f is the skin friction coefficient and for a flat plate is calculated with the $(1/7)^{th}$ power law profile from the equation:

$$C_f = 0.0576 Re_d^{-\frac{1}{5}} \tag{Eq. 3.6}$$

The Reynolds number can be calculated based on the velocity inside the flow domain and the characteristic length from the Equation:

$$Re = \frac{\rho u L}{\mu} = \frac{uL}{\nu} \tag{Eq. 3.7}$$

After choosing one of the two approaches, the y^+ is known as well and by replacing the known numbers vice versa from Equation (3.7) to Equation (3.4), the first layer height can be calculated.

Mixed-Reynolds Approach

The aforementioned approaches work well for $0 \leq y^+ \leq 5 \ \cup \ 30 \leq y^+ \leq 200$ however for y^+ values between 5 and 30, that corresponds to the buffer layer region, both approaches fail to accurately predict the wall shear stress. The linear and logarithmic curves, shown in Figure 3.9, intersect at y^+=11.25 but the discrepancy from the red line is noticeable across the whole width of the buffer layer. Most CFD codes does not recommend placing cells in that region. In addition, the use of a piecewise function for the near wall velocity is not recommended since most finite volume codes prefer to use the same approach of calculating a gradient and get the correct answer.

The solution to that problem is the use of either a fitted curve or a blended wall functions scheme. The aim of the first method is to fit a single smooth function through the entire range of y^+ that will slightly deviate from the DNS velocity variation *(black line)*. An example of a smooth function, continuous and valid for all y^+ values below 200, is the Spalding wall function [47] given by the Equation:

$$y^+ = U^+ + 0.1108[e^{0.4U^+} - 1 - 0.4U^+ - \frac{1}{2}(0.4U^+)^2 - \frac{1}{6}(0.4U^+)^3] \quad \text{(Eq. 3.8)}$$

A blended wall function scheme is also called automatic, as the user does not have to explicitly specify the boundary layer simulation approach or the y^+ value before starting the simulation. The value of y^+ is not constant across the walls and it varies as the simulation converges. The CFD code evaluates the wall distance and selects the appropriate wall function on the fly. A blended wall function scheme predicts linear velocity variation and in order to provide accurate prediction at the $30 \leq y^+ \leq 200$ region, it uses a modified viscosity called near wall viscosity (μ_w). This specific viscosity is calculated by equating the wall shear stress of the High and Low-Reynolds approaches and more precisely the Equations (3.1) and (3.3):

$$\mu_w \left(\frac{U_P}{y_P}\right) = \frac{u_t U_p}{\frac{1}{k} log(Ey^+)} \quad \rightarrow \quad \mu_w = \frac{u_t y_p}{\frac{1}{k} log(Ey^+)} \quad \text{(Eq. 3.9)}$$

The near wall viscosity is the viscosity that if is used in a linear expression will give the same shear stress as the one evaluated from the wall functions. Most CFD codes decompose the near wall viscosity into a laminar and a turbulent component:

$$\mu_w = \mu + \mu_t \quad \text{(Eq. 3.10)}$$

where

$$\mu_t = \begin{cases} 0 & y^+ < 11.25 \\ \mu \left(\frac{y^+}{\frac{1}{k} log(Ey^+)} - 1 \right) & y^+ > 11.25 \end{cases} \quad \text{(Eq. 3.11)}$$

If the cell adjacent to the wall is in viscous sublayer then the flow regime is laminar and the turbulent component will be zero and if the cell is in the fully turbulent region then the turbulent component is added. In that manner, the same gradient calculation method is used across the mesh and a conditional statement allows the CFD code to switch between the appropriate wall shear stress calculation as required. The blended function can treat a model with different y^+ values across the mesh, however it cannot provide accurate results for the buffer layer region and it is advisable to avoid placing nodes in that region.

3.1.4 Volume Meshing

The volume meshing, is the process of discretizing the volume of the flow domain by generating a three-dimensional computational grid. The most common cell elements used in a first order volume mesh are Tetrahedrons, Hexahedrons, Prisms, Pyramids and the Polyhedrons, which are clearly illustrated in Figure 3.11. The quality of the volume mesh is of utmost importance since it is explicitly linked with the final outcome of the numerical solution and thus the accuracy of the simulation. A computational grid of bad quality may lead to residuals overshoot and the solution process will be terminated. ANSA software provides three volume meshing algorithms based on the type of the cells as well as a function that converts an already existing mesh to a polyhedral one [18]. These algorithms are presented below.

Tetra Rapid – The Tetra Rapid algorithm generates an unstructured three-dimensional computational grid consisted mostly of tetrahedral elements, as seen in Figure 3.12(a). However, for one-directional flows devoid of excessive turbulence and vorticity, this type of mesh is prone to high numerical diffusion resulting in underestimation of the generated flow field and thus low accuracy. On the other hand, this algorithm is very robust and can generate high quality computational grids for very complex geometries.

Hexa Interior – This Hexa Interior algorithm generates a partially-structured, fully conformal variable-size hexahedral mesh at the core of the flow domain and the transition from one size to another is achieved with the use of prisms or pyramids [18][38].The fully conformal mesh ensures low numerical diffusion, however at the size transition regions the solution is prone to high numerical diffusion that can cause significant alternation on the flow field formed around the model. A wise selection of the refinement regions length and width can diminish the aforementioned problem and maintain high accuracy. The main volume is connected to the layers with pyramids and tetrahedral elements, as seen in Figure 3.12(b).

Hexa Poly – The Hexa Poly algorithm generates a semi-structured mesh consisting of combined variable-sized hexahedral and polyhedral elements; the main volume mesh is connected with the layers via tetrahedral elements, as seen in Figure 3.12(c). The key difference between Hexa Interior and Hexa Poly algorithms is that the latter uses polyhedral cells in the transition zone instead of prisms and pyramids. This transition from one size to another without the existence of a buffer zone is as well prone to numerical diffusion. Finally it should be mentioned that neither the Hexa Poly nor the Hexa interior algorithms can generate pure-hexa meshes; they generate hexa-dominated hybrid meshes.

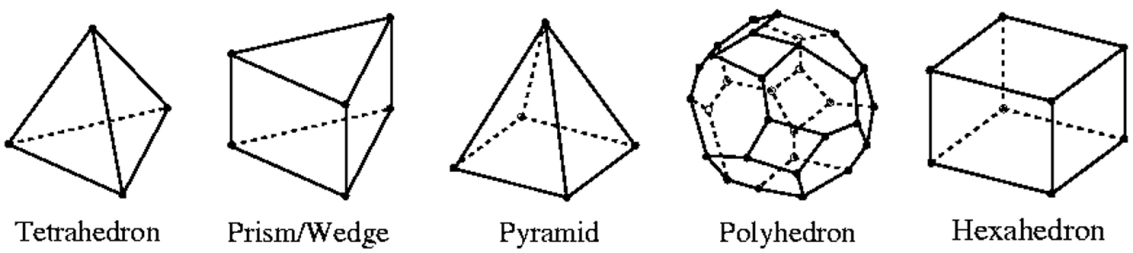

Figure 3.11: Three-dimensional cell types used for the volume mesh.

Convert to Polyhedral – A pure polyhedral mesh can be generated from the conversion of a tetrahedral or a hybrid hexahedral or polyhedral mesh, as seen in Figures 3.12(a,b). The pure polyhedral volume mesh is generated by splitting the already existing cells and reconstructing them in order to generate a high quality polyhedral mesh. This function provides the option of converting the surface mesh and the layers to polyhedral elements as well. However for Low-Reynolds approach, where the first layers are very thin, the conversion of the layers to polyhedral elements is prone to create warped bad quality elements and thus layers grids without layers conversion are used in this thesis, as seen in Figure 3.12(c).

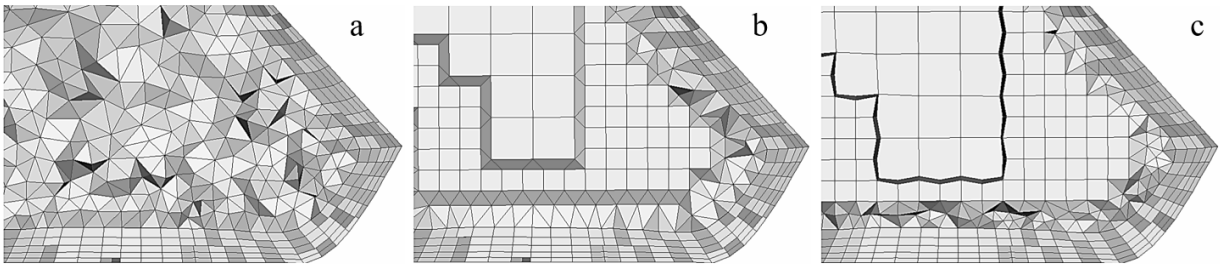

Figure 3.12: Computational grids generated by (a) Tetra Rapid algorithm, (b) Hexa Interior algorithm, (c) Hexa Poly algorithm [18] *(edited by the author).*

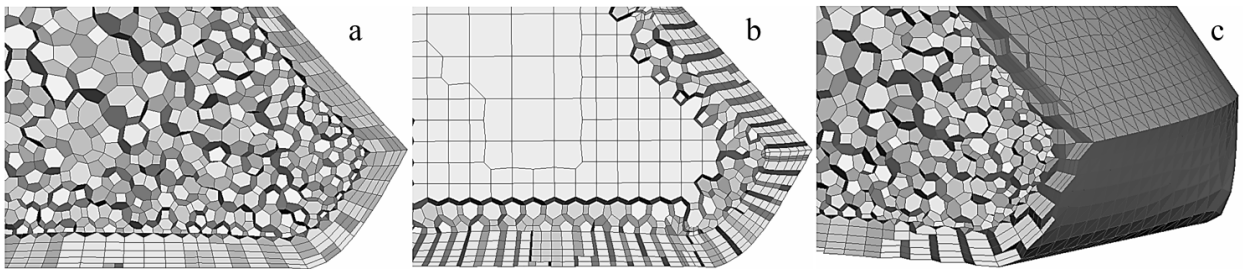

Figure 3.13: (a) Tetra Rapid mesh converted to polyhedral, (b) Hexa Interior mesh converted to polyhedral, (c) Shell mesh and layers are not converted to polyhedrals [18] *(edited by the author).*

Refinement Regions

To ensure high-resolution grid in all regions of interest around and downstream of the model, several refinement regions were introduced. A refinement region is declared with the use size-boxes (ANSA terminology) inside the computational domain. For each box, a minimum and maximum size length and a maximum growth factor is set. These values are also imposed to the surface mesh allowing a better control of the both the surface meshing, the layers generation and the volume meshing process. Size boxes are mainly placed downstream of the model in order to accurately capture the wake, in regions where high pressure gradients occur, in high vorticity regions and at surfaces where flow separation is likely to take place.

SAE Notchback The size-boxes used for the SAE Notchback reference model can be seen in Figure 3.14. It is clear that the size-boxes are mainly focused on the rear end of the model extending approximately five car lengths downstream of the car, as well as at the regions between the car and the floor and the backlight where the angle is very close to the critical one and boundary layer separation is likely to occur. In addition, size-boxes are placed approximately half model lengths upstream of the car to achieve high mesh resolution and thus low numerical diffusion at the stagnation point.

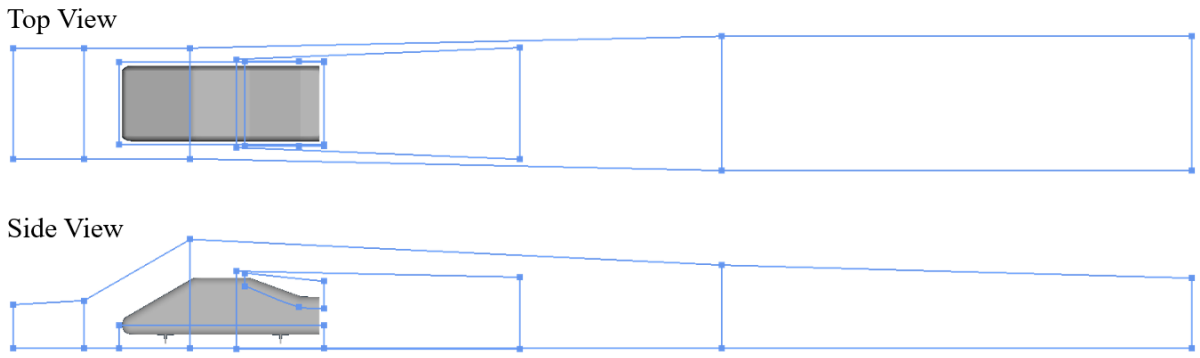

Figure 3.14: Refinement regions used for the simulation of the SAE Notchback reference model.

AeroSUV The AeroSUV is a more realistic model and thus it generates complex flow structures that interact with each other resulting in a more complex flow field that the one formed around the SAE Notchback reference model. To accurately capture all of these structures, several size-boxes were used as seen in Figure 3.15. The mesh is refined up to half model lengths upstream of the car and five model lengths downstream to ensure adequate mesh resolution at the wake of the car. Finally, size boxes were added at the contact patches were the flow is accelerated, cylindrical size-boxes were added to capture the mirror vortices and the roof size-box was extended forward to include the A-Pillar region. Figure 3.16 clearly depicts the multiple refinement regions near the car.

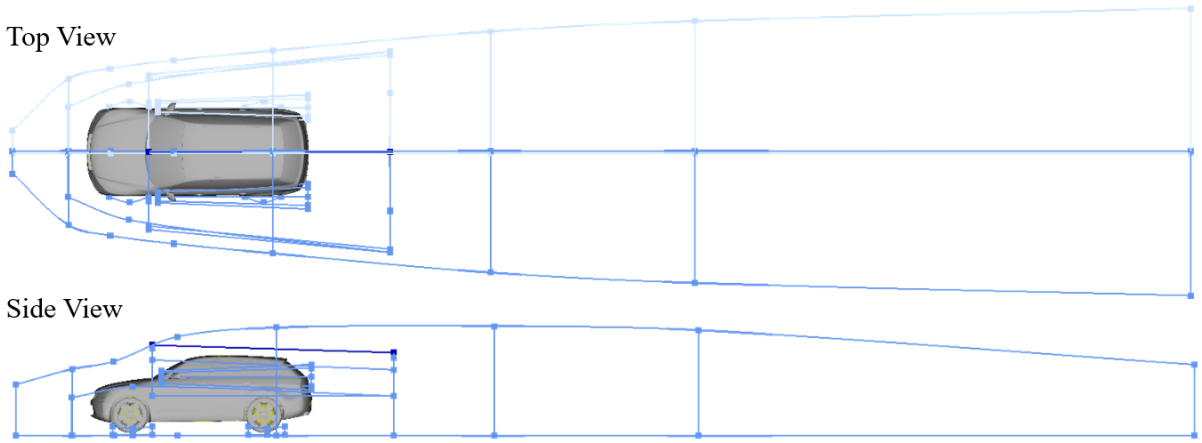

Figure 3.15: Refinement regions used for the simulation of the SAE Notchback reference model.

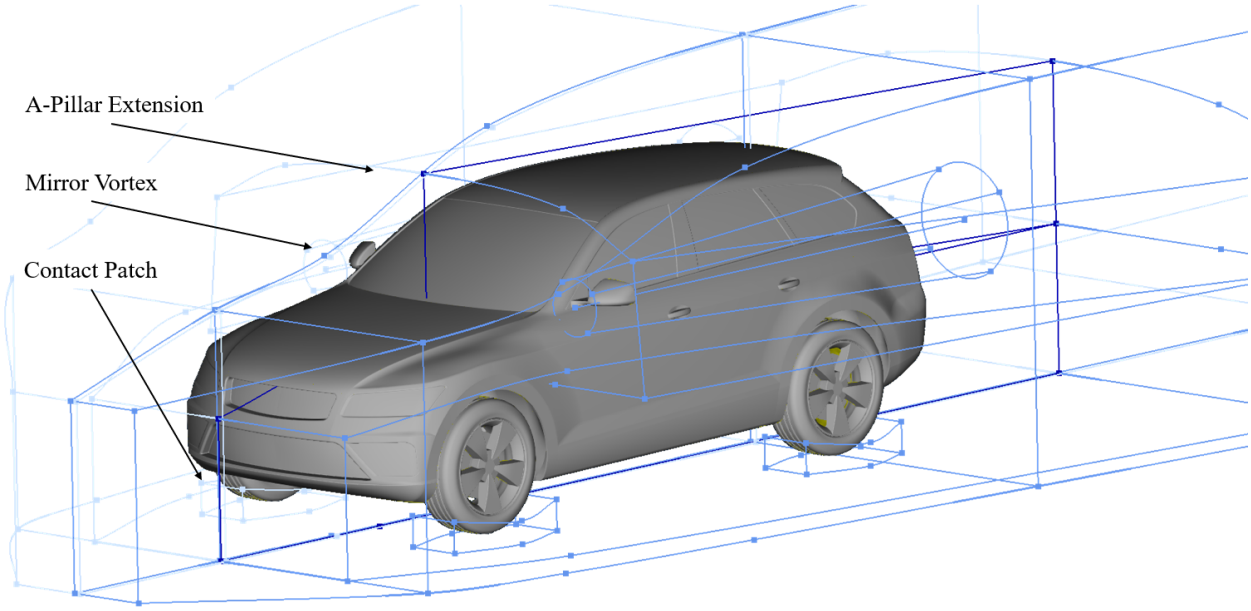

Figure 3.16: Closer image of the size-boxes used for the AeroSUV model.

Mesh Quality Criteria

To assess the quality of the computational grid, several metrics regarding the geometry of the cells were utilized, namely the skewness, non-orthogonality and warping factors.

Skewness The skewness of a cell is defined as the difference between the shape of the cell and the shape of an equilateral cell of equivalent volume. For example, perfect quadrilateral meshes will have vertex angles close to 90°and triangular ones close to 60°Highly skewed grids can cause instabilities to the solution resulting in high computational errors and thus low accuracy. Any deviation from the nominal values can increase the skewness which for OpenFOAM simulations should be lower than 4; for values greater but close to that, the case will still run but the accuracy will be reduced. If skewness over-exceeds 4 then the simulation will overshoot at the very first iterations and the simulation will be terminated.

Skewness can be also defined as the discrepancy between the location of the face center (f) and where the center-to-center vector intersects the face (f'), as it is illustrated in Figure 3.17. Skewness (ϵ) can be calculated from the following equation:

$$\epsilon = \frac{|f - f'|}{|d|} \qquad \text{(Eq. 3.12)}$$

where f is the face center, f' is the location where the center-to-center vector intersects the face and d is the distance between the cell centers.

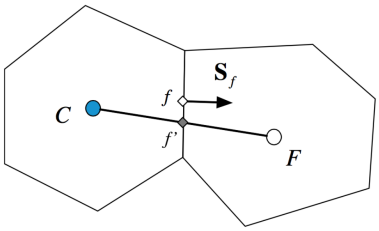

Figure 3.17: Skewness definition for OpenFOAM.

Non-Orthogonality Non-orthogonality is defined as the angle between the centroid vector and the unit vector that is normal to the mutual face of the two adjacent elements. The non-orthogonality metric is very important for the numerical solution since it can cause numerical errors when diffusive term are included in the governing equation [48]. In OpenFOAM source code, the face-non-orthogonality (θ) is used and can be calculated by the following equation:

$$\theta = cos^{-1}\left(\frac{\overrightarrow{d}\cdot\overrightarrow{n}}{|\,\overrightarrow{d}\,\overrightarrow{n}\,|}\right) \qquad \text{(Eq. 3.13)}$$

where d is the distance between the centers of two adjacent cells and $\overrightarrow{n}$ is the unit vector normal to the mutual face as seen in Figure 3.18.

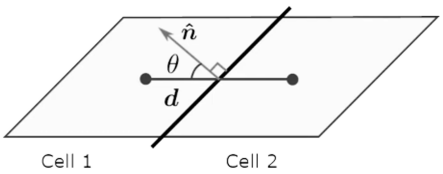

Figure 3.18: Face-non-orthogonality definition for OpenFOAM.

Warping Warping factor is applicable only on quad cells. It is defined as the angle between the normal vectors of two triangular planes formed by splitting a quad element along its diagonals, as seen in Figure 3.19. A perfect element has warping value equals to unit and for OpenFOAM it is recommended to be greater than 0.8 [49].

Mesh Sensitivity Analysis

To ensure that the numerical solution is independent of the mesh resolution, a mesh sensitivity study was conducted for every case investigating the dependency between the aerodynamic loads and the resolution of the mesh especially for the drag coefficient (C_D).

For the steady state simulations, the mesh sensitivity analysis process was conducted by increasing the resolution of the mesh by a constant sizing factor and checking the drag coefficient convergence as seen in Figures 3.20 and 3.21, where the left axis depicts the drag coefficient (C_D) value in every simulation and the right axis the divergence in drag coefficient between the current and the previous simulation (Delta Prev). To reduce the computational

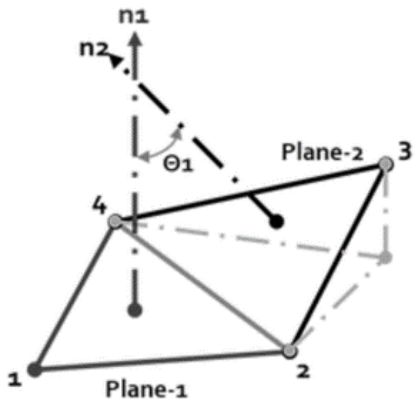

Figure 3.19: Warping definition for OpenFOAM.

time, the smallest mesh that will give results in a predefined threshold, for example Delta Prev lower than 1.5%, was selected for every case.

However, for the transient hybrid RANS-LES models, which will be further analyzed below, the mesh sensitivity analysis is trickier since the resolved turbulence is connected to the resolution of the mesh. Hence, different mesh resolution will always result in different drag coefficient results and with continuous increasing of the resolution the transient simulation will result to be a quasi-DNS one. It is clear that the mesh sensitivity study in this case demands excessive computational sources making this process impractical. For this purpose, the computational grids used for the transient simulations, were selected based on the available computational sources.

SAE Notchback For the SAE Notchback, four simulations were conducted starting from 32 million cells with a sizing factor approximately equal to 1.8 (see Figure 3.20). Assuming a threshold of 1.5% deviation from the previous simulation, the drag coefficient converges after the third simulation consisted of 95.3 million cells.

AeroSUV For the AeroSUV the , four simulations were conducted starting from 18 million cells with a sizing factor approximately equal to 2.1. Assuming a threshold of 1.5% deviation from the previous simulation as well, the drag coefficient converges again after the third simulation consisted of 117 million cells. Figure 3.21, illustrates the mesh sensitivity study for the squareback variant of the AeroSUV; similar analyses were conducted for the other two variants, namely the fastback and the notchback, resulting in the same number of cells as the squareback.

At the end of the research conducted in this thesis, when the CFD set-up that gives the best prediction was found, a mesh sensitivity analysis was conducted again to ensure that the set-up is robust and the high accuracy is the result of a good numerical solution and not a coincidence.

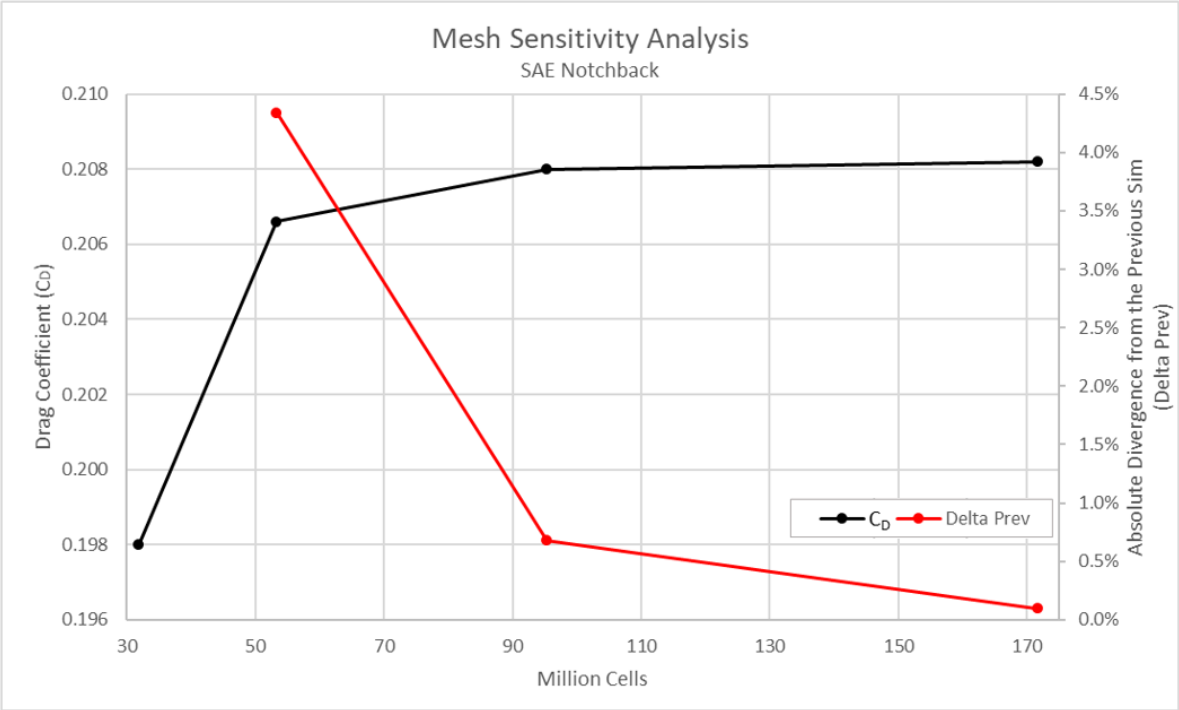

Figure 3.20: Mesh sensitivity analysis for the SAE Notchback reference model.

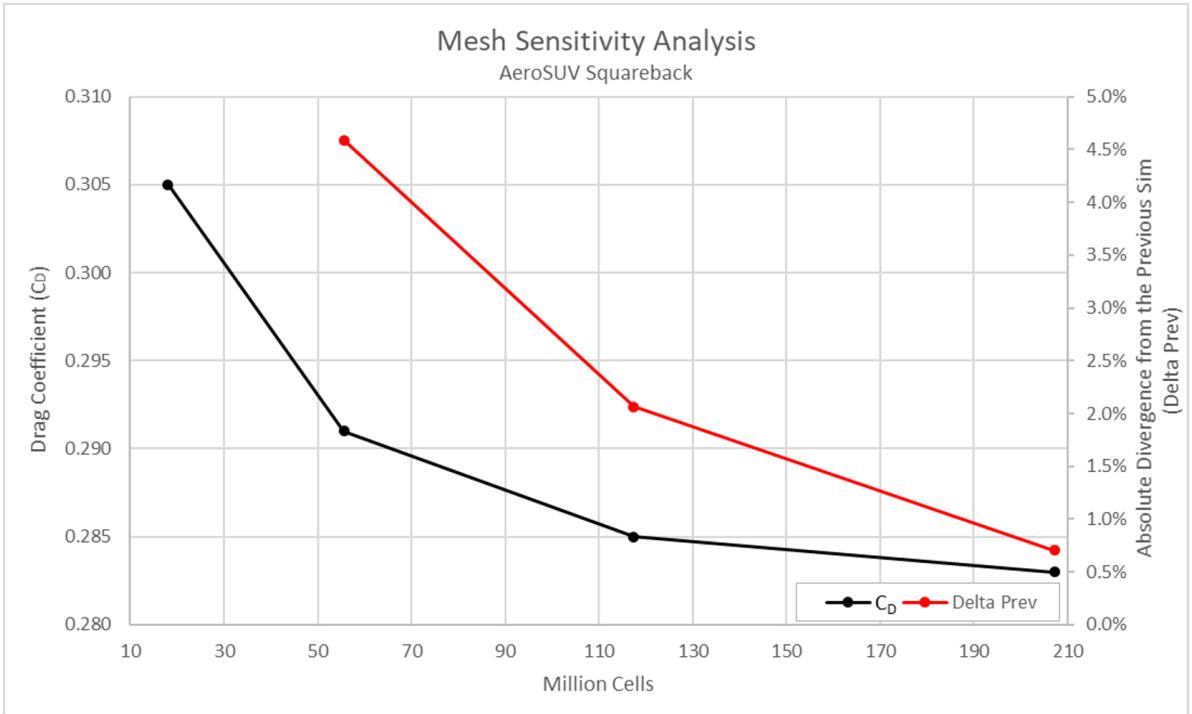

Figure 3.21: Mesh sensitivity analysis for the AeroSUV Squareback reference model.

3.2 Numerical Solution

Since a general analytic solution does not exist for the Governing Equations (2.7) and (2.8) mentioned in Chapter 2.4: "Governing Equations", these equations can be solved numerically through various methods, namely the finite-volume, the finite-difference, spectral methods, lattice-Boltzmann etc., however in this thesis, only the first method will be utilized. For the finite-volume method, the governing equations are integrated in each cell of the computational domain and with the use of discretization schemes, the integral equations are transformed into a system of algebraic equations which will then be solved via an iterative process

3.2.1 Turbulence Modelling

As it was mentioned before, automobiles operate at moderate to high Reynolds number where the flow can be characterized as fully turbulent, except of specific regions which are subjected to laminar flow but their influence to the flow-field is minor. Thus, turbulence is of utmost importance when it comes to vehicle aerodynamics since their irregular and chaotic behaviour can cause major instabilities which can strongly affect the aerodynamic forces.

Taking a closer look to a turbulent flow field, as the one depicted in Figure 3.22, it is consisted of various eddies with different size and shedding frequency. Near the vehicle, eddies of small size are generated which increase in size as they move further downstream of the vehicle. Small eddies are energized by bigger eddies that exist in the vicinity and finally the outer eddies extract their energy from the mean flow; this kinetic energy transfer is called energy cascade. The largest eddies seen in a turbulent flow field calculated through computational fluid dynamics can be comparable to the size of the model while the size of smallest ones is bounded by the so-called Kolmogorov scale [50]. In this scale of eddies, viscous effects are dominating and the whole kinetic energy of the fluid is dissipated into heat.

In computational fluid dynamics, the turbulence can be modelled instead of completely resolved in order to save time and computational sources. There are several methods of turbulence modeling which can be classified based on the amount modeled and resolved turbulence. The method in which all the turbulence is resolved and zero modelling is ap-

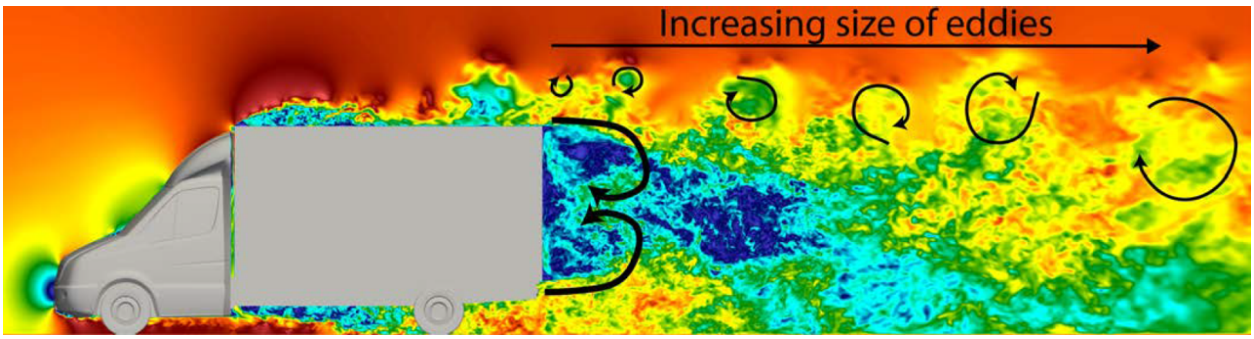

Figure 3.22: Velocity distribution on a y-normal plane depicting the turbulent flow around a big-sized vehicle. Blue and red colors indicated low and high velocity magnitude, respectively [4].

plied is called Direct Numerical Solution (DNS) and is achieved by the direct solution of the Navier-Stokes equations. This method demands a numerical grid with resolution equals to the Kolmogorov dissipation scale resulting in a very big amount of cells which can be solved only in supercomputers. On the other hand, the method in which all the turbulence is modeled is called Reynolds-Averaged Navier-Stokes (RANS) method that calculates a temporal and spatial average of the flow field based on the resolution of the mesh. This type of simulations can provide a fast and accurate prediction of the flow without the need of excessive computational sources and thus it is widely used in automotive industry. The RANS turbulence models used in this thesis were the k-ϵ, the k-ω SST and the Spalart Allmaras.

The gap between RANS and DNS is bridged by the so-called hybrid RANS-LES methods where a specific amount of turbulence is resolved and the rest is modelled. LES stands for Large Eddy Simulation and it is a metod based on the idea that the bigger eddies in a flow field transport the most of the momentum and thus they affect mostly the generated flow field. The LES method, resolves the turbulence of the large eddies and models the turbulence of the smaller ones. The classification of the eddies between large and small is achieved by filtering based on the local grid spacing; more precisely, eddies that are smaller than the local grid spacing are classified as Sub-Grid Scale (SGS) and are modelled. The hybrid method that was used in this thesis was the Delayed Detached Eddy Simulation (DDES) and will be further analyzed below.

3.2.2 Reynolds-Averaged Navier-Stokes

The main objective of turbulence modelling is to devise a set of partial differential equations regarding turbulence based on approximations of the exact Navier-Stokes and is achieved through the Reynolds Decomposition of the flow variables into a time-averaged ($\overline{\phi}$) and a fluctuating component (ϕ') as indicated in Equation (3.14) [51].

$$\phi(x_i, t) = \overline{\phi(x_i)} + \phi'(x_i, t) \qquad \text{(Eq. 3.14)}$$

where x is the location, t is the time and i is the direction in the cartesian coordinate system.

Reynolds decomposition assumes that a turbulent flow is oscillating along a "steady-state", represented by $\overline{\phi}$ and can be written as:

$$\overline{\phi(x_i)} = \frac{1}{\Delta t} \int_a^b \phi(x_i, t)\, dt \qquad \text{(Eq. 3.15)}$$

By replacing the instantaneous variables of the Equations (2.7) and (2.8) with the time-averaged values, the Reynolds-Averaged Navier-Stokes are exported given by the Equations (3.16) and (3.17).

$$\nabla \cdot \overline{\overrightarrow{u}} = \frac{\partial \overline{u}_i}{\partial x_i} = 0 \qquad \text{(Eq. 3.16)}$$

$$\rho\overline{u}_j\frac{\partial\overline{u}_i}{\partial x_j} = -\frac{\partial\overline{p}}{\partial x_i} + \frac{\partial}{\partial x_j}(2\mu\overline{S}_{ij} - \rho\overline{u'_j u'_i}) \quad \text{(Eq. 3.17)}$$

where

$$\overline{S}_{ij} = \frac{1}{2}\left(\frac{\partial\overline{u}_i}{\partial x_j} + \frac{\partial\overline{u}_j}{\partial x_i)}\right) \quad \text{(Eq. 3.18)}$$

Due to the Reynolds-average process, the average product of the fluctuating component ($-\rho\overline{u'_j u'_i}$) is introduced to the momentum equation and discrebes the effect of the fluctuations ought to turbulence in the mean flow. This term is also called Reynolds stresses and can have a significant influence on the mean flow since it can sometimes be greater than the mean viscous stresses ($2\mu\overline{S}_{ij}$) by several orders of magnitude.

With the addition of the unknown Reynolds stresses term, the number of available equations is smaller than the number of unknowns and to tackle this problem turbulence models were introduced to model these unknown stresses. The majority of these models are based on the hypothesis proposed in 1877 by Boussinesq which incorporates the fluctuations on a new term, the eddy viscosity (ν_t) [52]. The RANS turbulence models used in this thesis will be briefly presented below.

k-ω SST Turbulence Model The k-ω Shear Stress Transport (SST) proposed by Menter in 1993 [53] is a two-equation eddy-viscosity turbulence model designed to overcome the "weaknesses" of the previously used k-ε proposed by Launder and Spalding [54] and k-ω proposed by Wilcox [55] formulations. In this turbulence model, k represents the turbulent kinetic energy and ω the specific rate of dissipation, where ω =ε/k and ε is the turbulent kinetic energy.

More precisely, the k-ε model was unreliable near the surface due to the wall damping functions that were used to reduce the turbulent viscosity near the wall, where it should have zero value. For regions far from the model's surface, the model is stable and accurate in contrast to the k-ω model which is very sensitive to the free-stream value of ω applied as a boundary condition at the inlet. However k-ω does not demand near wall damping functions and works fine on solving the viscous sub-layer if an appropriate low-Reynolds volume mesh is provided.

The SST model is a combination of k-ε and k-ω formulations. For regions near the wall, the k-ω is used to solve the inner boundary layer and the k-ε formulation is applied at region far from the body. To achieve this, a blending function F1 is utilized to ensure a smooth and robust transition from one formulation to the other. This function is the hyperbolic tangent of a function that is inversely proportional to the distance from the wall. In that manner, when F1 is equal to unit then the formulation is k-ω and when it is zero then the model uses the k-ε model.

The turbulent viscosity used for the SST model is given by the following equation:

$$\nu_{t_{SST}} = \frac{k}{\omega} \frac{1}{max\left(\frac{1}{\alpha^*}\frac{SF_2}{\alpha_1 \omega}\right)} \tag{Eq. 3.19}$$

and

$$S = \sqrt{2S_{ij}S_{ij}} \tag{Eq. 3.20}$$

where a^* is a low-Reynolds number correction which suppresses the turbulent viscosity, S is the strain rate magnitude, a_1 is a constant used in this model and $F2$ is a blending function.

Spalart Allmaras Turbulence Model The Spalart Allmaras turbulence was proposed by Philipe Spalart and Steven Allmaras in 1992. It is an one-equation model that uses a modified eddy viscosity ($\tilde{\nu}$) which is modeled through a transport equation and an algebraic formula for the length scale (l) [56]. In the main fluid domain, $\tilde{\nu}$ is equal to the eddy viscosity ν_t, but near the wall the eddy viscosity is altered based on a damping function given by Equation (3.21).

$$\nu_{t_{SA}} = \tilde{\nu} f_{v1} \tag{Eq. 3.21}$$

where f_{v1} is the aforementioned wall-damping function given by Equation (3.22).

$$f_{v1} = \left(1 + \frac{C_{\nu 1}^3}{\chi^3}\right)^{-1} \tag{Eq. 3.22}$$

and

$$\chi = \frac{\tilde{\nu}}{\nu} \tag{Eq. 3.23}$$

In Equations (3.21),(3.22) and (3.23) ν is the kinematic viscosity of the fluid and $C_{\nu 1}$ is a constant used in this turbulent model. The length scale is given by $l = ky$ where k is the von Kármán constant and y is the distance from the wall which is used to calculate the rate of dissipation of the modified eddy viscosity ($\tilde{\nu}$). When complex geometries are present, the distance from the wall calculation is tricky fact that makes the Spalart Allmaras model unsuitable for internal flows and flows over complex surfaces. On the other hand the model gives accurate predictions for external aerodynamics containing boundary layers in adverse pressure gradient.

Unsteady RANS The RANS turbulence models can be also utilized in transient simulations if the transient term remains in the Navier-Stokes equations. This type of simulation is known as Unsteady-Reynolds Averaged Navier-Stokes (URANS) and it is used to capture the fluctuations of a time-averaged flow field, which at first sight seems to be unclear. This

approach does not provide accurate results in every simulation and it is mainly used for dynamic grids, unsteady flow fields behind bluff bodies, time-varying boundary conditions etc. Throughout this thesis, only one URANS simulation was conducted but the results did not reveal any potential in working on this direction and soon the concept was dismissed.

Delayed Detached Eddy Simulation Similar to the DNS, the computational cost of conducting an LES simulation can be high enough since it demands fine temporal and spatial discretization. As seen in Figure 3.22, small scale eddies are formed near the surface of the model and their size increases as they move further downstream. The basic concept of a hybrid RANS-LES method is to model the small-scale turbulent structures near the wall and resolve the larger eddies that exist further away from the vehicle, as it is illustrated in Figure 3.23.

With this method, the flow near the surfaces where the flow is attached is a modelled time-averaged result and very small oscillations will be present. The turbulence of the flow downstream of the car will be resolved and instabilities and oscillations will dominate in that region. At the backlight and in regions where boundary layer separation occurs, the flow is resolved based on the Wall-Modelled Large Eddy Simulation (WMLES) approach [57]. In that manner, the accuracy is enhanced compared to a simple RANS simulation, the spatial and temporal resolution is reduced compared to the LES simulation and thus hybrid RANS-LES models can be affordable without having significant computational demands, but they are still considered as computationally expensive [58]. In this thesis, the only hybrid RANS-LES method used is the Delayed Detached Eddy Simulation (DDES).

The DDES model is a variation of the original Detached Eddy Simulation (DES) that was proposed in 1997 by Spalart [59]. The simple DES model was designed for flows with thin boundary layer and sharp separations and it uses the RANS method wherever the flow is attached and the LES method in separated regions away from the surface of the model. However, the presence of thick boundary layers and surfaces in near-to-critical angle, the accuracy of the model is reduced since the transition from RANS to LES is erroneous resulting in very low eddy viscosity and thus underestimation of the skin friction. A key factor in the transition from RANS to LES is the local resolution of the computational grid, if the

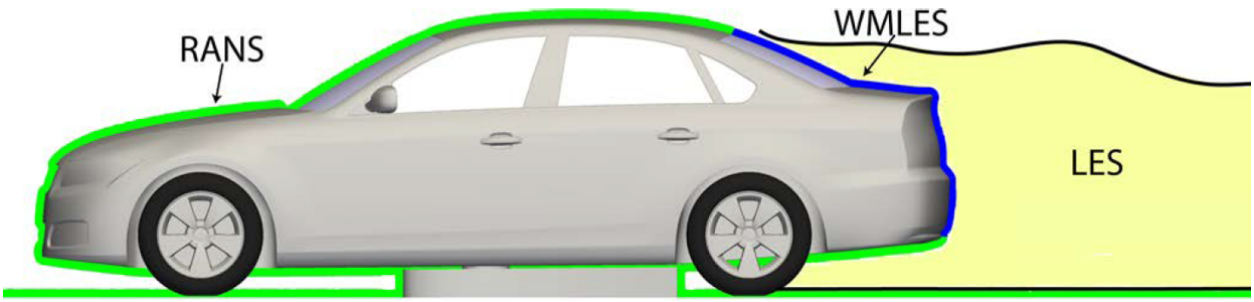

Figure 3.23: Regions where the turbulence is modelled (RANS) and resolved (LES) in a hybrid RANS-LES simulation [4].

grid size is locally bigger than the eddies formed there, then the model will switch to RANS and the flow is more likely to separate pre-maturely due to underestimated turbulence, this phenomenon is called Grid Induced Separation (GIS) and it was observed in this thesis when a coarse mesh was used for the DDES simulation of the SAE Notchback.

To address the GIS problem, in 2006 Spalart et al. proposed a revised version of the DES [60], the so-called Delayed Detached Eddy Simulation which reduces the RANS-LES transition sensitivity by providing a better shielding of the RANS region to ensure that the transition from RANS to LES will take place out of the boundary layer. This was achieved with the introduction of a shielding function (f_d) and a boundary layer sensor and the new modified length scale (L_{DDES}) of the DES model is calculated from Equation (3.24).

$$L_{DDES} = L_{RANS} - f_d max(0, L_{RANS} - C_{DDES}\Delta_{max}) \quad \text{(Eq. 3.24)}$$

where L_{RANS} is the lenght scale used in the RANS model, f_d is the aforementioned shielding function, C_{DDES} is an empirical constant with initial value equal to 0.65 and Δ_{max} is the maximum edge length of the current cell.

3.2.3 Solver Settings

The simulations presented in this thesis were conducted with the OpenFOAM software, version 7.0 developed by The OpenFOAM Foundation Ltd. The solver settings used were selected from a pre-existing library developed by OpenFOAM, no custom libraries where used.

All the simulations were initialized by completing 50 iterations with potentialFoam which is a potential flow solver; solves for the velocity potential to calculate the face-flux field from which the velocity field is calculated by reconstructing the flux. Afterwards, the applyBoundaryLayer function is used to apply a simplified bounary layer to the velocity and turbulence fields based on the 1/7th power-law in order to accelerate the solution process. The main part of the solution process for the steady state simulations was conducted with the simpleFoam solver, suitable for incompressible flows that utilizes the SIMPLE algorithm for the pressure-velocity coupling and solves the continuity and the Reynolds-Averaged Navier-Stokes equations. When low-quality grids were used, non orthogonal correctors were added for the first iterations to ensure a stable numerical solution.

For the pressure (p) and volumetric face-flux (Phi), the Geometric agglomerated Algebraic MultiGrid (GAMG) solver was used with Gauss Seidel smoother, faceAeraPair agglomerator, maximum number of internal iterations equal to 15 and relative tolerance per iteration equal to 0.05. For the rest of the variables, namely the velocity (U), the turbulent kinetic energy (k), the turbulent dissipation rate (omega) for SST simulations and the modified eddy viscosity (nuTilda) for the Spalart Almaras simulations, the smoothSolver was used with Gauss Seidel smoother, relative tolerance equal to 0.1 and one sweep per iteration.

Regarding the numerical schemes, the gradient terms (∇) were discretized with the Gauss linear method, the divergence terms ($\nabla\cdot$) with bounded Gauss upwind for the convection terms which adds a linearised implicit source of the transport equation to remove a component proportional to the continuity error. This is done in order to bound the solution as the calculation proceeds and when the convergence is achieved this term becomes zero and has no contribution to the final solution. This method is only applicable to steady state simulations. For the $div(div(phi, U))$ and $div((nuEff * dev2(T(grad(U)))))$, the Gauss linear method was used. The laplacian terms (∇^2) were discretized with the Gauss linear corrected method and the wall-distance was calculated with the meshWave function. Transient simulations were initialized from fully converged steady-state RANS simulations and the time derivatives were discretized with the Euler method and the rest of the numerical schemes were set to default based on the simpleFoam tutorials provided by OpenFOAM [61].

3.2.4 Convergence Criteria

The steady state simulations ran until the RMS solution residuals reach below $10^{-}3$ and until the aerodynamic forces reach a quasi-steady-state. Since the flow field behind a bluff body such as the SAE-Notchback and the AeroSUV is unsteady, the aerodynamic loads will always oscillate. To capture these oscillations, after the convergence state the simulation continues for 600 iterations and the results of them are averaged. The final output of the simulation is iteration-averaged data which are then used for the post-processing.

For the transient simulations, the time-step is computed based on the Courant-Friedrichs-Lewy (CFL) convergence condition [62] and more precisely, for the SAE Notchback model the timestep was selected so as the CFL number (or Courant number) of 90% of the cell elements to be below 1, and for the AeroSUV the percentage is 85% due to limited computational sources, as seen in Figure 3.24. The Courant number in every cell and the total percentage were calculated with a Python script developed by the author. Transient simulations ran for 5 convective flow units in order to complete the stabilization (or burn-in) phase and then data was averaged for 20 convective flow units. A convective flow unit is defined as the time a particle needs to travel in straight line, distance equal to the length of the model.

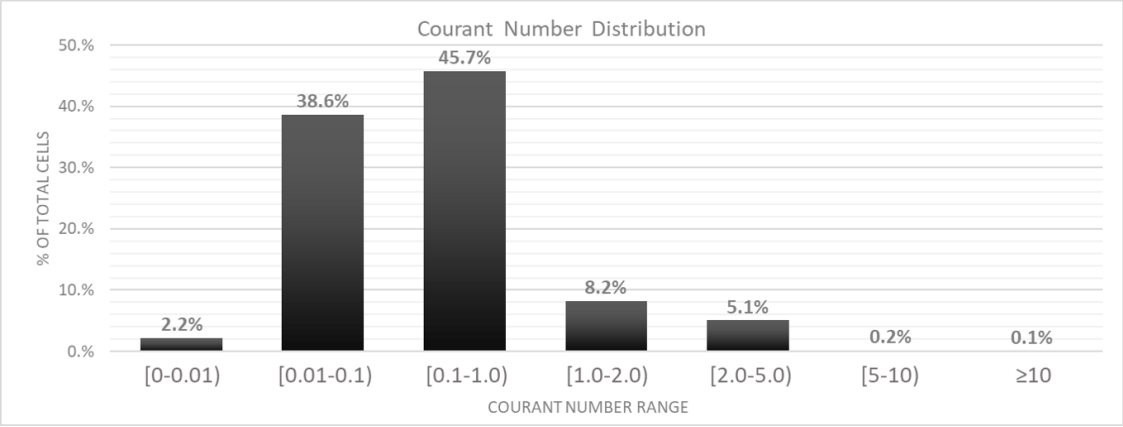

Figure 3.24: Courant Number distribution across the cells for an AeroSUV DDES simulation.

3.3 Post-processing

For the post-processing, the META software, developed by developed by BETA CAE Systems SA, was used in combination with python scripts developed by the author. All the variables used for the post-processing were iteration-averaged or time-averaged if the simulation was steady-state or transient respectively to ensure that the results are not affected by the unsteady behaviour of the flow field. The post-processing was automated via META-Python scripts in order to accelerate the procedure and capture the same images for all the models for easier comparison.

3.3.1 Flow descriptors

There are numerous indicators that can used to quantify a flow field and describe the flow regime in a certain region. In this thesis, only non-dimensional coefficients were used to ease the comparison process between different models. For the indicators that contain any kind of pressure, it is mentioned that the gauge pressure is subtracted from the measurements and only the divergence from the reference pressure is taken into consideration. For example when it is mentioned that the static pressure of the fluid is 50Pa at point A and -200Pa at point B, it is 50Pa greater and 200Pa lower than the reference pressure, respectively. The flow descriptors used are presented below:

Static Pressure Coefficient (C_p)

$$C_p = \frac{p_s}{0.5\rho_\infty U_\infty^2} \tag{Eq. 3.25}$$

where p_s is the static pressure, ρ_∞ is the density of the fluid and U_∞ is the free-stream velocity. The denominator of this fraction is also called free-stream dynamic pressure and is used to normalize various flow variables.

Total Pressure Coefficient ($C_{p_{tot}}$)

$$C_{p_{tot}} = \frac{p_s + 0.5\rho U^2}{0.5\rho_\infty U_\infty^2} \tag{Eq. 3.26}$$

where $(0.5\rho U^2)$ is the dynamic pressure of the fluid at a specific point and the sum of the static and the dynamic pressure is the total pressure of the fluid. In absence of energy sources in the domain, the total pressure in every point inside the domain must be equal or lower than the total pressure at the inlet of the domain, otherwise the numerical solution is erroneous. If the total pressure coefficient is plotted on a surface with no-slip boundary condition, it will be equal to the static pressure since on the surface the velocity will be zero. Hence, it is preferable to plot the total pressure coefficient on the volume and not on surfaces.

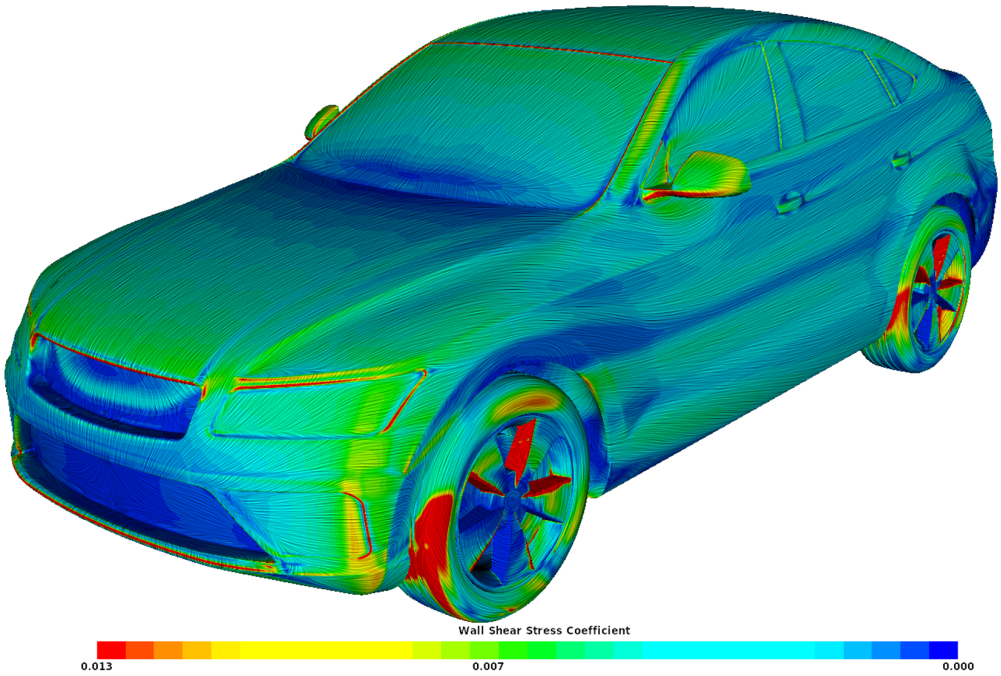

Figure 3.25: Wall shear stress coefficient contours combined with LIC lines on the surface of the AeroSUV Fastback.

Wall Shear Stress Coefficient (C_f)

$$C_{p_{tot}} = \frac{\tau_w}{0.5\rho_\infty U_\infty^2} \qquad \text{(Eq. 3.27)}$$

where τ_w is the wall shear stress. Since τ_w is proportional to the gradient of the velocity near the surface as seen in Equation (2.5) and since viscosity and surface roughness are constant, this discreptor is an indicator of the near-wall velocity magnitude. This scalar is plotted in surfaces and in most cases is combined with Linear Integral Convolution (LIC) lines [63] to visualise the near-wall fluid motion, as seen in Figure 3.25.

Turbulent Kinetic Energy Coefficient (C_k) This discreptor is used to indicate the mean kinetic energy associated with the eddies in turbulent regions and it calculated based on Equation (3.28).

$$C_k = \frac{k}{0.5\rho_\infty U_\infty^2} \qquad \text{(Eq. 3.28)}$$

where k is the turbulent kinetic energy.

Scalar Variation ($\Delta\Phi$) The static pressure coefficient and normalized velocity (U/U_∞, where U_∞ is the free-stream velocity) variation (ΔP) and (ΔU) respectively were calculated and plotted in order to check if the refinement regions were set correctly. OpenFOAM pro-

vides a function called prime2Mean that calculates the average of the product of fluctuations of a variable. For example if this function is applied to the velocity field it will return the $\overline{u'u'}$, which is also the Reynolds stresses. The square root of the prime2Mean of a variable is the variation of it or the fluctuations.

Lambda 2 Criterion Lambda 2 criterion is a vortex-core detection algorithm based on the velocity gradient tensor (∇u) which can be utilized only for three-dimensional fluid velocity fields. The velocity gradient tensor is decomposed into its symmetric (S) and anti-symmetric (Ω) parts and the eigenvalues of $S^2 + \Omega^2$ are calculated and sorted so as $\lambda_1 \geq \lambda_2 \geq \lambda_3$. A particle in a velocity field is part of a vortex core only if at least two if its eigenvalues are negative, or if $\lambda_2 < 0$.

3.3.2 Isosurfaces

An isosurface is a surface that represents points with constant values withing a volume. In this thesis, two kinds of isosurfaces were used, namely total pressure and Lambda 2 isosurfaces. Isosurfaces with total pressure value equals to zero are used to visualise low energy regions such as wakes, as seen in Figure 3.26. Isosurfaces with a constant value of Lambda 2 Criterion were used to visualise regions with high vorticity, the higher the Lambda 2 Criterion value, the higher the vortical content of the visualised vortices (see Figure 3.27).

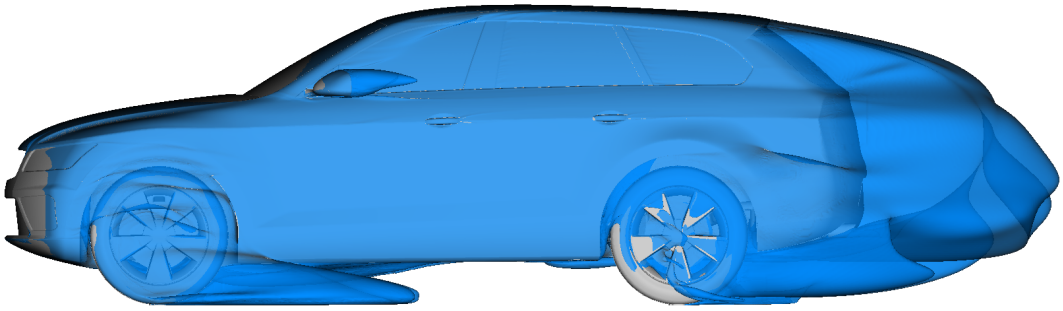

Figure 3.26: Total pressure equal to zero isosurfaces visualizing the wake regions of the AeroSUV Squareback.

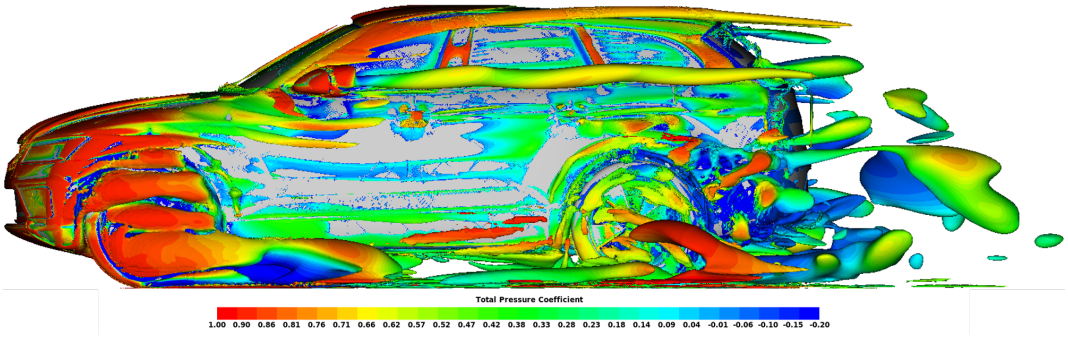

Figure 3.27: Lambda 2 Criterion equal to 50.000 isosurfaces coloured by total pressure coefficient for the AeroSUV Squareback.

4 Results I - SAE Notchback

"If I have seen further, it is by standing on the shoulders of giants"

-Isaac Newton

4.1 Model Overview

To start the CFD parameters investigation process, the SAE Notchback 20° backlight reference model was selected for the preliminary research. It is a simplified model that combines the flow field of a notchback vehicle, which is complicated and challenging to simulate, and an A-Pillar regime similar to a realistic road vehicle. The geometry and the dimensions of the model can be seen in Figure 4.1.

The length of the model is 840mm, similar to a 1:4 scaled realistic road vehicle. The front windshield is placed at an angle of 150° from the horizontal line to achieve a flow field in that region similar to a modern automobile. Downstream of the windshield, an extended surface with 216mm length is added in order to reduce the interaction between the flow structures formed at the front and at the rear end of the model. The backlight is placed at the critical angle of 20° making the accurate computation of the the flow field at that region very challenging. The main indicators that will be used to assess the performance of a CFD setup are the predicted total drag force and the pressure distribution across the backlight which will be compared with the relevant experimental values.

4.2 Experimental Data

Force and Momentum

The experiment of the SAE Notchback was conducted at the Loughborough's University wind tunnel, which is equipped with a high accuracy 6-component virtual underfloor scale, used to measure the force and momentum generated by the model. The measurement process was repeated until the deviation between the measurements was below an acceptable threshold

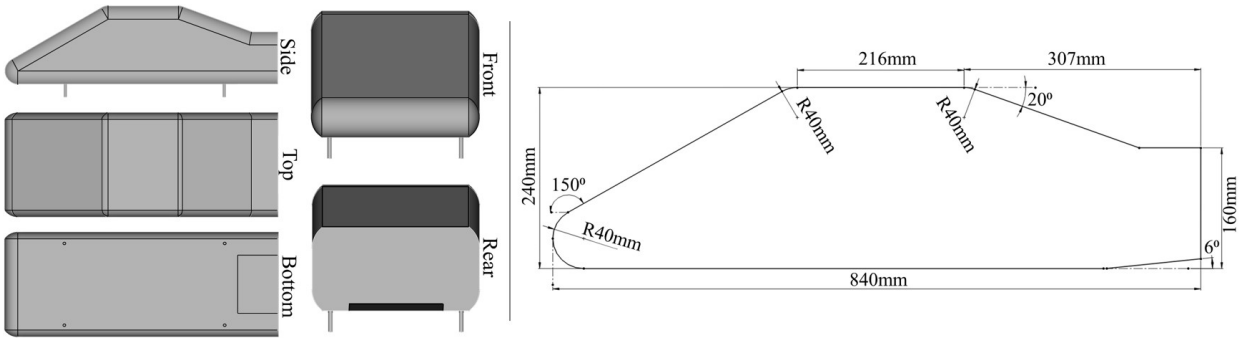

Figure 4.1: Basic views *(left)* and cross section at the centerline with dimensions *(right)* of the SAE Notchback 20° Backlight model.

which can be interpreted as 99% confidence [2]. The aerodynamic force and momentum coefficients measured through the wind tunnel testing for the SAE Notchback 20° Backlight model at straight line condition, are presented in Table 4.1.

Table 4.1: SAE Notchback 20° Backlight drag, lift and momentum coefficients measured through wind tunnel testing [2].

Case	C_D	C_L	C_M
SAE Notchback 20°	0.210	0.055	-0.068

Surface Pressure

The surface pressure distribution was measured with the use of two 64-channel electronic pressure scanners allowing the simultaneous pressure data acquisition at 128 points on the surface. The pressure taps and the area associated with each tap are presented in Figure 4.2. The pressure taps are piezoresistive sensors equipped with a temperature sensor used to correct the inaccuracies ought to different local temperature and thus local pressure; this combination of sensors, results in an accuracy of ±0.03%. The pressure sampling frequency was 20kHz and the two channels were synchronized to perform a spatial and temporal analysis by capturing the pressure fluctuations. Finally, the measurement accuracy in terms of pressure coefficient is $\pm 0.0045 C_P$ with 99% confidence [2]. Only the data from the centerline pressure tapping will be taken into consideration in this thesis as an attempt to reduce the complexity of the research, since the flow field on the rest of the backlight is strongly affected by the vortical structures of the trailing pillar and the pressure measurements there are the average of a wide range of values.

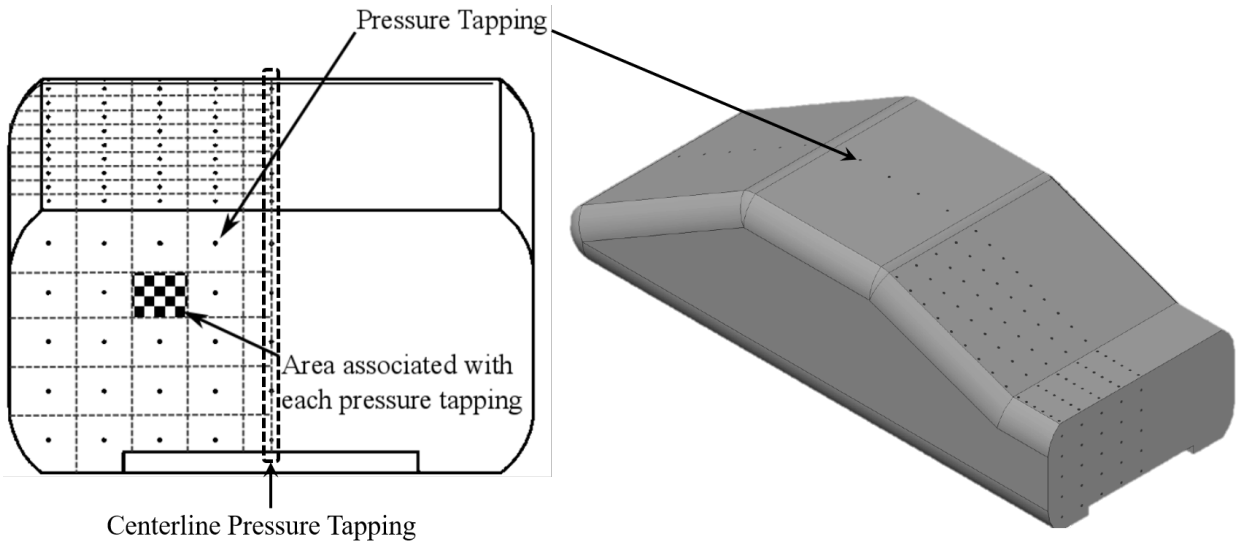

Figure 4.2: Pressure tapping cascade utilized for surface pressure data acquisition [2] *(edited by the author)*.

Surface Flow Visualisation

The surface friction was visualized with the use of titanium dioxide paint; a flow visualisation technique used in early aerodynamic experiments, capable of revealing stagnation and separation points, boundary layer transition locations and unsteady flow areas based on the different patterns generated by the paint. This method provides only quantitative results which are strongly affected by the properties of the paint and mainly the viscosity.

4.3 Flow Field Analysis

As it was mentioned in previous chapters, the SAE Notchback is a simplified model that from an aerodynamic perspective is very similar to a realistic road vehicle. More precisely, it exhibits a realistic impingement forming an A-Pillar separation and re-attachment in combination with significant trailing pillar vortical structures, as seen in Figure 4.3, that make this geometry a powerful test case for the development and validation of CFD tools and methods. The flow field generated by this model will be extensively analysed below.

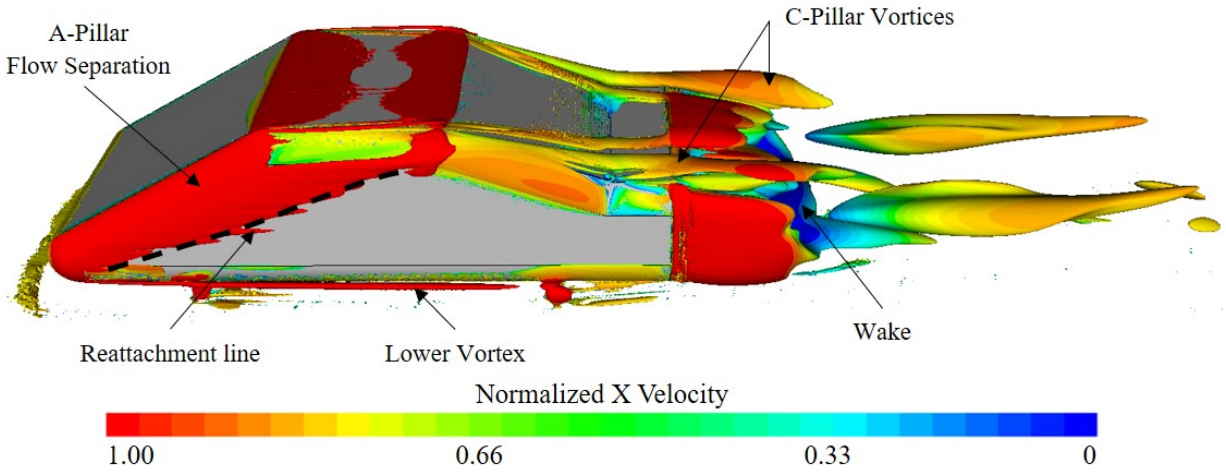

Figure 4.3: Basic flow structures generated by SAE 20°Notchback model visualised by Lambda 2 Criterion equal to 10.000.

Surface Pressure

Figure 4.3, 4.4 and all the images used in this section to present the flow field formed by the SAE 20° Notchback, are exported from the CFD simulation that provided the most accurate prediction of the flow field. The parameters of this simulation are presented in Tables 4.2 and 4.3. The static pressure distribution across the surface of the model reveals a big stagnation region in the front end accompanied by two low pressure regions, one in the transition between the windshield and the roof and one in the beginning of the undertray. The model consists of rounded edges except for those at the rear end, where clearly defined separation occurs. Side and Top views illustrate low-pressure regions at the A and C-Pillar ought to the local flow acceleration.

Table 4.2: Mesh parameters of the most accurate simulation of the SAE Notchback 20° Backlight.

Surface Mesh		**Layers**	**Volume Mesh**	
Algorithm	**Elements**(mi)	**Approach**	**Algorithm**	**Elements**(mi)
Trias	2.0	Low-Re	Hexa Int	53.3

Table 4.3: Solver parameters of the most accurate simulation of the SAE Notchback 20° Backlight.

Simulation Type	**Turbulence Model**	**Physical Time**(s)	**Cd Error**(%)
DDES	$k-\omega$	1.1	-0.26

A very important phenomenon in this model is the flow regime at the backlight and the trunk since it strongly affects the wake pattern and thus drag force generated by the model. The top view reveals a high pressure region at the trunk due to the collision of C-Pillar vortices on the surface of the trunk. Since the angle of the backlight is critical, a bad selection of CFD parameters can lead to erroneous prediction of the pressure distribution across the surface of the model and even in early boundary layer detachment at the backlight region.

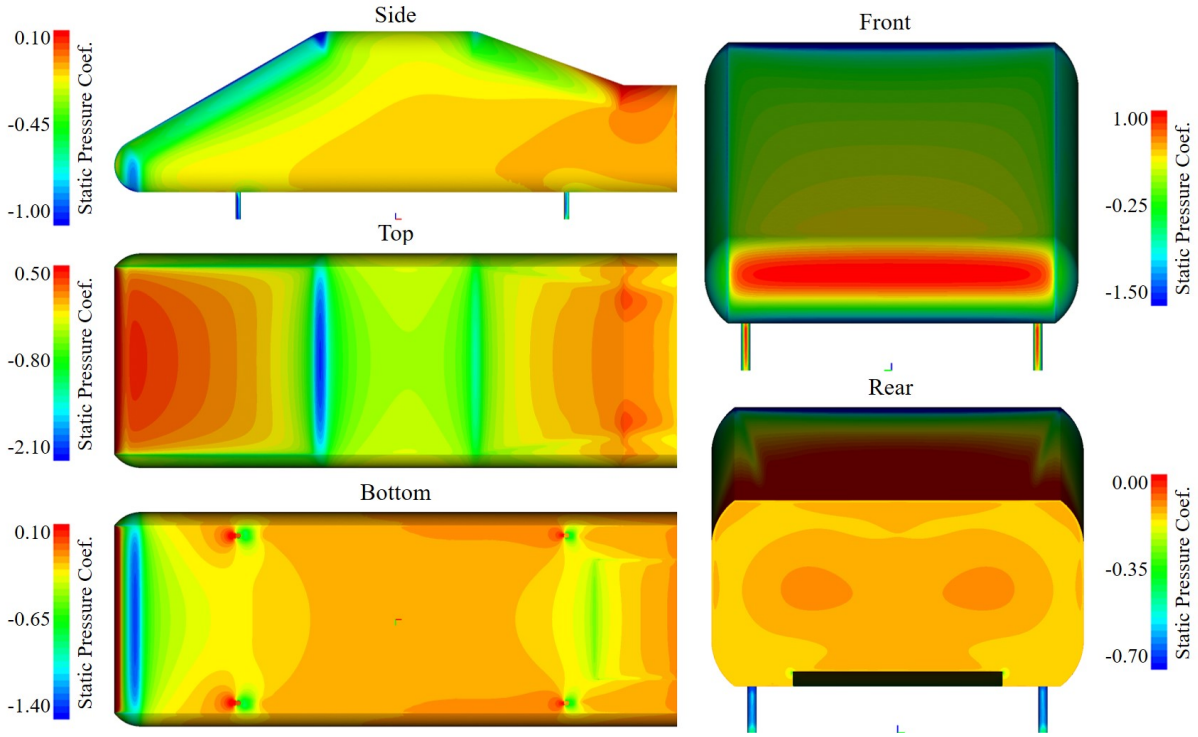

Figure 4.4: Mean surface pressure distribution on the SAE Notchback 20° Backlight model.

Centerline Pressure Distribution

The pressure distribution predicted by the most accurate CFD setup that was found in this thesis is depicted in Figure 4.5. The red and black solid lines represent the pressure at the upper and lower section, respectively and the x markers represent the experimentally derived pressure measurements. The Mean Absolute Percentage Error (MAPE) between the CFD and the experimentally derived pressure measurements was calculated for every pressure tap and was equal to 5.7% with a Standard Deviation (SD) equal to 1.1 and the Maximum Percentage Error (MaxPE) occurred at the 19th pressure tap and it was equal to 9%.

$$MAPE = \left| \frac{Experimental - Predicted}{Experimental} \right| * 100\% \qquad \text{(Eq. 4.1)}$$

Five pressure extrema occur at the centerline, namely one maximum at the stagnation point, two local minima at the upper section and two local minima at the lower section. At the low-pressure peaks, the flow exhibits an adverse pressure gradient since it is moving from a lower pressure region to a higher one, resulting in total pressure loss. If the CFD code predicts a higher total pressure loss at the roof of the model, then the boundary layer will have less energy and will not manage to follow the steep angle of the backlight, resulting in early separation and thus reduced accuracy. The CFD predicted and the experimental

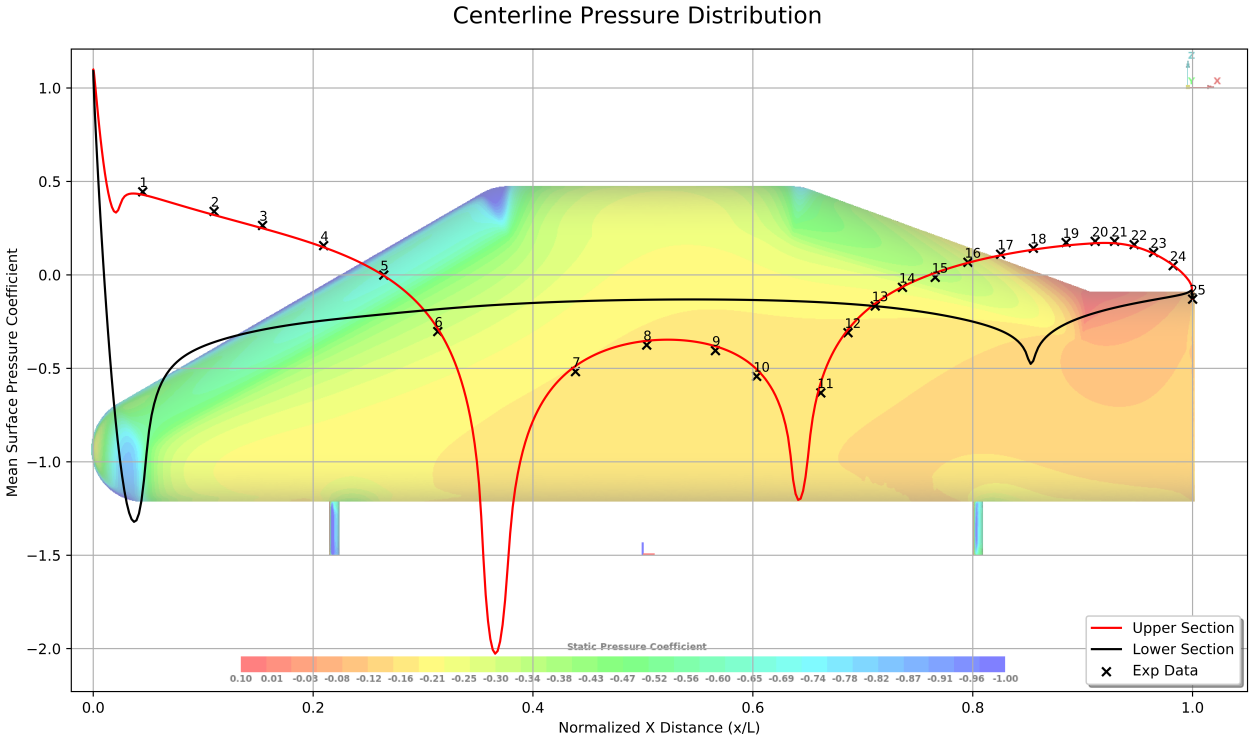

Figure 4.5: Mean surface pressure distribution along the centerline of SAE Notchback 20° Backlight combined with surface pressure measurements from 25 pressure taps used in the wind tunnel experiment.

pressure distribution seem to agree at the upper section; however, this is a necessary but not a sufficient condition in order to assess the accuracy of a CFD setup since the aerodynamic forces are also affected by shear forces.

Wall Shear Stress

The wall shear stress distribution across the model, provides information about the near-wall velocity since it is proportional to the gradient of the velocity at that region. From the top and side views of Figure 4.6, it is clearly depicted that the shear stress is enhanced at high-curvature regions at the front end and at the roof before the start of the convex section. From the side view, a low shear stress region is visible, extending from the A-Pillar up to the roof and it is due to the A-Pillar vortex which causes a boundary layer separation and re-attachment at that region, as seen in Figure 4.3.

The bottom view reveals a high shear stress region at the front of the undertray due to the local acceleration of the flow, something that can be also observed at the front supports of the model. Moderate to low shear stress dominates the middle section of the undertray until the start of the diffuser, where the flow is accelerated locally and then the flow diffusion takes place, where the pressure is increased and the velocity is decreased. The wake of the front supports affects the flow at the sides of the undertray, where local flow separations are present and finally, the wake of the rear supports is sucked by the low pressure region at the start of the diffuser causing an inward deviation.

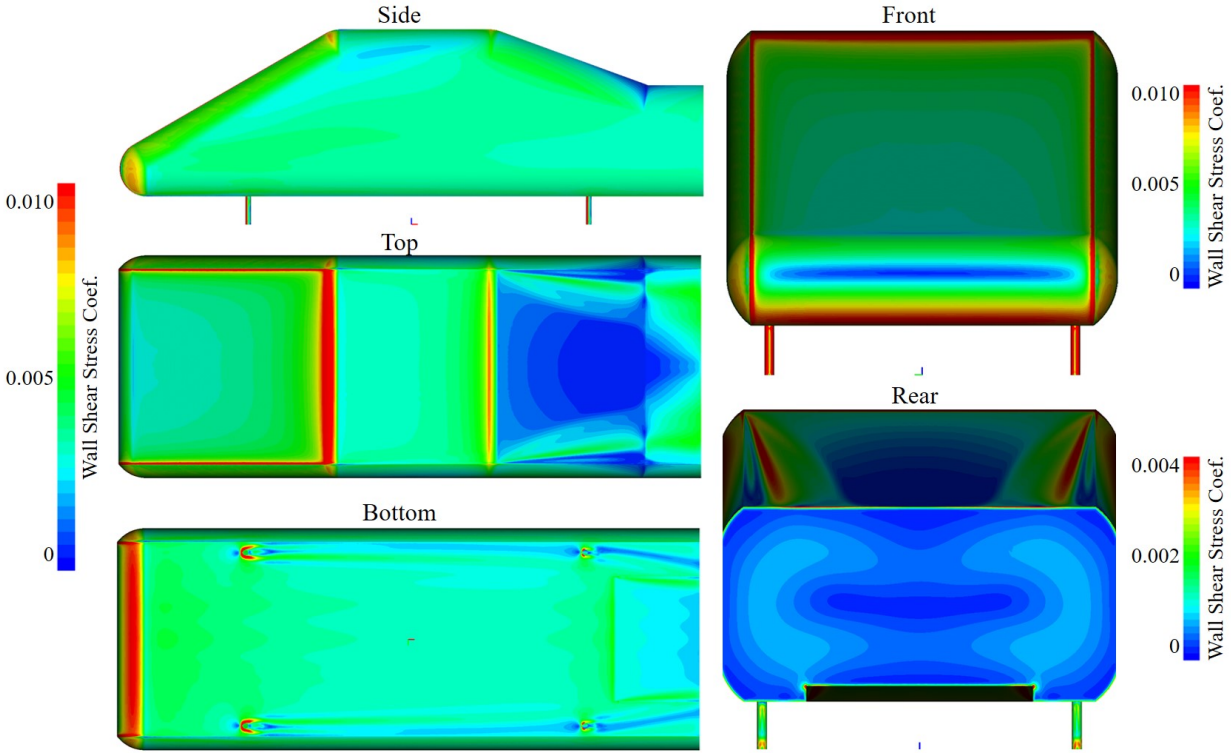

Figure 4.6: Mean wall shear stress distribution across the SAE Notchback 20° Backlight model.

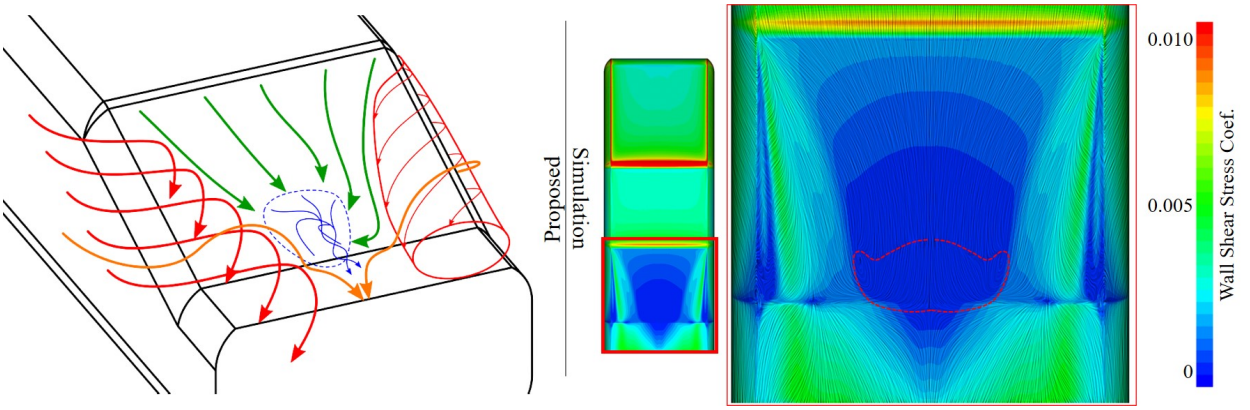

Figure 4.7: Flow field at the backlight of the SAE Notchback 20° Backlight, proposed by Wood *et al.* [2] *(left)* and predicted from a CFD simulation conducted by the author *(right)*.

The top view of Figure 4.6, reveals a complex distribution across the backlight and the trunk of the model. Low shear stress regions appear at the sides of the backlight, due to the flow detachment and the formation of the C-Pillar vortices, accompanied by high shear stress regions due to the re-attachment of the flow and the collision of the trailing pillar vortices on the surface of the backlight. At the centerline, the shear stress is reduced when moving from the roof to the trunk and the high pressure region on the trunk causes the flow to separate and reverse flow takes place. Figure 4.7 illustrates the flow field proposed by Wood on his PhD Thesis after the investigation of the model in the wind tunnel, compared to the flow field that was predicted by the most accurate CFD simulation conducted by the author. The two flow fields mostly agree regarding the trailing pillar vortices, the re-attachment of the vortices and the flow separation region at the middle of the backlight which is depicted with blue lines in the left image, and with red dashed lines in the right one.

Wake

The flow field at the rear end of the model can be also analysed with the use of x-normal total pressure planes, as seen in Figure 4.8, which provide information about the energy of the flow; red colour indicates high energy regions and blue low energy ones. At $x = 0.8l$ plane, the C-Pillar vortices are clearly illustrated along with two low-energy regions at the sides of the backlight, where the flow is detached. Moreover, the rotational motion of the vortices, forces the flow to move downwards by pushing high energy towards the surface, next to the main vortex core. At those regions, the flow near the wall is of higher energy, justifies the high shear stress regions at the backlight next to the C-Pillar location that was seen in Figure 4.6. Planes $x = 1.0l$ and $x = 1.2l$ depict the evolution of the wake formed downstream of the model, which is also responsible for the generated drag force. The downwash generated by the geometry of the backlight, in combination with the upward movement of high energy air ought to the diffuser, tend to increase the energy at the middle section behind the model, decreasing the wake region. On the sides, the C-Pillar vortices burst and are transformed into energy loss and thus wake.

The flow field downstream of the model can be also studied with the use of total pressure and x-velocity isosurfaces. With zero total pressure isosurfaces, regions with energy lower than the reference energy are visualised; these areas are mainly the wake of the model. Such areas can be seen in regions similar to a flat plate, such as the sides and the roof of the model and downstream of bluff faces, such as the rear end and the supports. Negative x-velocity isosurfaces are used to visualise regions where reversed flow occurs; these regions are mainly seen in circulation bubbles in the wake of a model and in the boundary layer separation regions, where reversed flow occurs near the wall. Figure 4.9 illustrates reversed flow regions at the bottom and the sides of the backlight, behind the supports and in the wake downstream of the car.

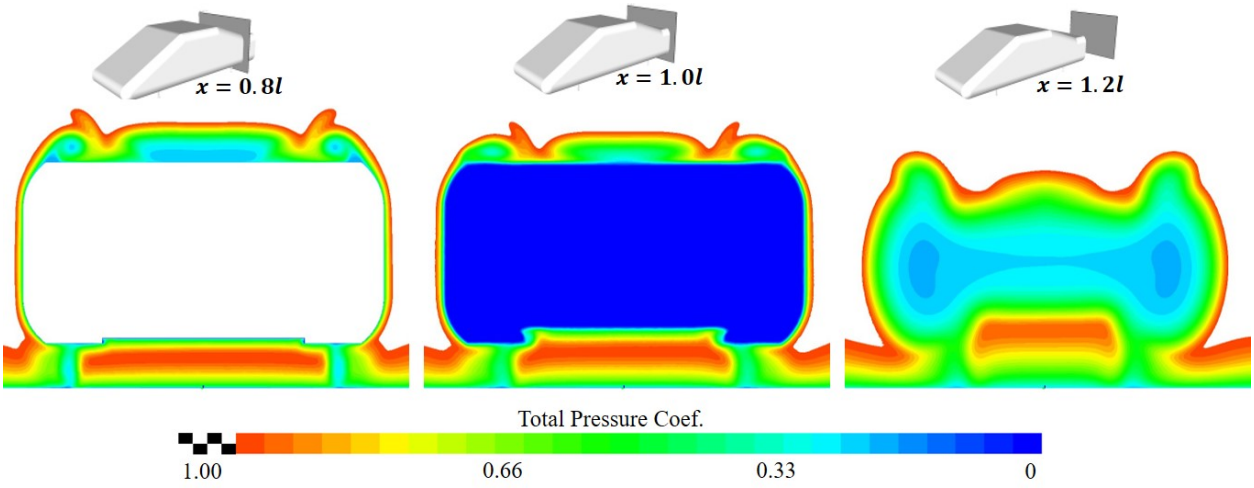

Figure 4.8: X-normal total pressure planes at the rear end of the SAE Notchback 20° Backlight.

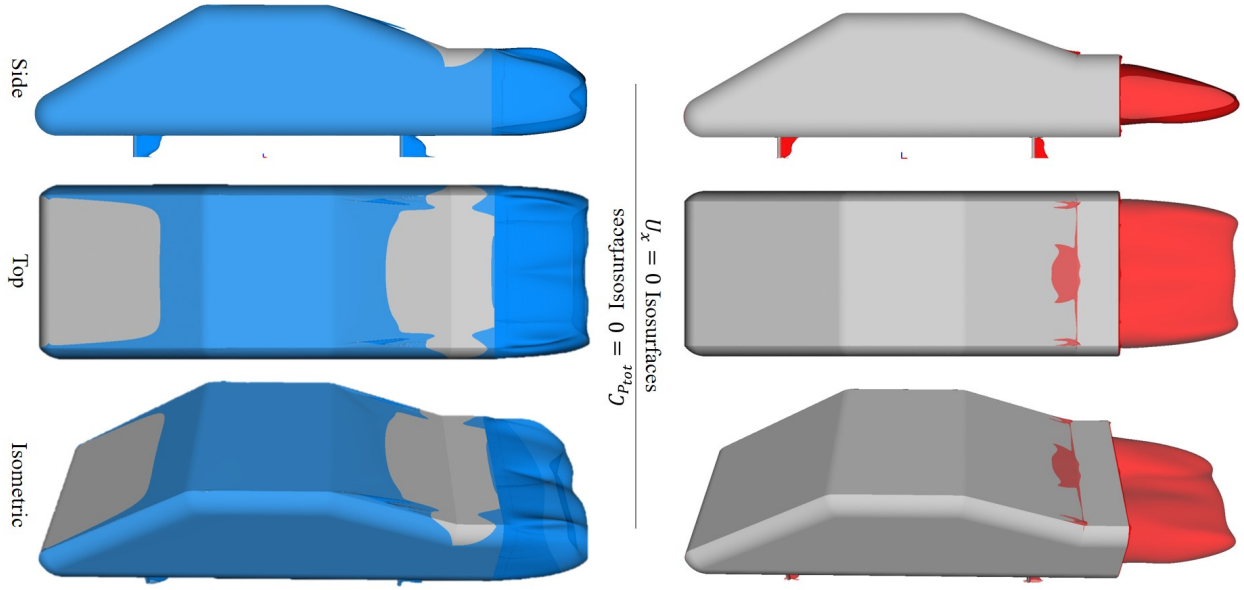

Figure 4.9: Total pressure equal to zero isosurfaces *(left)* and negative x-velocity isosurfaces *(right)*

Vortex Cores

The vortical structures formed in the flow field around the model are visualised with the use of Lambda 2 Criterion (L2) isosurfaces. Figure 4.10 represents two values of L2; the higher the value of L2, the stronger the visualized vortex. The isosurfaces are coloured with total pressure in order to have information about the energy content of the depicted flow structures. It is worth mentioned that this vortex core visualisation criterion identifies high velocity gradients and thus it is possible to visualise regions that are not vortex cores but the geometry of the model is such that steep velocity changes occur; such regions can be seen at the convex surfaces at the start and the end of the roof.

The main flow structures that dominate the flow field in this model are the A-Pillar and C-Pillar vortices that are clearly visualized in both $L2 = 150.000$ and $L2 = 50.000$ isosurfaces. The A-Pillar vortices have high energy content and are responsible for the flow separation at that region. However due to the elongated main section of the model, and the big radius of the A-Pillar, the vortices are are not as strong as those seen in a realistic road vehicle, and thus they do not interact with the C-Pillar vortices, reducing the complexity of the flow field.

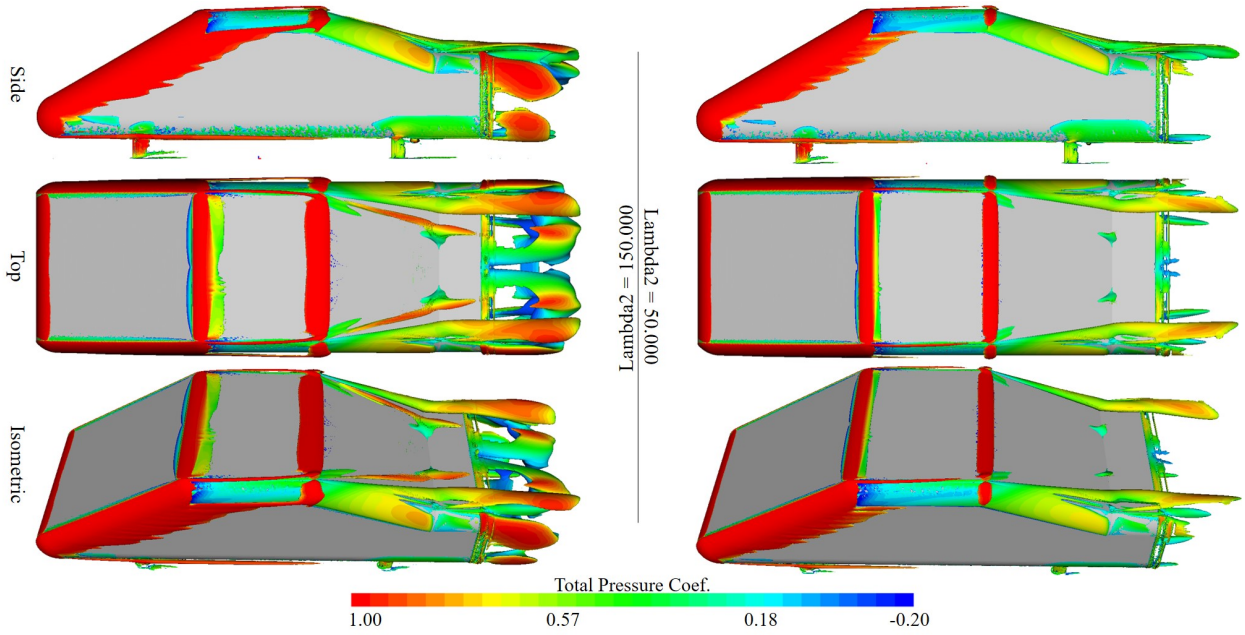

Figure 4.10: Side, top and isometric views of Lambda 2 Criterion isosurfaces depicting main vortex cores.

4.4 Computational Mesh

The CFD methodology process started with the investigation of the main computational parameters, namely the mesh resolution and the type of shell and volume elements used to discretize the surface of the model and the volume of the domain, respectively.

4.4.1 Mesh Resolution

The mesh resolution investigation is a process similar to the mesh independency study; different mesh resolutions are tested until the solution converges to a constant value. The main indicators used to assess the resolution of the computational grid is the number of shell elements, the number of volume cells and the scale of the flow structures that can be resolved near the model. The latter information is derived with the use of the non-dimensional cell size indicator (C_{size}/l_{ref}), defined as the maximum and the minimum size of the cells near the vehicle (C_{size}), divided by the length of the car (l_{ref}).

Table 4.4 depicts the cases that were analyzed during the mesh resolution investigation. The coarse resolution mesh consists of approximately 32 million cells and can resolve flow structures down to the size of $0.18\% \cdot l_{ref} = 1.4mm$. The medium resolution mesh is 1.7 times denser than the coarse one, capable of resolving flow structures down to $0.15\% \cdot l_{ref} = 1.2mm$ and the fine resolution mesh is 3 times denser than the coarse mesh, it consists of approximately 95 million elements and can resolve flow structures in the scale of $0.15\% \cdot l_{ref} = 0.96mm$; flow structures smaller than the aforementioned size are treated as sub-grid scale structures. The exact values of shell mesh parameters used during the surface mesh generation can be seen in Figure 4.11.

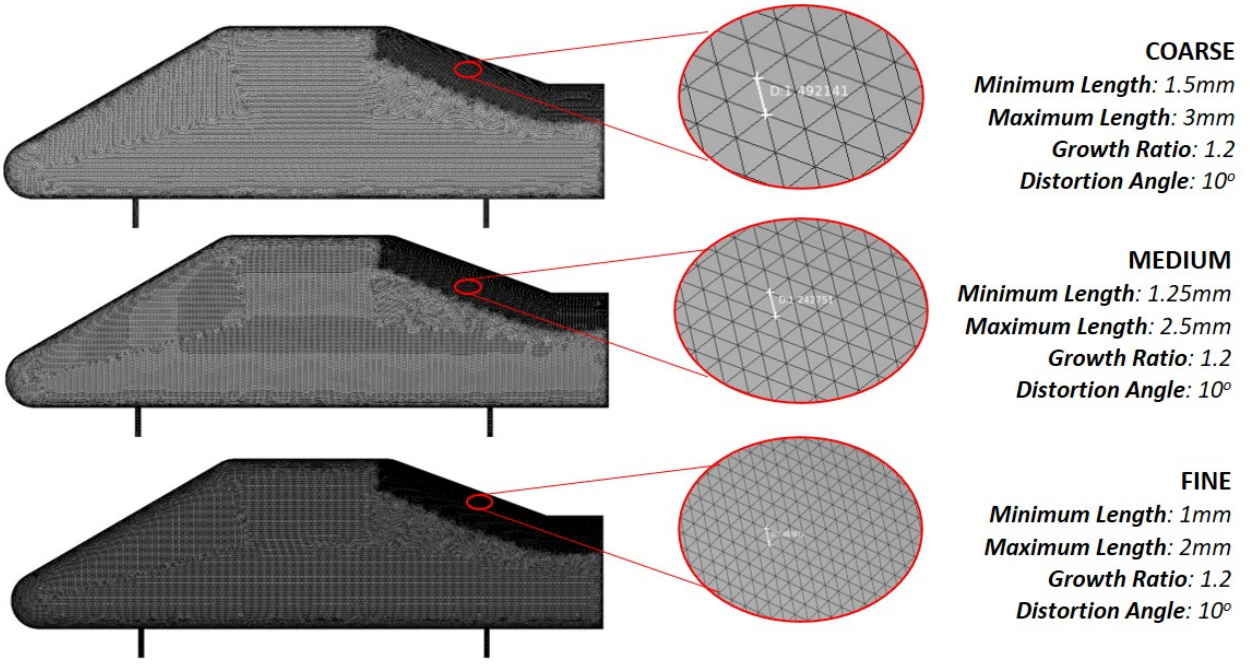

Figure 4.11: Surface mesh parameters used for the mesh resolution investigation

Table 4.4: Surface and volume mesh specifications of the simulations conducted for the mesh resolution investigation of the SAE Notchback 20° Backlight.

	Elements(mi)		**Layers**	C_{size}/l_{ref} (%)		
Case	**Shell**	**Volume**	**Approach**	**Max**	**Min**	**Mesh ID**
Coarse	1.4 *(Trias)*	31.8 *(HexaInt)*	Low-Re	0.71	0.18	sae_chi
Medium	2.0 *(Trias)*	53.3 *(HexaInt)*	Low-Re	0.60	0.15	sae_mhi
Fine	3.0 *(Trias)*	95.3 *(HexaInt)*	Low-Re	0.48	0.12	sae_fhi

The surface mesh used for the mesh resolution investigation, is dominated by trias shell elements, the layers were generated based on the low-Reynolds approach with the first layer height to be equal to 0.018mm, to achieve y^+ values below 1, and 25 layers in total with variable growth rate were generated to accurately resolve the boundary layer. As seen in Figure 4.12, the y^+ is lower than 1 almost in every point on the surface of the model, expect for some regions where enhanced flow acceleration occurs and values up to $y^+ = 2$ are observed; however this is an acceptable result and these layers parameters were used for all the low-Reynolds cases. The Hexa Interior volume meshing algorithm was used to achieve a hexa-dominated domain discretization and the refinement regions used are presented in Figure 3.14. For the numerical solution process, the steady state, isothermal and incompressible simpleFoam OpenFOAM solver was utilized, along with the k-ω SST turbulence model.

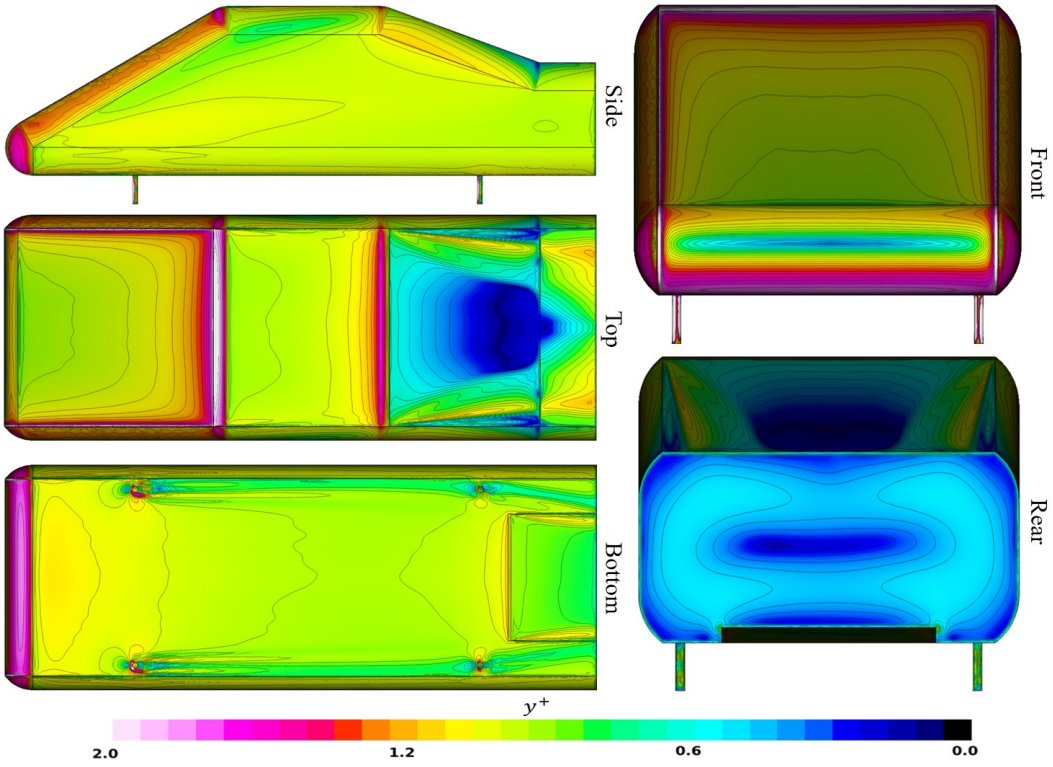

Figure 4.12: y^+ distribution across the SAE Notchback 20° Backlight for a low-Reynolds approach simulation.

Surface Pressure

The surface pressure distribution across the top of the model (see Figure 4.13) depicts that the finer the grid resolution, the more precise the flow prediction at the rear end. Red colour represents higher pressure computed by the fine case compared to the other cases, and black colour is the opposite scenario. Coarse resolution calculates lower surface pressure at the windshield, the roof, the backlight and the trunk as it is clearly illustrated in the results computed from the subtraction of the fine and coarse cases. However, in regions with negative surface pressure, such as the convex surfaces at the transition between the roof and the adjacent surfaces, the coarse case predicts higher pressure than the fine case; this result is depicted with the black colour at the top of the model.

As the mesh resolution increases, the results seem to converge to a steady mesh-independent solution, and the divergence between the predicted pressure distribution of the fine and the medium mesh cases is reduced. From the pressure field subtraction of these cases, it is revealed that the first predicts higher surface pressure at the start of the roof but the latter predicts higher negative pressure at the convex section of the roof. However, the divergence in surface pressure between these cases is minor and it cannot significantly affect the total drag force generated by the model. The pressure distribution across the centerline of the model, presented in Figure 4.15, shows an agreement between the fine and medium mesh resolution cases that verifying the aforementioned statement.

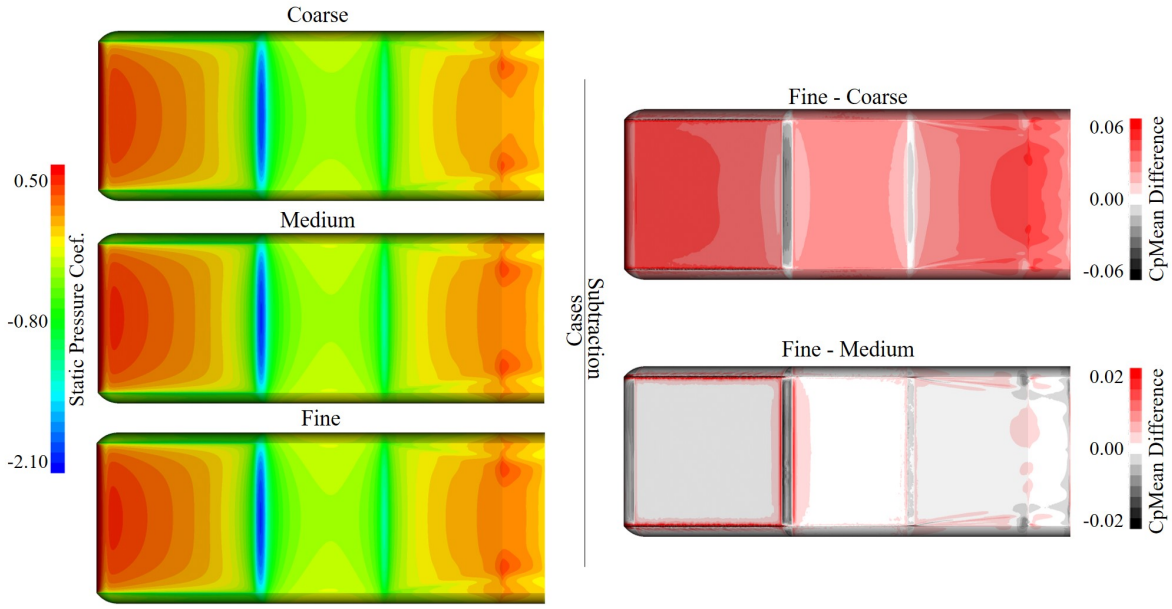

Figure 4.13: Top view of surface pressure distribution across the SAE Notchback 20° Backlight for a coarse, medium and fine mesh resolution *(left)* pressure divergence computed by subtracting the results of the cases and plotting the resultant pressure *(right)*.

The comparative bottom view (Figure 4.14), does not reveal significant differences between the models. The coarse resolution predicts lower pressure distribution across the surface of the model and as the mesh gets finer, the surface pressure becomes more precise. Similar to

the top view, the results seem to converge between the medium and the fine mesh, and zero divergence is observed almost in every point of the surface of the model, except for some minor regions at the A-Pillar and at the front of the model, where the fine resolution grid calculated higher pressure than the medium. The results behind the model supports seem to disagree since a black region is present, depicting that the fine mesh predicts lower negative pressure downstream of the supports which can affect the wake produced by these bluff faces.

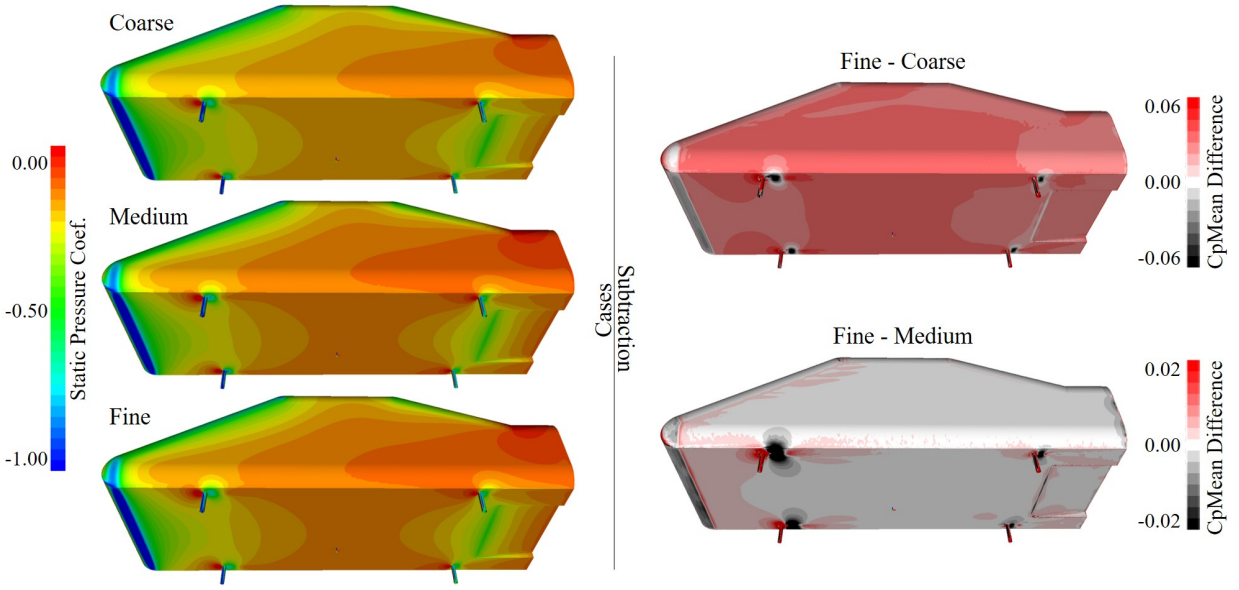

Figure 4.14: Bottom view of surface pressure distribution across the SAE Notchback 20° Backlight for a coarse, medium and fine mesh resolution *(left)* pressure divergence computed by subtracting the results of the cases and plotting the resultant pressure *(right)*.

The pressure distribution across the centerline of the model that was predicted by these simulations is depicted in Figure 4.15 along with the experimental pressure measurements. Medium and the fine results are almost identical, however the coarse resolution results deviate from the other two. The Mean Absolute Percentage Error from the experimental measurements is 25.4%, 6.6% and 5.7% for the coarse, medium and fine resolution, respectively as. The maximum divergence from the experimental pressure measurements was observed at the coarse simulation and it was 85.5% at the 15th pressure tap, as mentioned in Table 4.5.

Table 4.5: Deviation between the experimental measurements and the predicted pressure distribution across the SAE Notchback 20° Backlight for the mesh resolution investigation.

Case	**MAPE**(%)	**SD**	**MaxPE**(%)	**@Pres_Tap**
Coarse	25.4	21.5	85.5	15
Medium	6.6	6.6	14.5	24
Fine	5.7	1.1	9.0	19

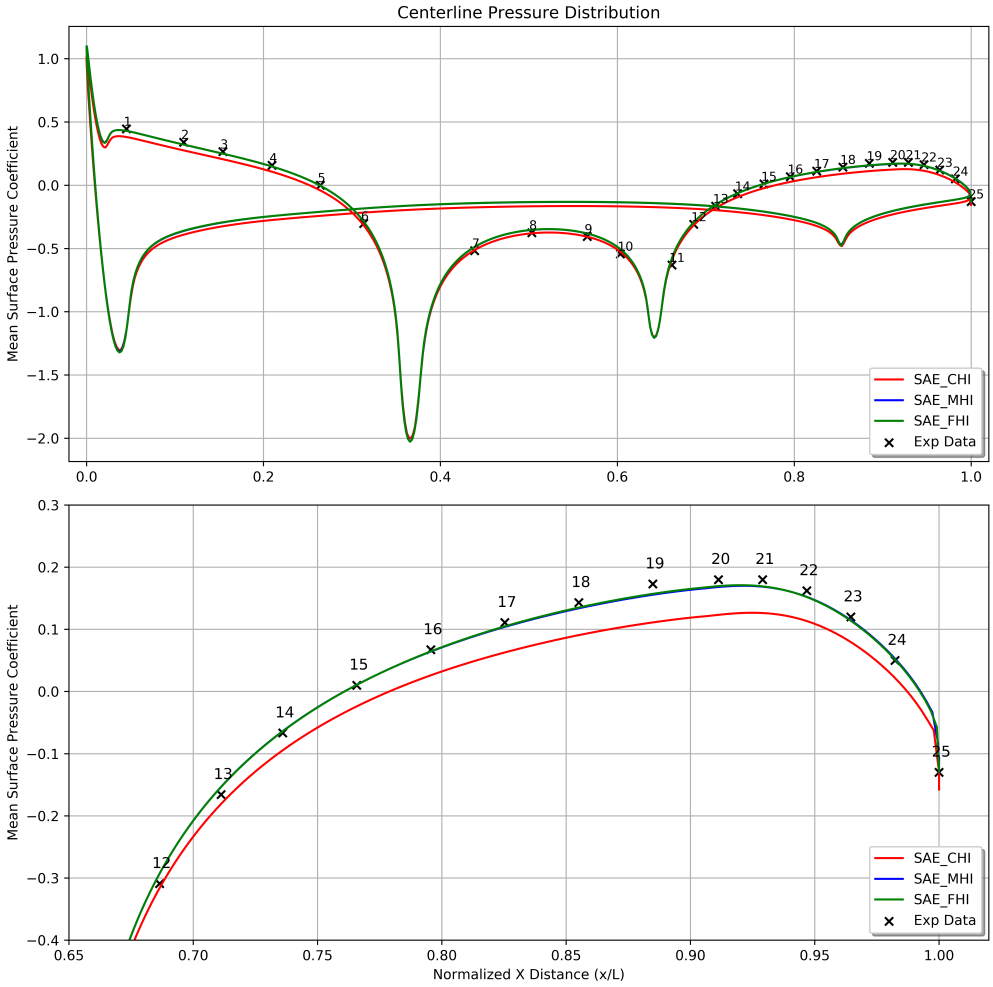

Figure 4.15: Surface pressure distribution at the centerline of the SAE Notchback 20° Backlight *(top)*, focused on the backlight region *(bottom)* for the Coarse Hexa Interior (SAE_CHI), Medium Hexa Interior (SAE_MHI) and Fine Hexa Interior (SAE_FHI) cases.

Vortex Cores

Lambda 2 Criterion isosurfaces, illustrated in Figure 4.16, visualize the vortical structures generated by the model. All the cases managed to capture the A-Pillar and C-Pillar vortices, in addition to the collision of the latter vortex on the surface of the trunk. The coarse mesh is prone to numerical diffusion and as a result, early energy dissipation can be seen near the trailing pillar and at the vortices formed there, and many flow structures are merged to one bigger structure based on the minimum scale of phenomena that can be analyzed by the local grid resolution. As the mesh resolution becomes finer, the resolution of the A-Pillar vortices is increased and some sub-vortices can be seen inside the main structure; one of them extends up to the start of the C-Pillar and it is visible only on the medium and fine resolution cases. Similar to the A-Pillar, the lower vortex formed at the bottom of the model near the front supports, seems to have enhanced energy content as the grid resolution increases. All the cases seem to predict the same vorticity at the convex regions of

the roof and small differences can be observed at the backlight, the trunk and downstream of the model. The low resolution case, underestimates the energy content of the flow at the rear end of the model, which can be clearly seen in the lower portion of the C-Pillar and on the vortices generated at that region. Consequently, the vortices of both $L2 = 50.000$ and $L2 = 150.000$ are shorter and contain less energy in the lower grid resolution case compared to the fine resolution case, making them prone to early burst.

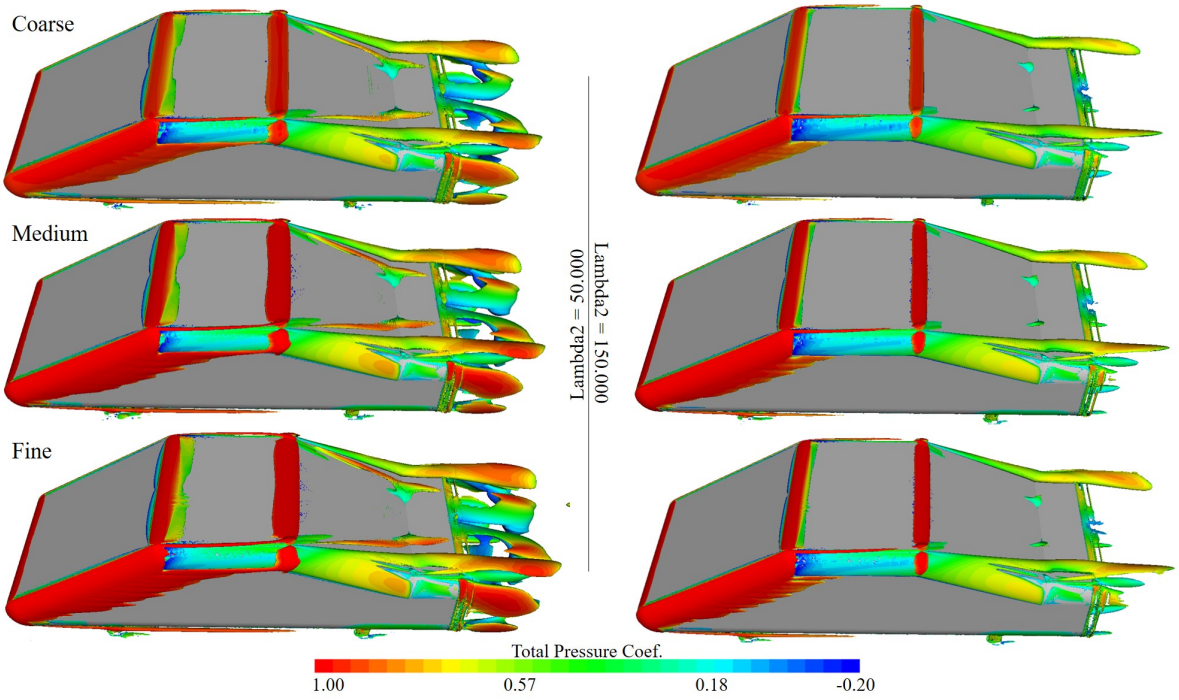

Figure 4.16: Lambda 2 Criterion isosurfaces depicting the vortical structures for a coarse, medium and fine resolution grid.

Wake

The Y-normal centerline planes, seen in Figure 4.17, reveal that all the cases agree at the predicted flow field on the backlight. However, the coarse mesh simulation, predicts thicker boundary layer between the model and the road resulting in early boundary layer merging and thus lower energy content below the model. This is also clearly depicted at the X-normal planes, where a white region is present below the diffuser for the medium and the fine cases, but not for the coarse one; subsequently the finer the mesh , the smaller the wake of the model resulting in better prediction of the generated pressure drag force.

Conclusion

The outcome of the mesh resolution investigation is presented in Table 4.6. The fine resolution mesh predicted the drag coefficient with -0.76% deviation from the experimental drag coefficient, demanded 45 seconds per iteration and approximately 96GB of RAM during the solution process. The medium grid resolution case provided an accurate prediction of the

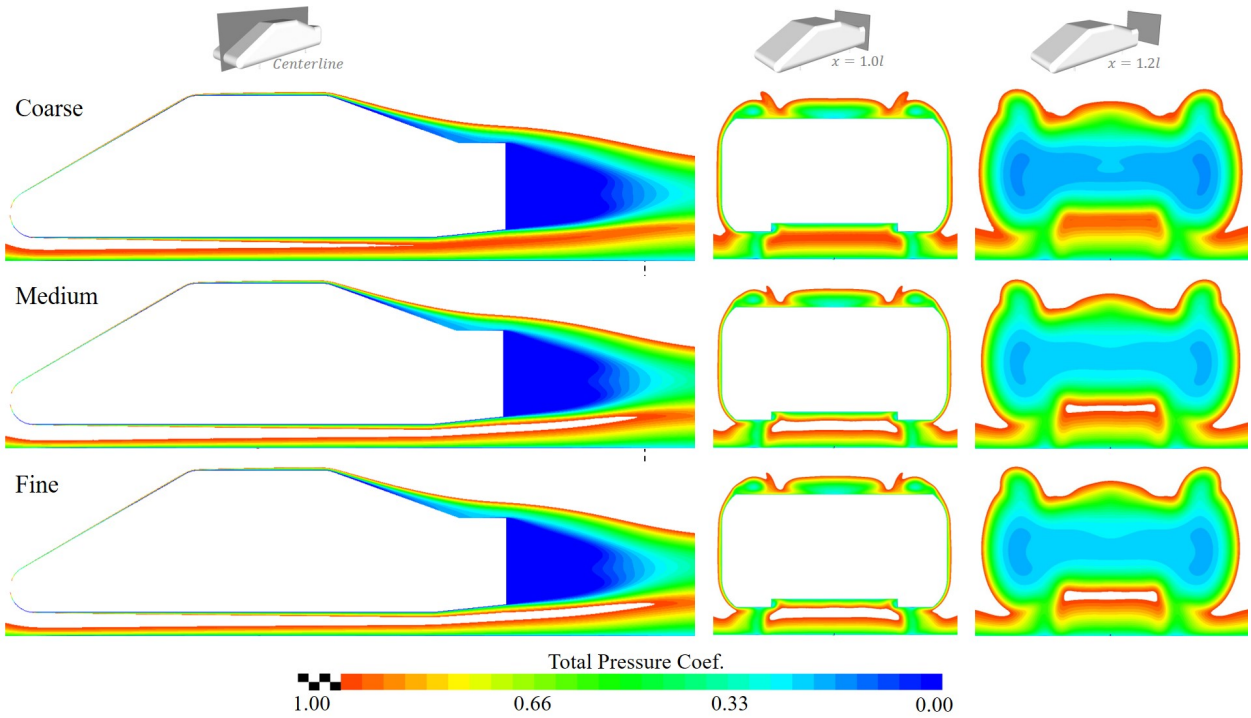

Figure 4.17: Y-normal centerline and X-normal total pressures planes depicting the wake downstream of the model.

aerodynamic drag force generated by the model, with deviation equal to -1.56% and with approximately half computational sources and time demands. The coarse resolution computational grid, had a deviation of -5.52% on the drag coefficient and the aforementioned analysis showed that the solution is not converged for this mesh density, hence this resolution should be avoided due to low accuracy and high mesh dependency.

The fine mesh resolution is the optimal one for this investigation, however the medium resolution can be also used to decrease the computational time by 46% with a small sacrifice in the accuracy of the predicted drag value.

Table 4.6: Computational mesh resolution investigation results for the SAE Notchback 20° Backlight.

Case	C_D	**Error**(%)	**t/iter**(s)	**RAM**(GB)
Coarse	0.198	-5.52	15	33
Medium	0.207	-1.56	24	54
Fine	0.208	-0.76	45	96

4.4.2 Surface Mesh Type

Two surface mesh algorithms were used in this thesis, namely the *Trias* and the *Mixed* algorithm. The former algorithm generates a surface mesh dominated by triangular elements and the latter mostly of quad elements. The mixed surface mesh consists of less elements since two trias are equal to one quad element, thus the computational demands are reduced compared to the *Trias* surface mesh algorithm. The layers generated from a trias-dominated surface mesh, are mainly prisms and pyramids which are prone to numerical diffusion due to the complexity imposed during the data transfer between adjacent cells. In contrary, the layers generated from a quad-dominated surface mesh are mainly hexahedral elements and in many cases are aligned with the direction of the flow, reducing the numerical diffusion and increasing the accuracy and stability of the simulation. Hence, the mixed mesh is very likely to achieve the same accuracy with the trias mesh, by using less elements.

The aforementioned algorithms were studied by using a fine resolution computational grid with low-Reynolds approach for the layers generation and the volume in both cases was discretized with the use of the Hexa Interior volume meshing algorithm. For the numerical solution process, the steady state, isothermal and incompressible simpleFoam OpenFOAM solver was utilized along with the k-ω SST turbulence model. The mesh specifications of every case are presented in Table 4.7. The *Trias* case is the same as the fine resolution case used in the previous investigation. The mixed mesh case consists of one million shell elements, the mesh around the model is slightly finer compared to the *Trias* case and it is capable of resolving flow structures in the scale of $0.11\% \cdot l_{ref}$, resulting in a volume mesh with approximately 83 million cells.

Table 4.7: Surface and volume mesh specifications of the simulations conducted for the surface mesh type investigation of the SAE Notchback 20° Backlight.

	Elements(mi)		**Layers**	$\boldsymbol{C_{size}/l_{ref}}$ (%)		
Case	**Shell**	**Volume**	**Approach**	**Max**	**Min**	**Mesh ID**
Trias	3.0 *(Trias)*	95.3 *(HexaInt)*	Low-Re	0.48	0.12	sae_fhi
Mixed	1.0 *(Mixed)*	82.6 *(HexaInt)*	Low-Re	0.48	0.11	sae_fhi_m

Wall Shear Stress

The top view of the wall shear stress distribution across the model, presented in Figure 4.18, depicts almost identical distribution. However, by subtracting the results of the two cases it is revealed that the trias surface mesh case predicts higher shear stress on the front windshield, the roof and at the location where the C-Pillar vortices collide with the backlight and the trunk. On the center of the backlight, the mixed mesh case predicts lower shear stress, and thus lower velocity of the air which can lead to a false prediction of the flow separation at that region.

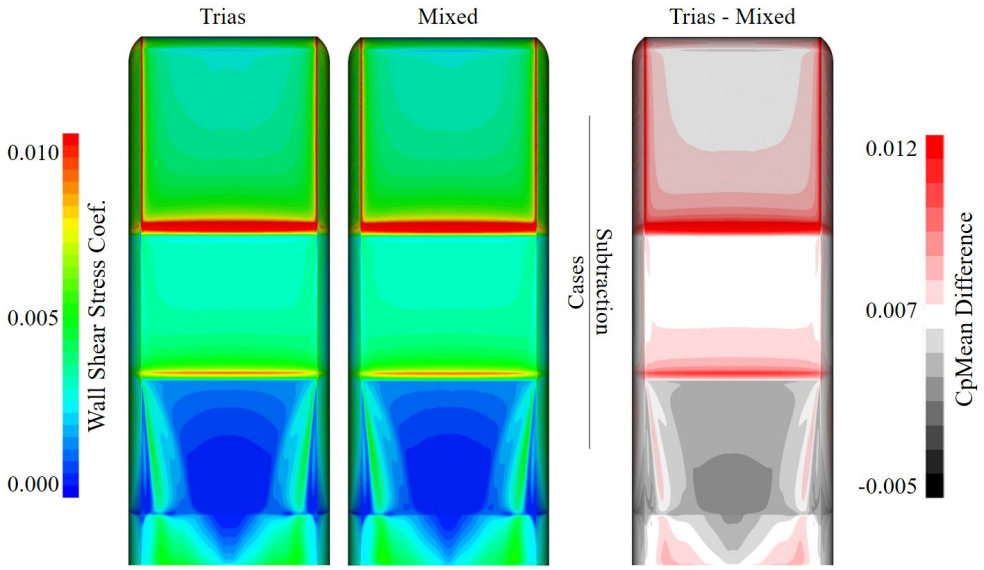

Figure 4.18: Top view of wall shear stress distribution across the SAE Notchback 20° Backlight for a trias and mixed surface mesh *(left)* pressure divergence computed by subtracting the results of the cases and plotting the resultant pressure *(right)*.

Surface Pressure

The pressure distribution across the rearmost face of the model, presented in Figure 4.19, shows that the trias surface mesh case predicts higher surface pressure at this region compared to the mixed surface mesh case. This divergence can lead to noticeable difference at the calculated drag force and consequently at the accuracy of each simulation.

The surface pressure distribution, illustrated in Figure 4.20 at the centerline, is nearly the same for the two cases except for the region near the twentieth pressure tap located at the start of the trunk. There, the mixed mesh predicts higher pressure than the experimental, resulting in greater adverse pressure gradient and thus bigger separation region than the trias case. This fact, justifies the aforementioned lower shear stress predicted at the lower

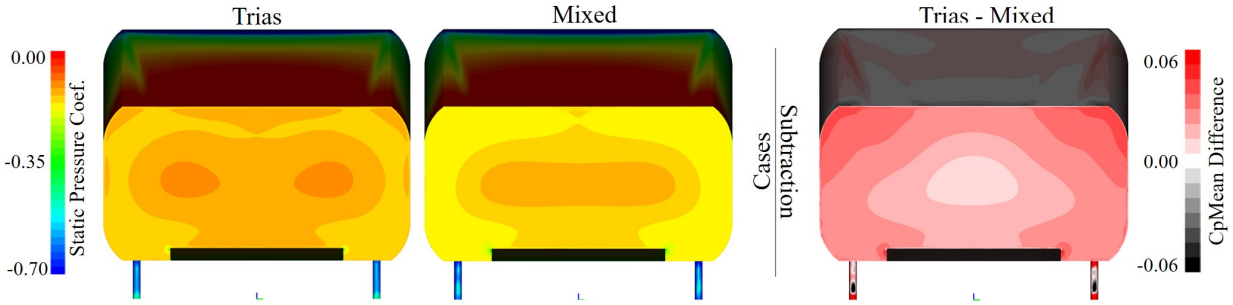

Figure 4.19: Rear view of surface pressure distribution across the SAE Notchback 20° Backlight for a trias and mixed surface mesh *(left)* pressure divergence computed by subtracting the results of the cases and plotting the resultant pressure *(right)*.

portion of the backlight compared to the trias surface mesh case. The Mean Absolute Percentage Error for the trias and mixed surface mesh cases is 5.7% and 6.1%, respectively (see Table 4.8). The mean deviation from the experimental measurements is almost equal for both cases, however the mixed surface mesh case has greater standard deviation and greater maximum error.

Table 4.8: Deviation between the experimental measurements and the predicted pressure distribution across the SAE Notchback 20° Backlight for the surface mesh type investigation.

Case	**MAPE**(%)	**SD**	**MaxPE**(%)	**@Pres_Tap**
Trias	5.7	1.1	9.0	19
Mixed	6.1	2.9	11.2	24

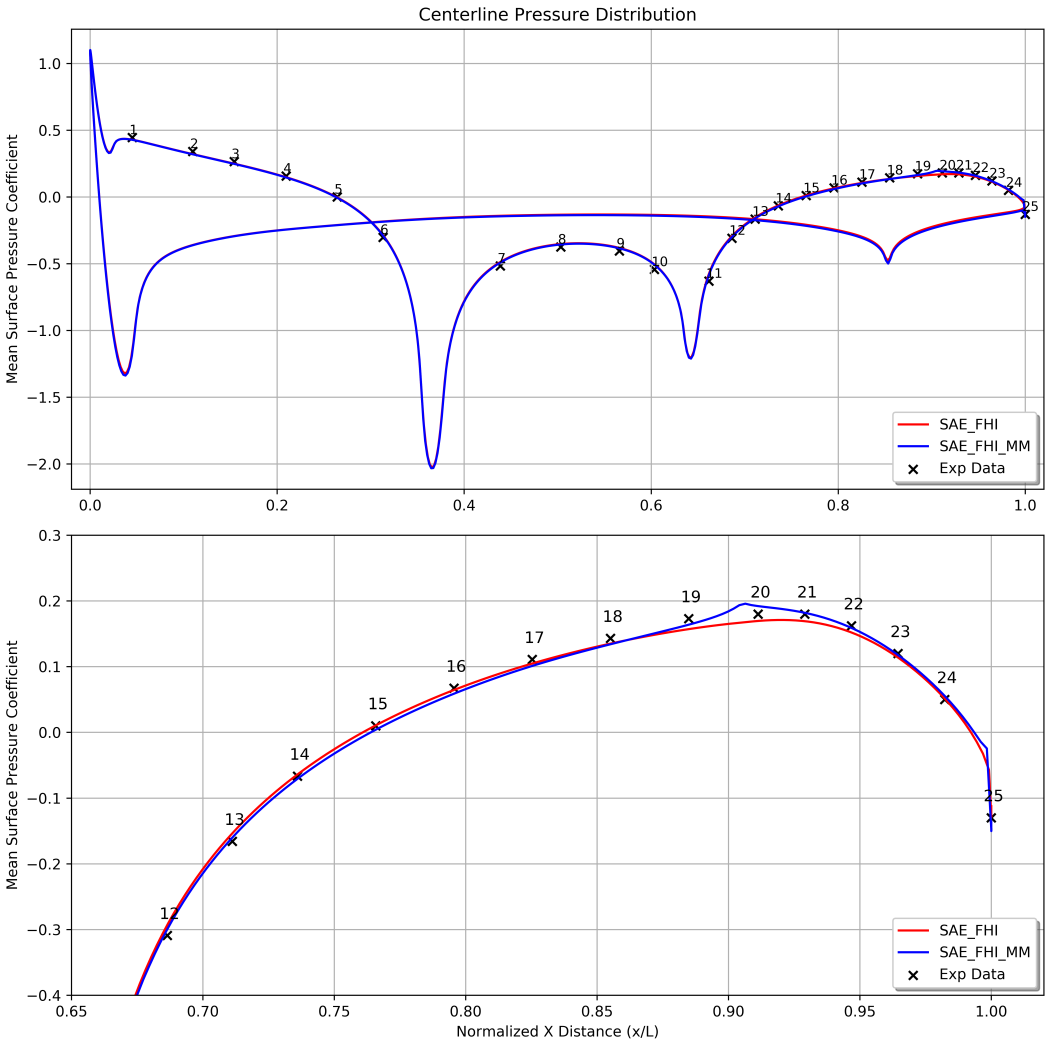

Figure 4.20: Surface pressure distribution at the centerline of the SAE Notchback 20° Backlight *(top)*, focused on the backlight region *(bottom)* for the Fine Hexa Interior with trias surface mesh (SAE_FHI) and Fine Hexa Interior with mixed surface mesh (SAE_FHI_MM) cases.

Conclusion

The outcome of the surface mesh type investigation is presented in Table 4.9. The trias surface mesh simulation predicted the drag coefficient with -0.76% deviation from the experimental drag coefficient, demanded 45 seconds per iteration and approximately 96GB of RAM during the solution process. The mixed surface mesh provided a prediction of the aerodynamic drag force generated by the model, with deviation equal to -2.86% by demanding 63 seconds to complete one iteration and in total 85GB of RAM. The *Trias* model has more computational nodes to calculate and store information, both on the surface mesh and on the layers, compared to the mixed mesh and in this case the latter failed to give an accurate prediction with the same mesh resolution parameters. Taking into account these information and the data presented in Table 4.8, the trias surface mesh seems to work better for this model and it was selected as the most accurate for this investigation.

Table 4.9: Surface mesh type investigation results for the SAE Notchback 20° Backlight.

Case	C_D	**Error**(%)	**t/iter**(s)	**RAM**(GB)
Trias	0.208	-0.76	45	96
Mixed	0.216	+2.86	39	85

4.4.3 Volume Mesh Type

Three volume mesh algorithms were tested during the volume mesh type investigation, namely the Hexa Interior, Hexa Poly and Tetra Rapid algorithm. Further information regarding these algorithms can be found in Chapter 3.1.4 : "Volume Meshing". Table 4.10 presents information regarding the computational grid of the simulations conducted for this investigation.

Table 4.10: Surface and volume mesh specifications of the simulations conducted for the volume mesh type investigation of the SAE Notchback 20° Backlight.

	Elements(mi)		**Layers**	C_{size}/l_{ref} (%)		
Case	**Shell**	**Volume**	**Approach**	**Max**	**Min**	**Mesh ID**
Hexa Interior	1.4 *(Trias)*	31.8 *(HexaInt)*	Low-Re	0.71	0.18	sae_chi
Hexa Poly	1.4 *(Trias)*	31.2 *(HexaPol)*	Low-Re	0.71	0.18	sae_chp
Tetra Rapid	1.4 *(Trias)*	84.2 *(TetraRap)*	Low-Re	0.71	0.18	sae_ctr

All the cases were discretized with the same medium resolution surface mesh with the use of the *Trias* surface meshing algorithm, and the layers were generated with the low-Reynolds approach. The Hexa Interior and Hexa Poly algorithms generate hexa-dominated volume mesh in contrast to the Tetra Rapid algorithm that generates tetras-dominated mesh. One hexahedral cell is equal to two tetras, consequently the volume mesh produced by the Tetra Rapid algorithm consists of more than twice as many cells as the hexa-based algorithms. Both grids can resolve flow structures in the scale of $0.18\% \cdot l_{ref}$. The cases were tested with

the use of the incompressible, isothermal simpleFoam OpenFOAM solver along with the k-ω SST turbulence model.

Surface Pressure

The surface pressure distribution across the model is illustrated in Figures 4.21, 4.22 and 4.23. The top view depicts an almost identical pressure distribution across the surface of the model for all the cases, however the subtraction of the results reveals differences between the models that cannot be neglected. The Hexa Poly volume mesh case predicts lower negative pressure than the Hexa Interior at the start of the backlight, resulting in enhanced downwash at that region. Consequently, the flow, calculated with the Hexa Poly grid, collides on the trunk with higher momentum and the pressure calculated at the bottom of the backlight and the trunk is greater than the Hexa Interior case. In addition, the Hexa Poly grid predicts C-Pillar vortices with lower negative pressure compared to the Hexa Interior case, which is presented at that region with the red colour (Figure 4.21).

From the subtraction of the Tetra Rapid pressure field from the Hexa Interior, significant divergence is revealed at the front end of the roof, the backlight and the trunk. Starting from the roof, the simulation conducted with the Tetra Rapid volume mesh, predicted higher negative pressure at that region, presented with the black colour that dominates that convex surface. At the rear end of the model, the Hexa Interior case calculated higher surface pressure at the backlight and the trunk which can strongly influence the drag force predicted by each simulation; since the Tetra Rapid surface mesh case resulted in lower pressure at the

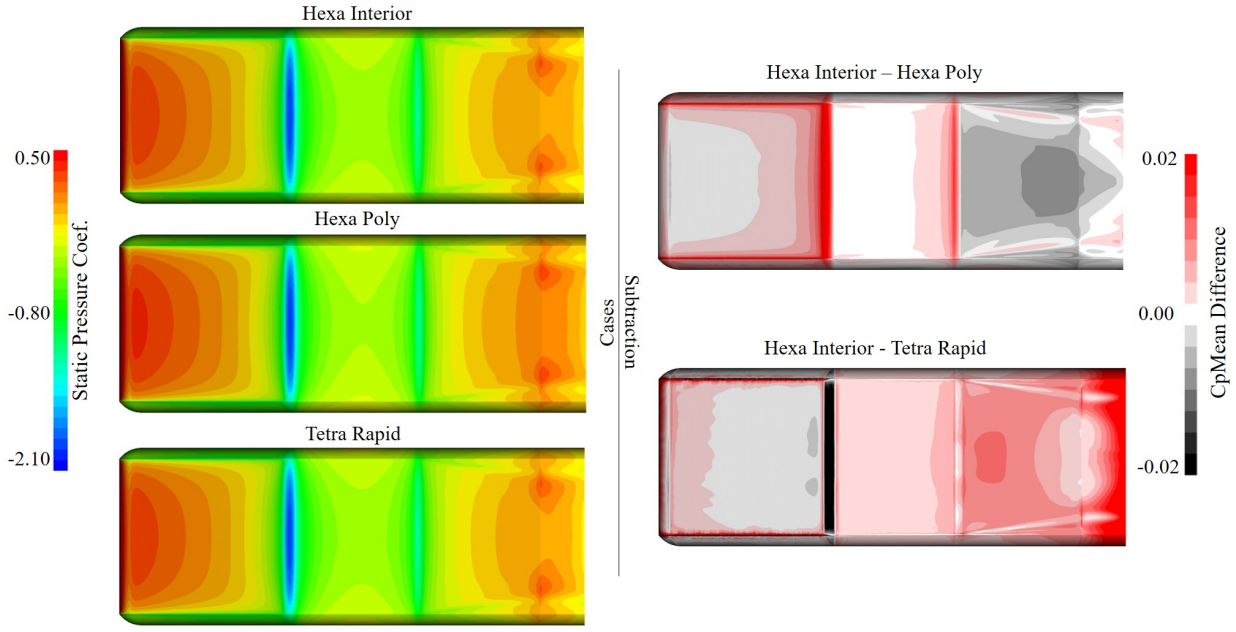

Figure 4.21: Top view of surface pressure distribution across the SAE Notchback 20° Backlight for a Hexa Interior, Hexa Poly and a Tetra Rapid volume mesh case *(left)* pressure divergence computed by subtracting the results of the cases and plotting the resultant pressure *(right)*.

backlight, it is very likely that the Tetra Rapid simulation will overestimate the drag force value.

The pressure distribution at the rearmost face of the model, depicted in Figure 4.22, agrees with the aforementioned results. The highest surface pressure is predicted by the simulation using the Hexa Poly grid, next comes the Hexa Interior and last is the Tetra Rapid case that predicted lower negative pressure compared to the rest cases.

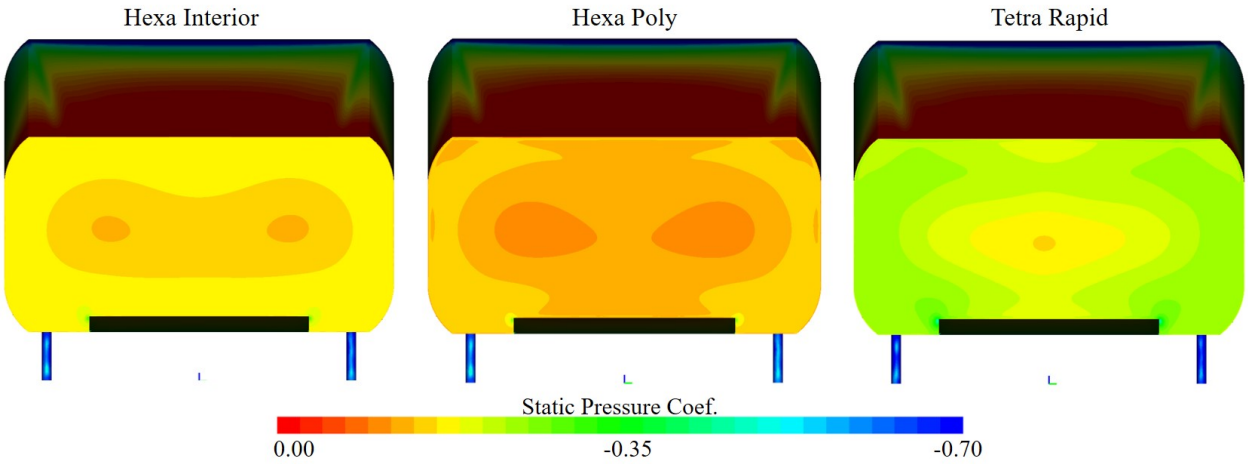

Figure 4.22: Rear view of surface pressure distribution across the SAE Notchback 20° Backlight for a Hexa Interior, a Hexa Poly and a Tetra Rapid volume mesh case.

The simulation with the Hexa Poly volume mesh, provided the most accurate prediction of the pressure distribution across the centerline of the model, with Mean Absolute Percentage Error equal to 7.1%, 4.1 standard deviation and maximum percentage error equal to 18.7% at pressure tap number 24, as seen in Table 4.11. Hexa Interior and Tetra Rapid volume mesh cases had a Mean Absolute Percentage Error equal to 25.4% and 29.6%, respectively.

Table 4.11: Deviation between the experimental measurements and the predicted pressure distribution across the SAE Notchback 20° Backlight for the volume mesh type investigation.

Case	**MAPE**(%)	**SD**	**MaxPE**(%)	**@Pres_Tap**
Hexa Interior	25.4	21.5	85.5	15
Hexa Poly	7.1	4.1	18.7	24
Tetra Rapid	29.6	24.9	97.2	24

Wake

The wake formed downstream of the model for every simulation is presented in Figure 4.24. Hexa Interior and Hexa Poly cases predicted almost the same wake region, with the first one to calculate lower energy at the x-normal plane located in $x = 1.2l$. The main difference between these two cases is the flow field between the model and the road; Hexa Poly calculates higher energy at that region which is similar to the fine mesh resolution case that was

presented in Figure 4.17, and gave a prediction of the drag force with divergence below 1%. The simulation using the Tetra Rapid case resulted in a very diffusive illustration of the flow field downstream of the car mainly ought to the inability of OpenFOAM solvers to handle computational grids devoid of hexahedral cells.

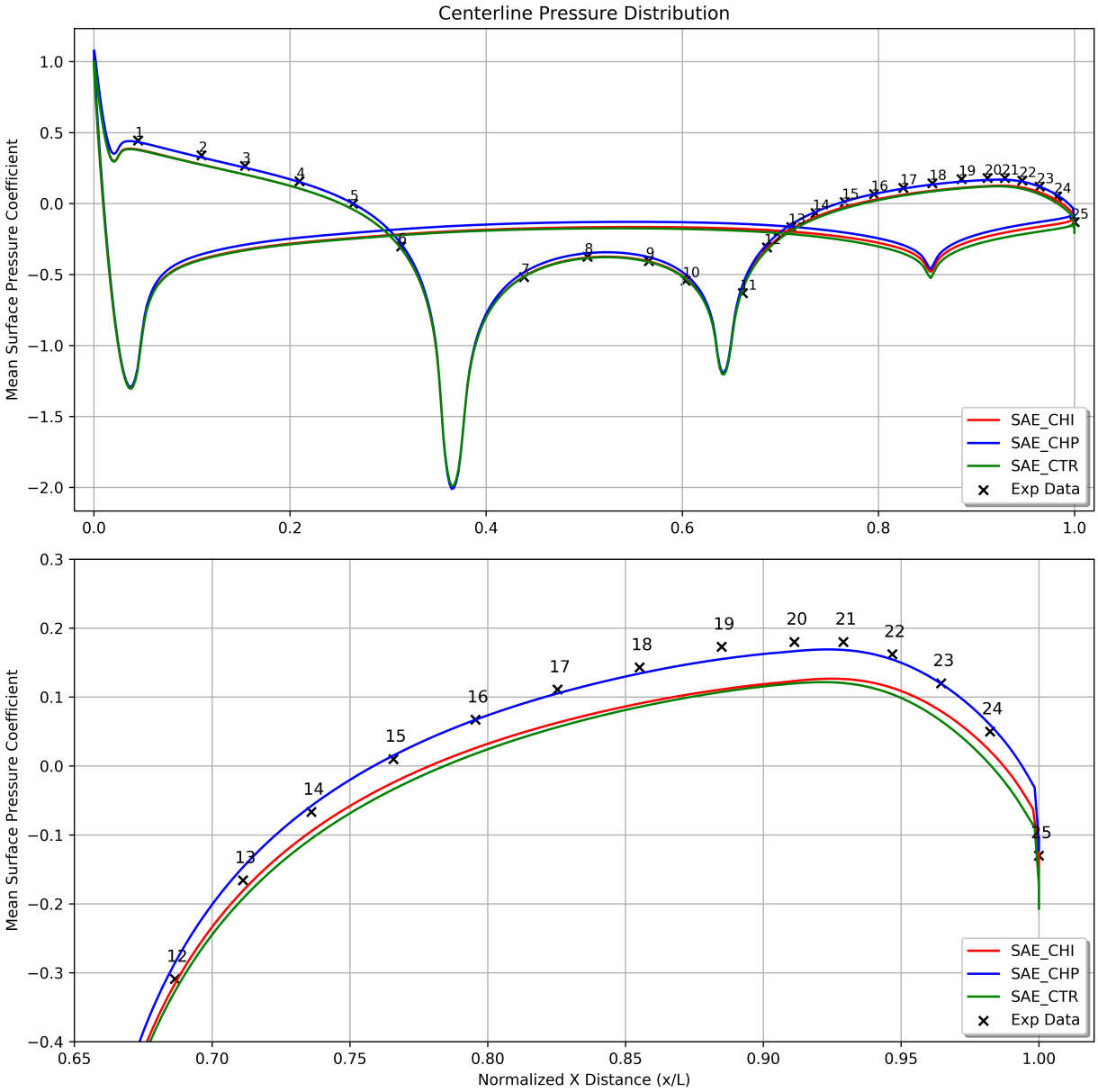

Figure 4.23: Surface pressure distribution at the centerline of the SAE Notchback 20° Backlight *(top)*, focused on the backlight region *(bottom)* for the Coarse Hexa Interior (SAE_CHI), the Coarse Hexa Poly (SAE_CHP) and the Coarse Tetra Rapid (SAE_CTR) cases.

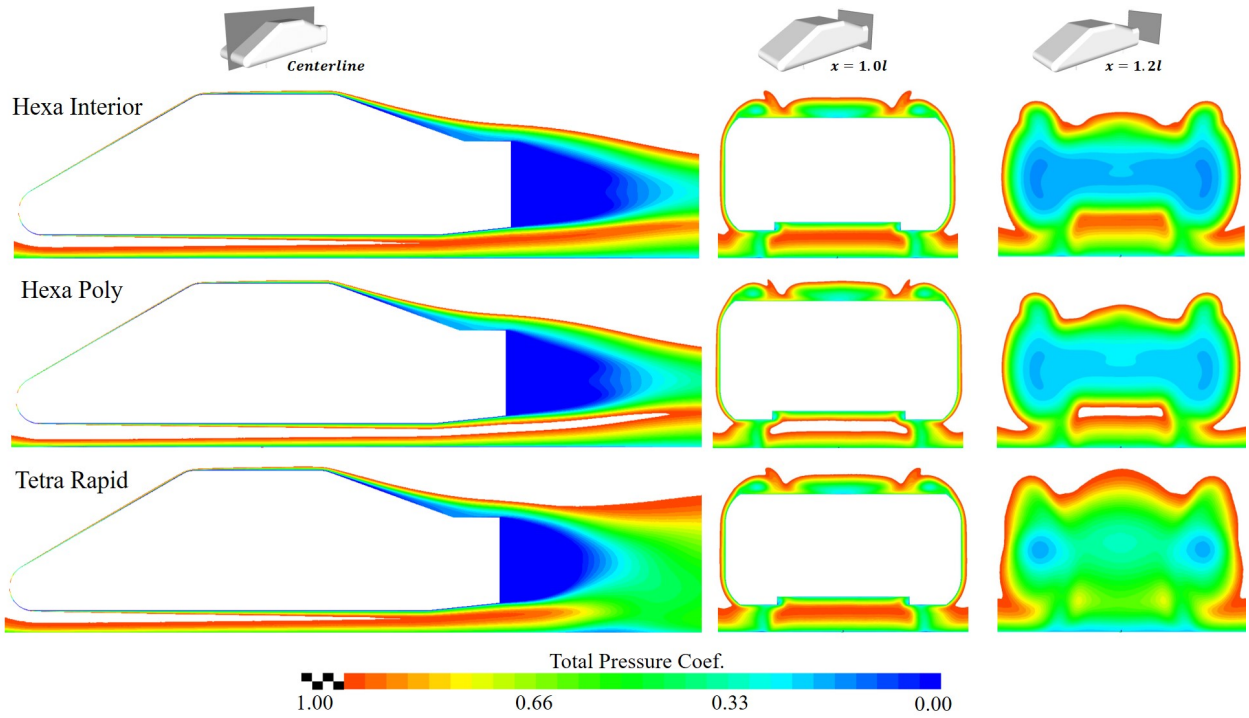

Figure 4.24: Y-normal centerline and X-normal total pressures planes depicting the wake downstream of the model.

Conclusion

The results occurred through the volume mesh type investigation are presented in Table 4.12. The best prediction of the drag force for a coarse resolution mesh was achieved with the Hexa Poly algorithm, with -2.08% deviation from the experimental value. Next is the Hexa Interior case with -5.52% error and finally the Tetra Rapid was the only case to predict higher drag force than the experimental, with error equal to +13.07%. To ensure that the Hexa Poly volume mesh is capable of predicting the flow with high accuracy for higher resolution meshes, a finer mesh was tested, with refinement factor equal to 1.8, to assess the trend of the drag force prediction with regards to the number of cells elements. This study showed that the prediction of the Hexa Poly case had a tendency to diverge from the experimental value as the mesh resolution increases and thus the Hexa Interior mesh was selected as the most appropriate from this investigation, since Table 4.6 showed that the numerical solution converged to the experimental drag force as the mesh resolution becomes higher.

Table 4.12: Volume mesh type investigation results for the SAE Notchback 20° Backlight.

Case	C_D	**Error**(%)	**t/iter**(s)	**RAM**(GB)
Hexa Interior	0.198	-5.52	15	33
Hexa Poly	0.206	-2.08	17	36
Tetra Rapid	0.237	+13.07	36	83

4.5 Turbulence Model

Three first order turbulence models were tested in this thesis for the SAE Notchback 20° Backlight model, namely the two equations k-ω SST and k-ϵ Realizable, and the one equation Spalart Allmaras (SA) model. For the k-ω SST and the Spalart Allmaras models, the layers were generated based on the low-Reynolds approach since these turbulence models can accurately solve the near-wall. In contrast, the k-ϵ turbulence model use wall damping functions, to reduce the turbulent viscosity near the wall, which increase the error of the calculations since the model cannot resolve directly the near wall flow. Hence, the high-Reynolds layers generation approach was utilised and the boundary layer was modelled based on semi-empirical equations.

These turbulence models were tested with a coarse resolution computational grid consisting of a trias surface mesh and a volume mesh that was generated with the use of the Hexa Interior volume meshing algorithm. For the numerical solution process, the steady state, isothermal and incompressible simpleFoam OpenFOAM algorithm was utilized and for the k-ϵ Realizable simulation, the standard wall function algorithm was used to model the boundary layer. The mesh specifications of every case are presented in Table 4.13. The surface mesh was the same for all the cases and it consists of 1.4 million shell elements. The k-ω SST and the Spalart Allmaras cases are also using the same volume mesh that consists of approximately 32 million cells and finally, the k-ϵ consists of less layers and thus of less cell elements, approximately 23 million. All the cases use the same refinement regions, which means that all the meshes are capable of resolving flow structures, away from the walls, of exactly the same size.

Table 4.13: Surface and volume mesh specifications of the simulations conducted for the turbulence model investigation on the SAE Notchback 20° Backlight.

	Elements(mi)		**Layers**	C_{size}/l_{ref} (%)		
Case	**Shell**	**Volume**	**Approach**	**Max**	**Min**	**Mesh ID**
k-ω SST	1.4 *(Trias)*	31.8 *(HexaInt)*	Low-Re	0.71	0.18	sae_chi
Spalart Allmaras	1.4 *(Trias)*	31.8 *(HexaInt)*	Low-Re	0.71	0.18	sae_chi_sa
k-ϵ	1.4 *(Trias)*	22.6 *(HexaInt)*	High-Re	0.71	0.18	sae_chi_ke

Surface Pressure

The surface pressure distribution across the model is presented in Figures 4.25, 4.26 and 4.27. The SST turbulence model predicts lower pressure on the middle section of the backlight and the trunk. The subtraction of the pressure fields of the SST and the SA case, revealed that the SST model predicts lower pressure at the C-Pillar vortices which is clearly depicted in Figure 4.25 with black colour on this region. The Spalart Allmaras turbulence model, predicts an enhanced negative pressure region at the start of the backlight, resulting in a stronger downwash at the centerline and consequently in the higher pressure at the trunk. The comparison between the k-ω SST and k-ϵ Realizable cases revealed divergence at the backlight region as well. Similar to the Spalart Allmaras turbulence model, the subtraction showed a minor pressure difference at the top of the backlight which affects the low regime

at the lower section of the backlight and the trunk. The case solved with the SST turbulence model, underestimates the positive pressure at the trunk, as seen in Figure 4.25, where the Spalart Allmaras case provided better pressure prediction at the backlight region compared to the other cases.

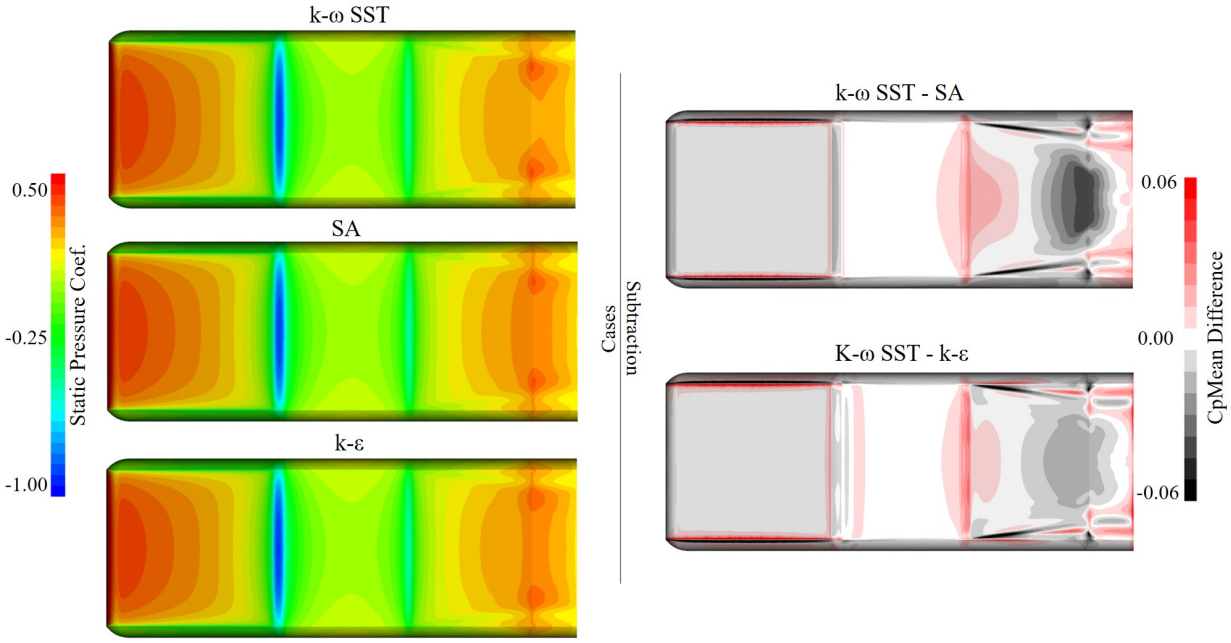

Figure 4.25: Top view of surface pressure distribution across the SAE Notchback 20° Backlight for different turbulence models *(left)* pressure divergence computed by subtracting the results of the cases and plotting the resultant pressure *(right)*.

Table 4.14 presents the deviation between the experimental pressure measurements and the pressure predicted by the CFD simulations at the centerline of the SAE Notchback 20° Backlight. All of the cases seem to agree with each other in almost every point except for the backlight region. The lowest Mean Absolute Percentage Error was achieved by the k-ϵ Realizable simulation and it is equal to 22.3%. The Spalart Allmaras simulation also predicted the pressure distribution with Mean Absolute Percentage Error equal to 22.7% but the standard deviation and the maximum error were higher compared to the k-ϵ Realizable case. The k-ω SST turbulence model had the highest deviation among all cases, equal to 25.4% and maximum error 85.5% at pressure tap number 15.

Table 4.14: Deviation between the experimental measurements and the predicted pressure distribution across the SAE Notchback 20° Backlight for the surface mesh type investigation.

Case	**MAPE**(%)	**SD**	**MaxPE**(%)	**@Pres_Tap**
k-ω SST	25.4	21.5	85.5	15
Spalart Allmaras	22.7	22.5	87.1	15
k-ϵ	22.3	15.8	61.0	24

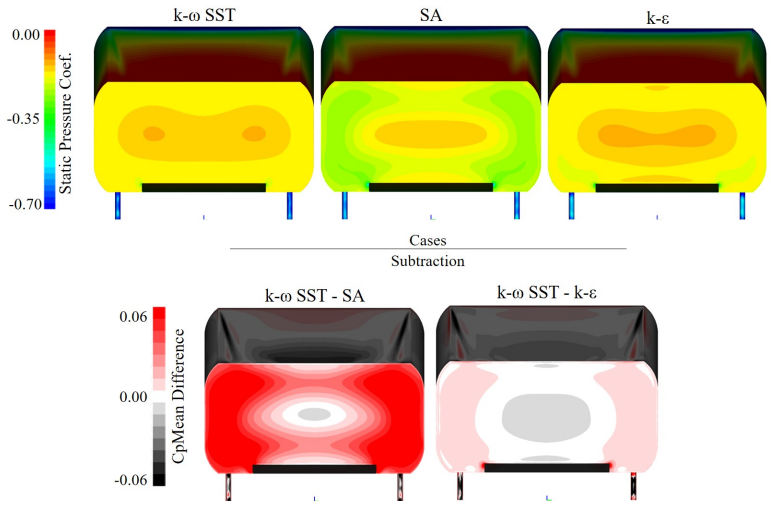

Figure 4.26: Rear view of surface pressure distribution across the SAE Notchback 20° Backlight for different turbulence models *(top)* pressure divergence computed by subtracting the results of the cases and plotting the resultant pressure *(bottom)*.

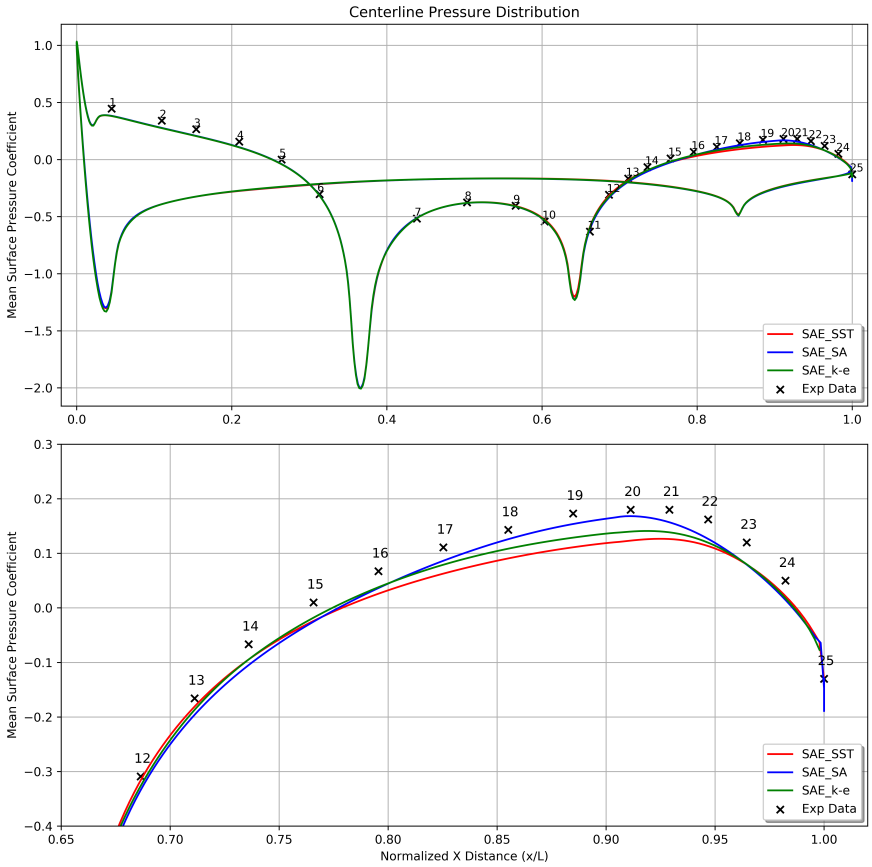

Figure 4.27: Surface pressure distribution at the centerline of the SAE Notchback 20° Backlight *(top)*, focused on the backlight region *(bottom)* for the k-ω SST (SAE_SST), Spalart Allmaras (SAE_SA) and k-ϵ Realizable (SAE_k-e) cases.

Wake

The comparison between the wake formed downstream of SAE Notchback 20° Backlight for every turbulence model is illustrated in Figure 4.28. The k-ω SST and k-ϵ Realizable turbulence models, predict almost similar wake regions near the car and the only noticeable divergence is at the cut plane located at $x = 1.2l$. The wake calculated with the k-ω SST model has lower static pressure at the center, compared to the k-ϵ-predicted wake, hence it is more likely to predict higher drag value. Finally, the Spalart Allmaras turbulence model predicts the smallest wake region among the tested cases and greater boundary layer region between the model and the road, underestimating the energy of the flow beneath the model.

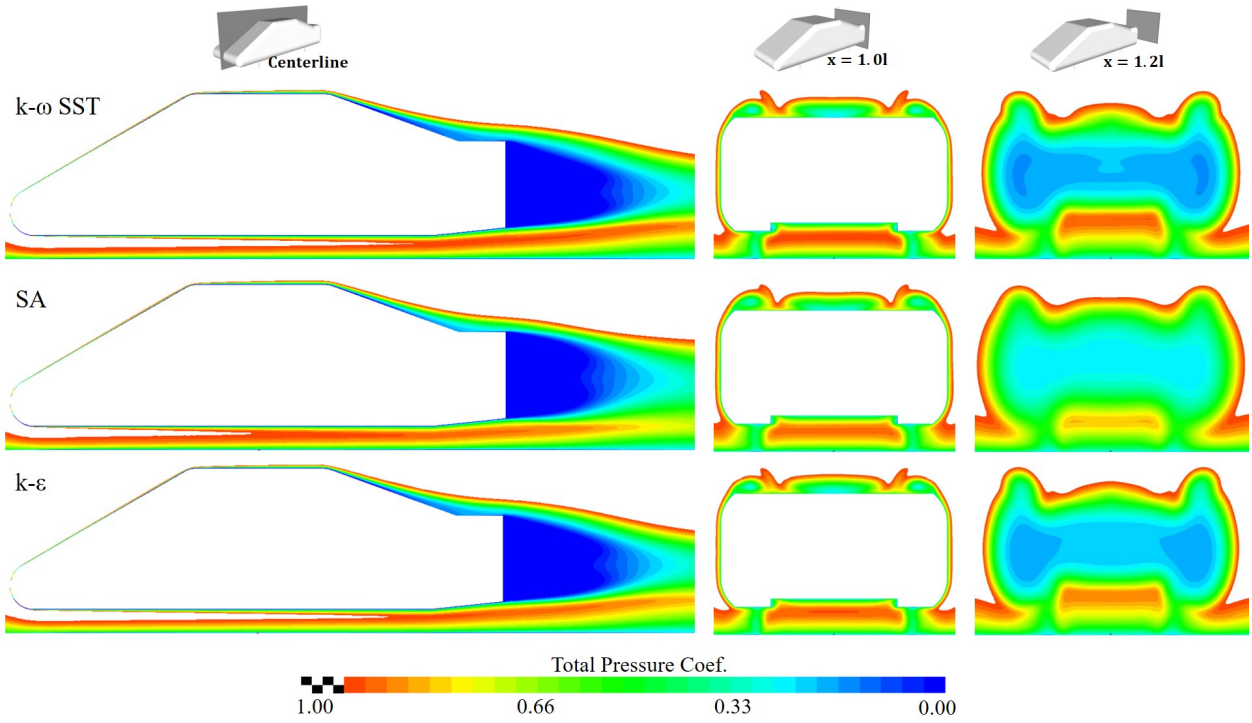

Figure 4.28: Y-normal centerline and X-normal total pressures planes depicting the wake downstream of the model.

Conclusion

The outcome of the turbulence model investigation is presented in Table 4.15. The best drag force prediction was 0.198 with error -5.52% and was achieved with the use of the two-equation k-ω SST turbulence model with low-Reynolds layers approach. The second most accurate turbulence model was the two-equation k-ϵ Realizable with the high-Reynolds layers approach and the least accurate was the Spalart Allmaras model. The latter was the only model that predicted higher drag coefficient than the experimental value, which is justified based on the small wake region depicted in Figure 4.28. Table 4.14 shows that the most accurate prediction of the pressure distribution across the centerline is achieved with the k-ϵ model, however this model fails to predict the drag coefficient accurately. The body pressure

prediction accounts only for the centerline of the model, so it is reasonable to have a discrepancy between the model that best predicts the pressure distribution on the centerline, and the model that best predicts the total drag coefficient of the body.

Since the computational grid used for these simulations was of low resolution, and consequently mesh independency was not achieved, a simulation with finer mesh was conducted for every case to get a first estimation of the trend of the drag coefficient prediction with regards to mesh resolution. The simulation using the k-ω SST turbulence model was the only one that the drag converged closer to the experimental value as the mesh resolution increase as seen in Figure 4.29. The other two turbulence models diverged from the experimental drag coefficient and were rejected as less accurate.

Table 4.15: Turbulence model investigation results for the SAE Notchback 20° Backlight.

Case	C_D	**Error**(%)	**t/iter**(s)	**RAM**(GB)
k-ω SST	0.198	-5.52	15	33
Spalart Allmaras	0.229	+9.19	15	33
k-ϵ	0.195	-7.00	9	24

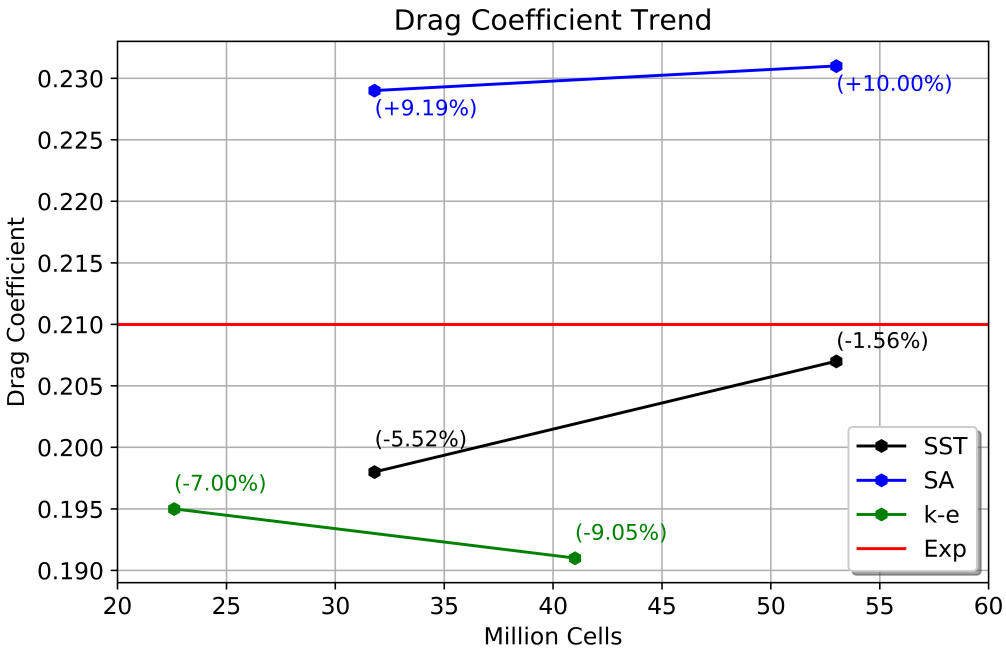

Figure 4.29: Drag coefficient trend with regards to increasing mesh resolution. The value in the parenthesis represents the deviation of each simulation from the experimental drag coefficient.

4.6 Transient Simulation

The last step of the CFD methodology investigation of the SAE Notchback 20° Backlight was to conduct transient simulations. Due to limited computational resources, only the coarse and the medium computational grids were tested since higher resolution grids demand excessive computational power and time. The simulations were conducted with the use of a hybrid RANS-LES method, namely the Delayed Detached Eddy Simulation (DDES) that is extensively analysed in Chapter 3.2: "Numerical Solution". This model utilizes a spatial filter to either resolve or model the turbulence, and consequently the mesh resolution strongly affects the outcome of the simulation.

The computational mesh specifications of every case are presented in Table 4.16. The coarse mesh consists of 1.4 million shell elements, 31.8 million volume cells and it is capable of resolving flow structures in the scale of $0.18\% \cdot l_{ref} = 1.44mm$. The medium mesh is refined by 1.7 times and consists of 53.3 million cells. Both grids were generated with the trias surface mesh, and Hexa Interior volume mesh algorithms and with the low-Reynolds approach for the layers.

Table 4.16: Surface and volume mesh specifications of the simulations conducted for the transient DDES mesh resolution investigation of the SAE Notchback 20° Backlight.

	Elements(mi)		**Layers**	$\boldsymbol{C_{size}/l_{ref}}$ (%)		
Case	**Shell**	**Volume**	**Approach**	**Max**	**Min**	**Mesh ID**
DDES-Coarse	1.4 *(Trias)*	31.8 *(HexaInt)*	Low-Re	0.71	0.18	sae_chi
DDES-Medium	2.0 *(Trias)*	53.3 *(HexaInt)*	Low-Re	0.60	0.15	sae_mhi

For the numerical solution, the pimpleFoam OpenFOAM solver was used, which is an incompressible and isothermal, transient solver that utilizes a combination of the PISO and SIMPLE algorithms for pressure-velocity coupling. For the turbulence resolution, the hybrid k-ω DDES model was used and the time step applied in each simulation was selected so as the Courant number to be below 1 for 90% of the cells for the coarse mesh and below 2 for the medium mesh due to limited computational sources. The transient cases were initialized with fully converged steady state simulations and the first 5 convective flow units were ignored to ensure that the solution is not affected by remaining steady state RANS phenomena. The results reported in this chapter are averaged based on the method presented at Chapter 3.2.4: "Convergence Criteria", so the presented results are the mean and not the instantaneous values of the flow field variables.

Surface Pressure

The surface pressure distribution across the model's surfaces and the pressure measurements across the centerline are presented in Figures 4.30 and 4.31, respectively. The coarse mesh resolution case predicts an early flow separation at the backlight which does not agree with the experimental values. Due to the coarse mesh, the solver underestimates the turbulence at that region, as seen in Figure 4.32, resulting in boundary layer separation.

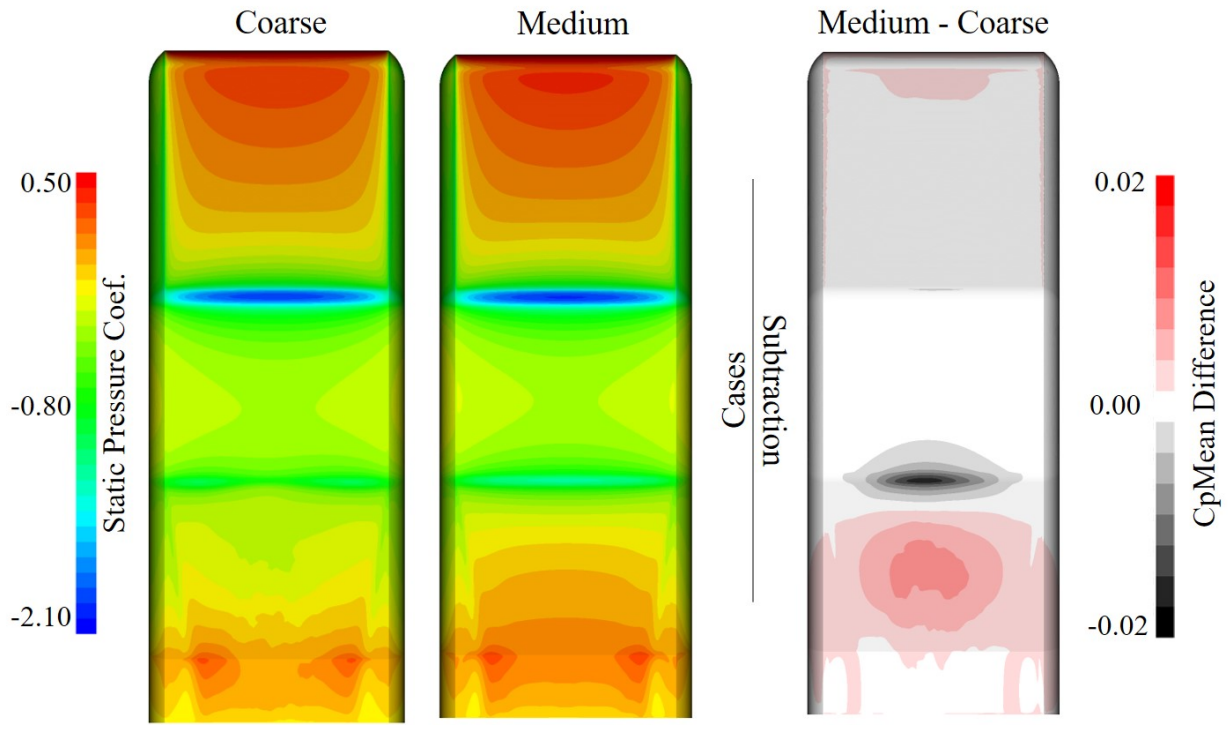

Figure 4.30: Top view of surface pressure distribution across the SAE Notchback 20° Backlight for mesh resolution for a DDES simulation *(left)* pressure divergence computed by subtracting the results of the cases and plotting the resultant pressure *(right)*.

Except for that region, the results subtraction reveals that the two models predict almost the same surface pressure across the rest of the surfaces. Table 4.17 presents the deviation between the predicted pressure distribution and the experimental values. The coarse mesh simulation predicted the pressure distribution at the centerline with a deviation equal to 29.5%, 21.5 standard deviation, the Maximum Percentage Error was 186.4% at the 15th pressure tap and as mentioned before, the model failed to predict the flow regime at the rear end of the model. On the other hand, the medium mesh simulation gave a prediction very close to the experimental data with Mean Absolute Percentage Error equal to 8.9%, 5.3 standard deviation and 21.7% maximum error at pressure tap number 23.

Table 4.17: Deviation between the experimental measurements and the predicted pressure distribution across the SAE Notchback 20° Backlight for the DDES mesh resolution investigation.

Case	**MAPE**(%)	**SD**	**MaxPE**(%)	**@Pres_Tap**
DDES - Coarse	29.5	21.5	186.4	15
DDES - Medium	8.9	5.3	21.7	23

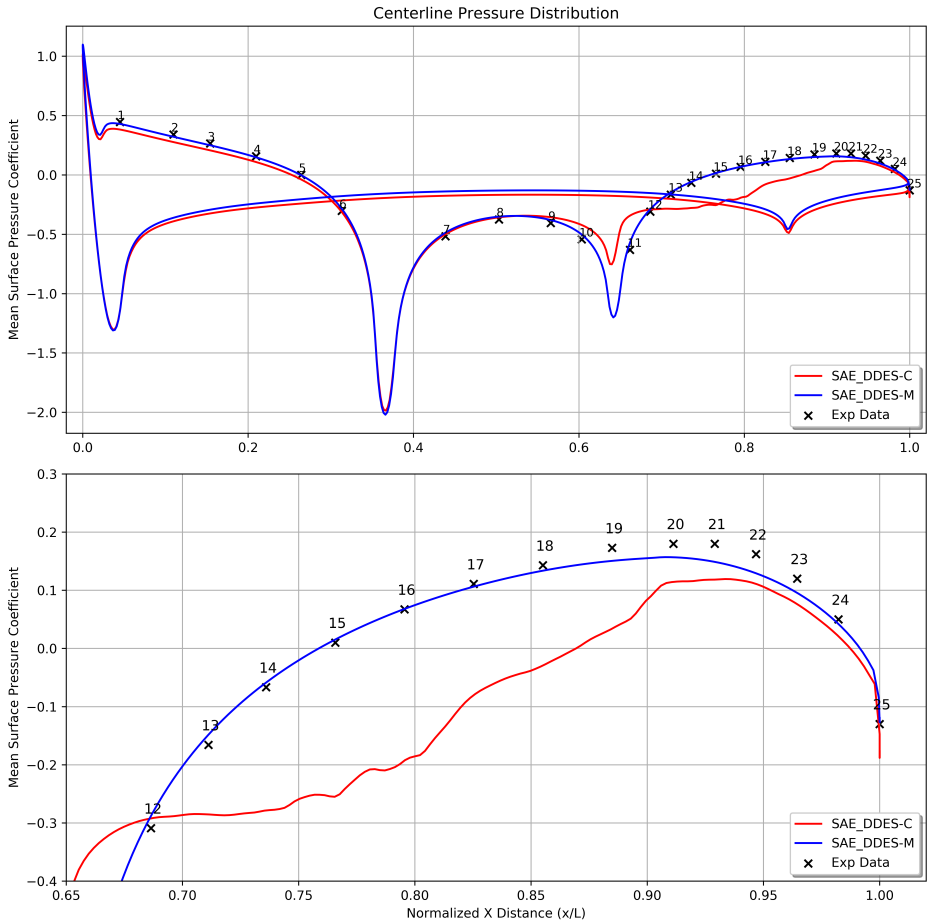

Figure 4.31: Surface pressure distribution at the centerline of the SAE Notchback 20° Backlight *(top)*, focused on the backlight region *(bottom)* for the DDES Coarse mesh resolution mesh (SAE_DDES-C), and the DDES Medium mesh resolution (SAE_DDES-M) cases.

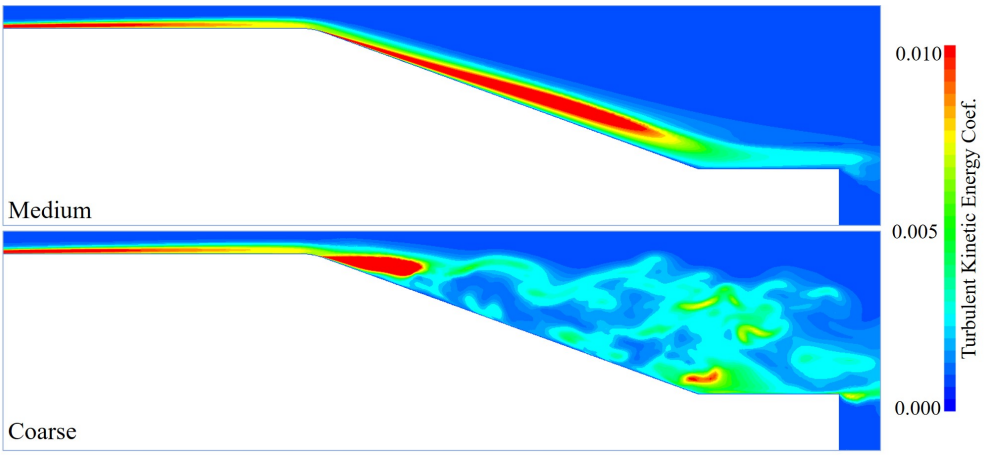

Figure 4.32: Turbulent kinetic energy distribution at the backlight region across a y-normal plane located at the centerline for the coarse *(top)* and the medium *(bottom)* mesh resolution cases.

Vortex Cores

Figures 4.33 and 4.34 illustrate the high vorticity regions around the model. Lambda 2 Criterion isosurfaces also visualise regions where turbulence is resolved such as inside the wake downstream of the model. The simulation with the coarse mesh predicts high vorticity at the backlight due to the early flow separation and the C-Pillar vortices are shifted closer to the centerline due to the lower pressure on the trunk compared to the medium resolution

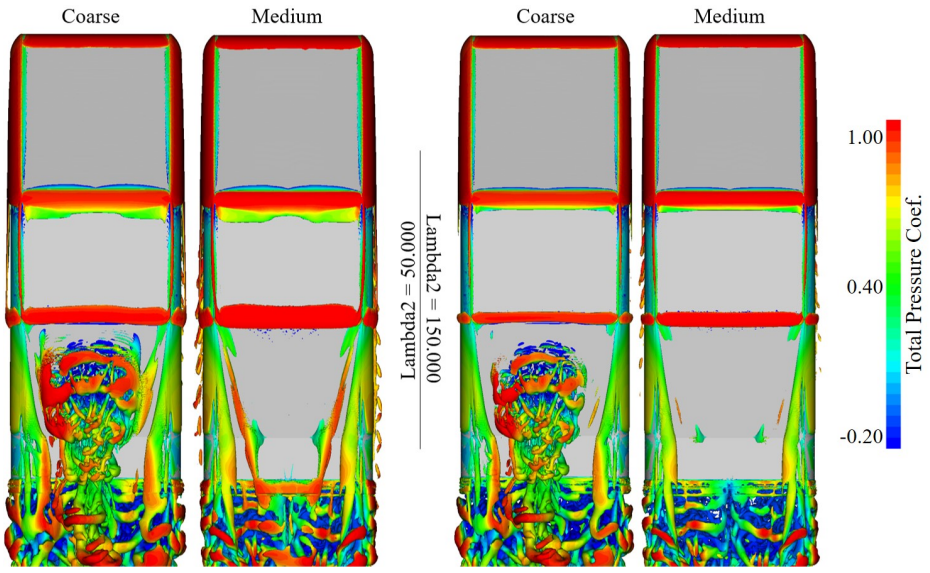

Figure 4.33: Top view of vortex cores visualised with Lambda 2 Criterion with L2=50.000 *(left)* and L2=150.000 *(right)*, coloured with total pressure.

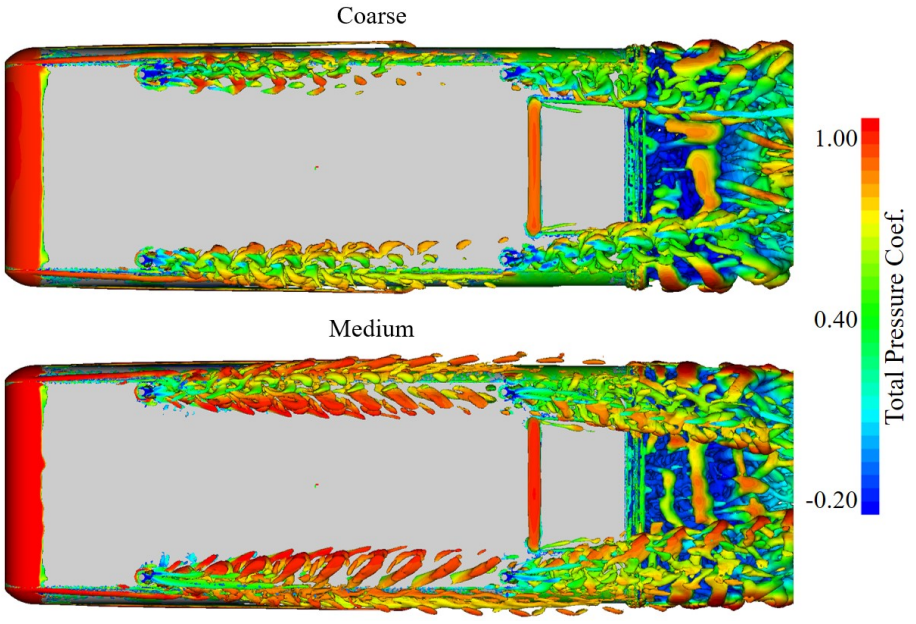

Figure 4.34: Bottom view of vortex cores visualised with Lambda 2 Criterion for L2=50.000, coloured with total pressure, for a Coarse *(top)* and a Medium *(bottom)* resolution mesh.

mesh. Finally, the bottom view of the L2 isosurfaces (see Figure 4.34) depicts the difference between the turbulent flow structures that are resolved; the medium resolution grid allows the solver to resolve greater amount of turbulence downstream of the model supports compared to the coarser mesh.

Wake

Figure 4.35 presents a comparison between the medium and coarse resolution DDES simulation and the most accurate steady state RANS simulation that occurred through the aforementioned investigations. The medium DDES seems to agree with the fine RANS case in the predicted wake downstream of the car and in the flow field beneath the model. However, the wake calculated by the coarse mesh splits the wake into two regions, one behind the backlight and one behind the trunk, resulting in a greater wake in total compared to the other cases which will affect the predicted drag coefficient.

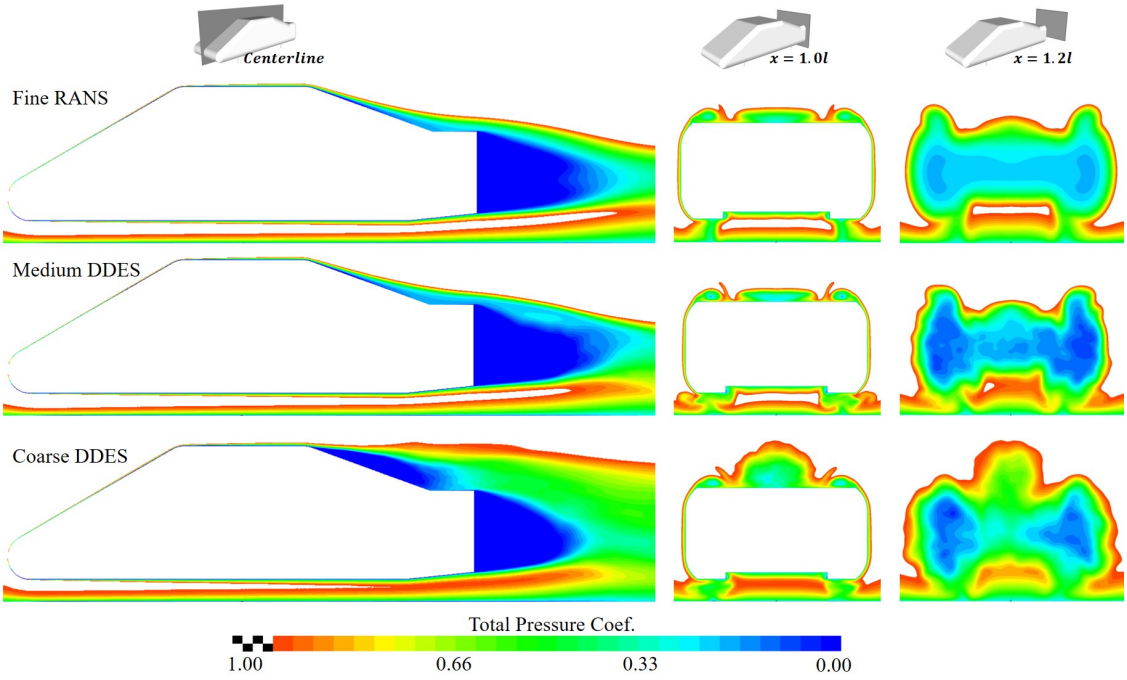

Figure 4.35: Y-normal centerline and X-normal total pressures planes depicting the wake downstream of the model.

Conclusion

The outcome of the mesh resolution investigation for a transient Delayed Detached Eddy Simulation is presented in Table 4.18. The best drag force prediction was 0.209 with error -0.26% and was achieved with the transient simulation of the medium resolution mesh which demanded approximately 7200 core hours to complete. The coarse resolution mesh failed to predict the flow field downstream of the model resulting in +8.55% overestimation of the generated drag force compared to the experimental drag value. The medium resolution mesh

was selected as the most suitable for the transient DDES simulation of the SAE Notchback 20° Backlight.

Table 4.18: Mesh density for a transient DDES simulation investigation results for the SAE Notchback 20° Backlight.

Case	C_D	**Error**(%)	**t/iter**(s)	**RAM**(GB)	**CPU Time**(h)
DDES - Coarse	0.228	+8.55	18	33	4650
DDES - Medium	0.209	-0.26	29	55	7199

4.7 Conclusion

The CFD methodology study of the SAE Notchback 20° Backlight consisted of five different investigations, namely the mesh resolution investigation for a steady state simulation, the examination of how the surface mesh type affects the simulation, the volume mesh type investigation, the turbulence model investigation and finally the examination of the influence of the mesh resolution in a transient DDES simulation. The data used to assess the accuracy of each simulation, were the pressure distribution measured across the centerline of the model, during a wind tunnel test, with the use of pressure taps and the total drag force generated by the model, measured with a high accuracy scale.

In terms of accuracy, the best prediction of the total drag force was achieved with the transient k-ω DDES simulation with the medium resolution mesh consisted of trias shell elements, volume cells generated by the Hexa Interior algorithm and low-Reynolds layers approach, resulting in a predicted drag coefficient equal to 0.209 which corresponds to -0.26% deviation from the experimental drag coefficient. The pressure distribution across the surface of the model was also predicted with high fidelity and more precisely with Mean Absolute Percentage Error (MAPE) equal to 8.9%. The error of the predicted pressure values is an order of magnitude greater than the error of the drag coefficient, since some pressure values are very close to zero, which means that a very small deviation from the experimental values will give a great percentage error that will lead to a higher MAPE value. However, the major drawback of this simulation was the excessive computational time needed to complete. The total time needed to conduct a transient simulation is the sum of the time that the steady state simulation, used for the initialization, needed to converge and the time needed for the DDES to complete, resulting in 8532 core hours.

The next most accurate and by far most time efficient simulation was the steady state RANS simulation with *k-omega* SST turbulence model, using a fine resolution mesh consisted of trias surface elements, volume cells produced with the Hexa Interior algorithm and low-Reynolds layers approach. This simulation predicted the drag force and the pressure distribution across the centerline with -0.76% and 5.7% error, respectively. This computational time was 2500 core hours, which is 3 times lower compared to the transient simulation's time. The setup used to generate the mesh, and the solver settings of this case were selected as the most accurate and time efficient and will be used as a baseline CFD setup for the AeroSUV simulations, presented in the next chapter.

5 Results II - AeroSUV

"The noblest pleasure is the joy of understanding"

-Leonardo da Vinci

5.1 Model Overview

The last step of this thesis was the numerical investigation of the three AeroSUV variants, namely the fastback, the notchback and the squareback, presented in Chapter 1.5.1 : "Introduction to the AeroSUV Reference Model". The AeroSUV, was proposed by Zhang *et al.* [1] in 2019 as a modern fully-detailed road-vehicle capable of representing the geometry of a generic SUV model for three different rear ends. The geometry was optimized with main parameters being the angles shown in Figure 5.1, and it is used as a reference model for CFD investigations.

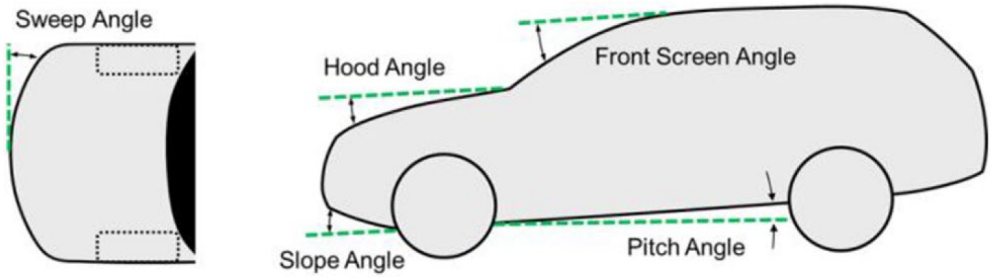

Figure 5.1: Optimisation parameters for the AeroSUV model [1] *(edited by the author).*

The length of the model is 4619mm with a wheelbase equal to 2786mm and front and rear track equal to 1552mm. The height of the model is 1608mm and the lowest ground clearance is 196mm as illustrated in Figure 5.2. The approach, break over and departure angles are 25°, 19°and 24°, respectively. During the wind tunnel testing, an 1:4 scaled down model was used with projected frontal area equal to $0.154m^2$ and the velocity was set to 50m/s to maintain the Reynolds analogy [1]. In contrast to the SAE Notchback 20° Backlight model, the AeroSUV is designed to form a very complex flow field with enhanced interaction between the flow structures. The fully detailed rims further increase the complexity by introducing a swirling motion to the flow in addition to the tyre squirt generated by the compression of the air towards the road. The flow structures generated at the front end are almost the same for every variant, however the rear end geometry strongly affects the surface pressure distribution and the wake formed downstream of the model. Finally, the fully detailed underfloor, seen in Figure 5.3 of the model consists of many flow separation and stagnation points introducing numerous reversed flow regions, enhanced total pressure losses and high turbulence between the road and the model.

The three variants analyzed in this chapter are depicted in Figure 5.3. The fastback and notchback models have similar geometry but the latter has greater backlight angle, resulting in a steeper transition from the roof to the rear windshield. The squareback model, also

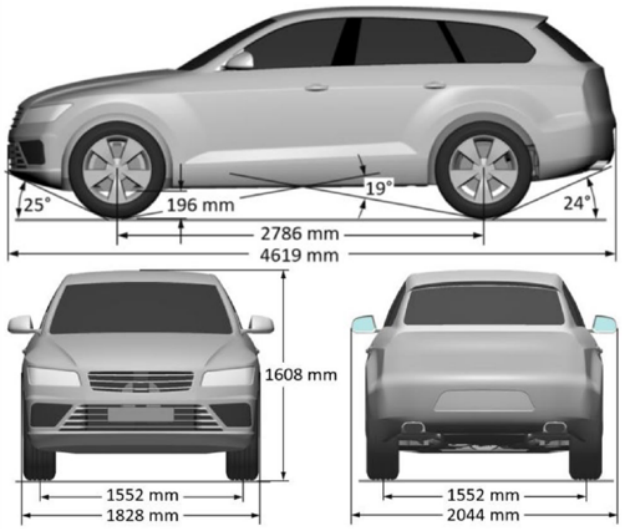

Figure 5.2: Overall dimensions of the full scale AeroSUV Squareback model [1].

known as estate, is the least aerodynamic configuration, compared to the other two, generating the highest drag force. The grilles at the front end are closed to reduce the complexity of the flow, minimize the potential sources of uncertainty and maintain an affordable cell count for the computational grid. At the time that this thesis was conducted, the data gathered from the pressure taps were not available at the European Car Aerodynamic Research Association (ECARA) website and consequently the main indicator used to assess the accuracy of a simulation was the deviation between the predicted drag force and the force measured through the wind tunnel testing.

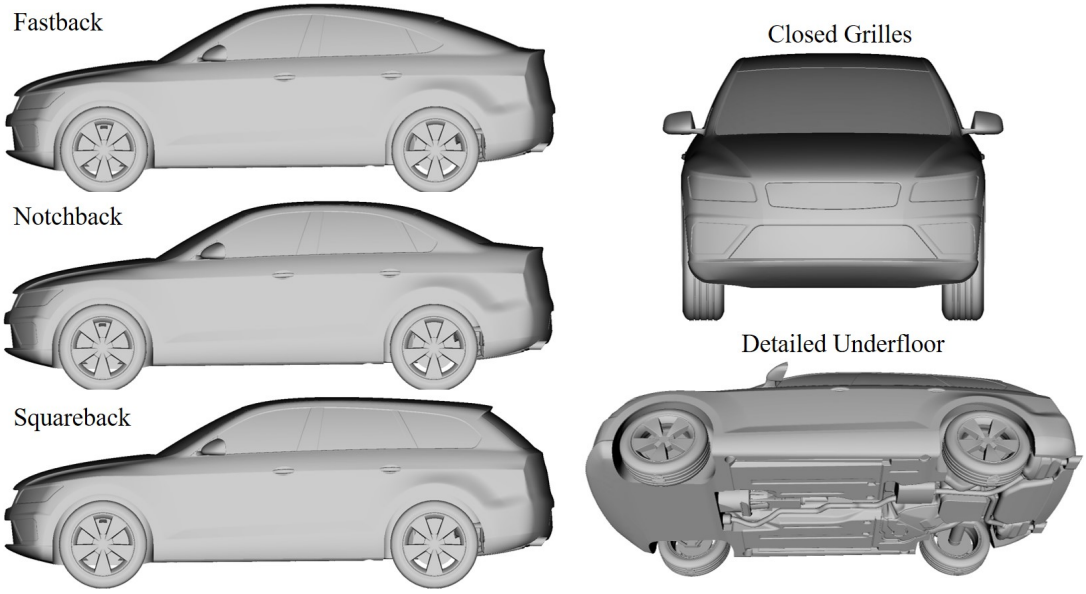

Figure 5.3: The AeroSUV variants *(left)* the front end depicting the closed grilles and an isometric view of the detailed underfloor *(right)*.

5.2 Experimental Data

Force and Momentum

The experiment of the AeroSUV was conducted at the wind tunnel of University of Stuttgart, which is operated by the *Forschungsinstitut für Kraftfahrwesen und Fahrzeugmotoren Stuttgart (FKFS)* [64]. A previous research carried out by Wickern *et al.* [65] revealed that the rotating wheels are responsible for the 25% of the total drag force generated by a moving vehicle. To model the rotational motion of the tyres, the FKFS wind tunnel is equipped with a 5-belt system, one belt for every wheel and one located beneath the vehicle to model the translational motion of the road, as seen in Figure 5.4. The model is supported by 4 struts located downstream of the front and upstream of the rear wheels and the tyres are free to move on the rolling belts. Zhang *et al.* designed modular rims in order to test different rim geometries and to evaluate the influence they have on the performance of the model; however in this thesis only one type of rims was modelled. Furthermore, the wind tunnel is equipped with a boundary layer suction system upstream of the belt representing the moving road to ensure a realistic flow regime between the model and the floor. The drag and lift force generated by the model while moving in a straight line were measured in every axle and are presented in Table 5.1.

Table 5.1: Aerodynamic forces measured through the wind tunnel testing of the AeroSUV variants [1].

Model	C_D	$C_{L,f}$	$C_{L,r}$
Fastback	0.286	0.053	0.061
Notchback	0.286	0.057	0.080
Squareback	0.314	0.024	-0.016

Figure 5.4: The AeroSUV model inside the FKFS windtunnel and the 5-belt system [1] *(edited by the author).*

5.3 Flow Field Analysis

The AeroSUV is a realistic reference model and the flow field generated around it is described by high complexity and enhanced interaction between various flow structures. For all the variants, the A-Pillar and the mirror vortices dominate at the front end, however the evolution of these structures is strongly connected to the rear end geometry, resulting in a completely different flow field at that region for the fastback,notchback and squareback configuration. The flow field generated by each model will be extensively analysed below. The images used in this chapter to describe the flow field of each variant, are exported from the CFD simulations that predicted the drag coefficient with the smallest deviation from the experimental drag value.

Surface Pressure

The surface pressure distribution across the centerline of each model is illustrated in Figure 5.5. All three models have the same stagnation pressure at the front bumper and the windshield, and two negative pressure peaks, one beneath the front bumper and one at the start of the roof due to the curvature of these surfaces that cause the flow to accelerate. The

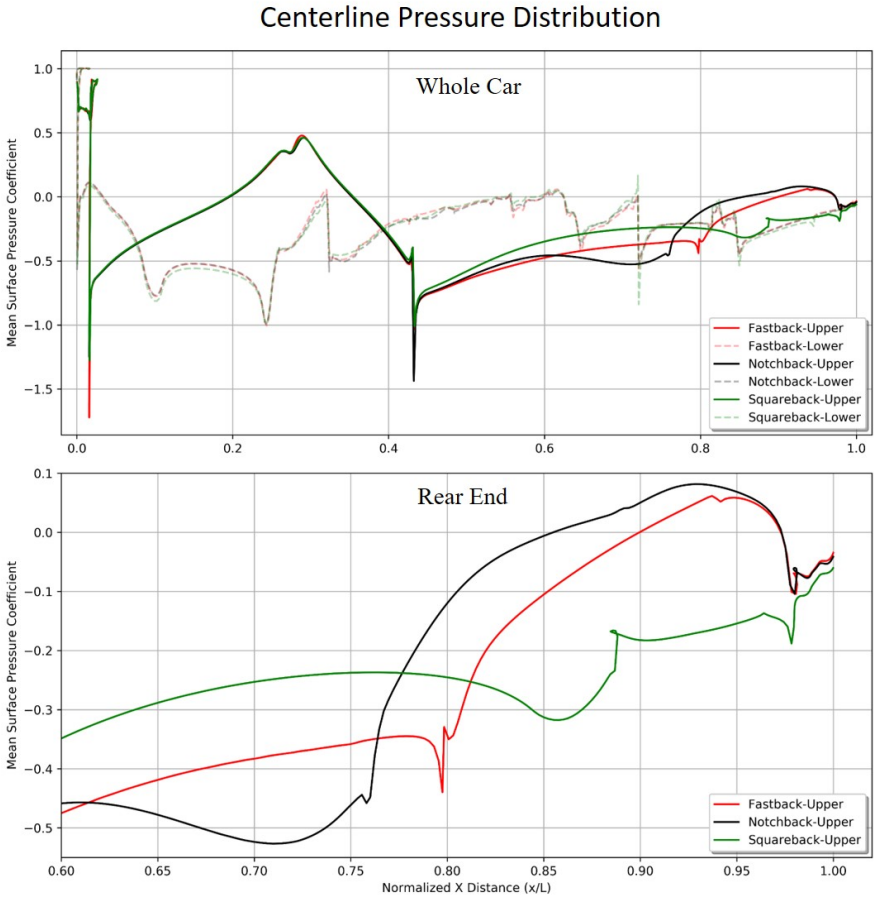

Figure 5.5: Pressure distribution across the centerline of the fastback, notchback and squareback models.

fully detailed underfloor, introduces pressure fluctuations on the chart and consequently only the pressure distribution at the upper section of the vehicle will be used to directly compare different cases. The rear end geometry seems to affect the pressure field up to the front windshield; the collected chart at the right of Figure 5.5 shows that the pressure distribution downstream of the front windshield is different for every case. More precisely, the notchback model has a lower pressure region due to the highly angled backlight compared to the fastback. The notchback configuration has a bigger trunk compared to the fastback, where a positive pressure region is generated due to the collision of the flow on that surface.

The geometry of the fastback is aligned to the flow, making the model more aerodynamic compared to the notchback since it consists of lower backlight angle and smoother transition between the roof, the backlight and the trunk. This is also depicted in the pressure chart, where the transition from negative to ambient pressure is smoother compared to the notchback and the squareback. The latter is the least aerodynamic model; the pressure remains negative until the rearmost portion of the roof where flow separation occurs due to the abrupt rear end geometry. This steep transition from negative to ambient pressure is responsible for the big wake formed downstream of the model and the greater drag coefficient compared to the other two configurations.

Wall Shear Stress

Figure 5.6 illustrates a combined view of the surface pressure, the wall shear stress and the vortical structures generated by every model. These three metrics can be used to describe the flow field at the rear end of each model and justify the flow structures formed there. The fastback has greater C-Pillar radius compared to the notchback that allows the flow to remain attached, which is revealed by the high wall shear stress at that region. The small-sized trunk, generates a high pressure region which has minor influence on the backlight, causing local flow separation near the centerline. From the Lambda 2 Criterion isosurfaces, the A-Pillar vortices seem to follow the curvature of the roof until they burst at the start of the backlight due to the reduced energy content of the flow.

The notchback configuration has smaller C-Pillar radius, greater backlight angle and bigger trunk area compared to the fastback. The steep curvature of the trailing pillar is responsible for the formation of the C-Pillar vortices visualised clearly by the L2 isosurfaces. These vortices collide on the trunk and expand further downstream of the car until they burst. The wall shear stress is high on the trunk due to these vortices which also contribute to keep the flow attached at the backlight since a downwash is generated ought to the rotating motion of the flow. Finally, the A-Pillar vortices seem to extend further rearwards, compared to the fastback, until they burst and this is mainly a result of the low pressure region generated at the highly angled backlight.

A completely different flow field is generated at the rear end of the squareback variant compared to the other 2 configurations. The angle of the backlight is adequately high resulting in clearly defined flow separation at the end of the roof. A small spoiler extends at the rear end of the roof to divert the flow downwards reducing the wake formed downstream

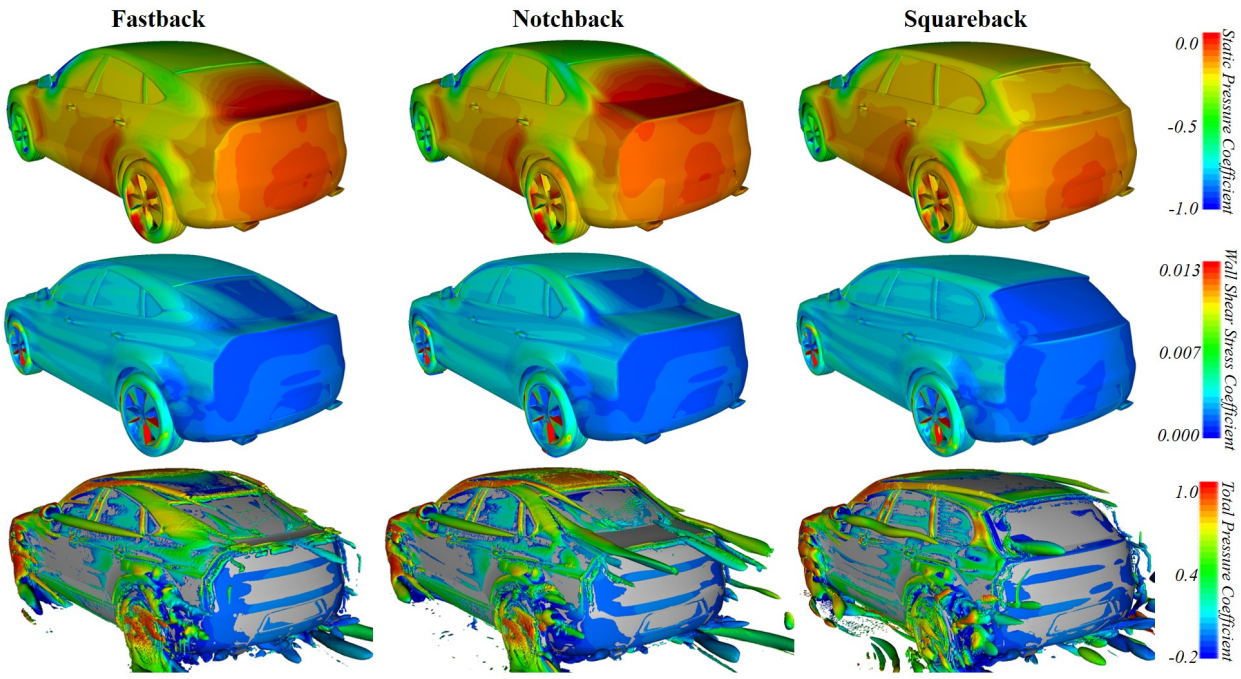

Figure 5.6: Rear isometric view of the surface pressure *(top)*, wall shear stress *(middle)* and Lambda 2 Criterion isosurfaces coloured by total pressure *(bottom)* for the variants of the AeroSUV model.

of the car. The rearmost face of the model is dominated by almost zero wall shear stress and negative pressure which pulls the model rearwards opposing to its movement and, among others, is responsible for the higher drag force compared to the fastback and the notchback. The mirror vortices seem to have equal length in all configurations regardless of the rear end geometry. Finally the A-Pillar vortices follow the curvature of the roof and burst at the start of the backlight.

Wake

The wake formed downstream of each model is illustrated in Figures 5.7 and 5.8. The zero total pressure isosurfaces indicate that on the fastback and notchback cases, the flow regains energy due to the high pressure region generated at the trunk that squeezes the boundary layer, increasing the energy of the flow near the wall resulting in a decrease of the boundary layer width. The zero x-velocity isosurfaces visualise almost zero backflow at the backlight of the fastback in contrast to the notchback, where a small region with negative x-velocity is present at the middle of the backlight. From Figure 5.8, the wake formed beneath the model at the centerline seems to be the same for all the geometries, however the wake downstream of the car varies significantly.

As mentioned before, the fastback configuration produces the smallest wake behind the car since the smooth transition from the roof to the backlight and the trunk allows the flow to remain attached without significant total pressure loss. On the other hand, the higher angle of the backlight of the notchback model, causes an expansion of the boundary layer

resulting in separation at the trunk and greater wake region than the fastback. Finally, the squareback model forms a low energy region downstream of the backlight that extends further rearwards compared to the other models, which is also visible at the x-normal plane located at $x = 1.2l$.

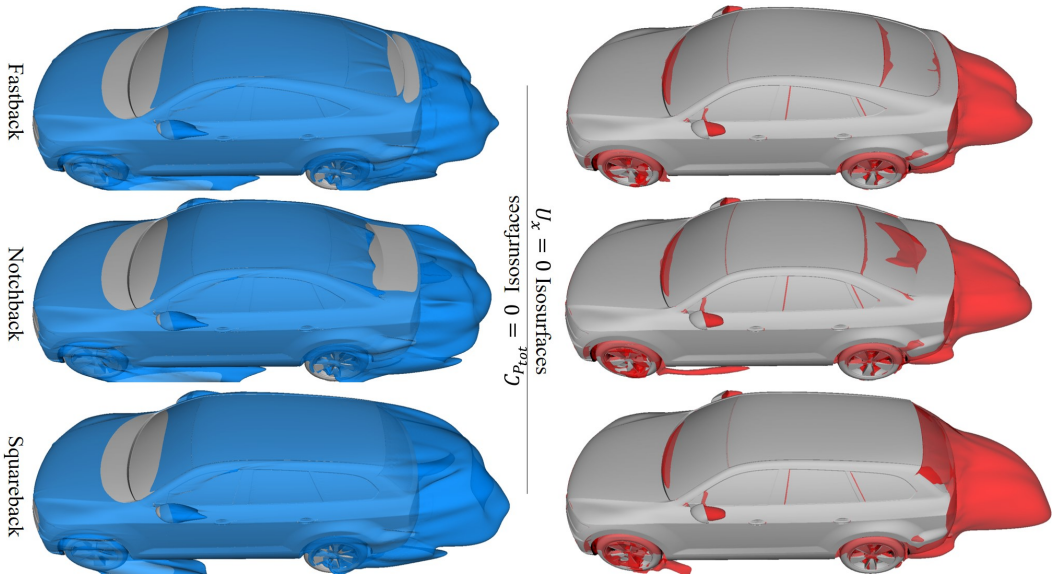

Figure 5.7: Zero total pressure isosurfaces, depicting the wake *(left)* and negative x-velocity isosurfaces, revealing the backflow regions *(right)*.

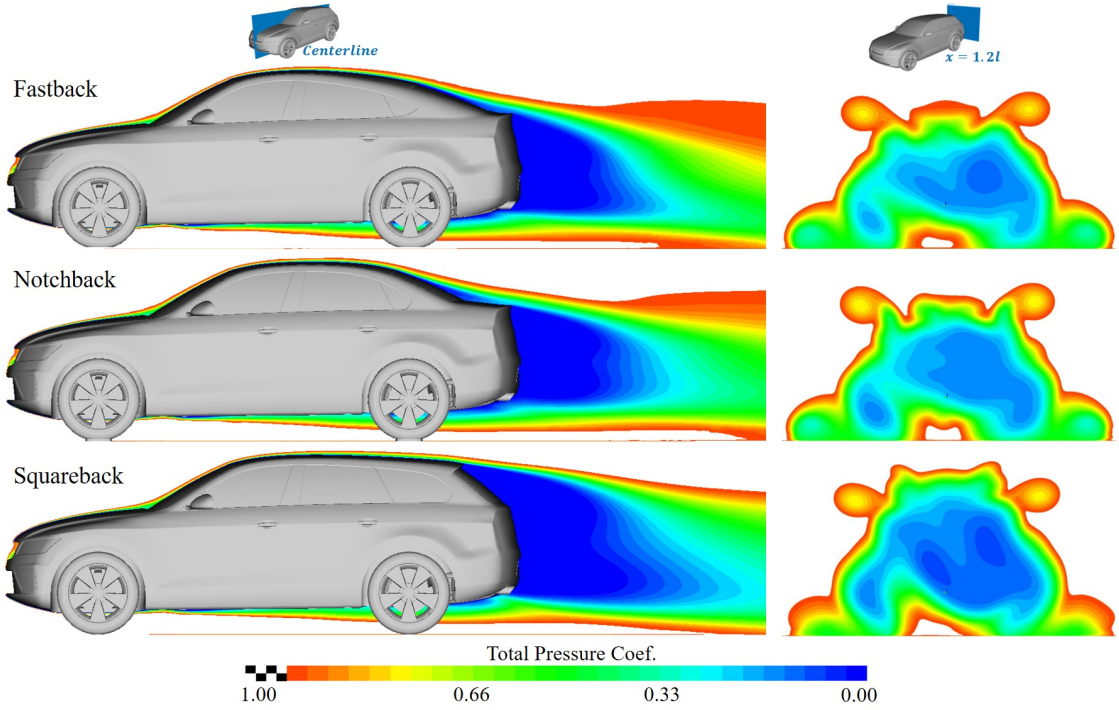

Figure 5.8: Y-normal centerline and X-normal total pressure planes depicting the wake downstream of the model.

5.4 CFD Simulations

The CFD setup that provided the best prediction for the SAE Notchback 20° Backlight reference model, was used as a baseline case for the numerical investigation of the AeroSUV model. More precisely, the surfaces of the model were discretized with the Trias surface meshing algorithm with 2mm maximum length, 1.2 growth rate and distortion angle equal to 10°. The volume of the domain was discretized with the Hexa Interior volume meshing algorithm and the refinement regions were declared with the use of the size boxes presented in Figure 3.15.

The rotating motion of the tyres was simulated with the use of a moving wall boundary condition and with the Multiple Reference Frame (MRF) technique, used to simulate the swirling motion of the air between the spokes of the rims; for transient simulations, the Dynamic Mesh technique was used with the use of non-conformal interfaces. For the numerical solution, the simpleFoam and pimpleFoam OpenFOAM solvers were used, for the steady RANS and transient DDES simulations, respectively, with the parameters used for the SAE Notchback. The maximum accepted deviation from the experimental drag coefficient was set to ±1.5%; if the baseline CFD setup is not able achieve this level of accuracy, then a new parameters investigation should be conducted to improve the predicted results.

5.4.1 Fastback

The specifications of the mesh generated on the fastback model by using the baseline CFD parameters are presented in Table 5.2. The layers were generated by following the low-Reynolds approach with main objective to achieve a y^+ value lower than 1 on the surfaces of the model. The y^+ distribution presented in Figure 5.9, reveals that y^+ values lower than 1 were achieved in almost every surface of the model, except for some small regions at the front bumper, the underfloor, the A-Pillar and the mirrors, where values up to 1.5 are observed due to local flow acceleration caused by the convex curvature of the geometry.

Table 5.2: Surface and volume mesh specifications of the baseline simulation conducted on the AeroSUV fastback.

	Elements(mi)		**Layers**	$\boldsymbol{C_{size}/l_{ref}}$ (%)		
Model	**Shell**	**Volume**	**Approach**	**Max**	**Min**	**Mesh ID**
Fastback	6.0 *(Trias)*	150.3 *(HexaInt)*	Low-Re	0.35	0.17	fpd_fhi

The minimum and maximum cell size indicator (C_{size}/l_{ref}) used for the volume meshing of each AeroSUV configuration was selected after a mesh independency study conducted on a simplified model with smooth underfloor due to limited computational sources. Hence, for the fastback configuration, the baseline mesh was capable of resolving flow structures in the scale of $0.17\% \cdot l_{ref} = 1.96mm$. It is worth mentioning that the computational grid was further refined at the tyre contact patch regions, where the flow inside the grooves of the tyre was simulated as well, however this cell size is not considered during the calculation of the minimum cell size indicator.

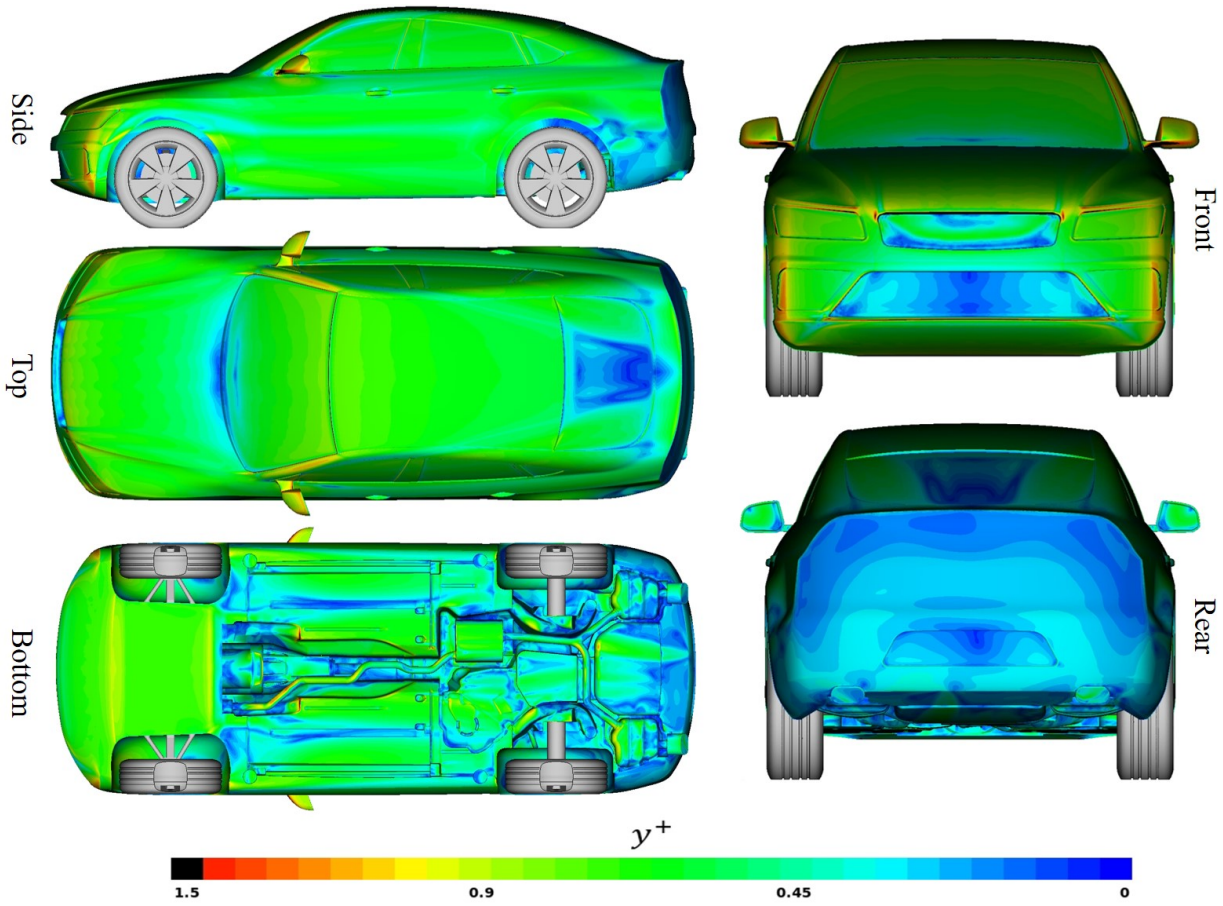

Figure 5.9: y^+ distribution across the AeroSUV fastback model.

The outcome of the fastback configuration simulation is presented in Table 5.3. The simulation ran for ten thousand iterations and the results of the last 1500 iterations were averaged since the drag coefficient did not converge to a sole value due to the unsteady flow field formed downstream of the model. The simulation was conducted in 24 cores running in parallel; each iteration demanded approximately 79 seconds to complete and the RAM used for the numerical solution was 162GB. The Root Mean Square (RMS) residuals dropped below 10^{-3} and the deviation from the experimental drag coefficient was -0.28% which satisfies the maximum accepted deviation condition that was set, and consequently no further investigation is needed.

Table 5.3: Results of the baseline simulation of the AeroSUV fastback model.

Case	C_D	**Error**(%)	**t/iter**(s)	**RAM**(GB)
Exp	0.286	-	-	-
Baseline	0.285	-0.28	79	162

5.4.2 Notchback

The baseline CFD setup was also used for the simulation of the AeroSUV notchback configuration and the specifications of the computational grid generated with the these parameters are presented in Table 5.4.

Table 5.4: Surface and volume mesh specifications of the baseline simulation conducted on the AeroSUV notchback.

	Elements(mi)		**Layers**	C_{size}/l_{ref} (%)		
Case	**Shell**	**Volume**	**Approach**	**Max**	**Min**	**Mesh ID**
Notchback	6.6 *(Trias)*	183.9 *(HexaInt)*	Low-Re	0.35	0.17	npd_fhi

The surface mesh was refined at the C-Pillar, where boundary layer separation is likely to occur and consists of 6.6 million elements. Moreover, extra size-boxes were added to declare refinement regions downstream of the C-Pillar in order to increase the accuracy of the solver at these regions, resulting in a volume mesh with approximately 184 million cells, capable of resolving flow structures in the scale of $0.17\% \cdot l_{ref} = 1.96mm$. The layers were generated based on the low-Reynolds approach, and the y^+ distribution across the surfaces of the model is illustrated in Figure 5.10. In almost every surface of the model, y^+ values lower than 1 were achieved except for some regions where local flow acceleration takes place and values up to 1.5 are observed. At the middle section of the backlight, the boundary layer height is

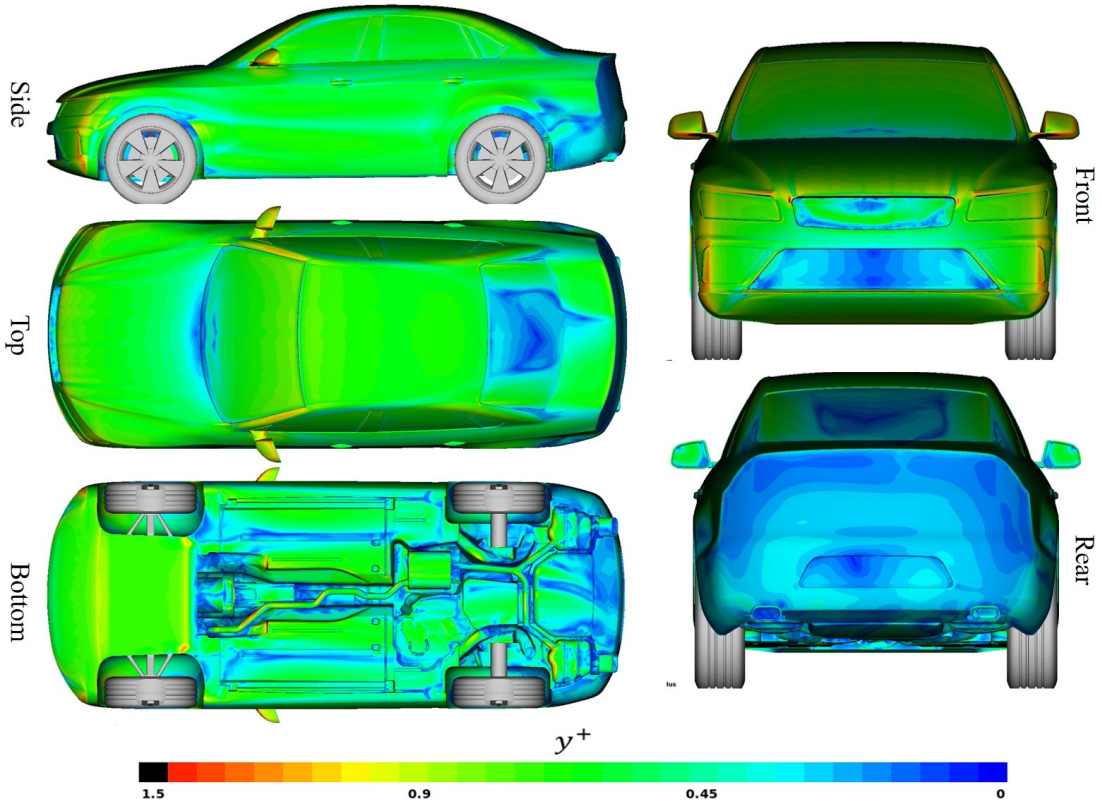

Figure 5.10: y^+ distribution across the AeroSUV notchback model.

increased, due to the energy consumed by the flow to remain attached at the highly angled backlight, and consequently the y^+ is almost zero due to low wall shear stress. The baseline simulation was conducted with the use of the steady state, isothermal and incompressible simpleFoam OpenFOAM solver along with the k-ω SST turbulence model. Similar to the fastback, the simulation ran for ten thousand iterations until the RMS residuals dropped below 10^{-3} and the last 1500 iterations were averaged to calculate the mean flow variables used for the post processing.

The outcome of this simulation is presented in Table 5.5; the simulation was conducted in 24 cores running in parallel, each iteration demanded 109 seconds to complete and the computational grid in combination with the solver settings used, demanded 191GB of RAM in order to conduct the simulation. The baseline simulation predicted the drag coefficient of the model with -0.97% error from the experimental value, which satisfies the maximum accepted deviation condition that was set and consequently no further investigation is needed for this configuration. The CFD methodology study carried out on the SAE Notchback 20° Backlight reference model, worked well for the fastback and notchback models which have similar rear end geometry with the SAE Notchback.

Table 5.5: Results of the baseline simulation of the AeroSUV notchback model.

Case	$\boldsymbol{C_D}$	**Error**(%)	**t/iter**(s)	**RAM**(GB)
Exp	0.286	-	-	-
Baseline	0.283	-0.97	109	191

5.4.3 Squareback

The baseline CFD setup was finally used for the AeroSUV squareback configuration as well. The same surface and volume mesh parameters with the other two cases were used and the only modification was the extension the refinement region further downstream of the model to ensure adequate mesh resolution at the wake area. A visualisation of the refinement regions that were used is depicted in Figure 5.11, where the maximum cell size set for the volume mesh around the model is 2.5mm, except for the volume mesh on the bonnet, the mirror vortices area which are meshed with maximum cell size equal to 1.25mm and the tyre patches are further refined to 0.625mm. These values comprise a computational grid consisting of 6.6 million shell elements and 173.2 million volume cells with a minimum cell size indicator equal to 0.13%, as presented in Table 5.6.

Table 5.6: Surface and volume mesh specifications of the baseline simulation conducted on the AeroSUV squareback.

	Elements(mi)		**Layers**	$\boldsymbol{C_{size}/l_{ref}}$ (%)		
Model	**Shell**	**Volume**	**Approach**	**Max**	**Min**	**Mesh ID**
Squareback	6.6 *(Trias)*	173.2 *(HexaInt)*	Low-Re	0.35	0.13	epd_fhi

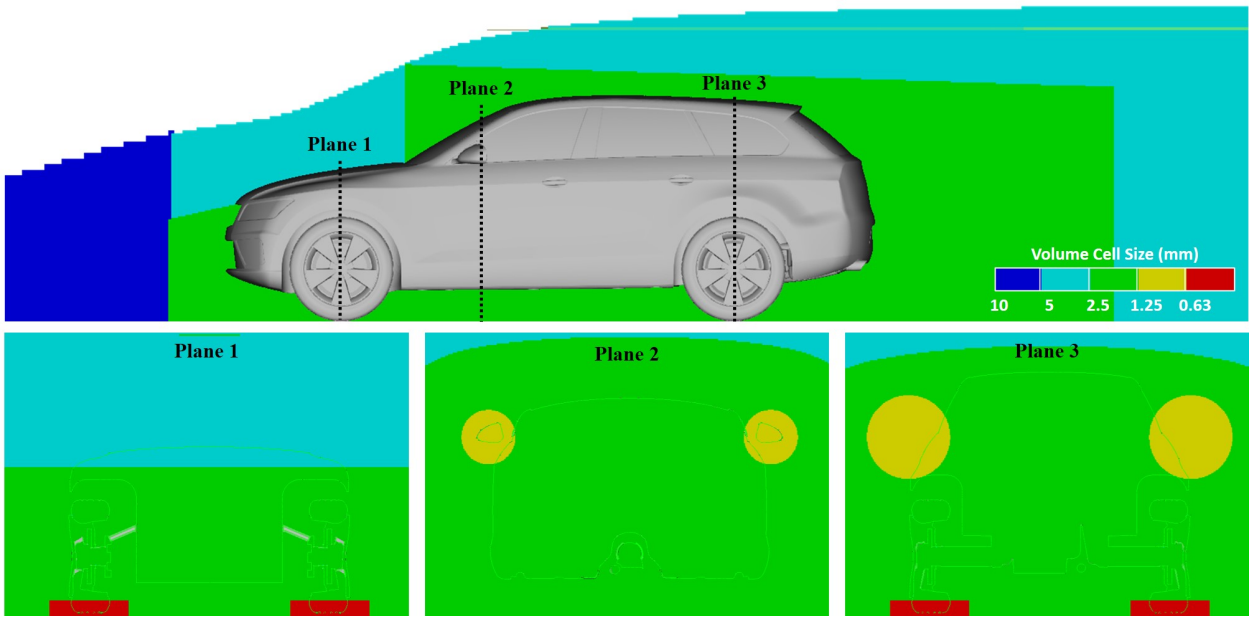

Figure 5.11: Refinement regions used for the AeroSUV squareback model.

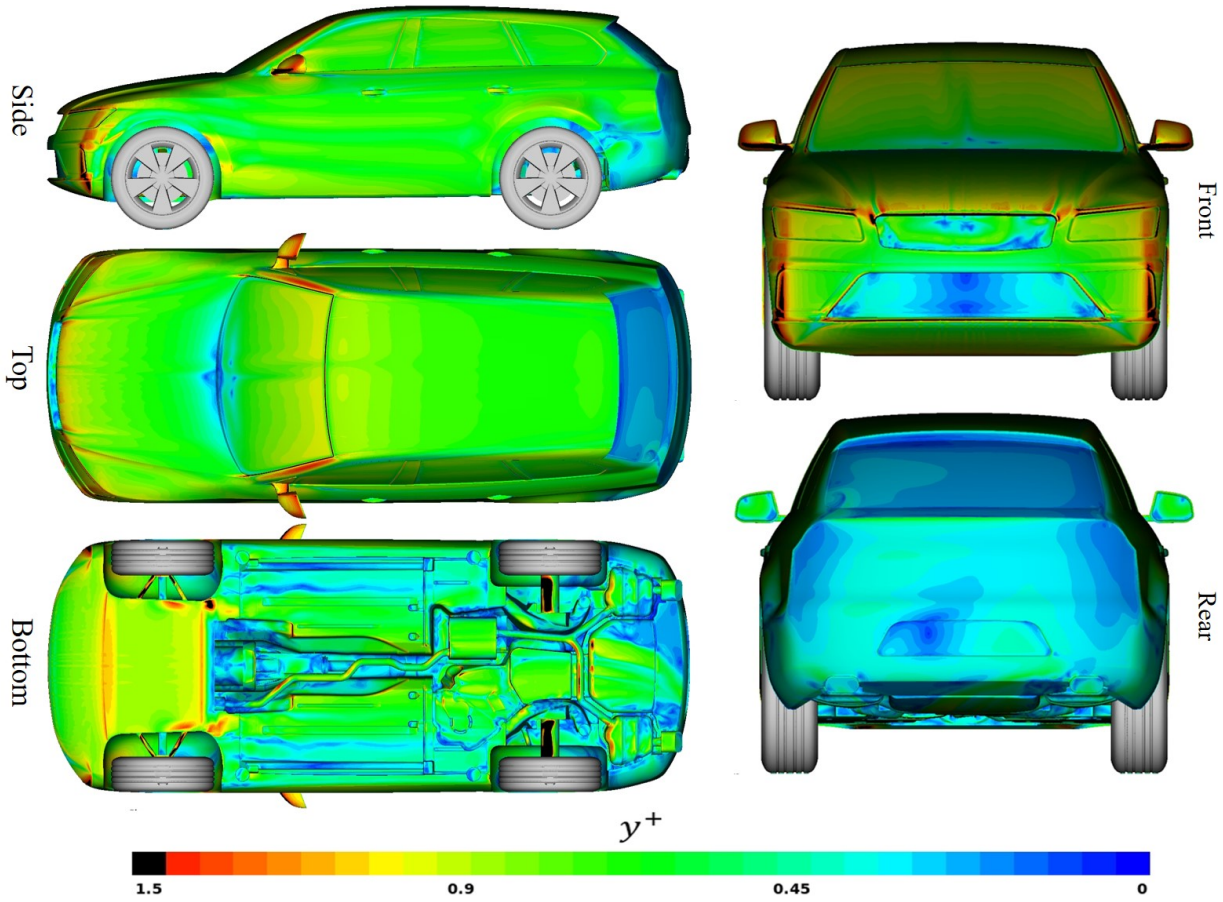

Figure 5.12: y^+ distribution across the AeroSUV squareback model.

The low-Reynolds approach was used for the generation the layers aiming for a $y+$ below one in almost every point on the model. The y^+ distribution across the model, presented in Figure 5.12, reveals values below 1 in almost every region of the model except for some convex surfaces where local flow acceleration and thus high wall shear stress occurs. The baseline simulation of this model was also conducted in 24 cores running in parallel, demanding 108 seconds to complete one iteration and 188GB of RAM. The simulation predicted the drag coefficient with -5.89% error, as presented in Table 5.7 which does not comply with the maximum accepted deviation condition that was set, and a new investigation of the CFD parameters should be carried out to find the most suitable setup for this model.

Table 5.7: Results of the baseline simulation of the AeroSUV squareback configuration.

Case	C_D	**Error**(%)	**t/iter**(s)	**RAM**(GB)
Exp	0.314	-	-	-
Baseline	0.295	-5.89	108	188

5.5 Squareback Investigation

5.5.1 Mesh Resolution

The CFD parameters investigation started with a mesh density study conducted on a simplified squareback model with smooth underfloor, due to limited computational resources. To further reduce the computational time needed for this investigation, since the model is symmetric, only the one side of the model was simulated with the use of a symmetric boundary condition at the centerline. Four different grid resolutions were put to test, presented in Table 5.8. The study started with a coarse mesh consisting of 11.5 million cells and the other grids were generated by refining the previous mesh by the refinement factor that is mentioned in every case. The coarse and fine cases were selected for direct comparison in order to see clearly the differences of the results.

Table 5.8: Surface and volume mesh specifications of the cases tested for the mesh density study of the simplified symmetric AeroSUV squareback.

	Elements(mi)		**Layers**	C_{size}/l_{ref} (%)		**Ref.**	
Case	**Shell**	**Volume**	**Approach**	**Max**	**Min**	**Factor**	**ID**
Coarse	0.3 *(Trias)*	11.5 *(HexaInt)*	Low-Re	0.66	0.13	-	efs_chi
Medium	0.7 *(Trias)*	27.8 *(HexaInt)*	Low-Re	0.41	0.19	2.41	efs_mhi
Fine	1.7 *(Trias)*	57.2 *(HexaInt)*	Low-Re	0.31	0.16	2.05	efs_fhi
Ultra-Fine	2.4 *(Trias)*	104.1 *(HexaInt)*	Low-Re	0.32	0.11	1.82	efs_ufhi

**Ref. Factor: refinement factor*

Surface Pressure

Figures 5.13 and 5.14 illustrate the pressure distribution across the model for a coarse and a fine mesh resolution case. The pressure distribution on the coarse mesh is of low quality

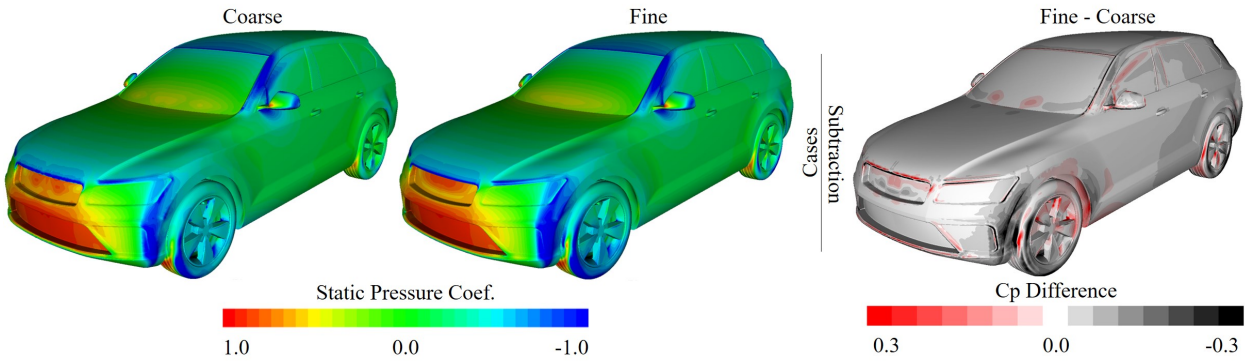

Figure 5.13: Front isometric view of surface pressure distribution across the AeroSUV squareback model for a coarse and a fine mesh resolution case *(left)* pressure divergence computed by subtracting the results of the cases and plotting the resultant pressure *(right)*.

and the pressure contours are sharp. On the other hand, the fine mesh resolution predicts a smoother pressure distribution on the upper grille and the bonnet. In addition, it calculates higher pressure at the stagnation point on the windshield and on the upper grille which is also clearly visible from the subtraction of the results.

Another difference worth mentioning is the pressure prediction on the side of the front bumper, upstream of the front wheels, also known as fender. The black contour at the results subtraction image indicates that the fine resolution mesh predicts lower negative pressure and thus higher near wall velocity at that region, compared to the coarse mesh. This difference on the fender can affect the accuracy of the simulation since the coarse mesh calculates lower wall shear stress at that point. The pressure distribution at the fender also affects the flow field at the front wheels, where a sizeable pressure difference is also depicted with black colour on the front and on the bottom of the front tyre. The subtraction of

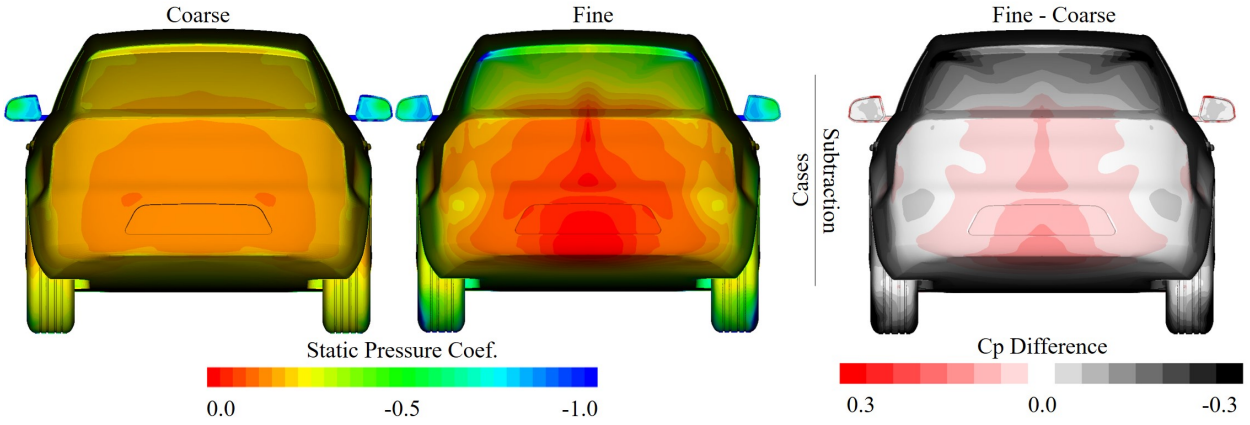

Figure 5.14: Rear view of surface pressure distribution across the AeroSUV squareback model for a coarse and a fine mesh resolution case *(left)* pressure divergence computed by subtracting the results of the cases and plotting the resultant pressure *(right)*.

the results reveals also a difference at the A-Pillar and the region where the A-Pillar vortex collides with the side glass. The fine mesh calculates lower negative pressure at the A-Pillar, but higher negative pressure at the side glass, compared to the coarse.

The rear view of the model depicts a completely different pressure distribution for the two cases. The coarse mesh predicts lower negative pressure at the rear bumper and higher at the backlight compared to the fine mesh. Moreover, the pressure distribution on the coarse mesh case is very diffusive and presents a uniform pressure field devoid of pressure fluctuations similar to those seen in the fine mesh case. Figure 5.15 presents the pressure distribution across the centerline of each model. At the front end of the model, the two cases predict almost similar pressure, however downstream of the windshield, the pressure predictions seems to deviate both at the upper and at the lower section. The fine mesh calculates lower negative pressure at the underfloor, higher flow velocity at that region and thus higher pressure at the rear bumper as it was mentioned above. This pressure difference can strongly affect the wake formed downstream of the model and consequently the drag force generated by the car.

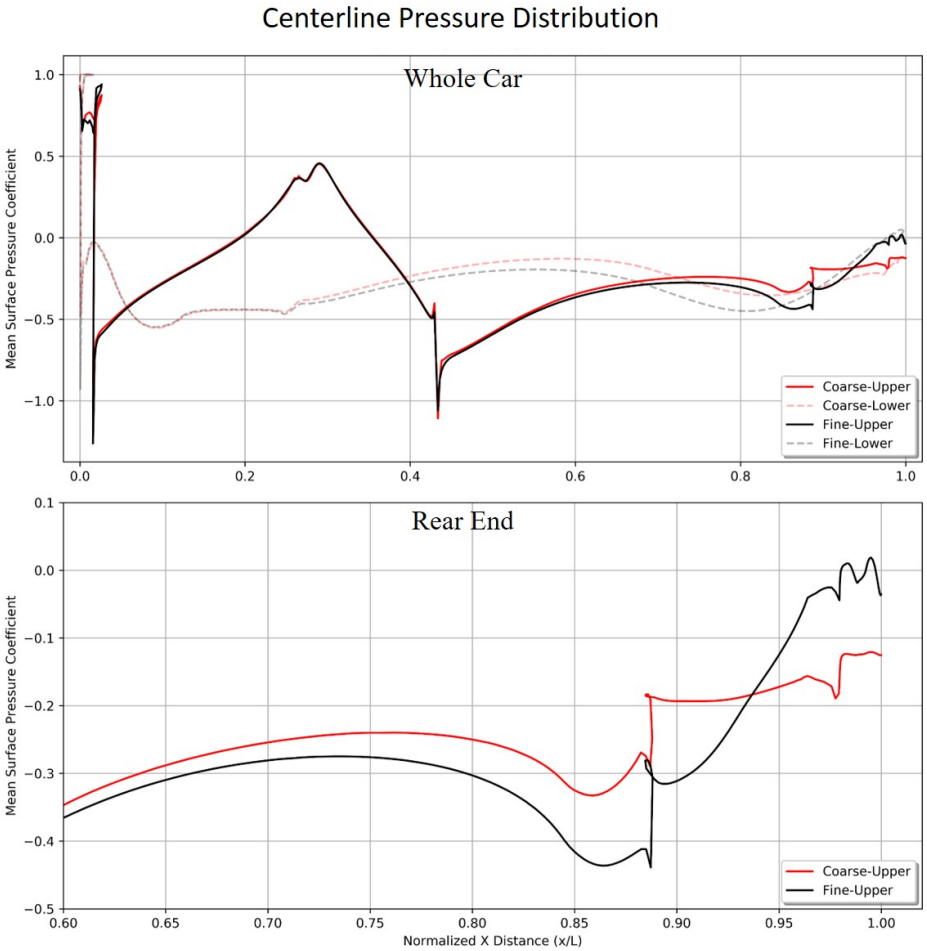

Figure 5.15: Pressure distribution across the centerline of the squareback model for a coarse and a fine mesh resolution case.

Vortex Cores

Figure 5.16 presents high vorticity regions visualised with the use of Lambda 2 Criterion isosurfaces for the coarse and the fine mesh simulations. The isosurfaces are also coloured with total pressure contours to provide information about the energy content of the flow. The vortical structures generated at the front end are almost the same for the two cases, however downstream of the windshield some differences can be observed. More precisely, focusing at the roof and the side windows, the fine mesh simulation shows clearly defined vortex regions in contrast to the coarse mesh were a more chaotic condition is predicted for both the L2=50.000 and L2=150.000 isosurfaces. Moreover, the A-Pillar and the mirror vortices seem to have lower energy content at the coarse simulation compared to the fine mesh, making them prone to early burst.

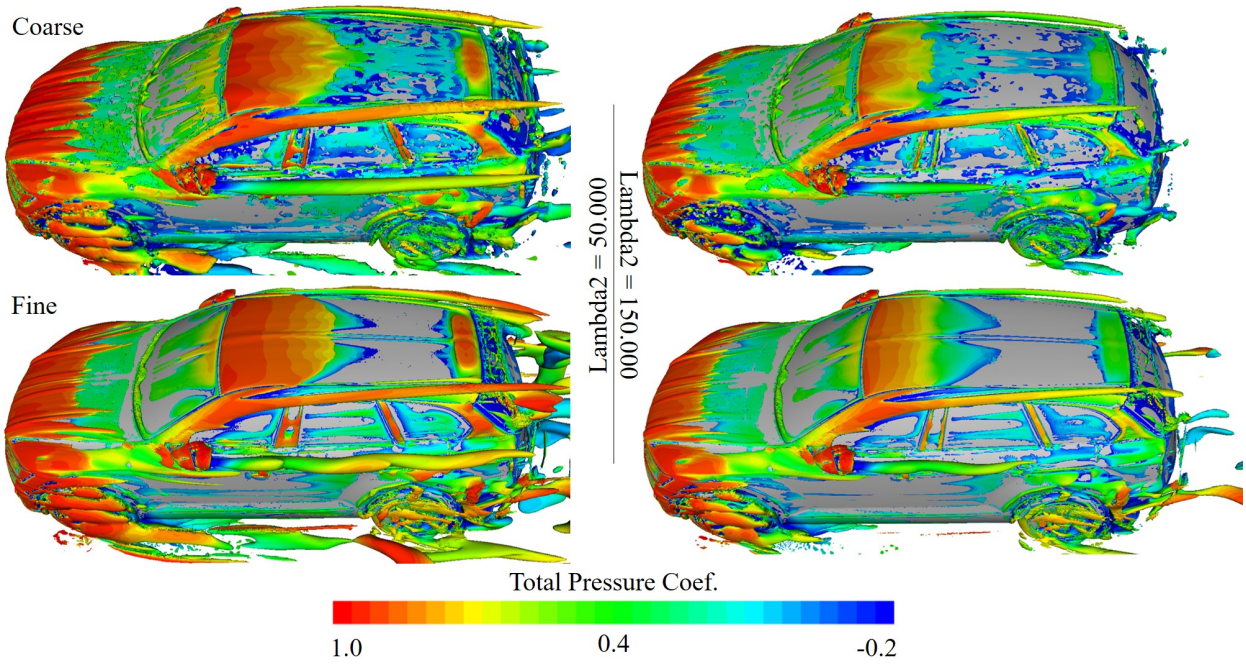

Figure 5.16: Vortex core visualisation through Lambda 2 Criterion isosurfaces, coloured with total pressure, for coarse and a fine resolution mesh case of the AeroSUV Squareback.

Wake

The wake formed downstream of the model for the two cases is presented in Figure 5.17. The coarse and fine mesh resolution simulations predicted a completely different wake pattern downstream of the model; the coarse mesh overestimates the wake's length resulting in lower energy at the $x = 1.2l$ plane. Finally, the two cases predict different boundary layer height at the bonnet and the underfloor, with the coarse mesh to predict less total pressure loss at these regions.

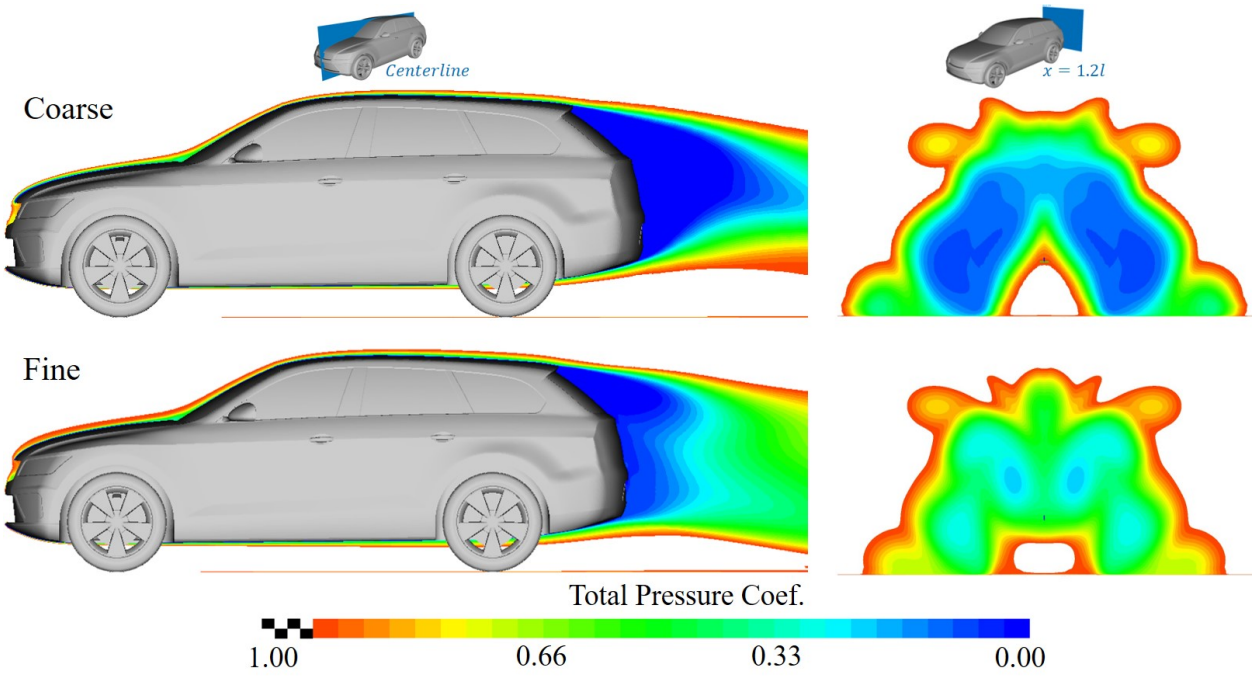

Figure 5.17: Y-normal centerline and X-normal total pressures planes depicting the wake downstream of the AeroSUV squareback model.

Conclusion

The outcome of the mesh resolution investigation for the simplified AeroSUV squareback investigation is presented in Table 5.9; the Delta_Cd parameter indicates the percentage change of the drag coefficient due to the increased mesh resolution. The experimental drag coefficient is not mentioned here since there are not available wind tunnel data for the AeroSUV model with smooth underfloor. From this investigation, the fine mesh setup was selected as the most suitable by making a compromise between the Delta_Cd parameter and the computational demands of each simulation due to limited computational sources.

Table 5.9: Mesh resolution investigation for the simplified AeroSUV squareback model.

Case	C_D	**Delta_Cd**(%)	**Error**(%)	**t/iter**(s)	**RAM**(GB)
Coarse	0.306	-	4.5	15	14
Medium	0.291	-4.91	16	29	31
Fine	0.285	-2.06	27	61	64
Ultra Fine	0.283	-0.84	43	107	111

5.5.2 Surface Mesh Type

The mesh parameters selected as the most suitable at the previous investigation were used to generate the surface and volume mesh for the cases simulated in this investigation, where the only variable was the surface mesh type. In contrast too the previous investigation, the

model used for this one was a fully detailed one. Two different surface meshing algorithms were used, namely the Trias and the Mixed algorithm. The mixed surface meshing algorithm has two key advantages. Firstly, it generates a shell mesh consisting of less elements, since two triangular elements are equal to one quadrilateral. The second advantage is that the layers generated from a quad dominated surface mesh are hexahedral elements which increase the accuracy and the stability of the numerical solution at the boundary layer region and decrease significantly the numerical diffusion. The surface and volume mesh specifications of the simulations conducted in this investigation are presented in Table 5.10.

Table 5.10: Surface and volume mesh specifications of the cases tested for the surface mesh type study of the one half of the symmetric AeroSUV squareback.

	Elements(mi)		**Layers**	C_{size}/l_{ref} (%)		
Case	**Shell**	**Volume**	**Approach**	**Max**	**Min**	**Mesh ID**
Trias	6.6 *(Trias)*	193.2 *(HexaInt)*	Low-Re	0.32	0.13	epd_fhi_2
Mixed	4.2 *(Mixed)*	174.8 *(HexaInt)*	Low-Re	0.31	0.11	epd_fhi_m

The case was meshed with the trias algorithm consists of 6.6 million shell elements, approximately 193 million volume cells and it is capable of resolving flow structures in the scale of $0.13\% \cdot l_{ref} = 1.5mm$. The computational grid generated with the mixed surface meshing algorithm consists of 4.2 million shell elements, 174.8 million volume cells and can resolve flow structures equal to $0.11\% \cdot l_{ref} = 1.3mm$; a detailed preview of the mixed surface mesh generated at the squareback model is illustrated in Figures 5.18 and 5.19.

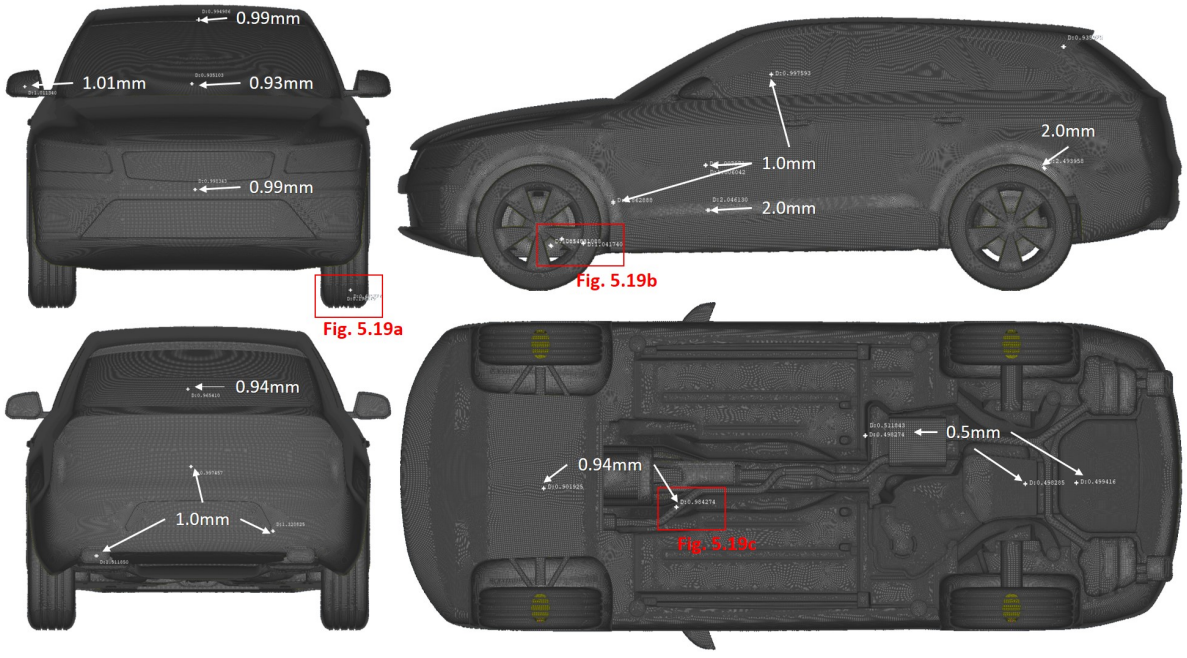

Figure 5.18: Basic views of the AeroSUV Squareback depicting the mesh resolution across the surfaces..

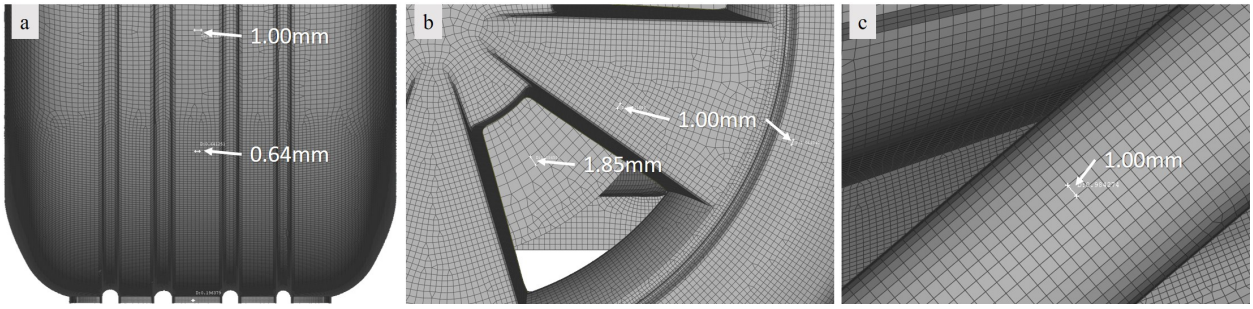

Figure 5.19: Surface mesh resolution across the (a) wheel and tyre patch, (b) rim and discbrake, (c) exhaust pipe.

Wall Shear stress

The wall shear stress distribution across the model, presented in Figure 5.20, reveals difference in the predicted flow field at the windshield, the fenders, the bonnet and the mirrors. The trias surface mesh case calculates higher wall shear stress at the start of the windshield, where the stagnation point exists. In almost every convex surface, where the flow accelerates locally, the mixed surface mesh case predicts higher wall shear stress, which is clearly illustrated by the red colour at the results subtraction contours. The surface pressure distribution, does not reveal any noteworthy difference on the model.

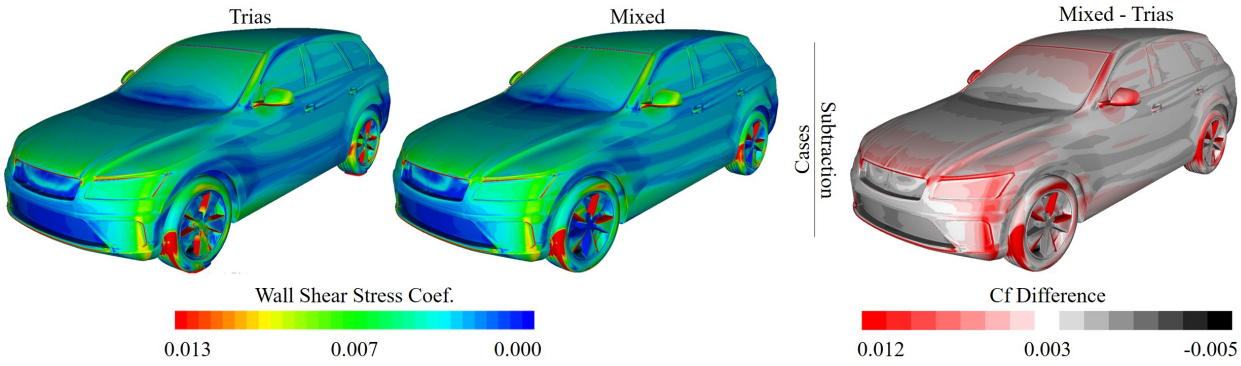

Figure 5.20: Front isometric view of wall shear stress distribution across the AeroSUV squareback model for a trias and a mixed surface mesh *(left)* wall shear stress divergence computed by subtracting the results of the cases and plotting the resultant value *(right)*.

Vortex Cores

The vortical structures formed around the model are presented in Figure 5.21 with the use of Lambda 2 Criterion isosurfaces. The flow field at the front bumper, the bonnet and the wheels seems to be almost identical for the two cases. The major difference is the prediction of the A-Pillar vortices; these vortices are located inside the boundary layer of the roof and the side windows. The mixed surface mesh case consists of hexahedral elements at the layers, generated to resolve the boundary layer with high accuracy. This case predicts longer

expansion of the A-Pillar vortices compared to the trias surface mesh case that presents an early burst of these vortices upstream of the trailing pillar.

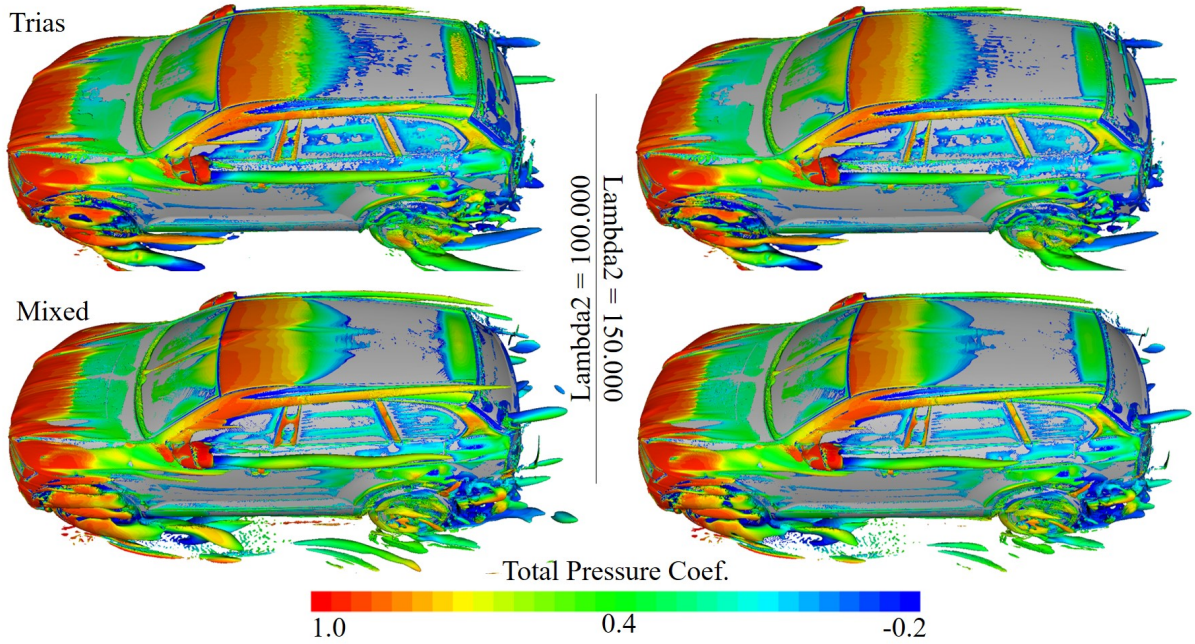

Figure 5.21: Vortical structures formed around the AeroSUV squareback mode, visualised with Lambda 2 Criterion isosurfaces.

Conclusion

The AeroSUV squareback model is a challenging case to simulate accurately due to the extended and unsteady wake formed downstream of the model. The wake pumping phenomenon, further increases the fluctuations on the generated drag force. The aerodynamic forces acting on the model do not converge to a constant value; the history of the drag and lift coefficient during the mixed surface mesh simulation is presented in Figure 5.22. The values used for the post processing were exported by averaging the last 1500 iterations, where the drag and lift coefficients seem to fluctuate around a constant value and the RMS residuals have dropped below 10^{-3}. The outcome of the surface mesh type investigation is presented in Table 5.11.

Table 5.11: Results of the surface mesh type investigation for the fully detailed AeroSUV Squareback model.

Case	C_D	**Error**(%)	**t/iter**(s)	**RAM**(GB)
Exp	0.314	-	-	-
Trias	0.305	-2.75	110	204
Mixed	0.309	-1.76	101	189

The simulation conducted on the trias surface mesh case, provided a better drag coefficient prediction compared to the baseline simulation, presented in Table 5.7, with -2.75% deviation

from the experimental value. The mixed surface mesh case provided the most accurate drag force prediction, with -1.76% deviation from the experimental value, demanding 189GB of RAM and 101 seconds to complete one iteration. Taking into consideration the high complexity of the wake formed downstream of the model, the sizeable computational time needed for such a simulation (9520 CPU hours) and the -1.76% error of this simulation, which is very close to the maximum deviation value set at the start of the research, this simulation will be considered as the most accurate and no further investigation will be conducted on the mesh and solver settings.

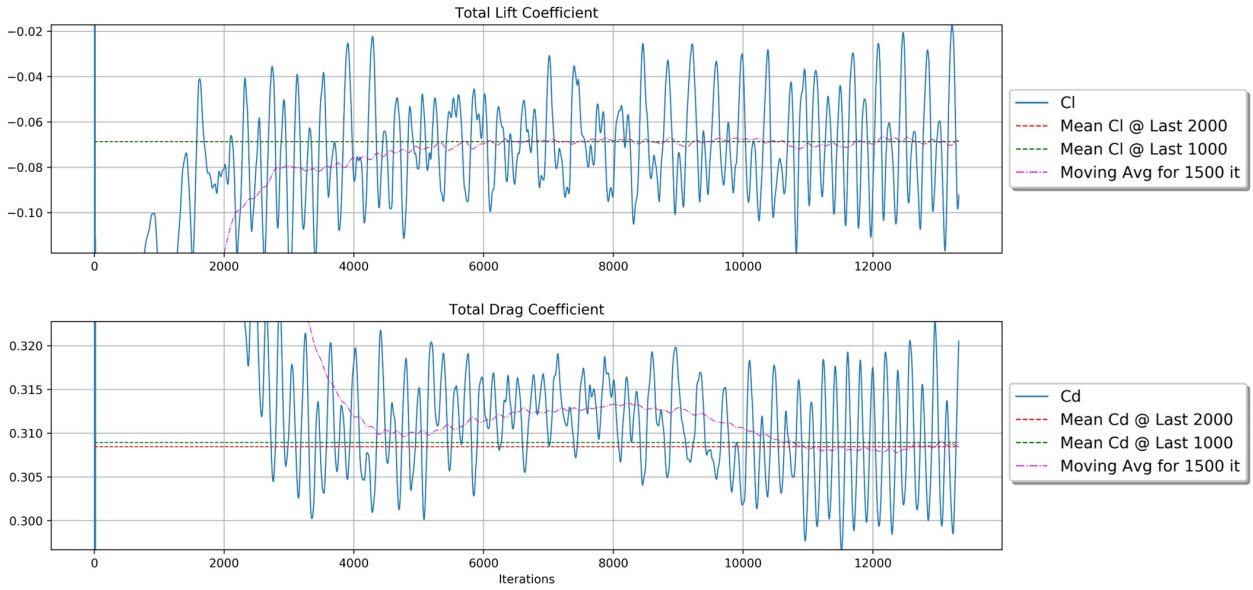

Figure 5.22: Total lift and drag coefficient convergence history for the steady state simulation of the mixed surface mesh AeroSUV Squareback case.

5.5.3 Transient Simulation

The last step of the AeroSUV Squareback investigation was to test whether a transient simulation of a medium resolution mesh is able to predict the generated drag force with high accuracy. A transient simulation will account for the unsteady nature of the wake and will provide a more accurate result compared to a steady state RANS simulation, where the flow field is time and space averaged. The surface mesh was generated with the mixed surface mesh algorithm, and specifications regarding both the shell and volume elements are presented in Table 5.12. The simulation was conducted with the use of the hybrid RANS-LES

Table 5.12: Surface and volume mesh specifications of the case used for the transient DDES simulation of the AeroSUV squareback.

	Elements(mi)		**Layers**	C_{size}/l_{ref} (%)		
Case	**Shell**	**Volume**	**Approach**	**Max**	**Min**	**Mesh ID**
k-ω DDES	3.1 *(Mixed)*	150 *(HexaInt)*	Low-Re	0.42	0.21	epd_mhi_m

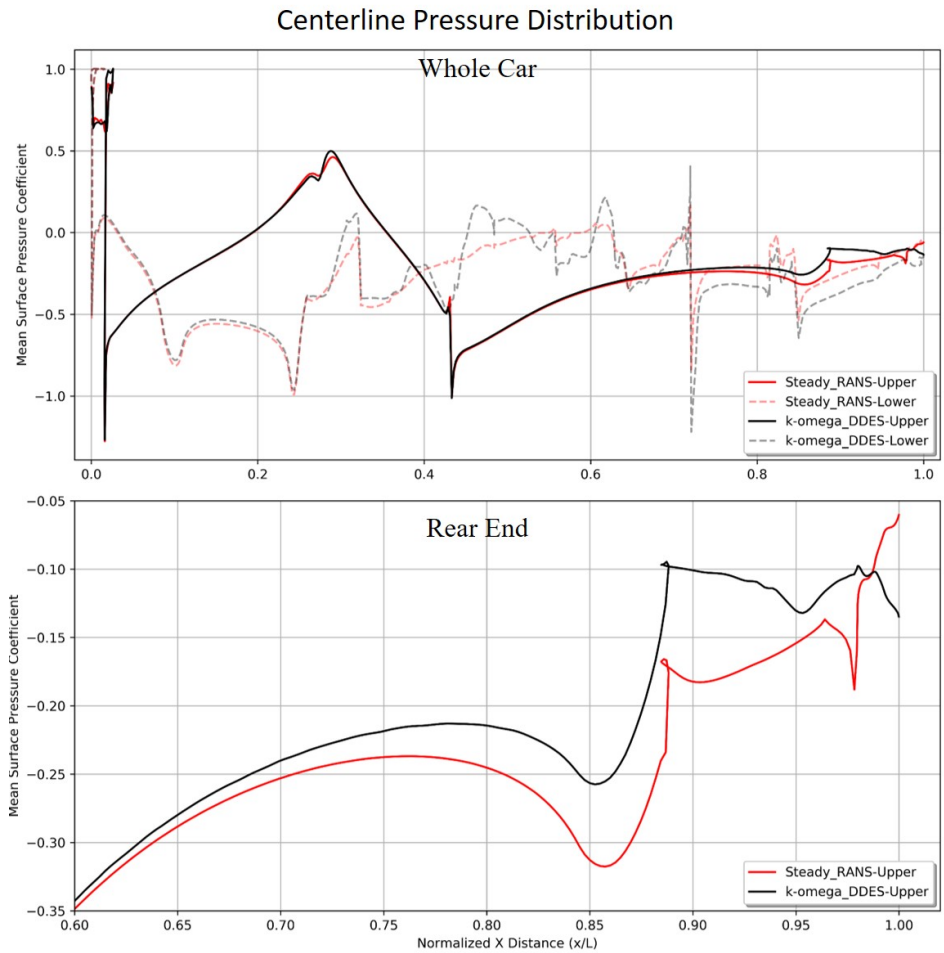

Figure 5.23: Pressure distribution across the centerline of the squareback model for a RANS and a DDES simulation.

method, namely the Delayed Detached Eddy Simulation (DDES) combined with the k-ω SST turbulence model. The incompressible, isothermal and transient pimpleFoam solver was used and the time step was selected so as 85% of the volume cells to have Courant number less than 1.

The medium resolution mesh used, consists of 3.1 million shell elements, 150 million volume cells and it is capable of resolving flow structures in the scale of $0.21\% \cdot l_{ref} = 2.42mm$; structures with size smaller than this are treated as subgrid scale phenomena. The results of the transient simulation reported below are averaged based on the method presented at Chapter 3.2.4: "Convergence Criteria", so the presented results are the mean and not the instantaneous values of the flow field variables. In this section, the results of the transient simulation will be compared with the most accurate steady state RANS simulation, namely the Mixed case presented in Table 5.11, to assess the similarity of the predictions.

Surface pressure

The pressure distribution across the squareback model for the RANS and DDES simulations is depicted in Figures 5.23 and 5.24. The surface pressure at the upper section, presented at the chart, seems to agree for the two cases except for the rear end of the car, where the transient simulation predicts higher negative pressure at the backlight and the spoiler. The pressure peaks at the stagnation and acceleration regions of the model have almost the same values for both cases. The surface pressure distribution presented in Figure5.24 reveals many similarities as well, both at the rear end and at the underfloor but the cases cannot be characterised as identical. More precisely, the two cases seem to agree at the A-Pillar, the B-Pillar and the region around the mirror, however the steady state case predicts higher pressure at the side of the vehicle and especially at the rear fenders. In addition, the two cases predict completely different distribution inside the rims; this is mainly due to the numerical error introduced by the non-conformal interfaces used for the Dynamic Mesh technique to simulate the rotating motion of the rim at the DDES simulation.

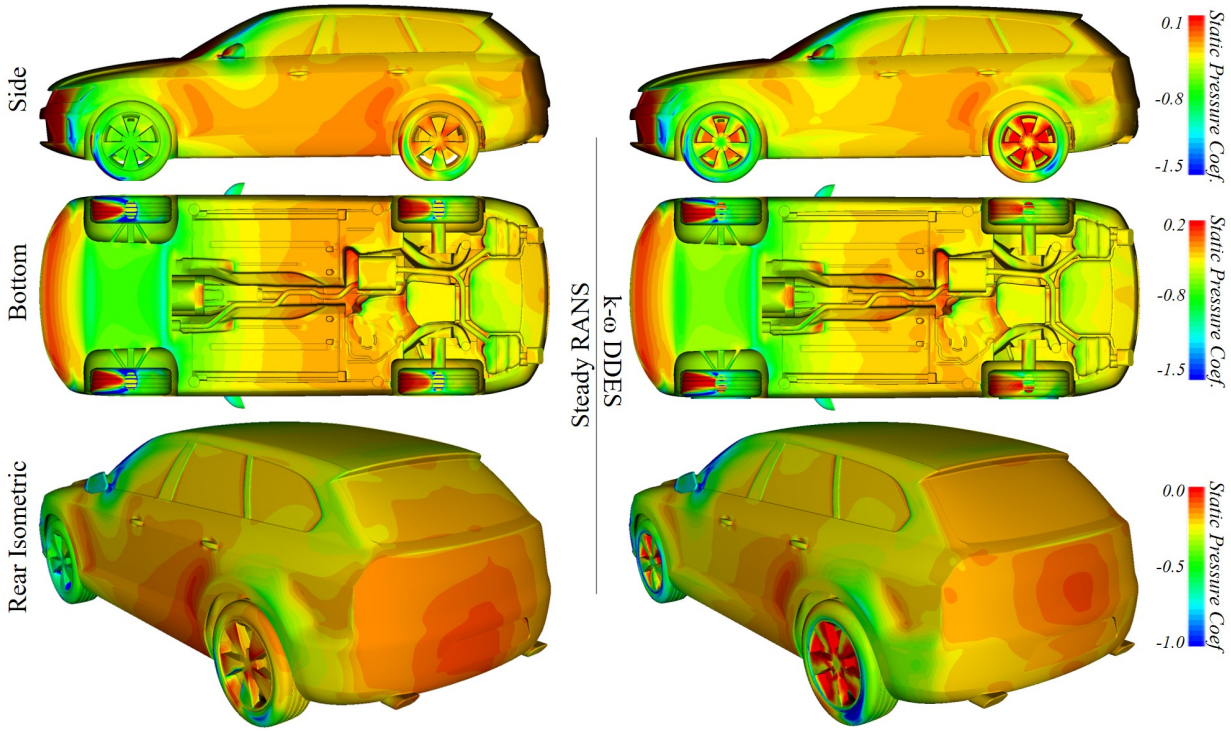

Figure 5.24: Surface pressure distribution for a RANS *(left)* and a DDES *(right)* simulation of the AeroSUV squareback model.

Vortex Cores

The isosurfaces visualising high vorticity regions, seen in Figure 5.25, depict almost similar flow field at the front end including the front bumper, the front tyre, the bonnet and the windshield. In addition, the A-Pillar regime predicted by both models, reveal the same vortical structures for both L2=50.000 and L2=150.000 isosurfaces. However, the medium

mesh used for the transient simulation is prone to numerical diffusion, due to inadequate spatial resolution, and thus it predicts earlier A-Pillar vortex burst than the steady state RANS case. The flow field downstream of the mirrors cannot be compared between the cases since the DDES case splits the main vortex into several smaller vortices acting more like a wake than a coherent vortical structure.

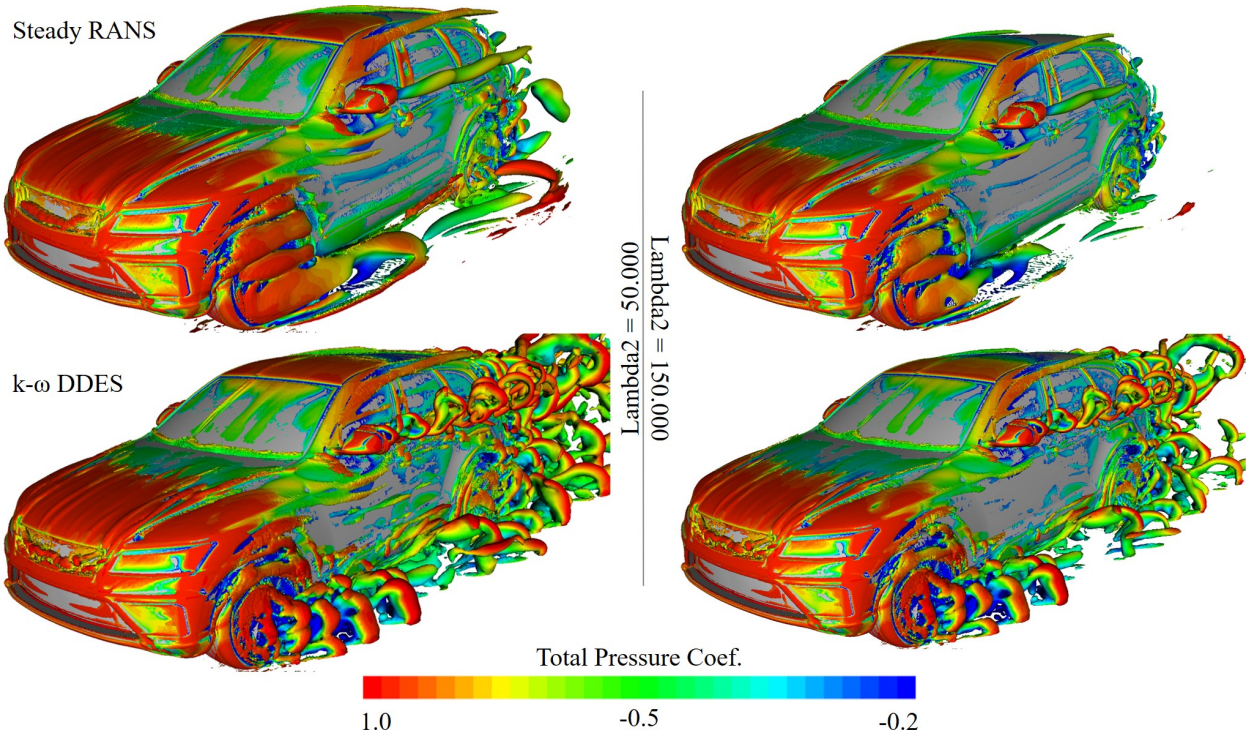

Figure 5.25: Vortical structures visualised by Lambda 2 Criterion isosurfaces for a RANS *(left)* and a DDES *(right)* simulation of the AeroSUV squareback mode.

Wake

The wake formed downstream of the squareback model for the two cases is illustrated in Figure 5.26. The transient simulation predicts a larger wake expansion than the steady state case, which can lead to overestimation of the drag force generated by the model. The boundary layer formed at the upper surface of the model seems to be the same for both cases, however the transient case calculates lower total pressure at the underfloor resulting in greater wake. The medium resolution mesh used for the transient simulation is not able to resolve accurately the turbulent kinetic energy of the flow, and consequently, the solver merges small flow structures into bigger ones which are then transformed into wake due to numerical diffusion. This phenomenon can be also seen in $x = 1.2l$ plane, where the wake pattern of the transient case expands in a greater area than the steady state case.

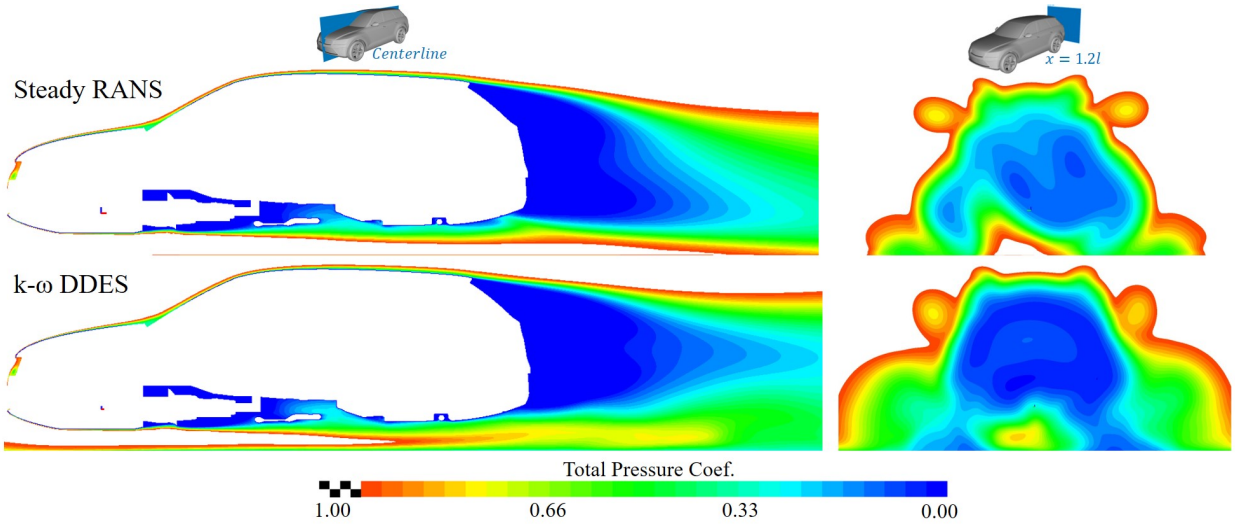

Figure 5.26: Y-normal centerline and X-normal total pressures planes depicting the wake downstream of the AeroSUV squareback model.

Conclusion

The outcome of the comparison between the steady state RANS and the transient k-ω DDES case is presented in Table 5.13. The last 20 convective flow fields were averaged to calculated the drag force predicted by the transient simulation, resulting in a higher drag coefficient than the experimental value, with +6.55% deviation. This simulation demanded 159GB of RAM, 86 seconds to complete one iteration and a 58266 CPU hours to simulate 0.575 seconds of physical time. It is clear that a transient simulation of this case is not efficient since to achieve high accuracy, a high resolution mesh is needed to allow the solver to resolve adequate amount of turbulent kinetic energy. However, due to limited computational resources, it was not affordable to run a DDES on a finer mesh and the most efficient way to simulate an SUV model with squareback-like rear end geometry is to conduct a steady state RANS simulation with the fine mesh resolutions setup.

Table 5.13: Results of the a transient k-ω DDES and a steady state RANS simulation of the fully detailed AeroSUV Squareback model.

Case	C_D	**Error**(%)	**t/iter**(s)	**RAM**(GB)	**CPU Hours**
Exp	0.314	-	-	-	-
k-ω DDES	0.334	+6.55	86	159	58266
RANS	0.309	-1.76	119	211	9520

5.5.4 Conclusion

The CFD setup that was exported through the SAE Notchback 20° Backlight investigation was used as a baseline setup for the numerical investigation of the AeroSUV variants. The fastback and notchback configurations have similar rear end geometry with the SAE

Notchback model and the simulations conducted with the baseline setup predicted the drag coefficient with high accuracy, namely -0.28% and -0.97% deviation from the experimental value, respectively.

However, the AeroSUV squareback configuration generates a completely different flow field downstream of the car, compared to the other two variants. The abrupt surface of the backlight leads to a clearly defined separation at the rear end of the roof that forms a greater wake region resulting in higher drag force. Inside the wake, several phenomena take place, such as trapped vortices, reversed flow regions, wake pumping and shear layer interaction increasing the complexity of the wake and making the flow field unsteady and difficult to simulate accurately. A new investigation had to be conducted especially for the squareback variant, with main variables being the mesh parameters. Finally, the most accurate simulation predicted the drag force generated by the vehicle with -1.76% deviation from the experimental data.

The final outcome of the AeroSUV investigation is that the CFD parameters that was exported from simplified geometries, such as the SAE Notchback 20° Backlight, can be utilized for the simulation of more realistic models, as long as they have similar geometries, especially at the rear end, and they generate similar flow patterns. For geometries with less similarities with the SAE Notchback model, such as the squareback variant, another simplified model should be used for the preliminary research, such as the generic SUV reference model corresponding to Wood *et al.*, presented in Chapter 1.5: "Reference Models".

6 Concluding Remarks

"In the end, there is no end."

-Robert Lowell

6.1 Conclusion

Increasing the accuracy of the CFD simulations while maintaining computational time in an affordable level is of utmost importance for the design and optimization of modern day road vehicles. The objective of this research was to check whether a simplified model can be used to export a CFD setup which will be also valid for a realistic fully detailed model. The SAE Notchback 20° Backlight was used to test different meshing algorithms and parameters and these computational grids were then used to test various solver settings and simulation approaches. To check the validity, the most accurate CFD setup was applied on the three different variants of the AeroSUV reference model.

SAE Notchback 20° Backlight

The outcome of the research conducted in the SAE Notchback 20° Backlight model is presented in the following bullets.

- The experimental values used to assess the accuracy of the simulations conducted on this model was the drag coefficient, measured via a high accuracy scale, and the pressure distribution on the centerline of the model, measured with the use of pressure taps.
- Mesh independency was achieved for computational grids consisting of more that 90 million elements. For some investigations where coarser grids were used to reduce the computational time, a finer mesh was simulated to find the trend of the solution with regards to the mesh resolution.
- For this model, the trias surface meshing algorithm provided a better prediction compared to the mixed surface meshing algorithm but the results of both cases were very close to the experimental data.
- The low-Reynolds approach was selected as the most suitable for this kind of simulations since the complex flow field generated at the rear end of the model requires accurate solution of the boundary layer at this region.
- The Hexa Interior volume meshing algorithm was selected as the most suitable after the completion of the investigation, with the Hexa Poly being the next most accurate. The Tetra Rapid algorithm provided the worst results and this is mainly due to the inability of OpenFOAM solvers to work with tetrahedral elements.

- The k-ω SST turbulence model provided the best prediction compared to the k-ϵ Realizable and the Spalart Allmaras with deviation from the experimental drag coefficient equal to -5.52% and -1.56% for a coarse and a medium grid resolution case.
- The best prediction was achieved with a transient k-ω DDES simulation conducted on a medium resolution grid and has -0.26% deviation from the experimental drag coefficient. However the computational time needed (7199 CPU hours) indicates that this simulation is not time efficient, and should be replaced by a fine resolution mesh steady-state RANS simulation, which was used as the baseline CFD setup for the investigation of the AeroSUV models.

AeroSUV

The CFD setup that predicted the drag coefficient with the highest accuracy and does not demand excessive computational time was selected to proceed with the study of the AeroSUV variants. For these models, the only experimental value that was used to assess the accuracy was the drag coefficient, since the surface pressure measurements were not available. The maximum accepted deviation from the experimental value was set to 1.5%. If the baseline CFD setup was unable to achieve this level of accuracy, a new investigation will be conducted to decrease the error.

The outcome of the research conducted in the AeroSUV variants, namely the fastback, notchback and squareback models, is presented in the following bullets.

- The fastback and notchback models have similar rear end geometry with the SAE Notchback 20° Backlight and the baseline CFD setup managed to achieve the needed accuracy; the deviation from the experimental values was -0.28% and -0.97% respectively. For the squareback model, the error was -5.89%, the needed accuracy was not achieved and a new CFD setup investigation was conducted with main variables being the mesh parameters.
- The mesh independency for the simplified AeroSUV squareback model was achieved for computational grids with more than 114 million cells. Taking advantage of the symmetric geometry of that model, only the one half was used for the mesh sensitivity study, due to limited computational resources.
- The refinement regions were extended, and a surface mesh type investigation was carried out. The mixed surface meshing algorithm provided a better prediction of the drag coefficient with -1.76% compared to the -2.75% error of the trias surface mesh simulation. Taking into consideration the complexity of the flow field generated by this model as well as the sizeable time needed to conduct a high resolution simulation, the investigation of the CFD parameters was terminated and the mixed surface mesh case was selected as the most suitable.
- The last step of the investigation of the squareback model was to test whether a transient simulation of a medium resolution mesh can provide an accurate prediction of the drag coefficient. The DDES simulation conducted on the squareback model, failed

to predict the drag coefficient accurately and demanded 58266 CPU hours; hence a transient simulation with a medium resolution mesh is not recommended.

- The SAE Notchback 20° Backlight reference model can be used to export a high accuracy CFD Setup for a more realistic model as long as they have similar geometries, such as the fastback and the notchback models. However, the squareback model has different rear end geometry and in order to export an accurate CFD setup, a squareback-like simplified model should be used, such as the generic SUV reference model corresponding to Wood *et al.*

6.2 Future Work

Various different parameters and experimental data sets have been left uninvestigated due to lack of time, and for maintaining the complexity of this research in a manageable level. Future work concerns deeper analysis of the results of every simulation and further investigation of meshing technics and solver parameters. The following ideas are proposed by the author for further investigation and evolution of this research:

- Utilize the whole set of surface pressure measurements of the SAE Notchback 20° Backlight exported through the wind tunnel testing at Loughborough University [2].
- Use the Particle Image Velocimetry (PIV) data set that is available for the SAE Notchback 20° Backlight to compare the CFD predicted flow field with the experimental one.
- Test whether a surface and volume mesh can be refined based on the generated flow field and whether the CFD accuracy can be improved.
- Delve deeper into OpenFOAM solver setting by altering the numerical schemes used during the solution process.
- Examine statistically the oscillations of the aerodynamic forces to find the right number of iterations to stop a simulation by assessing the level of uncertainty of the reported values.

References

[1] Chenyi Zhang, Max Tanneberger, Timo Kuthada, Felix Wittmeier, Jochen Wiedemann, and Juliane Nies. Introduction of the aeroSUV-a new generic suv model for aerodynamic research. *SAE Technical Papers*, 2019-April(April):1–11, 2019.

[2] Daniel Wood. The Effect of Rear Geometry Changes on the Notchback Flow Field. *PhD Thesis*, 304(September):285, 2015.

[3] W Hucho and G Sovran. Aerodynamics of Road Vehicles. *Annual Review of Fluid Mechanics*, 25(1):485–537, 1993.

[4] Petter Ekman. *Important Factors for Accurate Scale-Resolving Simulations of Automotive Aerodynamics*. Number 2068. 2020.

[5] Suv Stock Photos And Images - 123RF. https://www.123rf.com/stock-photo/suv.html?sti=mesmly4fai718f82f9%7C.

[6] Alexander Wäschle. The influence of rotating wheels on vehicle aerodynamics - numerical and experimental investigations. In *SAE Technical Paper*. SAE International, 04 2007.

[7] Hamed Shahmohamadi and Mohammad Mehdi Rashidi. Experimental investigation and a novel analytical solution of turbulent boundary layer flow over a flat plate in a wind tunnel. *International Journal of Mechanical Sciences*, 133:121 – 128, 2017.

[8] Richard Wood. Reynolds number impact on commercial vehicle aerodynamics and performance. *SAE International Journal of Commercial Vehicles*, 8:590–667, 09 2015.

[9] M. Van Dyke. *An Album of Fluid Motion*. An Album of Fluid Motion. Parabolic Press, 1982.

[10] Stephen B. Pope. Chapter 7: Wall Flows. *Turbulent Flows*, 2000(c), 2000.

[11] Wolfgang Mayer and Gerhard Wickern. The New Audi A6/A7 Family - Aerodynamic Development of Different Body Types on One Platform. *SAE International Journal of Passenger Cars - Mechanical Systems*, 4(1), apr 2011.

[12] Edward G. Duell and A. R. George. Experimental Study of a Ground Vehicle Body Unsteady Near Wake. mar 1999.

[13] Rob Littlewood and Martin Passmore. The optimization of roof trailing edge geometry of a simple square-back. In *SAE 2010 World Congress and Exhibition*. SAE International, apr 2010.

[14] Joshua Fuller and Martin A. Passmore. The importance of rear pillar geometry on fastback wake structures. *Journal of Wind Engineering and Industrial Aerodynamics*, 125:111–120, 2014.

[15] S.R. Ahmed, G. Ramm, and G. Faltin. Some salient features of the time-averaged ground vehicle wake. In *SAE Technical Paper*. SAE International, 02 1984.

[16] Takahide Nouzawa, Shigeru Haruna, Kazuhiko Hiasa, Takaki Nakamura, and Hiroshi Sato. Analysis of wake pattern for reducing aerodynamic drag of notchback model. In *SAE Technical Paper*. SAE International, 02 1990.

[17] Aidan Wimshurst. [cfd] what are wall functions and how do they work? https://www.youtube.com/watch?v=fJDYtEGMgzs.

[18] BETA-CAE System SA. ANSA for CFD brief user guide. pages 1–94, 2019.

[19] The Editors of Encyclopedia Brittanica. Nicolas-Joseph Cugnot — Facts, Invention, & Steam Car — Britannica. https://www.britannica.com/biography/Nicolas-Joseph-Cugnot, jul 1998.

[20] The Editors of Encyclopedia Brittanica. Model T — Description & Facts — Britannica. https://www.britannica.com/technology/Model-T, may 1999.

[21] History.com Editors. Energy Crisis (1970s) - HISTORY. https://www.history.com/topics/1970s/energy-crisis, aug 2010.

[22] European Commission. Transport emissions — Climate Action, 2014.

[23] Council of the EU. Cutting emissions: Council adopts CO2 standards for trucks - Consilium, 2019.

[24] Martin Dagan. Worldwide harmonized Light vehicles Test Procedure (WLTP) - Transport - Vehicle Regulations - UNECE Wiki. *wiki.unece.org*, 2012.

[25] S Tsiakmakis, G Fontaras, C Cubito, J Pavlovic, K Anagnostopoulos, and B Ciuffo. *From NEDC to WLTP: effect on the type-approval CO2 emissions of light-duty vehicles*. 2017.

[26] AUDI AG. How aerodynamics influence an electric car's range.

[27] Hideyuki Kawamata, Satoru Kuroda, Shingo Tanaka, and Munehiko Oshima. Improvement of Practical Electric Consumption by Drag Reducing under Cross Wind. *SAE Technical Papers*, 2016.

[28] UNECE. ECE R78 - Consolidated Resolution on the Construction of Vehicles. *United Nations Economic and Social Council*, (July), 2017.

[29] Daniel Wood, Martin A. Passmore, and Anna Kristina Perry. Experimental Data for the Validation of Numerical Methods - SAE Reference Notchback Model. *SAE International Journal of Passenger Cars - Mechanical Systems*, 7(1):145–154, 2014.

[30] Abdullah M. Al-Garni, Luis P. Bernal, and Bahram Khalighi. Experimental investigation of the flow around a generic SUV. *SAE Technical Papers*, 2004(724), 2004.

[31] Angelina I. Heft, Thomas Indinger, and Nikolaus A. Adams. Introduction of a new realistic generic car model for aerodynamic investigations. *SAE Technical Papers*, pages 1–5, 2012.

[32] Felix Wittmeier and Timo Kuthada. Open Grille DrivAer Model - First Results. *SAE International Journal of Passenger Cars - Mechanical Systems*, 8(1):252–260, 2015.

[33] Felix Wittmeier. The Recent Upgrade of the Model Scale Wind Tunnel of University of Stuttgart. *SAE International Journal of Passenger Cars - Mechanical Systems*, 10(1), 2017.

[34] Jochen Wiedemann and Juergen Potthoff. The new 5-belt road simulation system of the IVK wind tunnels - Design and first results. *SAE Technical Papers*, 2003(724), 2003.

[35] Philippe Angot and Jean-paul Caltagirone Pierre. Vector Penalty-Projection Methods for the Solution of Unsteady Incompressible Flows. *Methods*, (June 2008):1–8, 2008.

[36] R. Narasimha. The laminar-turbulent transition zone in the boundary layer. *Progress in Aerospace Sciences*, 22(1):29–80, 1985.

[37] G Eitel-Amor, Oscar Flores, and Philipp Schlatter. Hairpin vortices in turbulent boundary layers. *Journal of Physics: Conference Series*, 506:012008, 04 2014.

[38] H.K. Versteeg and W. Malalasekera. *An Introduction to Computational Fluid Dynamics: The Finite Volume Method*, volume 6. 2005.

[39] J.B. Southard. Introduction to Fluid Motions and Sediment Transport. *Book*, page 369, 2019.

[40] D. J. Tritton. *Physical Fluid Dynamics*. Springer Netherlands, Dordrecht, 1977.

[41] T. V. Karmann. *Aerodynamics*. McGraw-Hill, Dordrecht, 1963.

[42] The new all-electric EQS.

[43] Model S — Tesla United Kingdom.

[44] Lucid Air — Lucid Motors.

[45] Carr, G.W. Influence of Rear Body Shape on the Aerodynamic Characteristics of Saloon Cars. Motor Industry Research Association, Nuneaton (UK), 1974.

[46] Ilhan Bayraktar and Tuba Bayraktar. Guidelines for cfd simulations of ground vehicle aerodynamics. In *SAE 2006 Commercial Vehicle Engineering Congress Exhibition*. SAE International, oct 2006.

[47] F. Liu. A Thorough Description Of How Wall Functions Are Implemented In OpenFOAM. *CFD With OpenSource Software, edited by Nilsson H.*, 2016.

[48] Hrvoje Jasak. Error analysis and estimation for the finite volume method with applications to fluid flows. *Direct*, M, 01 1996.

[49] Pawel M Kurowski. Finite Element Analysis for Design Engineers, Second Edition. *Finite Element Analysis for Design Engineers, Second Edition*, 2016.

[50] A.N. Kolmogorov. The local structure of turbulence in incompressible viscous fluid for very large Reynolds numbers. *Proceedings of the Royal Society of London. Series A: Mathematical and Physical Sciences*, 434(1890):9–13, jul 1991.

[51] W. Bauer, O. Haag, and D.K. Hennecke. Accuracy and robustness of non-linear eddy viscosity models. *Engineering Turbulence Modelling and Experiments 4*, pages 113–124, 1999.

[52] G Schmitt. About Boussinesq ' s turbulent viscosity hypothesis : François G Schmitt To cite this version : HAL Id : hal-00264386 About Boussinesq ' s turbulent viscosity hypothesis : historical remarks and a direct evaluation of its validity. *Comptes Rendus Mécanique, Elsevier Masson*, 10:617–627, 2008.

[53] F. Menter. Zonal two equation k-w turbulence models for aerodynamic flows. *23rd Fluid Dynamics, Plasmadynamics, and Lasers Conference*, 1993.

[54] B. E. Launder and D. B. Spalding. Mathematical Models of Turbulence. *Academic Press*, 53(6):424–424, jan 1972.

[55] David C. Wilcox. Reassessment of the scale-determining equation for advanced turbulence models. *AIAA Journal*, 26(11):1299–1310, November 1988.

[56] P.R. Spalart and S. Allmaras. A one-equation turbulence model for aerodynamic flows. In *30th Aerospace Sciences Meeting and Exhibit*. American Institute of Aeronautics and Astronautics, January 1992.

[57] Pierre Sagaut, Sébastien Deck, and Marc Terracol. *Multiscale and Multiresolution Approaches in Turbulence*. World Scientific, may 2013.

[58] Jochen Fröhlich and Dominic von Terzi. Hybrid les/rans methods for the simulation of turbulent flows. *Progress in Aerospace Sciences*, 44:349–377, 07 2008.

[59] P. R. Spalart. Comments on the Feasibility of LES for Wings, and on a Hybrid RANS/LES Approach. In *first AFOSR international conference on DNS/LES*, pages 137–148. Greyden Press, 1997.

[60] P. R. Spalart, S. Deck, M. L. Shur, K. D. Squires, M. Kh Strelets, and A. Travin. A new version of detached-eddy simulation, resistant to ambiguous grid densities. *Theoretical and Computational Fluid Dynamics*, 20(3):181–195, jul 2006.

[61] OpenFOAM v6 User Guide: 4.4 Numerical schemes.

[62] R. Courant, K. Friedrichs, and H. Lewy. Uber die partiellen differenzengleichungen der mathematischen physik. *Mathematische Annalen*, 100(1):32–74, December 1928.

[63] Brian Cabral and Leith Casey Leedom. Imaging vector fields using line integral convolution. In *Proceedings of the 20th Annual Conference on Computer Graphics and Interactive Techniques*, SIGGRAPH '93, page 263–270, New York, NY, USA, 1993. Association for Computing Machinery.

[64] FKFS: Research In Motion: Wind Tunnels.

[65] G. Wickern, K. Zwicker, and M. Pfadenhauer. Rotating wheels - their impact on wind tunnel test techniques and on vehicle drag results. In *SAE International Congress and Exposition*. SAE International, feb 1997.